

**Experimental Investigation and Analytical Modeling of
Flow Boiling Characteristics in Silicon
Microchannel Arrays**

Ayman Megahed

A Thesis

in

The Department

of

Mechanical and Industrial Engineering

Presented in Partial Fulfillment of the Requirements
for the Degree of Doctor of Philosophy (Mechanical Engineering) at
Concordia University
Montreal, Quebec, Canada

April 2010

©Ayman Atef Megahed, 2010

**CONCORDIA UNIVERSITY
SCHOOL OF GRADUATE STUDIES**

This is to certify that the thesis prepared

By: Ayman Megahed

Entitled: Experimental Investigation and Analytical Modeling of Flow Boiling

Characteristics in Silicon Microchannel Arrays

and submitted in partial fulfillment of the requirements for the degree of

Doctor of Philosophy (Mechanical Engineering)

complies with the regulations of the University and meets the accepted standards with respect to originality and quality.

Signed by the final examining committee:

Dr. Sally Cole Chair

Dr. John Thome External Examiner

Dr. Amruthur Ramamurthy External to Program

Dr. Nabil Esmail, Dr. Lyes Kadem Examiner

Dr. Ali Dolatabadi, Dr. Hoi Dick Ng Examiner

Dr. Paula Wood-Adams Thesis Supervisor

Approved by

Chair of Department or Graduate Program Director

Dean of Faculty

ABSTRACT

Ayman Megahed, Ph.D.

Concordia University, 2010

In recent years, research in the field of flow boiling heat transfer at a microscale level has been constantly increasing due to rapid growth of technology applications that require the transfer of heat at high rates in a relatively small space and volume. The present study focuses on the experimental investigation and analytical modeling of flow boiling characteristics in silicon microchannel heat sinks. Two different designs of microchannel heat sinks were considered, namely, straight and cross-linked. The straight microchannel heat sink was composed of 45 parallel microchannels etched in a silicon wafer, for which each channel had a depth of 300 μm and a width of 242 μm . Three cross-link microchannels of width 500 μm were added to the straight microchannel design to create the cross-linked design. Experiments were carried out using FC-72 as the working fluid. Un-encapsulated Thermochromic Liquid Crystals were used, as full-field surface temperature sensors, to map the quantitative heat sink surface temperature and heat transfer coefficient measurements. In addition, the qualitative flow visualization was also considered to complement the experimental data for better understanding of two-phase flow characteristics.

In the straight microchannel heat sink, the results from the flow visualization study identified three major flow regimes: bubbly, slug, and annular. The frictional two-phase pressure drop was found to increase with exit quality for a constant mass flux. A new general correlation was developed to predict the two-phase pressure drop in microchannel heat sinks. The new correlation was verified with two extensive data sets from literature

in addition to the experimental data presented in this study. The present study provides the first qualitative and quantitative local experimental data on the characteristics of boiling incipience in microchannels, including the effect of mass and heat fluxes. Flow boiling heat transfer measurements showed that the heat transfer coefficient decreases sharply for low exit quality and then remains almost constant as the exit quality increases. Two-phase heat transfer coefficient asymptotic models and correlations in microchannels were found to underpredict the data in the nucleate boiling regime.

Based on fundamental conservation principles, an analytical model was proposed to predict the flow boiling heat transfer coefficient in the annular flow regime in mini- and microchannel heat sinks. The model was validated against collected data sets from literature produced by different authors under different experimental conditions with a mean absolute error of 10%. The presented analytical model could correctly predict the different trends of the heat transfer coefficient reported in the literature as a function of the vapor exit quality.

To investigate the effect of cross-link design on flow boiling in microchannel arrays, flow boiling characteristics in a cross-linked microchannel heat sink were experimentally investigated. The flow visualization study indicated that the observed flow regime was primarily slug. Visual observations of flow patterns in cross-links also demonstrated that bubbles nucleate and grow rapidly on the cross-links' surfaces and in the tangential direction at the microchannels' entrance due to the effect of circulations generated in those regions. The two-phase pressure drop strongly increased with increasing exit quality as compared with that in the straight microchannel heat sink. Addition of cross-links resulted in a substantial increase in the boiling heat transfer coefficient due to the

dominant nucleation boiling mechanism in the cross-link region. The flow boiling heat transfer coefficient showed a different trend in the cross-link design relative to the straight microchannel design. The flow boiling heat transfer coefficient increased with increasing exit quality at a constant mass flux.

To my grandmother Aisha

AKNOWLEDGEMENT

All praise is due to Allah, the lord of the worlds.

I would like to express my sincere appreciation to my advisor, Professor Ibrahim Hassan, for his invaluable patience, support and encouragement. This work could not have been accomplished without his guidance and support at every phase of the research. Many thanks go to my committee member Dr. Lyes Kadem, Dr. Hoi Dick Ng, and Professor Amruthur Ramamurthy for their contributions to this study and encouragement. I would like to acknowledge my fellow students in Prof. Hassan's group for their friendship, assistance and support. Finally, I would like to thank my parents and my brothers for the most needed encouragement to finish my studies. Last but not the least; special thanks are given to my wife for years of support. Without her sacrifice, it would have been impossible for me to complete this work.

TABLE OF CONTENTS

List of Figures	xii
List of Tables.....	xix
Nomenclature	xxi
1. INTRODUCTION	1
1.1 Thesis Organization.....	6
2. Literature Review	8
2.1 Fundamental Definitions in Two-phase Flow.....	8
2.1.1 Dimensionless Groups.....	10
2.2 Straight Microchannel Heat Sink	11
2.2.1 Two-phase Flow Pressure Drop and Flow Visualization	11
2.2.1 Flow Boiling Heat Transfer	19
2.2.1 Analytical Modeling of Flow Boiling Heat Transfer in Microchannels	29
2.3 Cross-linked Microchannel Heat Sink.....	36
2.4 Summary.....	40
2.4.1 Two-phase Pressure Drop.....	40
2.4.2 Flow Boiling Heat Transfer	41
2.4.3 Analytical Modeling of Flow Boiling Heat Transfer	42
2.4.4 Cross-linked Microchannel Heat Sink.....	43
2.5 Thesis Objectives	43
3. Experimental Facility.....	45
3.1 Flow Loop.....	45
3.2 Test Sections	47

3.2.1	Straight Microchannel Heat Sink	50
3.2.1	Cross-linked Microchannel Heat Sink.....	51
3.3	Data Acquisition and Flow Visualization Facility	58
3.4	Un-encapsulated Thermochromic Liquid Crystals	60
3.5	Experimental Procedure.....	61
3.6	Data Reduction.....	70
3.1	Measurement Uncertainty.....	75
4.	Two-phase Pressure drop and Flow Visualization in Straight Microchannel Heat Sinks	80
4.1	Flow Visualization	80
4.2	Two-phase Pressure Drop.....	83
4.3	Assessment of Correlations.....	86
4.4	Development of a New Correlation.....	91
4.5	Conclusions.....	96
5.	Flow Boiling Heat Transfer Characteristics in Straight Microchannel Heat Sinks	101
5.1	Onset of Boiling	101
5.2	Heat Transfer Characteristics.....	106
5.3	Comparison of Heat Transfer Models and Correlations.....	114
5.4	Suppression Factor Development.....	121
5.5	Asymptotic Model Validation.....	123
5.1	Conclusions.....	126
6.	Analytical Modeling of Annular Flow boiling Heat Transfer in Mini- and Microchannel Heat Sinks	136

6.1	Analytical Model.....	136
6.1.1	Assumptions.....	136
6.1.2	Two-phase Heat Transfer Coefficient	137
6.1.3	Mass Conservation	138
6.1.4	Momentum Conservation	141
6.1.5	Frictional Pressure Gradient	143
6.1.6	Acceleration Pressure Gradient.....	145
6.2	Data Analysis	148
6.3	Model Validation.....	155
6.4	Model Limitations	174
6.5	Conclusions.....	180
7.	Experimental Investigation of Flow Boiling Characteristics in Cross-linked Microchannel Heat Sinks	181
7.1	Test Matrix.....	181
7.2	Flow Visualization	182
7.3	Two-phase Pressure Drop.....	188
7.4	Two-phase Flow Instability	195
7.5	Flow Boiling Heat Transfer	201
7.6	Conclusions.....	208
8.	Conclusions and Future work.....	211
8.1	Conclusions.....	211
8.1.1	Straight Microchannel Heat Sink	211
8.1.2	Cross-linked Microchannel Heat Sink.....	213

8.2	Future Research.....	214
8.2.1	Experimental Study.....	214
8.2.2	Analytical Study.....	215
	References.....	219
	Publications.....	234
	Appendix A: Experimental Data.....	236

LIST OF FIGURES

Figure 1-1: Growth of transistors per integrated circuit for Intel microprocessors.....	2
Figure 1-2: Near and long term heat generation from personal computers and servers.....	3
Figure 3-1: Experimental test facility flow loop.	49
Figure 3-2: A photograph of the fabricated straight microchannel heat sink with (a) microchannels and Pyrex cover and (b) integrated heater on the back	52
Figure 3-3: Detailed schematic of the straight microchannel heat sink	53
Figure 3-4: Cross-section for the microchannels showing actual cross-sectional area and dimensions (dimensions are in μm).	54
Figure 3-5: A photograph of the fabricated Cross-linked microchannel heat sink.	55
Figure 3-6: Detailed schematic of microchannel heat sink (dimensions are in mm).	56
Figure 3-7: Microchannel heat sink mounted on the acrylic support.....	57
Figure 3-8: Schematic of the data acquisition system.	62
Figure 3-9: Schematic of the image acquisition system.	63
Figure 3-10: Images of the TLC undergoing color play (a) 56.7 °C (b) 59.4 °C (c) 64.9 °C (d) 70.1 °C	66
Figure 3-11: Representative TLC image divided into regions of interest (5×5 pixels).....	67
Figure 3-12: Examples of a 5 th order calibration curve.	68
Figure 3-13: Example of calibration curves: corrected calibration curve with 3 rd and 5 th order fits.	69
Figure 3-14: Schematic illustration of microchannel heat sink geometry.	76

Figure 4-1: Flow pattern observations in different microchannels at different time intervals for $G = 341 \text{ kg/m}^2 \cdot \text{s}$ and $q = 130.6 \text{ kW/m}^2$, flow from right to left, $t = 0$ reference time	84
Figure 4-2: Nucleation and flow pattern observations at in the mid-channels, $G = 341 \text{ kg/m}^2 \cdot \text{s}$, flow from right to left.	85
Figure 4-3: Two-phase pressure drop as a function of exit quality for different mass fluxes.	87
Figure 4-4: Frictional pressure gradient as a function of exit quality for different mass fluxes.	88
Figure 4-5: Martinelli parameter as a function of exit quality for different heat fluxes....	89
Figure 4-6: Comparison of measured pressure drop data with predicted data from macro and microchannel correlations.	92
Figure 4-7: Comparison of measured pressure drop data with predicted data for laminar-liquid laminar-vapor flow.	99
Figure 4-8: Predicted values of two-phase pressure gradient with the new correlation against the experimental data for laminar liquid-turbulent vapor.	100
Figure 5-1: Example of a raw RGB image for the present investigation of the heat sink at $q = 60.4 \text{ kW/m}^2$ and $G = 340 \text{ kg/m}^2 \text{ s}$	108
Figure 5-2: Local surface temperature distribution for the present investigation of the heat sink at $q = 60.4 \text{ kW/m}^2$ and $G = 340 \text{ kg/m}^2 \text{ s}$	109
Figure 5-3: Stream-wise surface temperature showing ONB for $G = 340 \text{ kg/m}^2 \cdot \text{s}$ and $q = 60.4 \text{ kW/m}^2$	110

Figure 5-4: Bubble nucleation and onset of nucleate boiling for $G = 340 \text{ kg/m}^2 \cdot \text{s}$ and $q = 60.4 \text{ kW/m}^2$	111
Figure 5-5: Stream-wise surface temperature showing ONB for $G = 531 \text{ kg/m}^2 \cdot \text{s}$ and $q = 69.4 \text{ kW/m}^2$	112
Figure 5-6: Effect of contact angle on Poh-Seng et al. model predictions.	113
Figure 5-7: Mean heat transfer coefficient as a function of exit quality for different mass fluxes.	115
Figure 5-8: (a) Nucleation and (b) flow patterns observations for FC-72 in the mid-channel for $G = 340 \text{ kg/m}^2 \cdot \text{s}$ (flow is from right to left).	116
Figure 5-9: Boiling curves at different mass fluxes.	117
Figure 5-10: Comparison of measured heat transfer coefficient data with predicted data from mini and microchannel correlations for $G = 531 \text{ kg/m}^2 \cdot \text{s}$	128
Figure 5-11: Temperature profile during convective flow boiling.....	129
Figure 5-12: Temperature plots against distance from the wall.....	130
Figure 5-13: Comparison of model predictions with flow boiling heat transfer coefficient data	132
Figure 5-14: Comparison between the measured and predicted boiling heat transfer coefficients at $G = 341 \text{ kg/m}^2 \cdot \text{s}$	133
Figure 5-15: (a) Experimental and predicted flow boiling heat transfer coefficients for Qu and Mudawar (2003b) data at $G = 135 \text{ kg/m}^2 \cdot \text{s}$ (b) Nucleate boiling suppression factor and forced convective heat transfer enhancement factor at $G = 135 \text{ kg/m}^2 \cdot \text{s}$	134

Figure 5-16: (a) Experimental and predicted flow boiling heat transfer coefficients for Qu and Mudawar (2003b) data at $G = 323 \text{ kg/m}^2 \cdot \text{s}$ (b) Nucleate and convective boiling factor predictions based on developed model at $G = 323 \text{ kg/m}^2$	135
Figure 6-1: Parameters in annular flow for force balance on liquid film.	139
Figure 6-2: Schematic of annular flow in a rectangular channel.	140
Figure 6-3: Control volume analysis of vapor differential element in annular flow.....	144
Figure 6-4: The Revellin and Thome (2007) flow regime map for diabatic two-phase flow in microchannels.....	152
Figure 6-5: (a) Liquid-phase Reynolds number as a function of exit quality (b) vapor-phase Reynolds number as a function of exit quality.....	154
Figure 6-6: Predicted and experimentally determined two-phase heat transfer coefficient.....	159
Figure 6-7: Comparison of heat transfer coefficient at constant mass flux: (a) Lee and Lee (2001b), R113, $G = 208 \text{ kg/m}^2 \cdot \text{s}$, $q = 5 \text{ kW/m}^2$. (b) Yun et al. (2006), R410A, $G = 400 \text{ kg/m}^2 \cdot \text{s}$, $q = 20 \text{ kW/m}^2$	163
Figure 6-8: Heat transfer coefficient predictions by the analytical model compared with: (a) Dong et al. (2008), R141b, $G = 500 \text{ kg/m}^2 \cdot \text{s}$, $q = 100 \text{ kW/m}^2$ and (b) Yen et al. (2006), R123, $G = 400 \text{ kg/m}^2 \cdot \text{s}$, $q = 25.32 \text{ kW/m}^2$	164
Figure 6-9: Two-phase heat transfer coefficient as a function of exit quality predicted by the analytical model compared with Agostini et al. (2008a) data, R236fa, $G = 984 \text{ kg/m}^2 \cdot \text{s}$	165

Figure 6-10: Contributions of f_1 , f_2 and f_3 terms to the estimated heat transfer coefficient, data of Yen et al. (2006), R123, $G = 400 \text{ kg/m}^2 \cdot \text{s}$, $q = 25.32 \text{ kW/m}^2$	169
Figure 6-11: Contribution of different terms representing the predicted heat transfer coefficient, data of Yun et al. (2006), R410A, $G = 400 \text{ kg/m}^2 \cdot \text{s}$, $q = 20 \text{ kW/m}^2$	171
Figure 6-12: The effect of mass flux on the experimental and predicted heat transfer coefficient, experimental data of Dong et al. (2008), $q = 100 \text{ kW/m}^2$	175
Figure 6-13: The dependence of the predicted two-phase heat transfer coefficient on the exit quality for different mass fluxes, data of Agostini et al. (2008a) $q = 236 \text{ kW/m}^2$	176
Figure 6-14: Comparison between the present model and the experimental results by Dong et al. (2008) for the variation of the heat flux for $G = 500 \text{ kg/m}^2 \cdot \text{s}$	177
Figure 6-15: Predicted influence of heat flux on the two-phase heat transfer coefficient as a function of exit quality, comparing with experimental data of Agostini et al. (2008a) $G = 810 \text{ kg/m}^2 \cdot \text{s}$	178
Figure 6-16: Effect of saturation temperature on the two-phase heat transfer coefficient, analytical predictions versus experimental data of Agostini et al. (2008a), $G = 810 \text{ kg/m}^2 \cdot \text{s}$ and $q = 18.6 \text{ kW/m}^2$	179
Figure 7-1: Schematic of flow visualization positions.....	184

Figure 7-2: Observed flow characteristics within the cross-link, $G = 109 \text{ kg/m}^2 \cdot \text{s}$, $x_{e,o} = 0.2$, at positions: (a) <i>I-23</i> , (b) <i>I-12</i> , (c) <i>I-1</i>	187
Figure 7-3: Sequential images of bubbles growing at <i>I-23</i> , $G = 147 \text{ kg/m}^2 \cdot \text{s}$, $q = 27.6 \text{ kW/m}^2$	189
Figure 7-4: Flow patterns at different exit quality, heat flux, and locations of the test section, $G = 109 \text{ kg/m}^2 \cdot \text{s}$, flow from right to left.	190
Figure 7-5 : Two-phase flow patterns observed at a high mass flux, $G = 195 \text{ kg/m}^2 \cdot \text{s}$...	192
Figure 7-6: Two-phase pressure drop as function of vapor exit quality for different mass fluxes	196
Figure 7-7 : Comparison of the present measurements and the correlation by Lee and Garimella (2008).....	197
Figure 7-8 : Oscillations of inlet pressure measurements, $q = 24.5 - 45.8 \text{ kW/m}^2$, and $G = 105 - 201 \text{ kg/m}^2 \cdot \text{s}$	199
Figure 7-9 : Oscillations of outlet temperature measurements, $q = 24.5 - 45.8 \text{ kW/m}^2$, and $G = 105 - 201 \text{ kg/m}^2$	200
Figure 7-10: Sample of spatially resolved temperature map and TLC-painted surface at $G = 99 \text{ kg/m}^2 \cdot \text{s}$ and $x_{e,o} = 0.15$	203
Figure 7-11: Sample of spatially resolved temperature map and TLC-painted surface at $G = 99 \text{ kg/m}^2 \cdot \text{s}$ and $x_{e,o} = 0.3$	204
Figure 7-12: Variation of two-phase heat transfer coefficient with vapor exit quality at different mass fluxes.	205

Figure 7-13 : Ratio of predicted to measured two-phase heat transfer coefficient at different mass fluxes as a function of exit quality using the Yu et al. correlation (2002).	207
Figure 7-14 : Typical boiling curve for FC-72 in the cross-linked microchannel heat sink, $\Delta T_{\text{sub}} = 4^{\circ}\text{C}$	210
Figure 8-1: Proposed enhanced microchannel heat sink.	217
Figure 8-2: Micropins geometry developed to enhance boiling characteristics.	218

LIST OF TABLES

Table 2-1: Summary of relevant studies of two-phase pressure drop in macro, mini, and microchannel heat sinks.	20
Table 2-2: Summary of flow boiling heat transfer studies in macro, mini, and microchannel heat sinks.	25
Table 2-3: Flow boiling heat transfer models and correlations.	30
Table 3-1: Properties of FC-72 at 25°C and 1 atm.	48
Table 3-2: Parameters and Estimated Uncertainties.	79
Table 4-1: Pressure drop data used in the present study.	98
Table 5-1: Investigated ranges and accuracy of the model.	131
Table 6-1: Description of data obtained for annular flow boiling heat transfer in mini- and microchannels	150
Table 6-2: Void fraction correlations for mini- and microchannels.	156
Table 6-3: Two-phase frictional multiplier for mini- and microchannels.	157
Table 6-4: MAE and AE between the experimental data and the predicted results for the present model.	160
Table 6-5: A comparison of refrigerant’s physical properties and channel geometry used in Yun et al. (2006) and Yen et al. (2006) experiments.	168
Table 7-1: Cross-linked microchannel heat sink test matrix	183
Table 8-1 : Two-phase flow pressure drop data in the straight microchannel heat sink .	236
Table 8-2: Flow boiling heat transfer data in the straight microchannel heat sink	238
Table 8-3 : Two-phase flow pressure drop data in the cross-linked microchannel heat sink	240

Table 8-4 : Two-phase flow heat transfer data in the cross-linked microchannel heat

sink.....243

NOMENCLATURE

A	area, m^2
AE	absolute error
Bo	Boiling number
C	two-phase multiplication factor
Co	Confinement number
c_p	specific heat, $J/kg \cdot ^\circ C$
c_1 to c_4	coefficients in Eqn. (4-2)
D	diameter, m
F	enhancement factor
fun	function
f	parameter in Eqn. (6-46)
f	friction factor
FDB	fully developed boiling
fRe	Poiseuille number
G	mass flux, $kg/m^2 \cdot s$
g	constant of gravity, m/s^2
h	heat transfer coefficient, $W/m^2 \cdot ^\circ C$
H_{ch}	channel height, m
h_{fg}	latent heat of vaporization, J/kg
I	electric current, A
j	superficial velocity, m/s
K	loss coefficient

k	thermal conductivity, W/m.°C
$K(\infty)$	Hagenbach's factor
L	length, m
m	fin parameter
MAE	Mean absolute error
M_w	Molecular weight
\dot{m}	mass flow rate, kg/s
N	total number of data points
Nu	Nusselt number
n	value of the power index
N_{ch}	total number of channels
Nu_3	Nusselt number for 3-side heating
Nu_4	Nusselt number for 4-side heating
ONB	onset of boiling
PDB	Partially developed boiling
Pr	Prandtl number
P_r	reduced pressure
ΔP	pressure drop, Pa
Q	heat, W
q	heat flux, W/m ²
\dot{Q}	volumetric flow rate, m ³ /s
r	radius, m
Re	Reynolds number

S	periphery, m
S_p	suppression factor
s	spacing between microchannels, m
T	Temperature, °C
t	heat sink wall thickness, m
T_{in}	manifold inlet temperature, °C
T_{out}	manifold outlet temperature, °C
ΔT_{sat}	wall superheat, °C
ΔT_e	mean superheat, °C
u	velocity, m/s
V	voltage, V
v	specific volume, m ³ /kg
We	Weber number
W_{ch}	channel width, m
x	x -coordinate
x_e	vapor quality
X^2	Martinelli parameter
y	y -coordinate
z	z -coordinate

Greek

α	void fraction
β	volumetric quality

μ	micro
μ	dynamic viscosity, N.s/m ²
ρ	density, kg/m ³
σ	surface tension, N/m
C_{12}	Two-phase pressure drop multiplier
γ	channel aspect ratio
η	fin efficiency
τ	shear stress, N/m ²
ε	coefficient in Eqn. (6-43)
λ	area ratio
Θ	fluid and heater surface contact angle, degree
ζ	adjusting parameter
δ	thickness, m

Subscripts

90	90° bend
a	acceleration component
axial	axial heat loss
b	outer wall temperature of the heat sink
c	contraction
cb	convective boiling
ch	channel
con	convection heat loss

cr	cross-link
dyn	dynamics
en	enlargement
expt	experimental
fg	liquid-vapor
fo	liquid only
fp	foot print
fr	frictional
g	vapor
gr	gravitational component
h	hydraulic
i	interfacial
input	input heat
L	liquid
loss	heat loss
nb	nucleate boiling
net	net heat
o	outlet
ONB	onset of boiling
pred	predicted
rad	radiation heat loss
s	surface
sat	saturated

sec	section
si	silicon
sp	single-phase
sub	subcooled
tot	total
tp	two-phase
vv	laminar-liquid laminar-vapor
vt	laminar-liquid turbulent-vapor
w	wall

Gradients

$\frac{dP}{dz}$ pressure gradient, Pa/m

$\frac{dP}{dz} F$ frictional pressure gradient, Pa/m

$\frac{dP}{dz} a$ acceleration pressure gradient, Pa/m

Abbreviations

RGB	Red-Green-Blue
ROI	region of interest
MEMS	Microelectromechanical systems
NIST	The National Institute of Standards and Technology

CHAPTER 1

INTRODUCTION

Developments in semiconductor technology have made it possible for extraordinary advances in the miniaturization of devices. Recently, there have been drastic increases in the heat density of integrated circuits due to rapid improvements in their speed and size. As a result, heat removal has become an important factor in the advancement of microelectronics due to increased current-voltage handling capability of power electronic devices.

In 1965, Intel co-founder Gordon Moore (1965) stated that the number of transistors on a chip is increasing exponentially and will be doubled about every two years. This exponential increase in the number of components on a chip became later known as Moore's Law. At the beginning of the 1990s, Moore's Law became commonly observed, as the doubling of microprocessor power takes place every 18 months. Figure 1-1 presents the exponential increasing of the number of transistors that can be inexpensively placed on an integrated circuit, for Intel microprocessors, in the past four decades. The increase in computing speed necessitates higher transistor densities to reduce the path that a signal needs to travel. This has led to the use of Multichip Modules (MCM), which are simply arrays of chips placed on one substrate. Heat generation from personal desktop computers has approached 100 W and 200 W for servers (Gurram et al., 2004), as illustrated in Fig. 1-2. This heat generation is not easily handled by solid heat sinks.

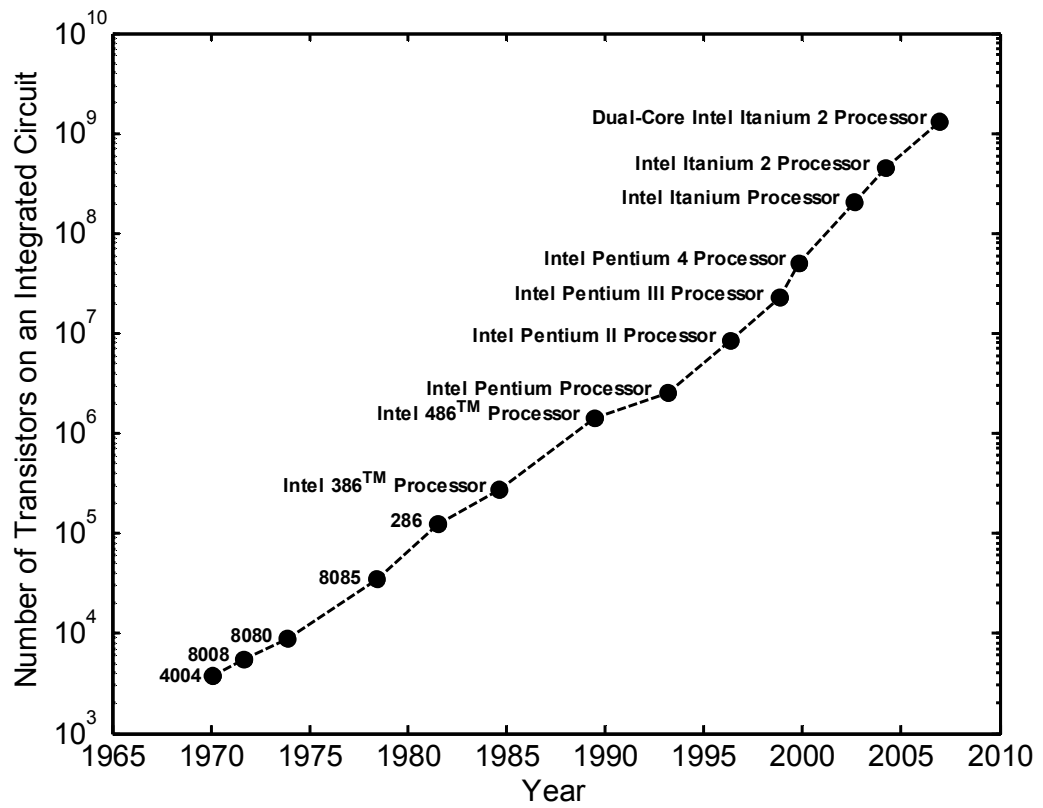


Figure 1-1: Growth of transistors per integrated circuit for Intel microprocessors.

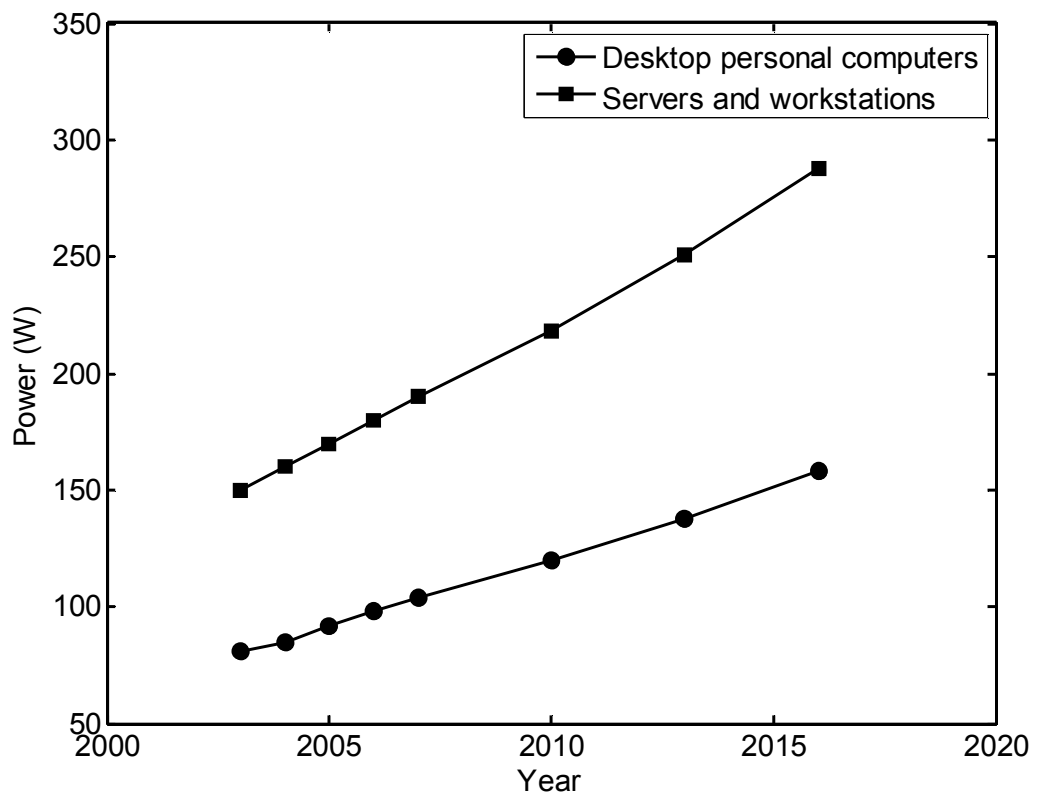


Figure 1-2: Near and long term heat generation from personal computers and servers.

Over the past decade or so, many research groups used micromachining technologies to develop different types of microfluidic devices in a variety of different materials, such as silicon, glass, quartz, and plastics. The large surface-to-volume ratios of microchannels make them excellent candidates for efficient heat transfer devices. More recently, research has been intensified on the use of microchannel heat sinks as a viable technology to resolve the thermal challenges of the next generation of high heat flux devices. This microelectromechanical system (MEMS) device has potential applications in the cooling of integrated circuits and the thermal management of operating systems, across a broad range of industries such as computer, biomedical, automotive, and aerospace.

The definition of microchannels has not been generally agreed. Fukano and Kariyasaki (1993) found the critical diameter, at which the surface tension surpasses gravity, to be between 5 to 9 mm and the effect of diameter dominated over flow direction when the tube diameters were smaller than 6 mm. These conclusions agreed with the criterion of Kew and Cornwell (1997). They found that two-phase flow exhibits different flow and heat transfer characteristics when the confinement number is greater than 0.5. Confinement of a growing bubble is represented by the restriction of channel size on bubble growth, such that the bubble length is greater than the channel diameter. This dimensionless number depends on the diameter as well as surface tension and density of the liquid and vapor. Brauner and Moalem-Maron (1992) thought the surface tension dominates over other forces when Eötvös number, defined as the ratio of buoyancy force to surface tension force, is greater than 1. Triplett et al. (1999) reported that the stratified flow vanished as Eötvös number is greater than 100. Kandlikar (2001) recommended the following channels size ranges: microchannels ($D_h = 50$ to $600 \mu\text{m}$),

minichannels ($D_h = 600 \mu\text{m}$ to 3 mm) and conventional/macrochannels ($D_h > 3 \text{ mm}$). Recently, many researchers argued that the criterion ought to be based on thermo-hydraulic properties rather than on channel dimension alone. However, although the bubble confinement looks like an appropriate criterion for identifying the threshold between micro- and macroscale, the discrepancy is quite significant.

Studies in microchannel heat transfer demonstrated the potential possibilities of thermal control of electronic devices. Early experimental studies, such as that carried out by Tuckerman and Pease (1981), showed that electronic chips can be cooled effectively using forced convection by running water through parallel microchannels mounted directly on the back of a circuit board. The approximate microchannel cross-sections were rectangular, and ranged in height from 50 to $56 \mu\text{m}$ and width from 287 to $320 \mu\text{m}$. Their work is considered a milestone in the development of microscale heat sinks. In addition, this initial study has led to continued research on microchannel heat transfer that will eventually lead to the development of high performance microheat exchangers.

Compared with channels of normal size, microchannels have many heat transfer advantages. Since microchannels have a large surface-to-volume ratio, they provide a much higher heat transfer. This feature allows heat exchangers to become compact and light weight. In addition, microchannels can support high heat flux with small temperature gradients. However, microchannels also have weaknesses such as high cost of manufacture, large pressure drop, and flow mal-distribution, especially for two-phase flows.

Flow boiling heat transfer in microchannels has received growing attention in recent years due to the efficiency in heat transfer of two-phase flow compared to single-phase

flow. The major advantages stem from the latent heat, which allows a reduced flow rate while achieving a higher heat transfer coefficient. In some electronics cooling applications, it is necessary to keep the cooling behavior steady, with uniform heat removal. Therefore, phase-change heat sinks, which allow constant coolant temperature in the stream wise direction, are becoming increasingly attractive. The rapid development of two-phase microfluidic devices has triggered the demand for a detailed understanding of the flow characteristics inside microchannel heat sinks to advance the cooling process of microelectronics.

1.1 Thesis Organization

This thesis is organized as follows:

Chapter 1 is the introduction to this thesis, and provides a summary of the background.

Chapter 2 provides an overview of the main variables and basic equations used in two-phase flow. It also examines the current literature in the field of flow boiling pressure drop and heat transfer in microchannel heat sinks. The thesis objectives are also provided.

Chapter 3 gives a detailed description of the experimental methodology in the present study. The test sections and experimental setup are explained. Data reduction and data collection methods are described.

Chapter 4 presents results of the two-phase pressure drop and flow visualization measurements in straight microchannel heat sinks. Experimental results are compared with available correlations for two-phase pressure drop in microchannels. A new correlation is introduced to predict two-phase pressure drop in microchannels.

Chapter 5 discusses the flow boiling heat transfer and onset of boiling results in the straight microchannel heat sink, and presents a comparison with the available models and correlations in the literature.

Chapter 6 consists of the development of an analytical model to predict the heat transfer coefficient during annular flow boiling. Model results and validation are presented using several datasets.

Chapter 7 presents flow boiling characteristics in the cross-linked microchannel heat sink. Flow patterns, two-phase flow instability, two-phase pressure drop, and heat transfer characteristics are presented and discussed.

Chapter 8 summarizes the present study and states the conclusions. It also provides recommendations for future research. Finally, a novel design of micropins microchannel heat sink is presented.

CHAPTER 2

LITERATURE REVIEW

This chapter starts by first introducing terminology and nomenclature of two-phase flow. Then, a comprehensive literature review on two-phase flow in microchannel heat sinks is presented, covering both experimental and theoretical work. Based on scientific literature, the earliest studies to the latest research on pressure drop, heat transfer, and flow visualization of flow boiling in microchannels is presented. The literature survey is followed by a summary that combines information from previous studies, in order to demonstrate the objectives of the present study. Finally, the motivation of the present thesis is presented.

2.1 Fundamental Definitions in Two-phase Flow

The mass flux is defined as the average mass flow rate (\dot{m}) per unit area of the channel (A_{ch}). It is also known as the mass velocity:

$$G = \frac{\dot{m}}{A_{ch}} . \quad (2-1)$$

The vapor quality is defined as the ratio of vapor mass flow rate (\dot{m}_g) to total mass flow rate:

$$x_e = \frac{\dot{m}_g}{\dot{m}} = \frac{\dot{m}_g}{\dot{m}_L + \dot{m}_g} . \quad (2-2)$$

To distinguish between liquid and vapor, the subscripts 'L' for liquid and 'g' for vapor will be used. The void fraction is defined as the fraction of channel cross sectional area that is occupied by vapor:

$$\alpha = \frac{A_g}{A_{ch}} = \frac{A_g}{A_L + A_g} , \quad (2-3)$$

where A_L is the cross sectional area occupied by the liquid phase. The homogeneous two-phase flow void fraction assumes that the liquid and vapor densities travel at the same velocity. It is also called the volumetric quality and defined as the vapor volumetric flow rate (\dot{Q}_g) to total volumetric flow rate (\dot{Q}):

$$\beta = \frac{\dot{Q}_g}{\dot{Q}} = \frac{\dot{Q}_g}{\dot{Q}_L + \dot{Q}_g} . \quad (2-4)$$

The superficial velocity of the phase (j) is defined as the volumetric flow rate of the phase divided by the channel cross sectional area as follows:

$$j_L = \frac{\dot{Q}_L}{A_{ch}} = \frac{G(1-x_e)}{\rho_L} , \quad (2-5)$$

and

$$j_g = \frac{\dot{Q}_g}{A_{ch}} = \frac{Gx_e}{\rho_g} . \quad (2-6)$$

The average velocities of the liquid and vapor phases, u_L and u_g , in their respective cross-sectional areas A_L and A_g are defined as:

$$u_L = \frac{\dot{Q}_L}{A_L} , \quad (2-7)$$

and

$$u_g = \frac{\dot{Q}_g}{A_g} . \quad (2-8)$$

2.1.1 Dimensionless Groups

The Reynolds number is defined as the ratio of inertial force to viscous force. Re_{fo} is the Reynolds number assuming the entire flow to be liquid

$$Re_{fo} = \frac{GD_h}{\rho_L} . \quad (2-9)$$

The liquid-phase Reynolds number Re_L , based on the superficial velocity of the liquid-phase, is defined as:

$$Re_L = \frac{G(1 - x_e)D_h}{\rho_L} , \quad (2-10)$$

similarly for the vapor-phase Reynolds number Re_g ,

$$Re_g = \frac{Gx_e D_h}{\rho_g} . \quad (2-11)$$

The Boiling number is the dimensionless ratio of the mass flux leaving the surface by evaporation due to the heat flux to the total mass flux flow through the channel.

$$Bo = \frac{q}{Gh_{fg}} . \quad (2-12)$$

The Weber number is the dimensionless ratio of the inertia force to the surface tension force.

$$We = \frac{\rho u^2 D_h}{\sigma} . \quad (2-13)$$

The confinement number includes the surface tension force and hydraulic diameter, and is used to represent the effect of confinement. It is defined as the ratio of a characteristic bubble departure size to the hydraulic diameter of the channel:

$$Co = \frac{\left[\frac{\sigma}{g(\rho_L - \rho_g)} \right]^{\frac{1}{2}}}{D_h} . \quad (2-14)$$

The Martinelli parameter, X^2 , is defined as the ratio of the liquid-phase frictional pressure gradient to the vapor-phase frictional pressure gradient as:

$$X^2 = \left(\frac{dP}{dL} F \right)_L / \left(\frac{dP}{dL} F \right)_g . \quad (2-15)$$

2.2 Straight Microchannel Heat Sink

2.2.1 Two-phase Flow Pressure Drop and Flow Visualization

Two-phase flow pressure drop depends on a large number of independent parameters like geometric configuration of the channel, mass and volume fractions of the individual phases, fluid properties, mass flux, and flow patterns. There have been numerous models and correlations developed to predict frictional pressure drop in two-phase flows in horizontal pipes. Among the more common models are the homogeneous and the separated flow models. The homogeneous model assumes that the two-phase flow is a homogeneous mixture, where the liquid and vapor phases are sufficiently well mixed and are traveling at the same velocity with a weighted average property of each phase. The separated flow model considers the two phases separately, with an inherent assumption that the two phases reach constant but not necessarily equal velocities, e.g., vapor and liquid velocities. This assumption of different velocities is important when the densities of each phase are sufficiently different in the presence of large pressure gradients. The separated model is more appropriate in pressure drop predictions in microchannels than the homogeneous model because of the considerable slip between the phases. The

homogenous model can be used to predict the pressure drop in cases involving bubbly and churn flow patterns, which are rarely detected in microchannels. However, the slug, plug, and annular flow patterns are dominant where both flow phases are separated, in these flow patterns.

Several pressure drop correlations have been proposed over the years, mostly based on experimental data. The method of calculation was based on the Lockhart and Martinelli (1949) analysis, which is a separated flow model. The Lockhart and Martinelli model appears to be the most current general model in the literature, although proprietary improvements have been made. They expressed the frictional two-phase flow pressure drop as

$$\left(\frac{dP}{dL} F \right)_{\text{tp}} = \phi_f^2 \left(\frac{dP}{dL} F \right)_{\text{L}} . \quad (2-16)$$

where ϕ_f^2 is the two-phase pressure drop multiplier defined as

$$\phi_f^2 = 1 + \frac{C}{X} + \frac{1}{X^2} . \quad (2-17)$$

where C is the two-phase multiplication factor. Parameter C can be expressed as a function of the mass flux and hydraulic diameter. An alternative approach is to express parameter C in terms of dimensionless groups (e.g. Re , We). Different values of C are given by different investigators. Relevant studies and correlations found in the literature for two-phase pressure drop in mini and microchannels are reviewed and summarized in this section.

Moriyama et al. (1992) studied flow boiling pressure drop in microchannels, 35 to 110 μm in depth and 30 mm in width, with R113 as a boiling fluid. They developed an analytical model for predicting flow boiling pressure drop as a function of the capillary

number. The effect of gravity, acceleration pressure drop, and variation of the liquid film thickness were ignored in their model. The frictional pressure drop equation required computing the ratio of the liquid film thickness to the channel width. A comparison of the predicted and experimental values showed that the pressure drop could be predicted fairly in the annular flow regime. However, the experimental values of pressure drop were slightly underpredicted by the model at low exit quality. This was explained by the inability of model to account for the interaction between the liquid slug and vapor bubble in the slug flow regime.

One of the first theoretical models of pressure drop in microchannels, which covers single-phase and two-phase regions, was developed by Bowers and Mudawar (1994). This model is based on the idea that the pressure drop in the microchannel can be subdivided into elementary terms: the single-phase inlet region, two-phase heated region, and the two-phase unheated outlet region. This simplified model describes the overall pressure drop as the sum of three terms: two-phase pressure gradient, single-phase pressure drop, and contraction and expansion pressure drops. The model was based on the widely used homogeneous flow model, which assumes that vapor and liquid phases flow with equal velocity. The proposed model was able to predict the experimental data within a $\pm 30\%$ error band. Model predictions have shown that the acceleration pressure drop is the main contributor to the total pressure drop in the heated region.

Following the channels' size ranges recommended by Kandlikar (2001): microchannels ($D_h = 50$ to $600 \mu\text{m}$), minichannels ($D_h = 600 \mu\text{m}$ to 3 mm) and conventional/macrochannels ($D_h > 3 \text{ mm}$), the literature review reveals that many studies concerning the flow boiling pressure drop inside mini- and macrochannels have been

published. However, few published studies discuss pressure drop of flow boiling in microchannels.

Mishima and Hibiki (1996) presented data for flow regime, void fraction and pressure drop for an air-water flow in conventional and minitubes with an inner diameter in the range of 1000 to 4000 μm . They have observed peculiar flow regimes in capillary tubes, and it was found that capillary force is important in describing the bubble shape. It was concluded that the two-phase frictional pressure drop should take into account the effect of hydraulic diameter. They developed a correlation that is an adaptation of the Lockhart and Martinelli correlation. The effect of tube size on parameter C was given as a function of the hydraulic diameter.

Lee and Lee (2001a) investigated adiabatic two-phase flow pressure drop in horizontal rectangular mini- and macrochannels using air and water as working fluids. A new correlation for two-phase pressure drop in horizontal mini- and macrochannels was proposed by correlating the two-phase multiplication factor to the viscous, surface tension, and inertia forces. This correlation can be used to predict the two-phase pressure drop for a wide range of Martinelli parameter and Reynolds number. The correlation was validated by 305 data points obtained for four different hydraulic diameters (780, 1910, 3640 and 6670 μm).

Additional experimental studies have focused on two-phase pressure drop in microchannels. Lee and Mudawar (2005a) published an extensive experimental investigation into flow boiling pressure drop in microchannels under high mass and heat flux conditions, using R134a as the coolant. Their test section consisted of 53 parallel, and presumably identical, rectangular channels, with a nominal cross-section of 231 μm

by 713 μm , constructed into an oxygen-free copper block. The channels were 2.5 cm long, and were all connected to a large plenum at the inlet and outlet. To predict the two-phase flow pressure drop in microchannels, a new correlation was proposed. The correlation by Lee and Mudawar allows calculating the pressure drop in terms of a two-phase multiplication factor as a function of an empirical combination of the liquid Reynolds and Weber numbers. The correlation has been developed by fitting the two-phase multiplication factor to 165 water data points and 87 R134a data points, collected by various authors between 2003 and 2005, carried out in microchannels of $D_h = 349 \mu\text{m}$.

Lee and Garimella (2008) reported experimental data on pressure drop characteristics for deionized water flow through a silicon microchannel heat sink with 25 integrated micro-temperature sensors. They found that since the Lockhart and Martinelli correlation was developed for adiabatic and turbulent-liquid turbulent-vapor flow, it gives poor predictions in microchannels of two-phase flow with imposed heat flux. They have proposed a new correlation to predict two-phase pressure drop in microchannels for $D_h = 160$ to $538 \mu\text{m}$ after a critical assessment of five correlations available in the literature. The mathematical expression of the correlation is the result of a regression analysis applied to a data bank covering a wide range of liquid and gas flow rates. The two-phase pressure drop is expressed in terms of a two-phase multiplication factor, which is assumed to be a function of the hydraulic diameter and the mass flux.

Singh et al. (2008) examined the effect of channel aspect ratio on two-phase flow pressure drop in microchannels. Seven rectangular microchannels were examined having a constant hydraulic diameter of $142 \mu\text{m}$ and a wide range of aspect ratios ranging from 1.23 to 3.75. Experiments were conducted at a fixed vapor quality of 0.29, and for mass

and heat fluxes ranging from 82.4 to 126.2 kg/m².s and 29 to 36.6 kW/m², respectively. For constant heat and mass fluxes, the two-phase pressure drop was found to drop rapidly and approach a minimum value corresponding to an aspect ratio of 1.56, before it starts to increase significantly with aspect ratio.

Kaew-On and Wongwises (2009) examined the effect of mass flux, heat flux, and saturation temperature on two-phase flow pressure drop in a macrochannel of hydraulic diameter of 3480 μm. Tests were performed for heat fluxes from 5 to 14.25 kW/m², mass fluxes from 200 to 400 kg/m².s, vapor qualities from 0 to 0.9, and saturation temperatures from 10 to 30 °C. They found a significant increase in pressure drop with increasing vapor quality at higher mass fluxes. At the same time, they reported that heat flux has almost no effect on two-phase pressure drop. They showed that the two-phase pressure drop increased as the refrigerant saturation temperature decreases. This outcome was attributed to the higher liquid viscosity and lower vapor density.

Sun and Mishima (2009) compared 11 pressure drop correlations, including the homogenous model, using a databank containing 2092 adiabatic and diabatic data points for 12 different fluids. Most of the data were from mini and macrochannels ranging in diameter from 506 to 12000 μm, Re_L from 10 to 37,000, and Re_g from 3 to 4×10^5 . The laminar-liquid laminar-vapor data represented approximately 16% of the total data points. Their assessment showed that the best results in the laminar region are obtained from the correlations proposed by Lockhart and Martinelli (1949), Mishima and Hibiki (1996), and Lee and Mudawar (2005a) with a mean absolute error of 42.7%, 45.9%, and 44.8%, respectively. On the other hand, the Muller and Heck (1986) correlation is the best out of the 11 correlations for the turbulent two-phase flow with a mean absolute error of 34.8%.

From their study, Sun and Mishima concluded that the homogenous model is as good as the other correlations in predicting the two-phase pressure drop over the range of parameters considered. It gave good results for all flow regimes with a mean absolute error of 41.4%. Some of the widely used correlations in the literature are given in Table 2-1.

Considerable attention has been given to flow pattern visualization within the microchannels (i.e. Jiang et al., 2001; Lee et al., 2003). A comprehensive study by Hetsroni et al. (2004) investigated convective boiling flow of clear water with surfactant for different flow patterns. Microchannel cross-sections in the shape of isosceles triangles were fabricated in a silicon substrate. The studied channels' base width ranged from 200 μm to 310 μm , while the angles at the base were 55 degrees. The authors employed a microscope and high-speed digital video imaging to visualize incipience of individual bubbles, bubble growth, flow patterns, and the motion of vapor-liquid flow. It was found that the bubble slug velocity is higher than the liquid-phase velocity in the film region.

A subsequent study of Garimella and Chen (2006) examined the heat transfer coefficient and pressure drop characteristics of a dielectric fluid for flow boiling through a microchannel heat sink. The heat sink consists of 24 microchannels, each of which was 389 μm wide and 389 μm deep. They indicated that bubbly flow was dominant at low heat fluxes. At high heat fluxes, the flow regimes in the downstream portion of the microchannels indicated that alternating wispy-annular flow and churn flow were the dominant mechanisms.

Revellin and Thome (2007) measured flow pattern data and bubble frequency of diabatic R134a and R245fa flows in 509 and 790 μm diameter glass channels using two

laser beams. They suggested that the transition from bubbly to slug flow is dominated by effect of the boiling number. The flow pattern map indicated that flow regimes observed at low mass flux are primarily annular and include slug and bubbly-slug regimes.

Harirchian and Garimella (2009) used a high-speed camera to focus on the effect of channel size on flow boiling regimes in mini and microchannels. Minichannels having a fixed depth of 400 μm and width in the range of 100 to 5850 μm were tested. They classified the observed flow regimes into bubbly, slug, churn, wispy-annular, and annular flow regimes. As the channel width increases, the slug flow was changed into bubbly flow and the annular flow into wispy annular flow. It was concluded that flow pattern maps developed for adiabatic two-phase flow in microchannels and diabatic two-phase flow in conventional sized channels are not applicable to predict flow boiling patterns in microchannels. Flow pattern maps are usually presented by either plotting the mass flux versus vapor quality or by plotting the superficial liquid velocity versus the superficial vapor velocity. Two flow regime maps were proposed based on the superficial gas and liquid velocities, and mass flux-vapor quality coordinates.

A recent comprehensive review of the literature on the adiabatic flow regimes in single microchannels was conducted by Shao et al. (2009). They revealed that six major flow patterns, namely bubbly, slug, churn, slug-annular, dispersed, and annular flows were identified in microchannels. These six flow patterns were classified into three flow regimes according to the dominant force, namely: inertia, surface tension, and transition. In the absence of inertial force, the surface tension force plays a dominant role in the bubbly and slug flow regimes. In dispersed and annular flow patterns, the magnitude of the surface tension force becomes relatively small and is overcome by the inertial force.

Then, a transition regime was represented by the churn and slug-annular flow patterns. They concluded that the existing flow maps, presented in superficial liquid velocity versus vapor superficial velocity, are capable of predicting the transition between the flow patterns well.

2.2.1 Flow Boiling Heat Transfer

In the following, the relevant literature on the boiling heat transfer in microchannel heat sinks is reviewed. Summaries of recent research on boiling in microchannels are reported by Bertsch et al. (2008a) and Cheng et al. (2009).

The literature review reveals that many investigations of flow boiling in microchannel heat sinks, mainly for water and refrigerants, have been performed. Qu and Mudawar (2003b) studied flow boiling heat transfer in a water-cooled microchannel heat sink. The heat sink contained 21 parallel microchannels having a 231 μm by 713 μm cross-section. It was shown that the empirical correlations were not able to predict the correct trend of the heat transfer coefficient with quality due to the unique nature of flow boiling in the microchannels. Steinke and Kandlikar (2004) conducted experimental investigations for flow boiling heat transfer using water in six parallel microchannels, each with a 207 μm hydraulic diameter. The mass flux was varied from 157 to 1728 $\text{kg}/\text{m}^2\cdot\text{s}$, the heat flux from 5 to 930 kW/m^2 , and the quality varied from 0 to 1. Results showed that the flow boiling heat transfer coefficient decreases with increasing quality. It was concluded that the effect of nucleate boiling is dominant. In addition, flow boiling correlations give poor predictions for the large peak in the two-phase heat transfer coefficient at low qualities corresponding to the onset of nucleate boiling.

Table 2-1: Summary of relevant studies of two-phase pressure drop in macro, mini, and microchannel heat sinks.

Reference	Year	Channel Geometry	Test Fluid(s)	Flow Conditions	Two-phase Multiplication Factor
Mishimi and Hibiki	1996	Single macro tubes, $D = 1000 - 1400 \mu\text{m}$	Air-water mixture	Adiabatic	$C = 21(1 - e^{-319D_h})$
Lee and Lee	2001a	3 single rectangular macro and mini channels with low aspect ratios, $D_h = 780 - 6670 \mu\text{m}$	Air-water mixture	Adiabatic	$C = a_1 \zeta^{a_2} \psi^{a_3} Re_{fo}^{a_4}$, $\zeta = \frac{\mu_L^2}{\rho_L \sigma D_h}$, $\psi = \frac{\mu_L j_L}{\sigma}$ a_1, a_2, a_3 , and a_4 from Table (4) in Lee and Lee (2001a)
Qu and Mudawar	2003a	21 narrow rectangular microchannels, $D_h = 349 \mu\text{m}$	Water	diabatic	$C = 21(1 - e^{-319D_h})(0.00418G + 0.0613)$
Lee and Mudawar	2005a	53 rectangular microchannels, $D_h = 349 \mu\text{m}$	Water and R134a	diabatic	laminar liquid - laminar vapor: $C = 2.16 Re_{fo}^{0.047} We_{fo}^{0.6}$ laminar liquid - turbulent vapor: $C = 1.45 Re_{fo}^{0.25} We_{fo}^{0.23}$
Lee and Garimella	2008	10-60 rectangular microchannels, $D_h = 160 - 538 \mu\text{m}$	Water	diabatic	$C = 2566G^{0.5466} D_h^{0.8819} (1 - e^{-319D_h})$
Sun and Mishima	2009	macro, mini, and micro channels and tubes, $D_{(h)} = 506 - 12000 \mu\text{m}$	R123, R134a, R22, R236fa, R245fa, R404a, R407C, R410a, R507, CO ₂ , and air and water mixture	Adiabatic/ diabatic	$C = 26 \left(1 + \frac{Re_L}{1000} \right) \left[1 - e^{\frac{-0.513}{0.27Co + 0.8}} \right]$

Additional experimental heat transfer studies have focused on boiling in microchannels. Lee and Mudawar (2005b) investigated experimentally flow boiling heat transfer in microchannels under high mass flux and high heat flux conditions, using R134a as the coolant. The test section used consisted of 53 rectangular channels with a nominal cross-section of 231 μm by 713 μm . They divided the overall vapor quality range into three regions: 0 to 0.05, 0.05 to 0.55, and 0.55 to 1. The first region was characterized by bubble nucleation, where the heat transfer coefficient is a function of $h_{\text{sp,L}}$ and X^2 . The second region, in the quality range 0.05 to 0.55, was associated with bubbly and slug flow and the heat transfer coefficient was correlated to Bo , We , X^2 , and $h_{\text{sp,L}}$. The third region corresponded to annular flow and is dependent on $h_{\text{sp,g}}$ and X^2 .

Agostini et al. (2008a&b) compared the flow boiling heat transfer data for refrigerants R236fa and R245fa in a silicon heat sink made of 67 rectangular channels of width 223 μm , depth 680 μm , and 20 mm in length. Their experiments were performed at mass fluxes from 281 to 1501 $\text{kg/m}^2\cdot\text{s}$, heat fluxes from 9 to 553 kW/m^2 and for vapor qualities ranging from 0.02 to 0.75. The heat transfer coefficient exhibited three distinct trends depending on the values of heat flux. At low heat flux, the heat transfer coefficient was found to increase with increasing vapor quality. This trend was attributed to the effect of bubble formation. At moderate values of heat flux, the heat transfer coefficient began to increase very slightly with exit quality, which may lead to the conclusion that the heat transfer is characterized by the nucleate boiling dominant regime. Further increase in heat flux resulted in a sudden decrease in the heat transfer coefficient with vapor quality at high heat flux. The comparison of heat transfer coefficients for R236fa and R245fa was presented at various heat fluxes, mass fluxes, and saturation

temperatures. R245fa showed a more advantageous heat transfer characteristic than that of R236fa. This was ascribed to the higher latent heat of vaporization, thermal conductivity and specific heat for R245fa.

Harirchian and Garimella (2008) studied, experimentally, the effect of channel size on flow boiling heat transfer coefficient in mini and microchannels. Seven different heat sinks were tested with mini- and microchannels of widths from 100 to 5850 μm with a fixed channel depth of 400 μm . Experiments were performed for mass fluxes from 250 to 1600 $\text{kg}/\text{m}^2\cdot\text{s}$ using FC-77. For microchannels of width 400 μm and greater, it was shown that the heat transfer coefficient and the boiling curves were independent of channel width. On the other hand, for channels of width 100 and 250 μm , the heat transfer coefficient was a weak function of channel width. The corresponding boiling curves exhibited a distinct trend for increasing heat flux compared to channels of greater width.

A similar study was carried out by Bertsch et al. (2009b) for refrigerants R134a and R245fa to investigate experimentally the effects of mass flux, heat flux, hydraulic diameter, and saturation temperature on flow boiling heat transfer coefficient in two arrays of mini- and microchannels of $D_h = 540$ and 1090 μm . Experiments were performed over a wide range of parameters: mass flux values ranging from 20 to 350 $\text{kg}/\text{m}^2\cdot\text{s}$, heat flux from 0 to 220 kW/m^2 , exit quality from -0.2 to 0.9, and saturation temperature from 8 to 30 $^\circ\text{C}$. They showed that the two-phase heat transfer coefficient increases slightly with increasing heat flux and saturation pressure for both refrigerants. As the hydraulic diameter increased, no obvious difference in heat transfer coefficient results was observed at a constant mass flux. They also found that the heat transfer coefficient increased remarkably with mass flux. Seventeen existing correlations were

assessed for convective and nucleate boiling in macro, mini, and microchannel. The empirical correlation of Balasubramanian and Kandlikar (2005) and the analytical model of Thome et al. (2004) captured the trend of the experimental heat transfer. Meanwhile, they showed that correlations have been developed specially for mini and microchannels, e.g. Lee and Lee (2001b), Lee and Mudawar (2005b), and Zhang et al. (2005), disagree considerably with the experimental data even though these correlations agree well with their own experimental database. Finally, developing more physically analytical models based on flow boiling mechanisms and their relation with flow regimes was identified as a future research requirement.

Hozejowska et al. (2009) presented flow boiling data for R123 and R11 in vertical minichannels using Thermochromic liquid crystals. Thermochromic liquid crystals were used to detect the two-dimensional temperature distribution and local heat transfer coefficient on the heated surface as well as incipience of boiling. Their experimental data showed that nucleate boiling was the dominant flow boiling mechanism. Boiling incipience, for a fixed heat flux, was characterized by a sudden decrease in surface temperature due to the mechanism of nucleation sites' activation and formation of bubbles. With the increase of heat flux, the boiling incipience shifted towards the channel inlet.

The flow boiling heat transfer coefficient was measured by Kaew-On and Wongwises (2009) for R410A flowing inside horizontal rectangular macrochannels having 3480 μm hydraulic diameter. Flow boiling experiments were conducted for mass fluxes varying from 200 to 400 $\text{kg}/\text{m}^2\cdot\text{s}$, heat fluxes from 5 to 14.25 kW/m^2 , and saturation temperatures from 10 to 30 $^{\circ}\text{C}$. The effects of the mass flux, heat flux, vapor

quality, and saturation temperature on the local flow boiling heat transfer coefficient were studied. Their data showed that the heat transfer coefficient increases with both heat and mass fluxes. On the contrary to microchannels, decreasing saturation temperatures moderately enhanced the heat transfer coefficient. At low exit quality, the heat transfer coefficient showed a small increase with increasing exit quality up to 0.6. As the exit quality is further increased, the heat transfer coefficient started to decrease gradually. Table 2-2 presents a summary of literature review on flow boiling heat transfer in macro, mini, and microchannel heat sinks.

2.2.1.1 Heat Transfer Correlations and Asymptotic Models

Several heat transfer correlations have been proposed, based primarily on the correlation of dimensionless groups with experimental data. Several asymptotic models have also been developed to estimate the two-phase heat transfer coefficient in convective boiling by accounting for the simultaneous effect of macro-convection associated with the bulk mass flow and by considering the liquid motion behind a departing bubble from the wall in nucleate boiling. These models may be classified according to how the nucleate boiling and forced convection coefficients are combined to obtain the two-phase heat transfer coefficient (h_{tp}). The first model proposed by Rohsenow (1952) used a simple addition of the nucleate and convective boiling effects in the form:

$$h_{tp} = h_{cb} + h_{nb} . \quad (2-18)$$

where h_{cb} and h_{nb} are the single phase forced convection and the nucleate boiling heat transfer coefficients, respectively.

Table 2-2: Summary of flow boiling heat transfer studies in macro, mini, and microchannel heat sinks.

Reference	Year	Channel Geometry	Test Fluid	Mass Flux (kg/m ² .s)	Heat Flux (kW/m ²)	$x_{e,o}$	Heat Transfer Coefficient	Flow Vis.**	Remarks
Lee and Lee	2001b	3 single rectangular macro and minichannels, $D_h = 780 - 6670 \mu\text{m}$	R113	50-200	3-15	0.15-0.75	-The heat transfer coefficient increases with the mass flux and exit quality.	N	-New correlation was developed to predict flow boiling heat transfer coefficient.
Warrier et al.	2002	5 rectangular minichannels, $D_h = 750 \mu\text{m}$	FC-84	557-1600	0-59.9	0.01-0.55	-The heat transfer coefficient decreases with the exit quality.	N	-New correlation was developed to predict two-phase heat transfer under subcooled and saturated boiling conditions.
Qu and Mudawar	2003b	21 narrow rectangular microchannels, $D_h = 349 \mu\text{m}$	Water	135-402	20-140*	0-0.17	-The heat transfer coefficient decreases with the exit quality.	N	- The empirical correlations are not able to predict the correct trend of heat transfer coefficient with quality.
Steinke and Kandlikar	2004	6 rectangular microchannels, $D_h = 207 \mu\text{m}$	Water	157-1782	0.5-93*	0-1	-The heat transfer coefficient decreases with the exit quality.	Y	- Flow reversal is observed during annular-slug flow regime. - Local heat transfer measurements.
Lee and Mudawar	2005b	53 rectangular microchannels, $D_h = 349 \mu\text{m}$	Water and R134a	127-654	15.9-93.8*	0.001-0.87	- The heat transfer coefficient is divided into three ranges based on the quality.	Y	-New correlation was developed to predict flow boiling heat transfer coefficient.

Table 2-2: (continue)

Reference	Year	Channel Geometry	Test Fluid	Mass Flux (kg/m ² .s)	Heat Flux (kW/m ²)	$x_{e,o}$	Heat Transfer	Flow Vis.	Remarks
Lee and Garimella	2008	10-60 rectangular microchannels, $D_h = 160 - 538 \mu\text{m}$	Deionized water	46-126 (ml/min)	10-340*	-0.01-0.2	-The heat transfer coefficient increases almost linearly with heat flux.	N	- Local heat transfer measurements. -New correlation was developed to predict flow boiling heat transfer coefficient.
Bertsch et al.	2008b	17 parallel rectangular microchannels, $D_h = 1090 \mu\text{m}$	HFC-134a	20.3-81	0-20	0-0.8	- As vapor quality increases, the heat transfer coefficient decreases.	N	- The effect of saturation pressure on the heat transfer coefficient is negligible
Agostini et al.	2008 (a&b)	67 parallel channels, $D_h = 336 \mu\text{m}$	R236fa, and R245fa	281-1501	3.6-221*	0.02-0.75	-Three different heat transfer trends were identified for a constant mass flux.	N	- At low heat flux, the heat transfer coefficient increased with vapor quality. - At medium heat fluxes the heat transfer coefficient was almost independent of the vapor quality. -At very high heat fluxes the heat transfer coefficient decreased sharply with increasing exit quality.

* Heat flux calculated based on the base area.

** Flow Visualization.

Kutateladze (1961) proposed a power type addition model for the boiling components:

$$h_{tp} = ((h_{cb})^n + (h_{nb})^n)^{\frac{1}{n}}. \quad (2-19)$$

Higher values of n give a smooth transition as the boiling mechanism changes from nucleate to convective. Then, Chen (1966) introduced the forced convective heat transfer enhancement factor F to the term h_{cb} , and the nucleate boiling suppression factor S_p to the term h_{nb} . These factors reflect the fact that nucleation conditions in forced convection are lower compared to pool boiling conditions, and also account for the diminished contribution of nucleate boiling, as convective boiling effects are increased with exit quality. The relation is given by:

$$h_{tp} = ((Fh_{cb})^n + (S_p h_{nb})^n)^{\frac{1}{n}}, \quad (2-20)$$

An effort was carried out by Steiner and Taborek (1992) to derive a universal asymptotic model by reviewing an extensive data base (water, hydrocarbons, refrigerants, and cryogenes). The goal was to obtain a general distribution of the data bank over the entire range of boiling conditions (reduced pressures, quality, flow rates, etc.). For this reason, it has been considered the best available model. Consequently, Liu and Winterton (1991) pointed out the deficiencies in Chen's model. It was remarked that Chen's model gives poor predictions of the data, especially refrigerants. A new approach was developed following Eqn. (2-20) with $n = 2$. Using a data bank consisting of 4202 data points for saturated boiling, using water and many refrigerants, F was represented by the ratio of the two-phase pressure drop to the single-phase pressure drop and Prandtl number (Pr), while S_p was represented by Re_{fo} and F . This model showed that the convective number should

have a Pr dependence. Shah's (1976) developed a correlation that is based on selecting the greater of the two components corresponding to the forced convection and nucleate boiling mechanisms, depending on the boiling regime. The heat transfer enhancement factor F was found to be a function of the convective number, while the nucleate boiling suppression factor S_p was found to be a function of Bo . Warrier et al. (2002) also applied the same correlation as Shah for FC-84 subcooled and saturated boiling experiments with $D_h = 750 \mu\text{m}$. It was concluded that the heat transfer coefficient is a function of $h_{sp,L}$, Bo , and $x_{e,o}$. Tran et al. (1996) modified Lazarek and Black's (1982) correlation by replacing Re_{f_0} with We_{f_0} to eliminate the viscous effects in favor of surface tension, since the dominant mechanism in the experiment was nucleation. Lee and Lee (2001b) used a more sophisticated correlation to predict the two-phase heat transfer coefficient within rectangular channels. Laminar-liquid turbulent-vapor boiling flow measurements were taken from R113 in macro and minichannels. The enhancement factor has been presented as a function of the channel's aspect ratio and the two-phase frictional multiplier. Recent flow boiling heat transfer models and correlations are summarized in Table 2-3.

Recently, Bertsch et al. (2008a) provided a critical review of experimental works relating to flow boiling in mini and microchannels including heat transfer, pressure drop, critical heat flux, flow patterns, and flow instabilities. Twenty five published flow boiling heat transfer correlations have been tested against a large number of experimental data collected from the open literature covering channels of hydraulic diameters ranging from 160 to 2000 μm . Their assessment of reported correlations for small channels showed that none of the tested correlations appear to provide good predictions over the conventional size tube correlations. This is mainly due to the fact that those correlations

rely heavily on the regression analysis of the tested data rather than on analytical modeling. In addition, the database of each correlation does not cover a wide range of fluid properties and channels sizes. More work on theoretically based models was recommended.

2.2.1 Analytical Modeling of Flow Boiling Heat Transfer in Microchannels

A limited number of analytical models have been developed to predict flow boiling heat transfer in microchannels. Moriyama et al. (1992) developed an analytical model for predicting the flow boiling heat transfer coefficient during slug flow in a very shallow microchannel. Their heat transfer model assumed that conduction through the thin liquid film is the dominant heat transfer mechanism and the heat transfer coefficient was expressed in terms of the thickness of the liquid film. They achieved good qualitative but not quantitative agreement with the experimental data for the heat transfer results.

Landram (1994) derived an analytical model to examine the effect of flow boiling mechanisms that lead to burnout in microchannels of high aspect ratios (width/height=1/10). The problem was approached by dividing the flow, within the channel, into three regimes namely: saturated boiling, subcooled boiling, and single-phase liquid. Saturated boiling was assumed to occur at the channel's bottom wall, which is followed by a subcooled boiling in the longitudinal direction (the direction normal to the flow), and then a single-phase flow at the top cover plate. Saturated boiling regime was characterized by the annular flow criteria. Results pointed out that, during flow boiling in microchannels of high aspect ratios, saturated boiling is the most significant boiling mechanism and subcooled boiling is less important.

Table 2-3: Flow boiling heat transfer models and correlations.

Reference	Model/Correlation
Liu and Winterton (1991)	$h_{tp} = \left(\frac{Nu_3}{Nu_4} \right) ((Fh_{sp})^2 + (S_p h_{nb})^2)^{0.5}$ $h_{sp} = Nu_3 \frac{k_L}{D_h} \text{ for laminar flow, } h_{sp} = 0.023 Re_L^{0.8} Pr_L^{0.4} \text{ for turbulent flow}$ $F = \left(1 + x_{e,o} Pr_L \left(\frac{v_g}{v_L} - 1 \right) \right)^{0.35}$ $h_{nb} = 55 P_r^{0.12} (-\log(P_r))^{-0.55} M_w^{-0.5} q^{0.67}$ $S_p = (1 + 0.055 F^{0.1} Re_L^{0.16})^{-1}$
Tran et al. (1996)	$h_{tp} = \left(\frac{Nu_3}{Nu_4} \right) \left[8.4 \times 10^5 (Bo^2 We_{fo})^{0.3} \left(\frac{v_g}{v_L} \right)^{-0.4} \right]$
Lee and Lee (2001b)	$h_{tp} = \left(\frac{Nu_3}{Nu_4} \right) (Fh_{sp})$ $F = 10.3 \gamma^{0.398} \phi_f^{0.598}, C = 6.185 \times 10^{-2} Re_{fo}^{0.726}$
Warrier et al. (2002)	$h_{tp} = \left(\frac{Nu_3}{Nu_4} \right) (Fh_{sp})$ $F = 1.0 + 6Bo^{1/16} + f(Bo)x_{e,o}^{0.65}, f(Bo) = -5.3(1-855Bo)$
Yu et al. (2002)	$h_{tp} = \left(\frac{Nu_3}{Nu_4} \right) \left[6.4 \times 10^6 (Bo^2 We_{fo})^{0.27} \left(\frac{v_g}{v_L} \right)^{-0.2} \right]$
Lee and Mudawar (2005b)	$h_{tp} = 3.856 X^{0.267} h_{sp,L} \text{ (For } x_{e,o} = 0 - 0.05)$ $h_{tp} = 436.48 Bo^{0.522} We_{fo}^{0.351} X^{0.665} h_{sp,L} \text{ (For } x_{e,o} = 0.05 - 0.55)$ $h_{tp} = \max(108.6 X^{1.665} h_{sp,g}, h_{sp,g}) \text{ (For } x_{e,o} = 0.55 - 1)$
Zhang et al. (2005)	$h_{tp} = h_{nb} + 0.64 \phi_f h_{sp}$ $h_{nb} = 0.00122 \left(\frac{k_L^{0.79} c_{p,L}^{0.45} \rho_L^{0.49}}{\sigma^{0.5} \mu_L^{0.29} h_{fg}^{0.24} \rho_g^{0.24}} \right) \Delta T_{sat}^{0.24} \Delta P_{sat}^{0.75}$

Table 2-3: (continue)

Reference	Model/Correlation
Lee and Garimella (2008)	$h_{tp} = \left(\frac{Nu_3}{Nu_4} \right) \left((Fh_{sp})^3 + (S_p h_{nb})^3 \right)^{\frac{1}{3}}$
	$F = (\phi_f^2)^{0.2743} \left(\frac{c_{p,tp}}{c_{p,L}} \right)^{0.2743} \left(\frac{k_{tp}}{k_L} \right)^{0.7257}$
	$S_p = 4.6809 - 0.6705 \log \left(\frac{q}{10^6} \right) + 3.908 \left(\frac{D_h}{0.001} \right)$
	$h_{nb} = 5600 F_{PF} \left(\frac{q}{20,000} \right)^{0.9-0.3P_r^{0.15}}$
	$F_{PF} = 1.73 P_r^{0.27} + \left(6.1 + \frac{0.68}{1 - P_r} \right) P_r^2$
Bertsch et al. (2009a)	$h_{tp} = (1 - x_e) h_{nb} + F h_{conv,tp}$
	$h_{nb} = 55 P_r^{0.12} (-\log(P_r))^{-0.55} M_w^{-0.5} q^{0.67}$
	$F = 1 + 80(x_e^2 - x_e^6) e^{-0.6Co}$
	$h_{conv,tp} = (1 - x_e) h_{conv,L} + x_e h_{conv,g}$
	$h_{conv,L} = \left(3.66 + \frac{0.0668 Re_L Pr_L \frac{D_h}{L}}{1 + 0.04 \left[Re_L Pr_L \frac{D_h}{L} \right]^{2/3}} \right) \frac{k_L}{D_h}$

This model allowed calculating the heat sink base temperature and the heat flux under burnout operating conditions. The results were tested against the measurements presented by Tuckerman (1984). The results obtained from the model underpredicted the experimental data of Tuckerman for annular flow boiling. Nonetheless, this two-phase flow model is not feasible for microchannels with low aspect ratios.

Peles and Haber (2000) derived a detailed analytical model for flow boiling heat transfer in a single triangular microchannel. The local variable values within the control volume, such as liquid radius of curvature, velocity, film thickness, and pressure drop were predicted by formulating the conservation equations for mass, momentum, and energy. They showed that when the amount of generated vapor increases, the vapor velocity is augmented, and hence the friction forces applied on the liquid-phase become considerable. The results have also shown a small change in the vapor pressure drop, but a considerable decrease in the liquid pressure along the evaporation region has been obtained.

Jacobi and Thome (2002) focused on the thin film evaporation mode into elongated bubbles during flow boiling in microchannels. Their analytical model was developed based on that, the evaporation of the thin liquid film, formed between the tube wall and the vapor bubble, is the dominant heat transfer mechanism. The basic assumption of their model is that the tube cross sectional area is occupied by one vapor bubble at any one time. The model results in a set of non-linear differential equations that has to be solved numerically. In addition, their model requires knowledge of the effective nucleation superheat and the initial film thickness for calculating the heat transfer coefficient. Their model captured the observed trend in the heat transfer coefficient as it increased with

increasing heat flux, particularly for high heat fluxes. This has been attributed to an increase in heat flux which causes a reduction in the thickness of the liquid film, resulting in a decrease in the conductive resistance, and consequently a higher heat transfer coefficient. The accuracy of the model was evaluated by only two data sets, and a comparison of the predicted and experimental values showed good agreement. They suggested that future work is needed to focus on flow, thermal, and geometrical effects on the film thickness.

Extending the model of Jacobi and Thome (2002), Thome et al. (2004) proposed a three zone model to predict the local time-averaged flow boiling heat transfer coefficient during liquid slug, elongated bubble, and vapor slug zones. Founded by the principles of the above boiling zones, the model was based on the evaporation of an elongated bubble, confined radially by the tube wall, and two alternate zones of liquid and vapor slugs in the tube. They divided one bubble cycle into three phases. The cycle started by passing a liquid slug followed by an elongated bubble, and then a vapor slug. Their basic assumption being that the flow was homogenous, and therefore they ignored the interfacial shear stress. The developed model was dependent of empirical constants. It used three empirical constants to predict the minimum thickness of the liquid film at dry out and the frequency of bubble formation, in addition to a correction factor to predict the initial thickness of liquid film. They showed that the heat transfer due to evaporation in the thin film was very large compared to that of the liquid slug. Nonetheless, heat transfer due to evaporation in the vapor slug was minor. The basic quantity determined in this model was the heat transfer coefficient, which was obtained through analyzing the three zones, and then averaging those values for one cycle.

Dupont et al. (2004) collected a total of 1591 data points for seven refrigerants (R11, R12, R113, R123, R134a, R141b, and CO₂) in circular tubes from seven different published sources to validate the model developed by Thome et al. (2004). The data consisted of the following parameter ranges: tube diameter from 770 to 3100 μm, mass flux values from 50 to 564 kg/m².s, heat flux from 5 to 178 kW/m², and exit quality from 0.01 to 0.99. The model predicted 67% of the data within ±30% tolerance. Results showed that the predicted heat transfer coefficients follow the trend observed through experimentation. However, large discrepancies were noticed between the predicted results and the experimental data available in the literature for boiling in multichannels. Due to the difficulty in measuring the real film thickness, more research is needed to develop accurate models which are capable of predicting the film formation thickness in microchannels.

Annular flow has been discussed in detail by Hewitt and Hall-Taylor (1970). Three analytical models have been presented in the literature to represent heat transfer during annular flow boiling. Fossa (1995) developed an analytical model using one dimensional steady flow analysis of air-water mixtures. The model accounts for variable flow through cross sections such as nozzles and diffusers. It allows the calculation of different flow parameters such as mean film thickness, pressure drop, temperature, and velocity distributions in each phase. To check for the existence of annular flow, the Turner et al. (1969) constraint was defined as follows:

$$\frac{u_g \rho_g^{0.5}}{[\sigma g(\rho_L - \rho_g)]^{0.25}} \geq 3.1 \quad (2-21)$$

However, to obtain a solution for this model requires solving sixteen ordinary differential equations. In addition, this model depends on many correlations to calculate the closure relationships such as interfacial friction factor, mean droplet diameter, and the evaporation rate. The model presented reasonable predictions with the isothermal experimental data.

Fu and Klausner (1997) developed an analytical model using the Reynolds' analogy involving energy balance at the liquid-vapor interface for evaporative heat transfer in vertical annular flow. Although their model can be applied for microgravity flow conditions, it requires the knowledge of the interfacial friction factor, liquid film eddy viscosity, turbulent Prandtl number, and entrainment rate. They used a data bank consisting of 1618 data points for annular flow boiling using water, n-Butanol, and many refrigerants. Their model was developed based on a turbulent flow assumption. The model's applicability to laminar flow is therefore questionable. Moreover, extending the model beyond the flow and thermal conditions for which it has been tested is also questionable, since the empirical closure relations were calibrated against the collected experimental database.

Annular flow pattern has been observed during flow boiling in rectangular microchannels by several authors in their flow pattern studies (Lee and Mudawar, 2005b; Yen et al., 2006; Garimella and Chen, 2006). Qu and Mudawar (2003c) developed an analytical model to predict the flow boiling heat transfer coefficient in microchannel heat sinks. Their model differs from the previous models in certain aspects. Their model included several unique features to microchannels, such as a very small hydraulic diameter and rectangular channel geometry. They had developed the model to suit a

variety of conditions including laminar-liquid laminar-vapor flow, smooth interface, droplet entrainment, and deposition effects. The onset of annular flow was determined using Taitel and Duckler model (1976), given as

$$X_{vv} = 1.6 . \quad (2-22)$$

The model resulted in a complicated system of equations that is difficult to solve analytically. Furthermore, a grid system was established containing a large number of nodes. Hence, an iterative procedure was required to solve the system of equations, and therefore a numerical code was developed. The verification of the model was done only with their experimental data and it showed good agreement.

2.3 Cross-linked Microchannel Heat Sink

Single phase flow in cross-linked microchannel heat sinks was first studied experimentally by Jiang et al. (2002). They introduced five microchannels, having a 100 by 100 μm cross-section, to cross-link eighteen stream-wise microchannels that were 700 μm wide and 300 μm deep with a hydraulic diameter of 420 μm . Due to lateral fluid transport and mixing, cross-linking of microchannels showed better temperature uniformity and more effective cooling performance, compared to straight microchannel heat sinks, especially under non-uniform heating conditions.

Cho et al. (2003) then extended the work of Jiang et al. The focus of their experiment was the single-phase and two-phase boiling heat transfer in cross-linked microchannel heat sinks. Their experiment was performed with a volumetric flow rate of 20 ml/min. Their results indicated that the temperature distribution along the lateral direction for the cross-linked channels demonstrated lower temperature level than that of the straight microchannel heat sink for single-phase flow. This indicated that the cross-

linked channels improved the heat sink cooling performance. They found that the lateral fluid transport and flow mixing occurred actively for liquid-phase fluid, which was attributed to the fluid viscosity difference caused by the different local fluid temperature. For two-phase flow, they observed that bubbles could resist the lateral fluid transport in microchannels when the bubble size was of the same order as the microchannel. Two-phase pressure curves showed that the pressure drop was higher in cross-linked channels than in straight microchannel heat sinks.

Later, Xu et al. (2005) showed that microchannel heat sinks with cross-links have better single-phase heat transfer characteristics than the straight microchannel heat sinks. This enhancement in heat transfer characteristics was explained from the viewpoint of redeveloping thermal boundary layers. It was shown that the cross-link channels caused thermally developing flow in each independent zone. As a result, the periodic formation of the thermal boundary layer yielded to improve the heat transfer characteristics for single-phase liquid flow. The Nusselt number for the cross-linked design was shown to be 1.2 times higher compared to the conventional straight microchannel heat sinks.

Muwanga and Hassan (2007) showed that the cross-linked microchannel heat sink achieves a much lower chip temperature compared to the straight microchannel heat sink for the same heat flux due to the lateral flow mixing effect when the fluid is in the liquid phase. However, it has a higher pressure drop than the straight microchannel heat sink.

Dang et al. (2007) explored adiabatic two-phase flow patterns in cross-linked minichannel heat sinks and compared results with straight minichannel heat sinks. Test sections had 45 rectangular channels and a hydraulic diameter of 1.59 mm. Water and air were used as working fluids, with flow quality ranging from 0 to 0.25, while the mass

flux ranged from 41 to 834 kg/m².s. Resulting flow patterns were presented in terms of a fractional time function and were classified into the following flow regimes: dispersed, intermittent, and annular. Intermittent flow patterns were slightly more frequent in the cross-linked heat sinks compared to the straight channel heat sinks, while annular flow patterns were less frequent. The latter observation may be due to the cross links effect of reducing the number of annular flow patterns observed.

Dang and Hassan (2008) presented an experimental study on horizontal adiabatic two-phase pressure drop in cross-linked minichannel heat sinks. Water and air were forced through forty-five channels of $D_h = 1.59$ mm and length of 131.3 mm with a mass flux and exit quality ranging from 42 to 834 kg/m².s and 0 to 0.25, respectively. Experiments were carried out for five test sections that differed in number, width, and location of cross-links in addition to a standard straight test section with the same hydraulic diameter. The number of cross-links varied from two to six with a width ranging from 1.58 to 4.76 mm. They found that the cross-links diminished the flow maldistribution compared to the straight microchannel heat sink design. However, their results showed an unclear trend relating the number of cross-links to the flow distribution and pressure drop. It was concluded that increasing the cross-link width would enhance flow distribution more significantly than increasing the number of cross-links with the same width. On the other hand, increasing the cross-link width beyond a certain limit did not lead to a more efficient flow distribution.

Xu et al. (2006) investigated transient flow boiling patterns and heat transfer behavior in a cross-linked microchannel array at low mass fluxes and high heat fluxes, using liquid acetone as the working fluid. The silicon chip used consisted of a cross-

linked microchannel array with ten triangular microchannels along the longitudinal direction, measuring 300 μm wide and 212 μm deep, with hydraulic diameters of 155.4 μm . Six independent zones were formed by placing five trapezoidal microchannels perpendicular to the flow direction, at centerline distances of 3.694 mm. Mass fluxes ranged from 40 to 80 $\text{kg}/\text{m}^2\cdot\text{s}$, heat fluxes ranged from 107 to 216 kW/m^2 , and exit vapor qualities ranged from 0.82 to 1.32. Flow patterns were repeated periodically, with a cycle period of 53 ms. The cycle period was inversely related to the heat flux: higher heat fluxes resulted in shorter cycle periods. Convective heat transfer caused by film evaporation at the liquid-vapor interface was responsible for changes in the heat transfer coefficient: the heat transfer coefficient showed an initial sharp increase (over the first few millimeters) in the single phase liquid flow region, and then decreased rapidly along the direction of flow. Two-phase pressure drop and the effect of cross-links were not investigated in their study.

Muwanga et al. (2007) studied flow boiling instability characteristics of straight and cross-linked microchannel heat sinks. Each design consisted of forty-five microchannels. Channels were etched in a silicon substrate with a width of 269 μm , height of 283 μm , and a cross-linked width of 269 μm . Distilled water was used as the working fluid. Tests were carried out at mass fluxes ranging from 91 to 228 $\text{kg}/\text{m}^2\cdot\text{s}$ and inlet temperatures of 70 $^{\circ}\text{C}$ and 80 $^{\circ}\text{C}$ for the straight microchannel heat sink, while an inlet temperature of 70 $^{\circ}\text{C}$ and a mass flux of 137 $\text{kg}/\text{m}^2\cdot\text{s}$ were used for the cross-linked microchannel heat sink. They concluded that the frequency of oscillations depends on the heat flux, flow rate, and inlet subcooling. The inlet temperature oscillation frequency was higher for the straight microchannels than the cross-linked microchannels. Also, the frequency of both designs

decreased with increasing heat flux and mass flux. The inlet pressure amplitude, and inlet and outlet temperature amplitudes were observed to increase with increasing heat flux. Results showed that the straight microchannels have higher inlet pressure amplitudes than the cross-linked microchannels, while the straight microchannels have lower inlet and outlet temperature amplitudes than the cross-linked microchannels.

2.4 Summary

As can be seen from the above review of literature, the knowledge and understanding of two-phase flow and heat transfer behavior in microchannels are far from being complete. A review of relevant literature studies demonstrates the necessity to pursue fundamental studies in these relatively new areas where studies devoted to some of these topics remain very limited.

2.4.1 Two-phase Pressure Drop

Most of the microchannels two-phase pressure drop correlations have been reviewed in Section 2.2.1. Some limitations of these correlations are given below:

1. It may be noted from the above that a general correlation for the evaluation of two-phase frictional pressure drop for laminar-liquid laminar-vapor and laminar-liquid turbulent-vapor flow, using multiple refrigerants, does not exist up to now.
2. There is a need to generate a databank for laminar-liquid laminar-vapor flow in microchannels, since this database is less extensive.

All the experimental investigations and correlations of two-phase frictional pressure drop reported in the literature (Lee and Lee, 2001a; Qu and Mudawar, 2003a; Lee and Mudawar, 2005a; Lee and Garimella, 2008), are based on data from microchannels with

hydraulic diameters larger than 349 μm . The two-phase pressure drop characteristics and applicability of correlations of frictional pressure drop to a rectangular microchannel with a smaller hydraulic diameter has not yet been investigated, and needs to be clarified. Furthermore, a general correlation to predict the frictional pressure drop in microchannels for different ranges of mass flux and several refrigerants has not yet been developed in the literature.

2.4.2 Flow Boiling Heat Transfer

A significant amount of fundamental research has focused primarily on heat transfer characteristics in straight microchannel heat sinks as shown in the previous review of the literature. Until recently, there are large discrepancies in literature between results reported by different investigators for flow boiling in microchannels. With respect to trends, the presented studies from the literature can be divided into two groups. In the first group of studies, (Kuznetsov and Shamirzaev, 2007; Yun et al., 2006; Lee and Lee, 2001b), the heat transfer coefficient increases with increasing exit quality. The second group of studies (Steinke and Kandlikar, 2004; Lee and Mudawar, 2005b, Ravigururajan, 1998; Yen et al., 2006) shows that as the exit quality increases, a significant decrease in the heat transfer coefficient is observed. Clearly, a comprehensive investigation of microchannel flows is needed to resolve the inconsistencies in the reported results. Furthermore, limited research has been conducted to understand the flow characteristics in microchannel heat sinks using flow visualization. This will provide crucial information to the fundamental understanding of these characteristics and explain discrepancies on experimental data. Nevertheless, although many models and correlations exist for two-phase flow in microchannels, their applicability needs to be clarified.

The majority of past flow boiling studies carried out in microchannel heat sinks were performed using thermocouples to measure the wall temperature on the outer surface of the channels. Thermocouples measure bulk average properties in the vicinity of the transducer, and have a great amount of difficulty measuring highly local temperatures, particularly as dimensions are reduced to the microscale. In some cases, however, flow and temperature measurements through the use of transducers are unavoidable; these measurement devices are typically intrusive and create losses and uncertainties, which are amplified at micro dimensions.

Newer measurement techniques were developed to measure experimental parameters in the micro domain, such as un-encapsulated Thermochromic Liquid Crystals (TLC) for fine wall temperature measurements. TLC's are a surface coating capable of qualitative temperature measurements through their color indicators and quantitative temperature measurements through a calibration process. This technique is particularly favorable for microscale temperature measurements due to TLC's non-intrusive nature, capability of full surface mapping and detection of onset of boiling, and very high spatial resolution, particularly in their un-encapsulated form.

2.4.3 Analytical Modeling of Flow Boiling Heat Transfer

A key element in flow boiling in mini- and microchannels – the heat transfer coefficient – is far from properly predicted. Though numerous correlations have been developed to predict the heat transfer coefficient during flow boiling in mini- and microchannel heat sinks (Lee and Lee, 2001b; Lee and Mudawar, 2005b; Bertsch, et al., 2009a; Zhang et al., 2004), very little is known about the validity of these correlations. The available heat transfer correlations for flow boiling in mini- and microchannels

satisfy only limited experimental data and there is little unanimity over a single correlation. Hence, their applicability to other test data and fluids may be questionable. Furthermore, these correlations rely heavily on regression analysis of the tested data, and none were derived based on analytical modeling. Therefore, it is essential to have an analytical model to describe the flow boiling heat transfer in mini- and microchannel heat sinks.

2.4.4 Cross-linked Microchannel Heat Sink

There has been much research on flow boiling in straight microchannel heat sinks up to the present time. Nevertheless, very limited studies have been conducted to investigate flow boiling characteristics in cross-linked microchannel heat sinks (Jiang et al., 2002; Cho et al., 2003; Muwanga and Hassan, 2007; Xu, et al., 2006), although the cross-linked designs have shown better characteristics compared to the straight design in terms of cooling performance, surface temperature, and flow distribution uniformity. Hence, the flow boiling characteristics of cross-linked microchannel heat sinks should be further investigated as such configurations have not been studied extensively.

2.5 Thesis Objectives

The objectives of this study are the experimental investigation of pressure drop and heat transfer of two-phase flow in silicon microchannel heat sinks. The experimental investigation will be assisted with two-phase flow visualization in microchannels, which will allow a better understanding of the experimental results. The experimental results will provide the basis for developing analytical models and empirical correlations that accurately predict the behavior of two-phase flow through microchannels. In contrast to

the available studies, where thermocouples have been used to determine the temperature on the outer surface of the channels, un-encapsulated TLC's are used in the present work to enable non-intrusive and high spatial resolution temperature measurements. This measuring technique is used to provide accurate local surface temperature and heat transfer coefficient measurements.

The specific objectives of the current work are to provide fundamental understanding of the following flow features in micro-scale by:

- Conducting experiments to measure flow boiling pressure drop in straight microchannel heat sinks.
- Developing a two-phase flow pressure drop correlation, using multiple refrigerants, for microchannels with hydraulic diameter of 349 μm or smaller.
- Investigating, experimentally, flow boiling heat transfer in straight microchannel arrays.
- Performing a flow visualization study to explore different flow regimes inside straight microchannel heat sinks and to identify dominant flow patterns.
- Developing an analytical model to predict the flow boiling heat transfer coefficient in the annular flow regime.
- Investigating, experimentally, flow boiling pressure drop, flow instability, and flow regimes in cross-linked microchannel heat sinks.
- To experimentally study heat transfer characteristics in cross-linked microchannel heat sinks and to compare obtained results with straight microchannel heat sinks.
- Proposing new designs of enhanced heat transfer microchannel heat sinks for a new generation of high-density electronic products.

CHAPTER 3

EXPERIMENTAL FACILITY

Chapter 3 gives a detailed description of the test facility and test sections. Details about the data acquisition system and image acquisition system are described. Next, calibration of Thermochromic Liquid Crystals (TLC) and experimental procedures adopted during this research work are included. Finally, data reduction and measurement uncertainties are discussed.

3.1 Flow Loop

The experimental flow loop used in the present study is shown in Figure 3-1, and is the same used by Muwanga and Hassan (2006). This test facility was built to distinctly acquire TLC wall temperature measurements of microchannels and microdevices, and was designed for both single-phase and two-phase flow experiments. The facility is capable of incorporating a number of different fluids to be analyzed, such as distilled water and a variety of refrigerants. The working fluid in the present investigation is FC-72, a low viscosity electronics cooling fluid widely used in industry, whose properties are shown in Table 3-1. Advantages of FC-72 is that it has a relatively low boiling point (56.1 °C at 1 atm) and dynamic viscosity (6.4×10^{-4} N.s/m² at 25 °C). Moreover, it has a high dielectric constant so it will not damage the electronic components in the case of leakage. However, it has very large air solubility, and therefore requires degassing prior to flow boiling experiments to eliminate non-condensable air from the working fluid.

The fluid operates in a closed system and is continuously circulated by means of a magnetically coupled gear pump (Cole-Parmer), as shown in Figure 3-1. The gear pump operates at a controlled speed and supplies a maximum flow rate of 290 ml/min, with a pressure of 517 kPa. Downstream from the pump is a 15 μm filter, to remove any particulates within the flow. The system flow rate is monitored by means of a nutating digital output flowmeter (DEA Engineering), equipped to handle corrosive refrigerants. The flowmeter outputs a 5-volt square wave signal at a frequency proportional to the time for the nutator to complete one cycle. Initial calibration of the flowmeter was carried out using a precise weighing method, and operates in a flow rate range from 10 to 250 ml/min.

Prior to entering the test section, the fluid enters a preheater for additional flow temperature control. The preheater is a counter flow, tube-in-tube heat exchanger with distilled water as the heating fluid. The FC-72 enters the test section at a temperature 4 $^{\circ}\text{C}$ below its saturation temperature and exits as two-phase. As shown in Figure 3-1, the test section is heated by means of Joule heating with the use of a power supply. Heater power was provided by one BK Precision DC power supply (Model 1623A), with a voltage range of 0 to 60 V. After flowing through the test section, the FC-72 was partially condensed in the tubing on its way to the tank. Also, apparent from the figure, are the image and data acquisition systems, details of which will be explained in a later section.

The degassing procedure was carried out to purge the system of air. As shown in the flow loop schematic (Figure 3-1), directly above the FC-72 tank is the degassing flow loop, which consists of valves, a water cooled condenser, a separator, and degassing bottles. With the test section installed, the fluid was circulated through the system at a

high flow rate (~50 ml/min). Through the use of the heating element, the FC-72 tank was heated until the fluid in the tank was boiling (~60 °C). The preheater, just upstream of the test section, was also turned on to maintain the fluid at a high temperature throughout the system, above 50 °C. The valves to the degassing flow loop were then opened, which allows the vapor from the FC-72 tank to travel through the condenser and condense. The condensed fluid then flowed to a separator, where the heavier liquid was returned to the tank, and the air was released to the degassing bottles. The degassing bottles were glass bottles filled with water to observe and track the degassing process, where the air escaped as bubbles. The fluid was circulated for about one hour, allowing the entire fluid to pass through all elements of the system. After this time, the bubbles in the degassing bottles were non-existent, indicating the FC-72 was completely degassed. Once the fluid was degassed, the valves to the degassing flow loop were shut off, and the system was left to cool down and to allow the FC-72 vapor in the tank to condense.

3.2 Test Sections

Recent developments in silicon processing technology have resulted in fabricating cost-effective three-dimensional feature geometries of silicon microfabrication, which offered the potential for fabrication of microdevices such as micropumps, heat pipes, and microchannel heat sinks. These feature geometries are followed by bonding processes to form complex devices and structures. Deep reactive ion etching (DRIE) is used for etching features with variable tapering and high aspect ratio microstructures. Deep channels and pits (up to a few tens of microns deep) with nearly vertical walls and of arbitrary shape can be etched using this method. The test sections used in the present study consist of the silicon heat sink including a resistance heater deposited on the back,

Table 3-1: Properties of FC-72 at 25°C and 1 atm.

Parameter	Value
ρ_L	1680 kg/m ³
μ_L	6.4×10^{-4} Ns/m ²
$c_{p,L}$	1100 J/kg°C
σ	0.01 N/m
T_{sat}	56.1 °C
h_{fg}	88 kJ/kg
Dielectric Constant	1.75

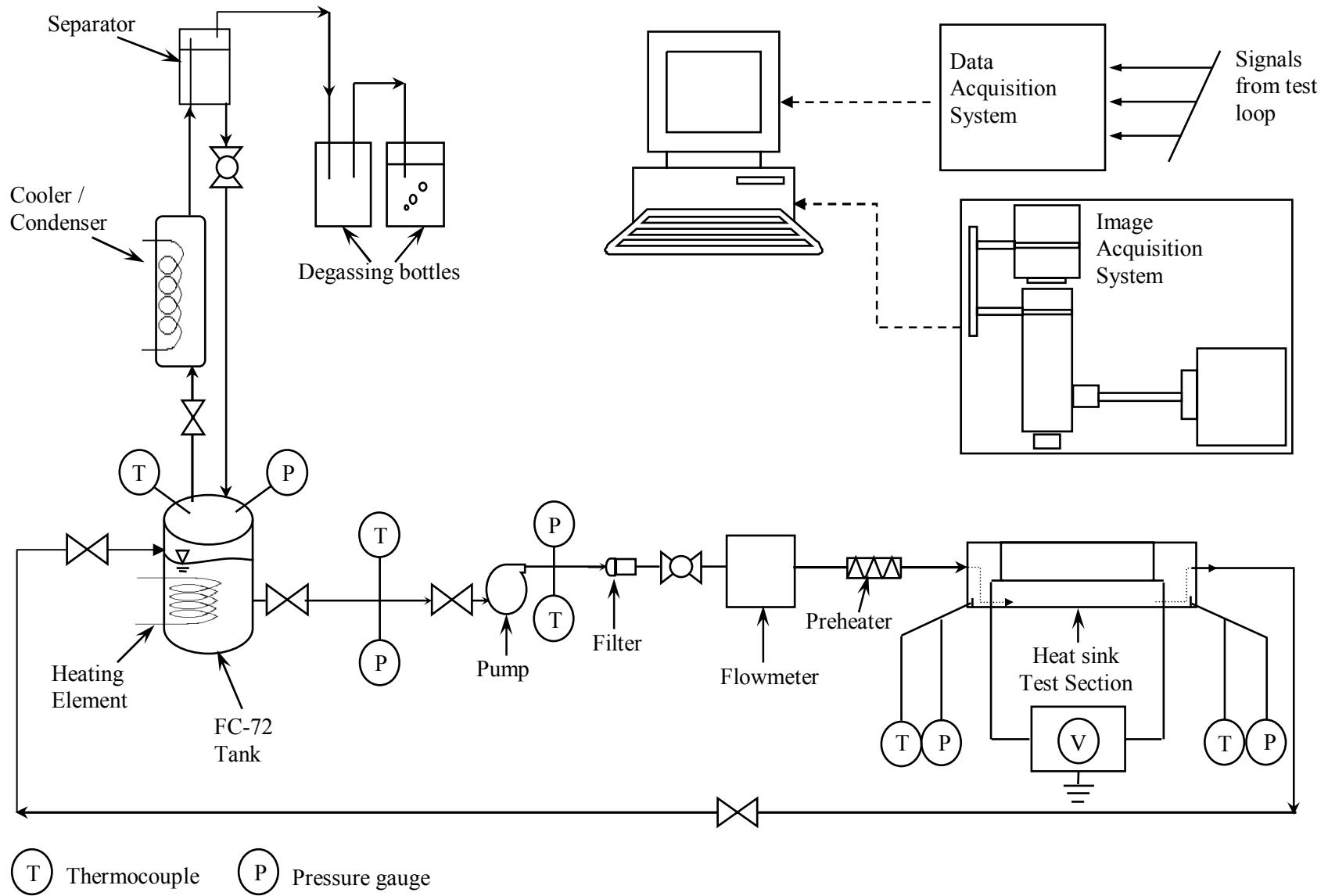


Figure 3-1: Experimental test facility flow loop.

and an acrylic support for laboratory manipulations. The microchannel heat sink is designed as an integrated microsystem consisting of an etched silicon wafer, a Pyrex cover plate, and platinum heater strips.

3.2.1 Straight Microchannel Heat Sink

Figure 3-2(a) and (b) show photographs of the straight microchannel heat sink, with top and bottom views. The etched silicon wafer consists of a rectangular silicon chip in which forty-five rectangular microchannels were etched using DRIE. Microchannels were realized by bonding the Pyrex cover anodically to the silicon wafer, resulting in a fourth wall to close the channels, as well as providing a transparent cover for flow visualization. The Pyrex cover also had an inlet and outlet hole, each of which were 1 mm in diameter. These holes extended to the inlet and outlet manifolds of the heat sink. These holes introduced a high pressure drop. However, they also served as throttling valves before the fluid entered the test section to reduce flow instabilities (Kandlikar 2002). The integrated heater, Figure 3-2(b), was deposited onto the backside of the silicon wafer under the microchannels to provide a uniform heat flux. The length of the heater strip was 186 mm and had a width of 1 mm. The serpentine heater was designed for a nominal resistance of 240 Ω with a potential applied serially through the entire length of the serpentine.

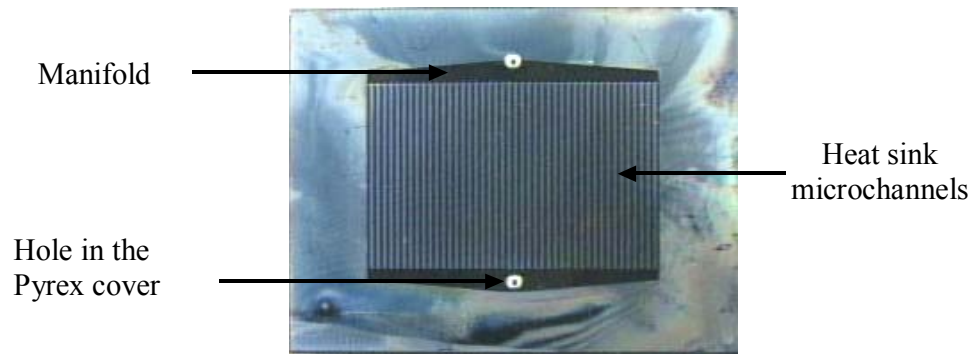
Figure 3-3 presents a schematic for the straight microchannel heat sink dimensions. Each channel had a depth of 300 μm , a width of 242 μm , and a length of 16 mm. As shown in this figure, the inlet and outlet manifolds were designed with tapered walls to provide better flow distribution throughout the entire channel array. Figure 3-4 shows a cross-section of the microchannels. The actual microchannel cross section is not perfectly

rectangular, but close to trapezoidal. Each channel has an actual depth of 276 μm and a width of 225 μm , as shown.

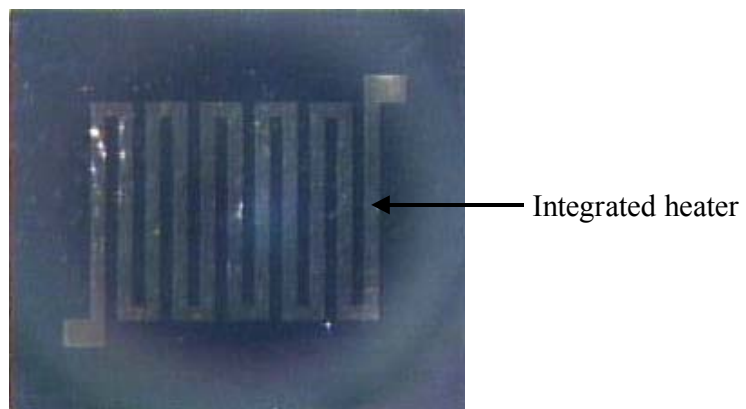
3.2.1 Cross-linked Microchannel Heat Sink

The cross-linked microchannel heat sink has the same design as the straight microchannel heat sink, except that three cross-links of width 500 μm were introduced, in the transverse direction, to divide the microchannels into four equal sections, each measuring 3.625 mm in length. Figure 3-5 shows the image of the cross-linked microchannel heat sink. These cross-link microchannels are introduced to avoid flow mal-distribution, and to achieve better temperature uniformity and more effective cooling due to the lateral fluid transport and mixing. Figure 3-6 illustrates the schematic construction of the cross-linked microchannel heat sink. The centerline distance between each section is 4.125 mm.

The heat sink was mounted on an acrylic support (Figure 3-7) designed to provide a rigid base for the heat sink and to create inlet and outlet plenum chambers to measure the fluid bulk temperature and static pressure. Also, a cavity was machined on the backside of the support to allow for flow visualization within the channels. To adequately seat the heat sink in the support, the acrylic support possessed a groove with a depth of 0.3 mm, and an area similar to that of the footprint area of the heat sink (30 \times 33.875 mm). The inlet and outlet holes of the heat sink's Pyrex cover were precisely aligned with the holes machined in the acrylic support. The heat sink was bonded to the support using a high temperature epoxy.



(a)



(b)

Figure 3-2: A photograph of the fabricated straight microchannel heat sink with (a) microchannels and Pyrex cover and (b) integrated heater on the back

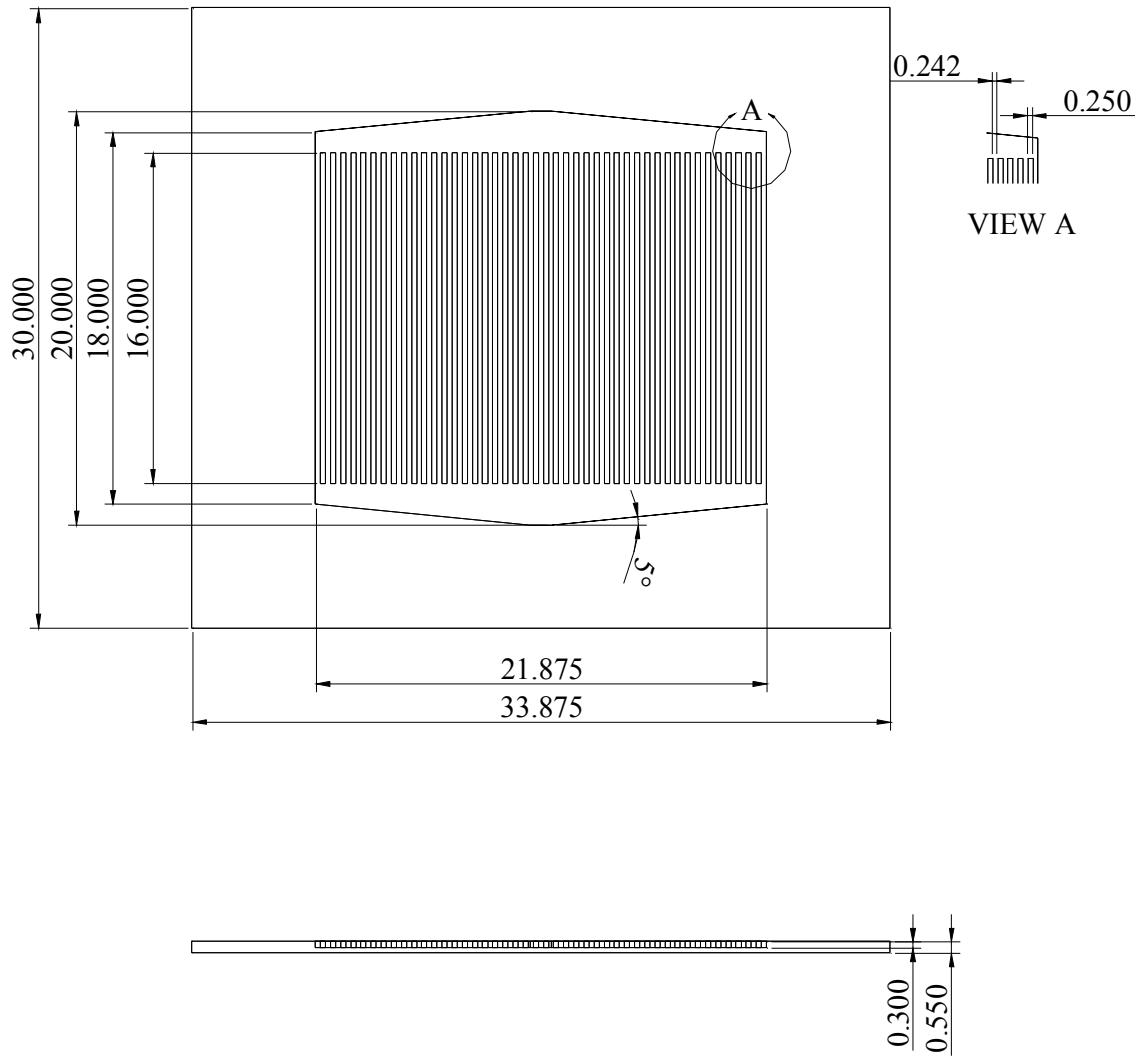


Figure 3-3: Detailed schematic of the straight microchannel heat sink
(dimensions are in mm).

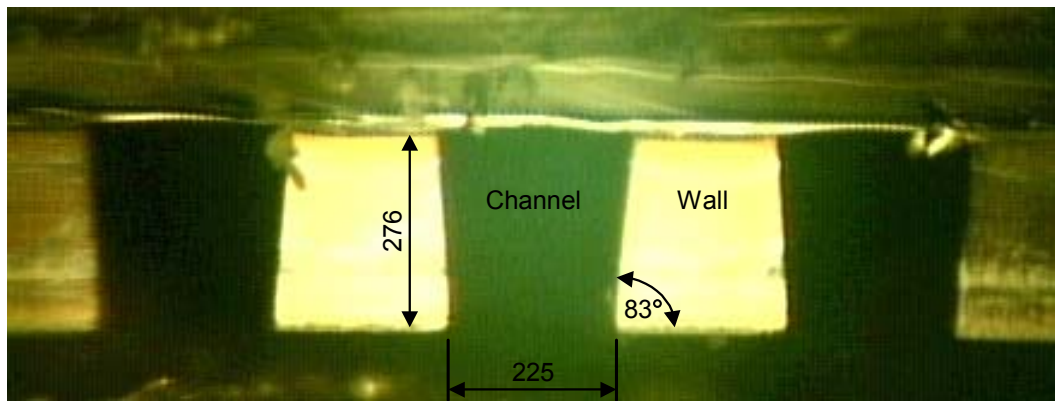


Figure 3-4: Cross-section for the microchannels showing actual cross-sectional area and dimensions (dimensions are in μm).

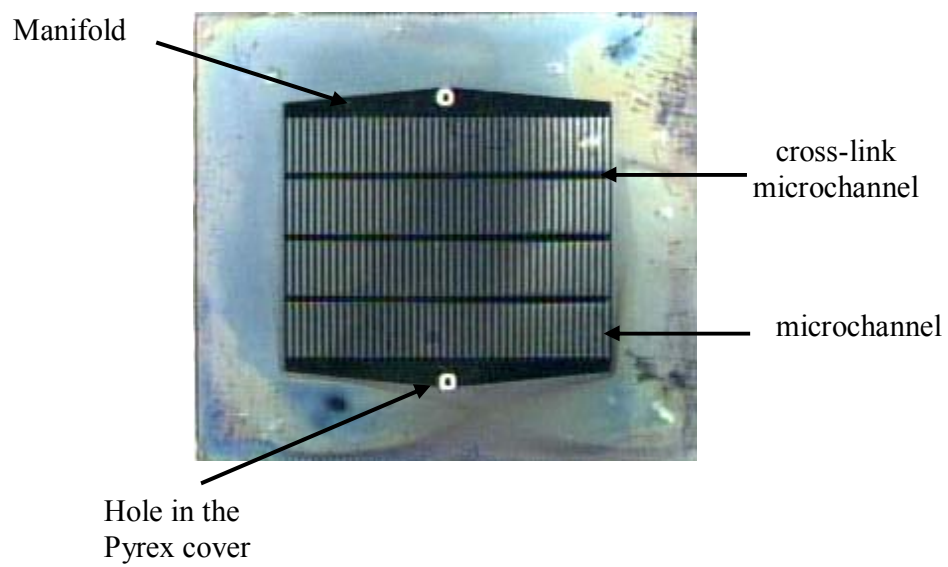
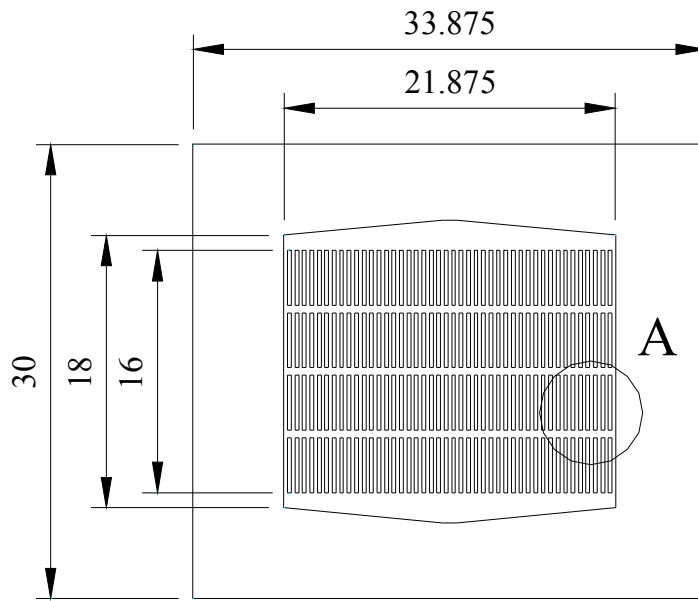
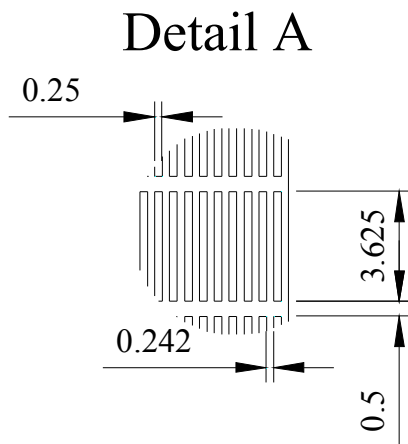


Figure 3-5: A photograph of the fabricated cross-linked microchannel heat sink.



(a)



(b)

Figure 3-6: Detailed schematic of the cross-linked microchannel heat sink (dimensions are in mm).

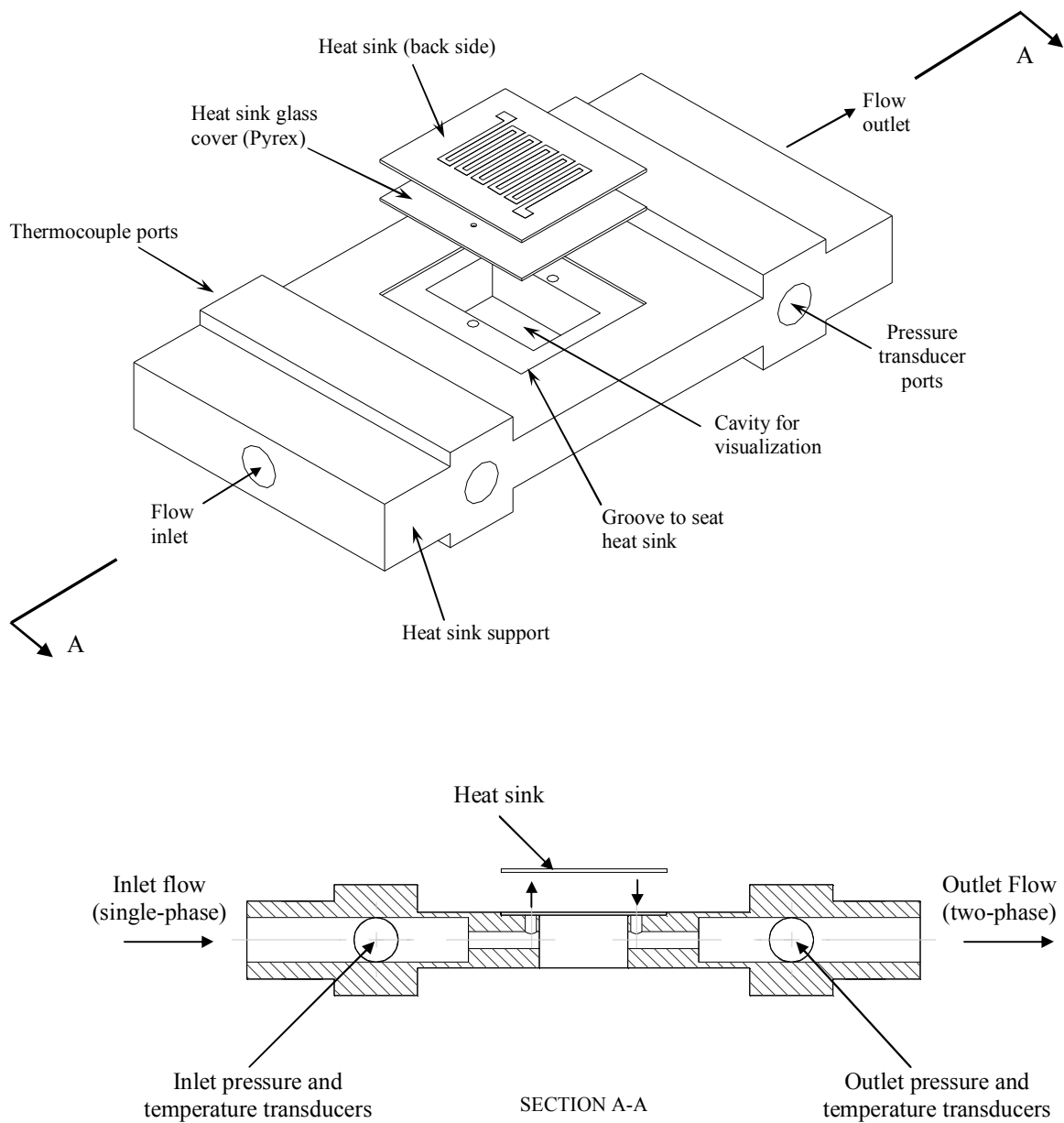


Figure 3-7: Microchannel heat sink mounted on the acrylic support.

3.3 Data Acquisition and Flow Visualization Facility

A schematic of the data acquisition system is shown in Figure 3-8. The signals from the transducers (i.e. pressure, temperature) are transferred through the signal conditioning unit to reduce noise and/or improve signal strength, then through the data acquisition (DAQ) card to the computer. The pressure transducers, both manufactured by Omega, are model PX01C1 at the heat sink outlet manifold and model PX02C1 at the inlet manifold, with ratings of 517 kPa (75 psi) and 345 kPa (50 psi), respectively. The output from these and other sensors was monitored through an automated data acquisition system using the LabVIEW™ software. The data acquisition hardware consists of a National Instrument's SCXI 1000 signal conditioning unit, with the appropriate modules as well as the NI 6052E 16-bit 333 kHz data acquisition card. However, signals from the metering devices (i.e. flowmeter) were directly transferred to the computer through the DAQ card, without the use of the signal conditioner. Image acquisition was carried out in the LabVIEW software and the images were captured in Red-Green-Blue (RGB) format. Hue planes were simultaneously extracted and saved in tagged image file format (TIFF). Image and data post-processing was carried out using an interactive in-house program in MATLAB software.

A schematic of the image acquisition system is shown in Figure 3-9. Light from an illuminator box (Optem Intl.) is directed through a fiber optic cable, keeping the heat generated from the light source away from the test section. From the figure, it is shown that the light was passed through a polarizer prior to entering the zoom lens casing, where it was deflected to the test surface by a beam splitter. However, even though the test facility has this capability, it was only used in acquiring flow visualization images and

not TLC images, due to the reduced intensity and poor light distribution which were found to be inadequate in obtaining a vibrant TLC image of the surface. Therefore, a ring light connected to the illumination source was incorporated into the setup to directly illuminate the TLC coated surface, which provided excellent illumination and light distribution. Upon reflection from the coated surface, the light was circularly polarized and was passed into the zoom lens through the analyzer, and was directed to the 3-CCD camera. Since the reflected light was circularly polarized, it traveled through the crossed polarizing pair unaffected. The acquired TLC image was then transferred directly to the computer to be processed.

Through the use of an LCD television, real time monitoring and positioning of the test section was possible. This allowed precise alignment of the test-section, as well as observation of the colors of the TLC coated surface. The video signal used in the television loop came from a separate output line directly from the camera. Image acquisition was obtained using a Sony 3-CCD analog camera (model DXC-9000) at 1/10,000 shutter speed, which was connected to a variable zoom microscopic lens. This combination was mounted onto a three-axis traverse, equipped with variable length stages with 1 μm resolution. The lateral and vertical axis stages allowed for fine-tuning of both focusing and positioning. A high resolution objective lens 10 \times (Optem) provided a higher magnification to allow optical access inside the microchannels. Using this objective lens, the resolution of the images was increased to 3.3 microns/pixel.

3.4 Un-encapsulated Thermochromic Liquid Crystals

The instantaneous measurement of local wall temperatures was achieved through the use of un-encapsulated thermochromic liquid crystals (TLC's). Compared with conventional bulk measurement techniques, such as thermocouples, TLC thermography is a non-intrusive thermal measurement technique capable of full surface mapping with high spatial resolution, particularly in its un-encapsulated form. Although there is a fair amount of difficulty regarding the application of un-encapsulated TLC's, these measurement characteristics are attractive in resolving fine thermal measurements.

The TLC's should be applied as a uniform coating capable of producing vibrant colors for surface temperature measurement. A thicker coating improves color vibrancy, however if the coating is too thick, the coating itself can produce non-negligible temperature gradients through the TLC layer. A relatively uniform application of the un-encapsulated TLC's was applied through the use of an airbrush using a similar method as Muwanga and Hassan (2006).

The un-encapsulated liquid crystal material used was provided by LCR-Hallcrest. The TLC material nominally has a red-start of 53 °C with a bandwidth of 17 °C. The TLC material was applied onto the back surface of the micro heat sink using a double action airbrush (Iwata-Eclipse). In order to provide an improved uniform layer of coating, the TLC material was dissolved in acetone with concentrations by weight of 5:1 (acetone to TLC). Prior to the application of the TLC coating on the heat sink, a water-based, black paint (Createx) coating was applied using the airbrush for improved color vibrancy of the TLC response.

3.5 Experimental Procedure

For the heat transfer experiments, there was no cover in direct contact with the TLC coated surface of the heat sink. In order to protect the TLC coated surface from dust and room lighting, a non-contacting, optically clear plastic cover was placed over the heat sink. Two 1.5 mm diameter Type-T (Omega special error limits material) thermocouples were placed in each plenum chamber of the test section (see Figure 3-7) to measure the bulk fluid temperature. Two static pressure transducers tracked the gage pressure in the inlet and outlet plenums.

To acquire quantitative temperature data from TLC thermal colors on the surface of the heat sink, it was required for the TLC material to be calibrated to relate the observed color to a temperature value. In the present study, similar to Muwanga and Hassan (2006), the hue angle was taken as the color descriptor to deduce temperature from the liquid crystal responses. The hue angle, given by Hay and Hollingsworth (1996) is defined as,

$$Hue = \arctan\left(\frac{\sqrt{3}(G - B)}{2R - G - B}\right), \quad (3-1)$$

where R , G , and B are red, green, and blue values, respectively. The observed TLC color depends on many aspects, such as camera distance, lighting intensity and distance, and the time the TLC coating was applied to the specimen. In order for a valid and confident calibration to be carried out, all the above aspects must be maintained the same for both the calibration and the experiment.

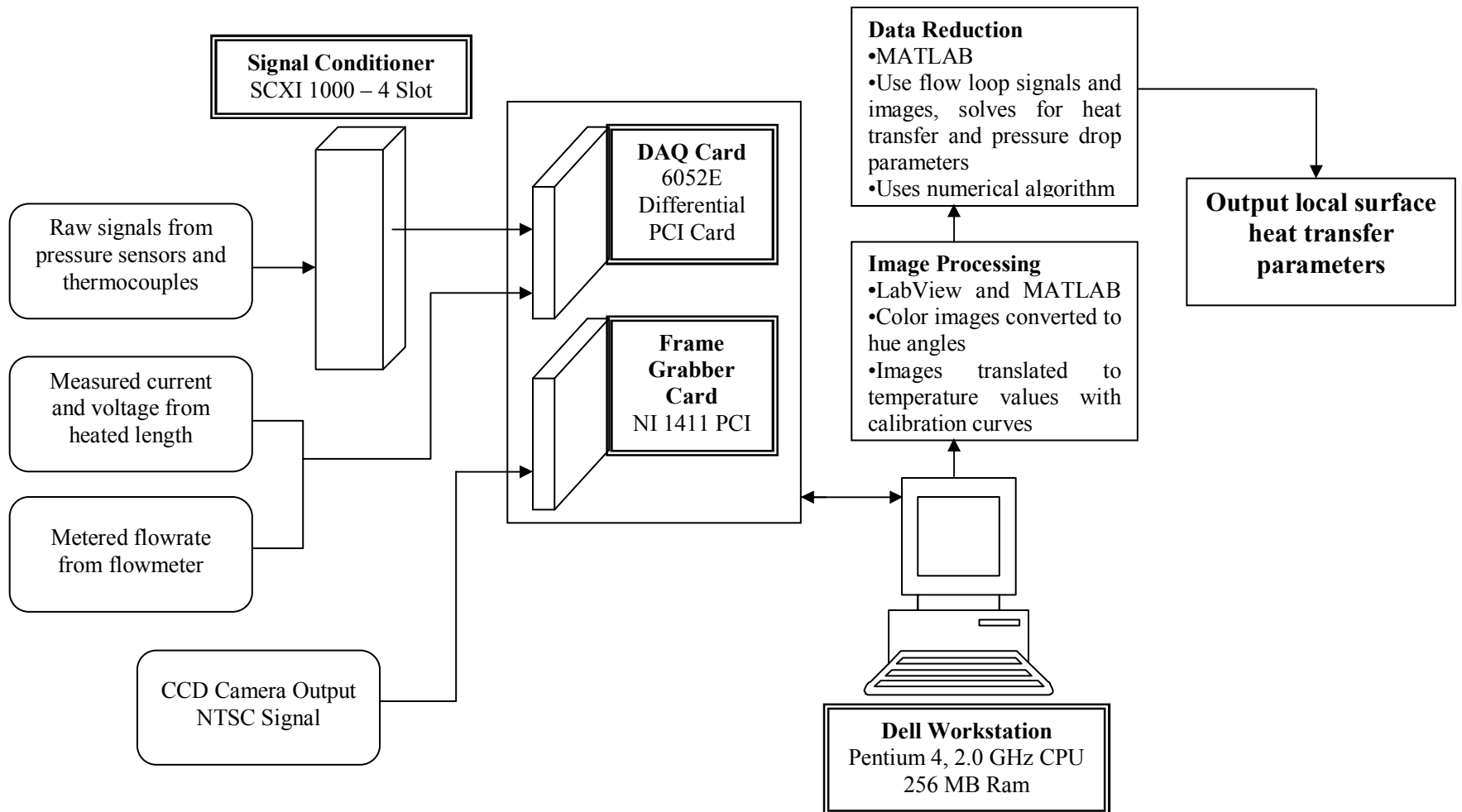


Figure 3-8: Schematic of the data acquisition system.

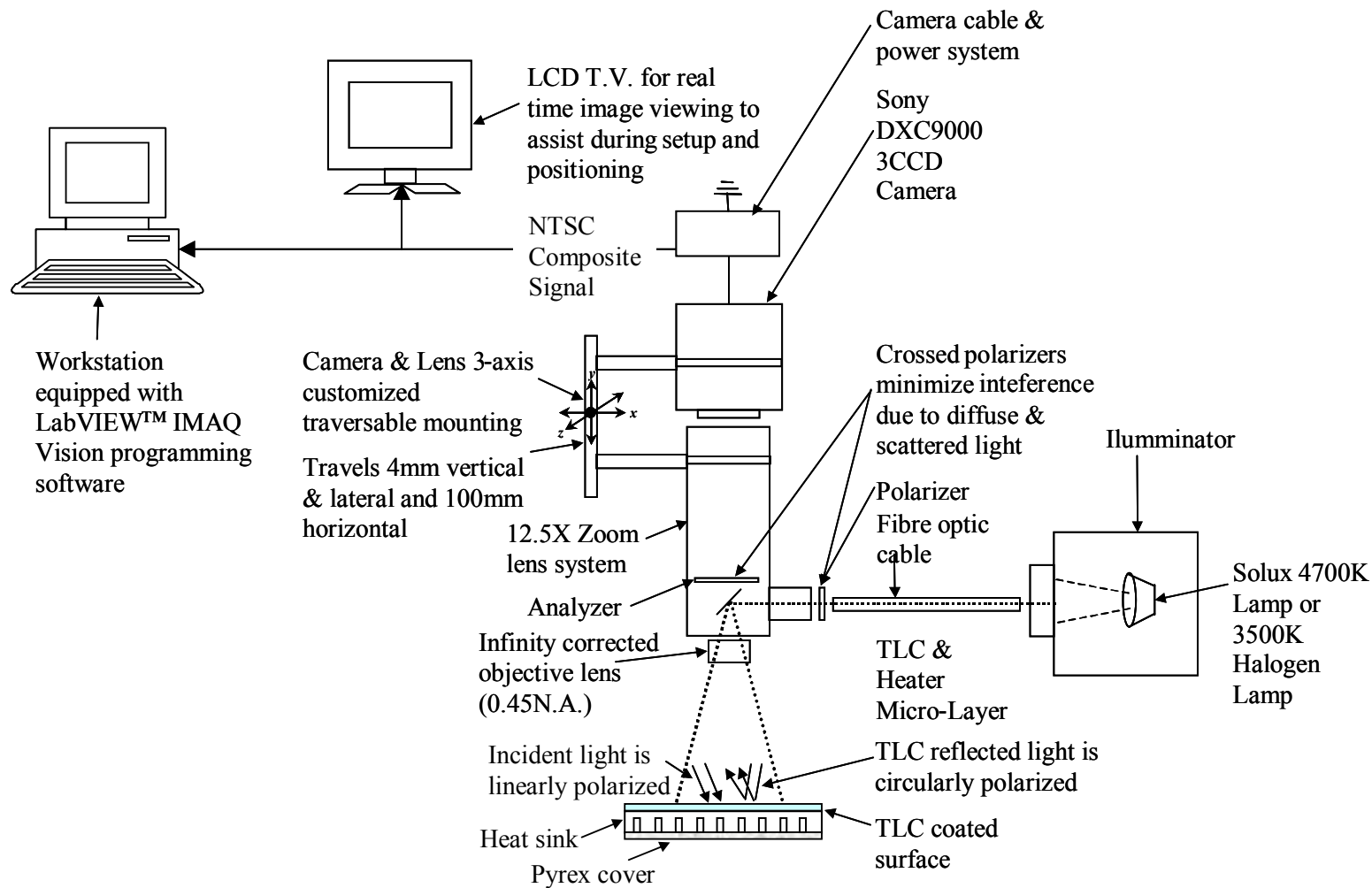


Figure 3-9: Schematic of the image acquisition system.

The calibration was based on heating of the TLC coated surface through the resistive heater on the heat sink using the power supply, and calibrating the material through the use of two fast response surface thermocouples installed at opposite ends of the heat sink surface. This method was found to be very practical and was selected since the temperature range of the TLC's (53 to 70 °C) is within the saturated region of the working fluid. Through the use of the power supply and observation of the thermocouples temperature readings, the power supply was adjusted to obtain different TLC color images over the whole range of the TLC material, starting from red (~53 °C) to dark blue (~70 °C). Some images acquired are presented in Fig. 3-10. Through the use of the CCD camera, images of the TLC coated surface were recorded at every 0.5 °C to cover the whole range of the TLC material.

Processing of the calibrated images was carried out as follows. Each calibration curve, which is a curve of Temperature vs. Hue Angle, represents a certain region of interest (ROI) on the heat sink surface. In the present study, a ROI of 5×5 pixels was selected, giving over 2728 calibration curves covering an entire image as shown in Fig. 3-11. The size of the ROI should be large enough to account for noisy pixels using statistics, but small enough to capture the local variability in the color change.

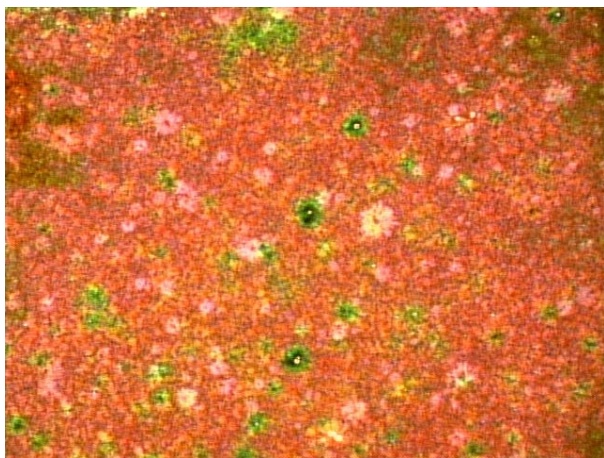
Through the use of MATLAB, an automated calibration curve fitting was utilized to fit the calibration data points. Initially a polynomial of fifth order was utilized to fit the points, however if any local extensive fluctuations were present within a predefined region, the polynomial order was reduced to third. An example of this case is shown in Figure 3-12, which shows a typical calibration curve of a good fit between the calibrated

data and a fifth order polynomial. Figure 3-13 shows a calibration curve with the data points originally set at a fifth order fit, and then corrected to a third order fit.

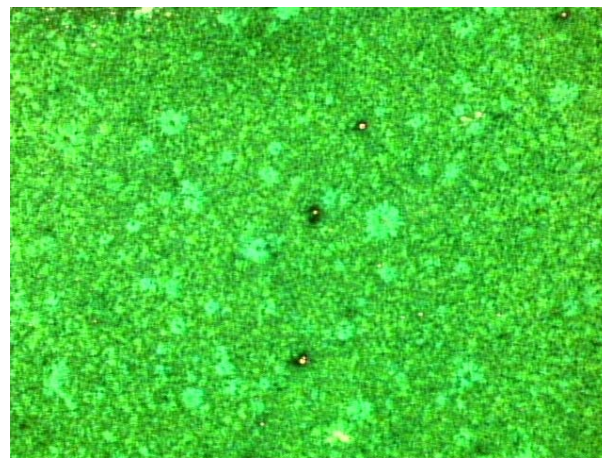
Through the use of TLC thermography, wall temperature data was obtained through images taken at a single measurement location for the heat sink microchannels outlet. As previously explained, prior to each experiment it was necessary to calibrate the coated TLC material. Also, since the experimental aspects (i.e. room lighting, test section position, etc.) must be maintained for both the calibration and measurements, the calibration and measurements are performed on the same day. Also, it should be noted that unless TLC images are being taken, the heat sink should remain covered (with a non-contacting cover) to reduce TLC degradation from exterior lighting.

To begin the measurements, the heating element in the FC-72 tank was adjusted to maintain the tank temperature at 50 °C, and the preheater was adjusted to raise the fluid temperature until the inlet fluid bulk temperature was just 4 °C subcooled (~52 °C). The flow rate was measured and held constant for each set of data collected. After running the flow through the system, measurements were ready to be taken, and the protective non-contacting cover was removed.

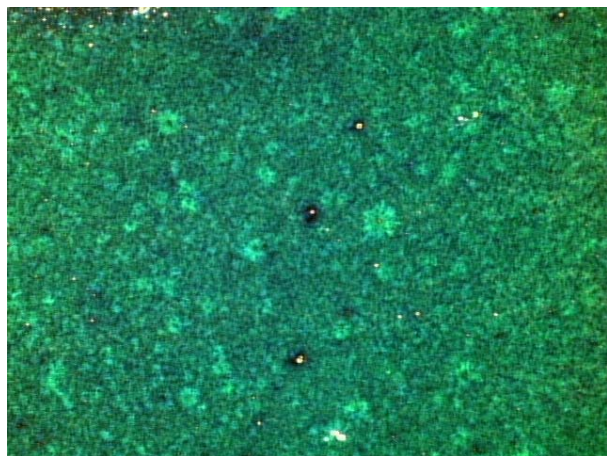
The illumination system was turned on and the voltage from the power supply (Joule heating) was adjusted until the TLC color response was predominantly in the blue and green range on the heat sink surface (~54 to 70 °C). The system was allowed to come to equilibrium (5 to 10 minutes), after which a measurement image was taken. Three colored images were taken at a speed of 30 frames/second. Through the automated system, these images were converted to hue angle and scaled, and then the median value for each ROI was calculated.



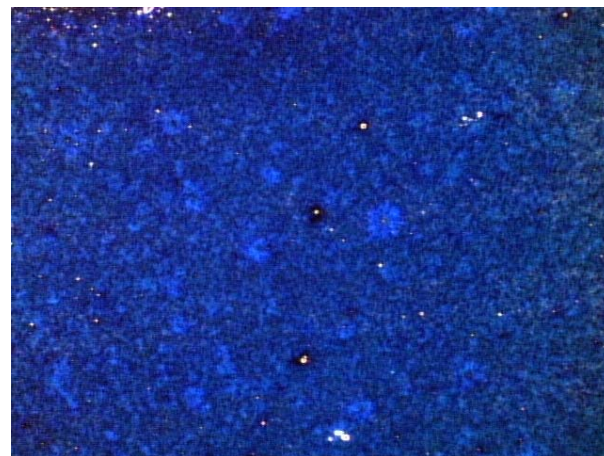
(a)



(b)



(c)



(d)

Figure 3-10: Images of the TLC undergoing color play (a) 56.7 °C (b) 59.4 °C (c) 64.9 °C (d) 70.1 °C

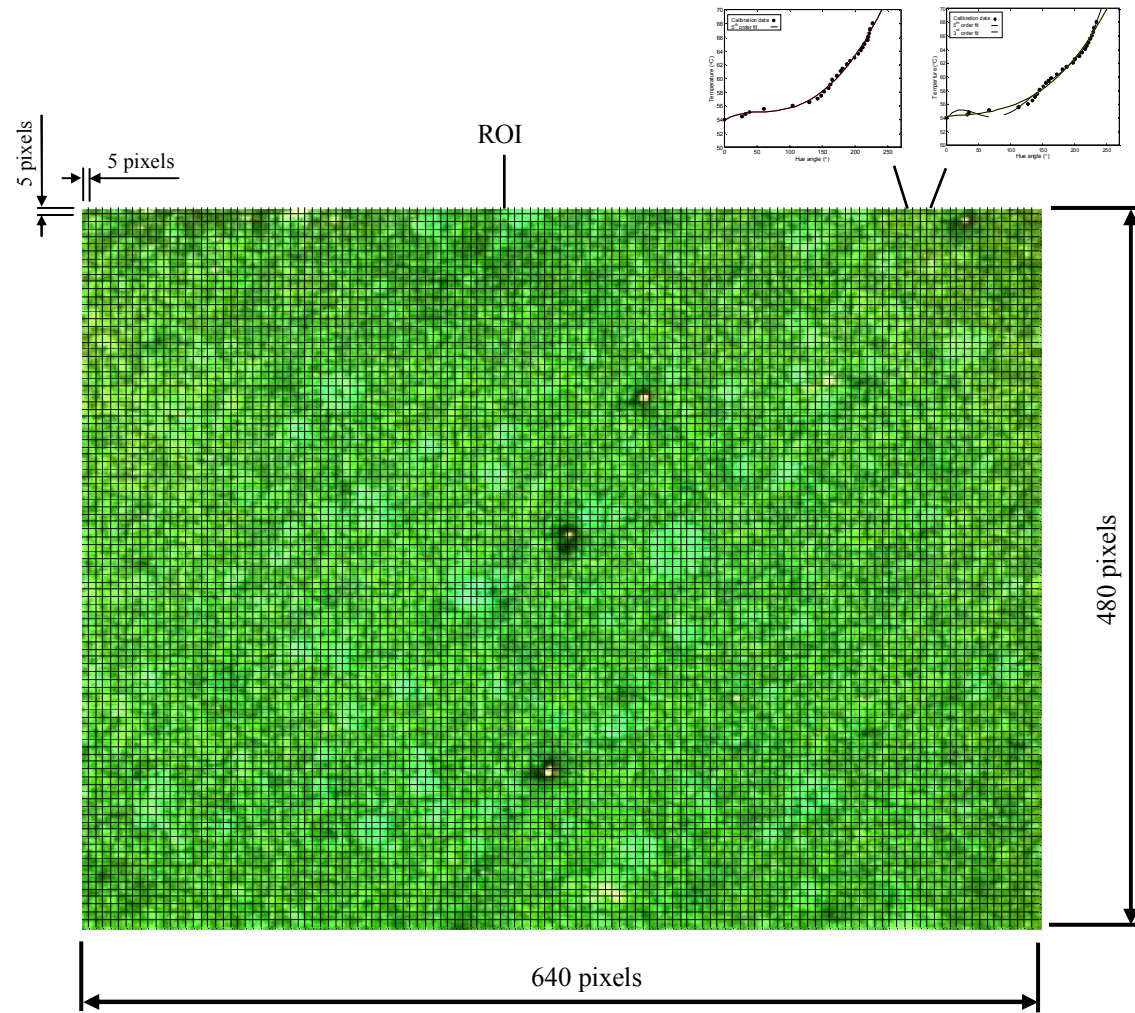


Figure 3-11: Representative TLC image divided into regions of interest (5×5 pixels).

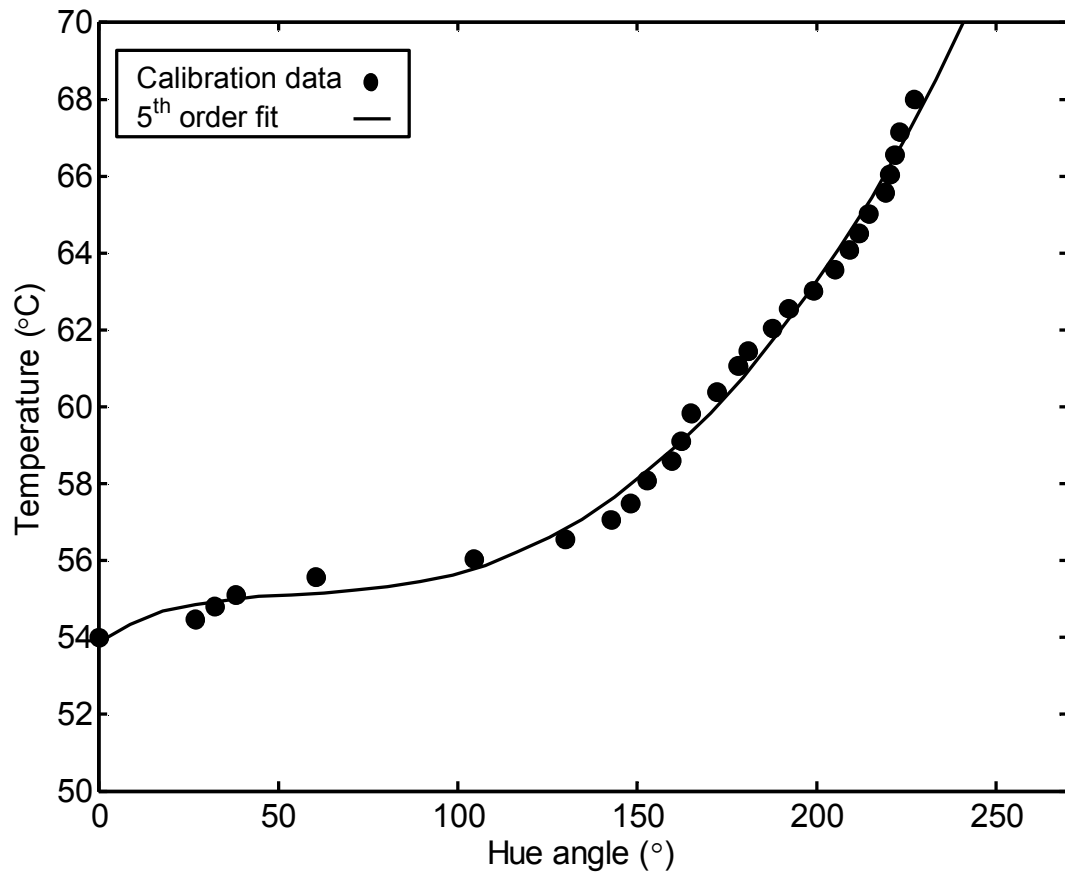


Figure 3-12: Examples of a 5th order calibration curve.

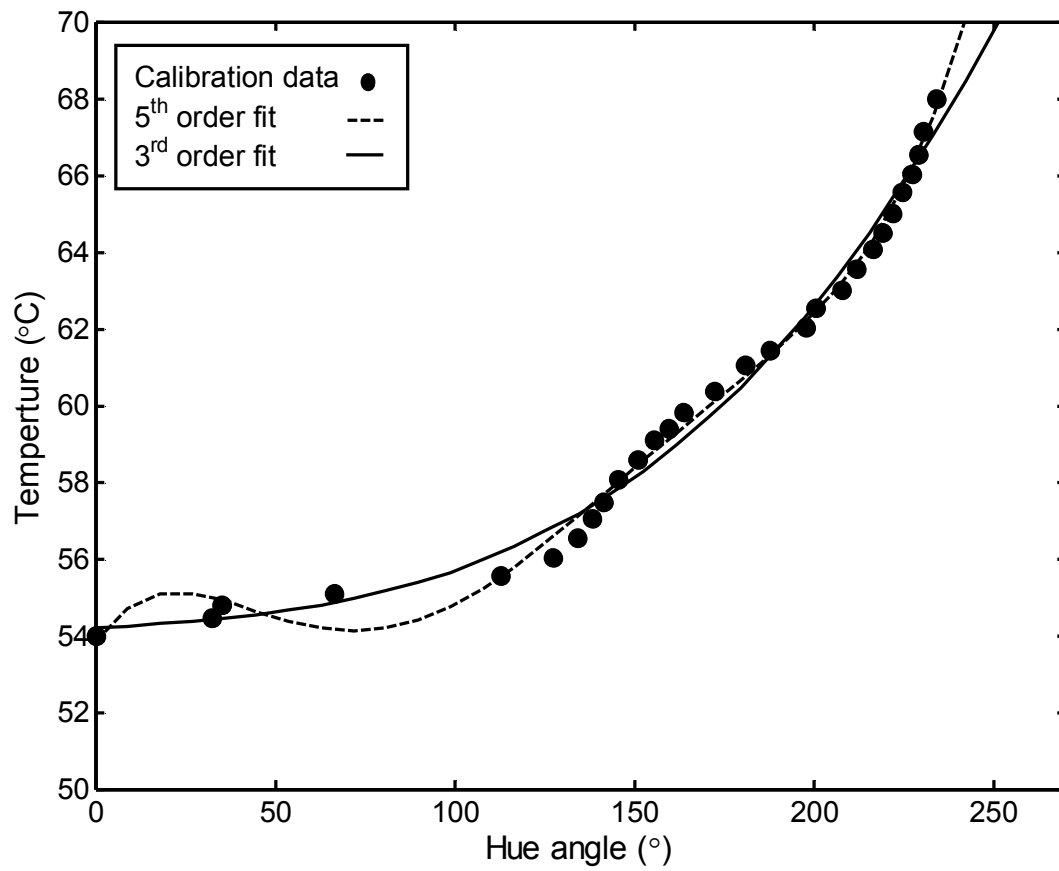


Figure 3-13: Example of calibration curves: corrected calibration curve with 3rd and 5th order fits.

Simultaneously, the bulk fluid temperature and gage pressure at the inlet and outlet, as well as flow rate measurements were captured and recorded.

3.6 Data Reduction

The total pressure drop across the heat sink can be expressed as:

$$\Delta P_{\text{tot}} = \Delta P_{\text{sp}} + \Delta P_{\text{tp}} , \quad (3-2)$$

where ΔP_{tot} is the sum of single-phase and two-phase pressure drop terms. The single-phase pressure drop term is defined as the sum of single-phase dynamic and friction pressure losses in the subcooled length of the microchannel and the acrylic support. The single-phase pressure drop term is represented by the following equation:

$$\Delta P_{\text{sp}} = \frac{\rho_L}{2} \left[\left(\frac{4f \text{Re} L_{\text{sub}}}{D_h} + (K_c + K(\infty)) \right) u_{\text{ch}}^2 + 2K_{90} u^2 \right] , \quad (3-3)$$

where u and u_{ch} are the mean velocity in the inlet manifold of the acrylic support and the microchannel, respectively. The contraction pressure loss coefficient (K_c), due to area contraction at microchannel's inlet is taken from Kays and London (1984). For the 90° bend pressure loss coefficient, Streeter (1961) recommended K_{90} to be 1.1 for macro-scale turbulent applications, and is not dependent on Reynolds number. The subcooled length can be calculated as

$$L_{\text{sub}} = \frac{\dot{m} c_p (T_{\text{sat}} - T_{\text{in}})}{q(2H_{\text{ch}} + W_{\text{ch}})N_{\text{ch}}} , \quad (3-4)$$

where T_{sat} is calculated based on the saturation pressure in the outlet manifold. The saturated length of the channel can be calculated as

$$L_{\text{sat}} = L_{\text{ch}} - L_{\text{sub}} . \quad (3-5)$$

For a single-phase fully developed laminar flow in rectangular channels with an aspect ratio, γ , the friction factor can be defined by the following equation provided by Shah and London (1978)

$$f = 24(1 - 1.3553\gamma + 1.9467\gamma^2 - 1.7012\gamma^3 + 0.9564\gamma^4 - 0.2537\gamma^5) / Re_{fo} . \quad (3-6)$$

Steinke and Kandlikar (2006) proposed the following equation to calculate Hagenbach's factor for the developing laminar length in terms of the microchannel aspect ratio

$$K(\infty) = 0.6796 + 1.2197\gamma + 3.3089\gamma^2 - 9.5921\gamma^3 + 8.9089\gamma^4 - 2.9959\gamma^5 . \quad (3-7)$$

On the other hand, the two-phase flow pressure drop in the saturated length of the microchannel is expressed as the sum of four components namely, frictional, acceleration, gravitational, and dynamic losses as follows,

$$\Delta P_{tp} = \Delta P_{tp,fr} + \Delta P_{tp,a} + \Delta P_{tp,gr} + \Delta P_{tp,dyn} . \quad (3-8)$$

Frictional pressure drop is due to the viscosity of liquid and vapor in motion. For two-phase flow, an additional frictional pressure drop may be due to the inter-phase friction between liquid and vapor phases (interfacial shear stress). Acceleration pressure drop is due to the energy spent in accelerating the molecules of the fluid. This component of pressure drop is caused by a change in flow area or density. The gravitational pressure drop is caused by the difference in elevation, and it is far smaller than the frictional pressure drop component in microchannels. Therefore, the effect of gravity can be reasonably neglected. Dynamic losses are caused by local disturbances of the flow, separation of flow from the walls, and formation of vortices. For the separated flow model, the frictional two-phase flow pressure drop is expressed as follows

$$\left(\frac{dP}{dL}F\right)_{tp} = \phi_f^2 \left(\frac{dP}{dL}F\right)_L, \quad (3-9)$$

where ϕ_f^2 is the two-phase pressure drop multiplier defined as

$$\phi_f^2 = 1 + \frac{C}{X} + \frac{1}{X^2}, \quad (3-10)$$

where C is the two-phase multiplication factor. The liquid-phase frictional pressure gradient is given by

$$\left(\frac{dP}{dL}\right)_L = f_L \frac{G^2(1-x_e)^2}{2\rho_L D_h}, \quad (3-11)$$

where

$$f_L = \frac{f \text{Re}}{\text{Re}_L}. \quad (3-12)$$

The two-phase acceleration pressure drop can be calculated from Zivi (1964)

$$\Delta P_{tp,a} = G^2 v_L \left[\frac{x_{e,o}^2 v_g}{\alpha v_L} + \frac{(1-x_{e,o})^2}{1-\alpha} - 1 \right], \quad (3-13)$$

where α is defined as

$$\alpha = \frac{1}{1 + \left(\frac{1-x_{e,o}}{x_{e,o}}\right) \left(\frac{v_L}{v_g}\right)^{2/3}}. \quad (3-14)$$

The dynamic pressure losses of two-phase flow are due to the combined effects of two-phase dynamic losses in the microchannel's outlet due to area enlargement and bends. The two-phase pressure loss term due to the enlargement from the microchannel's outlet to the manifold is calculated using the following equations provided by Collier and Thome (1994):

$$\Delta P_{en,tp} = \frac{G^2 v_L}{2} (1 - \lambda)^2 \left[1 + x_{e,o} \left(\frac{v_{fg}}{v_L} \right) \right]. \quad (3-15)$$

On the other hand, Fitzsimmons (1964) reported that the pressure drop around bends for two-phase flow can be approximated as 2.5 times higher than that predicted using single-phase pressure loss measurements. The exit quality can be calculated using the heat balance equation taking into account the sub-cooled region as,

$$x_{e,o} = \frac{1}{h_{fg}} \left[\frac{Q_{net}}{\dot{m}} - c_p (T_{sat} - T_{in}) \right]. \quad (3-16)$$

The net heat transferred to the fluid (Q_{net}) was determined as

$$Q_{net} = Q_{input} - Q_{loss}, \quad (3-17)$$

where Q_{loss} is the heat loss during the experiment and Q_{input} is the input power which corresponds to Joule heating. The heat loss during the experiment can be expressed as

$$Q_{loss} = Q_{axial} + Q_{con} + Q_{rad}, \quad (3-18)$$

where Q_{axial} is the heat loss due to axial heat conduction, and Q_{con} and Q_{rad} are the heat dissipated due to heat losses by convection and radiation, respectively. The heat losses due to free convection and radiation were calculated first, and then the heat loss due to axial conduction was determined as

$$Q_{axial} = \dot{m} c_p (T_{in} - T_{out}) - (Q_{con} + Q_{rad}), \quad (3-19)$$

where T_{in} and T_{out} are the inlet and outlet temperatures measured at the inlet and outlet manifold based on a single-phase flow, respectively.

Most of the heat lost during the experiment was primarily due to axial heat conduction to the heat sink support. The conduction heat loss was found to be 5.4% of the maximum heater power by performing single-phase test. Convection and thermal

radiation losses are a function of the heat sink surface temperature and were estimated to be less than 2.6% of the maximum power for all conditions. The convective heat loss was estimated by horizontal flat plate natural convection correlations. Radiation heat loss was calculated based on a horizontal black plate and the surroundings at the heat sink surface temperature with a radiation view factor equal to one. Figure 3-14 shows a schematic illustration of the heat sink for heat transfer data reduction. The net heat flux is found from the following equation:

$$q = \frac{Q_{\text{net}}}{A_{\text{tot}}} , \quad (3-20)$$

where A_{tot} is the total heat transfer area of the microchannels for three side heating, and may be expressed as:

$$A_{\text{tot}} = (2\eta H_{\text{ch}} + W_{\text{ch}})L_{\text{ch}}N_{\text{ch}} . \quad (3-21)$$

For the cross-linked design, total heat transfer area can be expressed as:

$$A_{\text{tot}} = (2\eta H_{\text{ch}} + W_{\text{ch}})L_{\text{sec}}N_{\text{ch}}N_{\text{sec}} + 8H_{\text{ch}}s(N_{\text{ch}} - 1) + W_{\text{cr}}L_{\text{cr}}N_{\text{cr}} . \quad (3-22)$$

The fin efficiency η was defined by Incropera (2002):

$$\eta = \frac{\tanh mH_{\text{ch}}}{mH_{\text{ch}}} , \quad (3-23)$$

and m is the fin parameter given by

$$m = \sqrt{\frac{2h_{\text{sp}}}{k_{\text{si}}s}} , \quad (3-24)$$

where k_{si} is the thermal conductivity of the silicon substrate at the mean silicon temperature. The single-phase heat transfer coefficient (h_{sp}) is represented by the following equation:

$$h_{sp} = \frac{k_L Nu_3}{D_h} . \quad (3-25)$$

The Nusselt number for three sides heating (Nu_3) is expressed in terms of the channels' aspect ratio (γ) by Shah and London (1978) correlation for a fully developed laminar flow:

$$Nu_3 = 8.235(1 - 1.883\gamma + 3.767\gamma^2 - 5.814\gamma^3 + 5.361\gamma^4 - 2.0\gamma^5) . \quad (3-26)$$

The local microchannels' surface temperature was estimated based on the one-dimensional heat conduction equation through the heat sink wall thickness. This relation is expressed by:

$$T_{s,x,y} = T_{b,x,y} - \frac{Q_{net} t}{k_{si} A_{fp}} , \quad (3-27)$$

where t is the difference between the wafer thickness and the height of the channel, A_{fp} is the heat sink footprint area, and $T_{b,x,y}$ is the outer wall temperature of the heat sink, based directly on the TLC temperature measurements. The local two-phase heat transfer coefficient ($h_{x,y}$) was obtained through the convective heat transfer relation:

$$h_{x,y} = \left[\frac{q}{T_{s,x,y} - T_{sat}} \right] , \quad (3-28)$$

where T_{sat} is the fluid saturation temperature.

3.1 Measurement Uncertainty

The experimental uncertainties of the measured parameters, associated with measurement devices and sensors, are tabulated in Table 3-2. Uncertainties in pressure drop and thermocouple measurements are 1.28% and ± 0.72 °C respectively, based on instrument specifications.

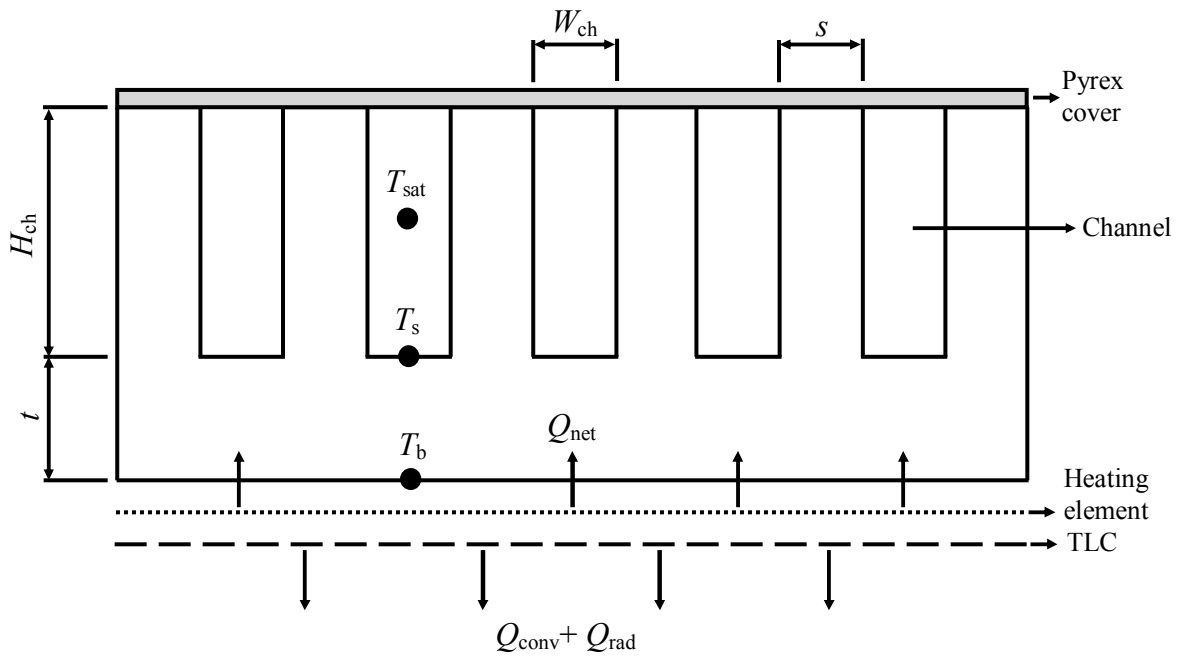


Figure 3-14: Schematic illustration of microchannel heat sink geometry.

The uncertainty in flow rate was estimated at 6.1%. TLC measurement uncertainty was obtained using similar methods described by Muwanga and Hassan (2006) and typical values are estimated to be ± 1 °C.

The uncertainties of the calculated parameters are determined by the procedures described by Kline and McClinton (1953) and are also given in Table 3-2. The uncertainty in Poiseuille number (fRe) is calculated by the following equation (Steinke and Kandlikar, 2006):

$$\frac{U_{fRe}}{fRe} = \left[2 \left(\frac{U_{\rho_L}}{\rho_L} \right)^2 + \left(\frac{U_{\mu_L}}{\mu_L} \right)^2 + \left(\frac{U_{\Delta P}}{\Delta P} \right)^2 + \left(\frac{U_{L_{ch}}}{L_{ch}} \right)^2 + 3 \left(\frac{U_{\dot{Q}}}{\dot{Q}} \right)^2 + 5 \left(\frac{U_{W_{ch}}}{W_{ch}} \right)^2 + 5 \left(\frac{U_{H_{ch}}}{H_{ch}} \right)^2 + 2 \left(\frac{U_{W_{ch} + H_{ch}}}{W_{ch} + H_{ch}} \right)^2 + 2 \left(\frac{U_{H_{ch}}}{W_{ch} + H_{ch}} \right)^2 \right]^{\frac{1}{2}} \quad (3-29)$$

Muwanga et al. (2007) conducted experiments to measure the friction factor in the straight and cross-linked microchannel heat sinks. Their experimental results of both microchannel heat sinks were in very good agreement with the theoretical values, represented by Eqn. (3-6), of the laminar flow in conventional rectangular channels. The uncertainty in local Nusselt number can be calculated from the following equation (Steinke and Kandlikar, 2005):

$$\frac{U_{Nu}}{Nu} = \left[\left(\frac{U_k}{k} \right)^2 + \left(\frac{U_I}{I} \right)^2 + \left(\frac{U_V}{V} \right)^2 + 4 \left(\frac{U_{T_b}}{T_b} \right)^2 + 2 \left(\frac{U_{T_{in}}}{T_{in}} \right)^2 + 2 \left(\frac{U_{T_{sat}}}{T_{sat}} \right)^2 + 3 \left(\frac{U_{L_{ch}}}{L_{ch}} \right)^2 + 4 \left(\frac{U_{W_{ch}}}{W_{ch}} \right)^2 + 5 \left(\frac{U_{H_{ch}}}{H_{ch}} \right)^2 + 2 \left(\frac{U_{\eta}}{\eta} \right)^2 \right]^{\frac{1}{2}} \quad (3-30)$$

Typical local Nusselt number uncertainty ranges from ± 15 to 25%. Uncertainty in the heat sink hydraulic diameter is based on the manufacturing tolerance which is estimated to be 5.1 μm .

Table 3-2: Parameters and Estimated Uncertainties

Parameters	Uncertainty
<i>1. Measured parameters:</i>	
Fluid temperature	$\pm 0.72 \text{ }^\circ\text{C}$
Heat sink surface temperature	$\pm 1 \text{ }^\circ\text{C}$
Pressure drop	$\pm 1.28\%$ of the reading
Mass flow rate	$\pm 6.1\%$ of the reading
Voltage	$\pm 0.2\%$ of full reading
Current	$\pm 0.2\%$ of full reading
<i>2. Calculated parameters:</i>	
Heat transfer coefficient	$\pm 15 - 25\%$
Heat flux	2.4%
Vapor quality	$\pm 5 - 10\%$
Hydraulic diameter	$5.1 \text{ } \mu\text{m}$

CHAPTER 4

TWO-PHASE PRESSURE DROP AND FLOW VISUALIZATION IN STRAIGHT MICROCHANNEL HEAT SINKS

The present chapter focuses on the experimental investigation of pressure drop characteristics and flow visualization of a two-phase flow in a straight microchannel heat sink. Experiments are carried out for mass fluxes ranging from 341 to 531 kg/m².s and heat fluxes from 55.5 to 154.2 kW/m². Pressure drop results are presented for two-phase flow of FC-72 as a function of exit quality and heat flux. Flow visualization was conducted for the determination of flow regimes in addition to characterizing the transient patterns that exist in different channels because of the inlet manifold configuration. Finally, the development and validation of a generalized pressure drop correlation for different refrigerants in microchannels are introduced after a critical assessment of the available correlations in the literature.

4.1 Flow Visualization

The main objective of the flow visualization study was to provide insight into flow distribution, flow regimes, and transition characteristics in a parallel array of microchannels. The qualitative flow visualization results can be used to support the quantitative experimental data for a better understanding of two-phase flow characteristics in microchannel heat sinks.

In order to check the manifold effect on the channels flow distribution, the flow patterns observed in different channels at different time steps are shown in Fig. 4-1. The following flow patterns were encountered at $G = 341 \text{ kg/m}^2\cdot\text{s}$ and $q = 130.6 \text{ kW/m}^2$. In channels 21 and 22, slug flow can be clearly seen. The vapor phase is distributed as discrete slugs in a continuous liquid phase. The vapor bubbles are approximately the diameter of the microchannel. Smaller entrained gas bubbles are also carried in the flow. These, images at different time steps, show the unsteady nature of two-phase flow.

Channels 12 and 13 show the transition from slug to churn flow, which is formed by the breakdown of a large vapor bubble in slug flow. The flow has a time varying character. It can be concluded that the mass flux is unevenly distributed in the microchannels since different flow regimes exist at a constant heat flux as was also observed by Cho and Cho (2004) from their reported flow visualization results.

Wispy-annular flow was identified in channels 3 and 4. The flow in these two channels takes the form of a relatively thick liquid film on the walls of the channel together with a considerable amount of liquid entrained in a central vapor core. The liquid in the film is aerated by small gas bubbles and the entrained liquid phase appears as large droplets which have agglomerated into long irregular filaments or wisps. This region occurs at a lower mass flux.

This analysis indicates that different channels can simultaneously have different flow regimes, while constant mass flux and quality flow conditions are maintained. It is concluded that the distribution of two-phase flow between the channels is uneven and depends on the manifold configuration. Nino et al. (2003) observed that typical flow

regime maps do not appear to be appropriate to describe the flow regimes, unless independent measurements of mass flux and quality are performed in each channel.

Figure 4-2 shows the observed flow patterns in the mid-channel of the heat sink for a constant mass flux of $341 \text{ kg/m}^2\cdot\text{s}$ and different exit quality. Three major flow patterns can be observed – bubbly flow, slug flow and annular flow, with annular flow being obtained at low exit quality.

Initiation of vapor bubble occurs at the preferred sites, randomly distributed on the heated microchannel surface (Fig. 4-2(a)). As the exit quality increases, the bubble size increases while it is still attached to the wall (Fig. 4-2(b)). At a higher value of exit quality, the vapor bubble grows to a size at which the buoyancy force overcomes the surface tension force, acting at the line of attachment of the bubble to the wall. The bubble then departs from the surface and enters the liquid with a bubble diameter smaller than that of the microchannel (Fig. 4-2(c)). Notably, bubbles are characterized by roughly spherical vapor regions surrounded by continuous liquid, and are distributed in the flow. An increase in exit quality increases the vapor bubble size. However, the geometry of the microchannel causes the vapor bubbles to be elongated after attaining a maximum size, which is the same diameter as the microchannel (Fig. 4-2(d) and (e)). It can also be noticed that slug flow does not result from the merging and coalescence of individual bubbles, but rather the bubbles are elongated and more cylindrical in shape. The elongated vapor bubbles are separated by liquid slugs. Further increase in exit quality leads to further elongation of bubbles and also decreases the thickness of the liquid slug separating elongated bubbles (Fig. 4-2(f-h)). Additional increase in exit quality results in bubble coalescence to form annular flow (Fig. 4-2(i)). In annular flow, the gas occupies

the central or core region of the microchannel, with the liquid remaining in a thin layer adjacent to the microchannel wall. Waves are presented on the liquid/gas interface and the instantaneous shape of the interface fluctuates with time. In their diabatic flow pattern map, Revellin and Thome (2007) observed that as the mass flux increases, the bubbly flow diminishes, and the transition from slug to annular flow takes place early at lower exit quality. These flow patterns and their transition characteristics match quite well with the flow visualization presented by Revellin and Thome.

4.2 Two-phase Pressure Drop

Figure 4-3 shows the experimental results for the two-phase pressure drop for five different mass fluxes. In general, the two-phase pressure drop increases as the exit quality and the mass flux increase. This is because the increase in exit quality tends to increase both the acceleration and frictional losses for a constant mass flux. At low mass flux, it shows that increasing exit quality for a constant mass flux increases pressure drop up to a particular exit quality value beyond which the pressure drop increases slightly. As the mass flux increases, the pressure drop increases almost linearly with increasing exit quality due to a decrease in the vapor-to-liquid density ratio. The slope of the two-phase pressure drop starts to increase with an increase in the mass flux, as shown in Fig. 4-3.

The two-phase frictional pressure gradient is shown as a function of exit quality in Fig. 4-4. The experimental data indicates that when the exit quality is lower, the pressure gradient increases sharply with the increase of vapor quality. The pressure drop increases almost linearly as the two-phase flow exit quality increases at low values of exit quality.

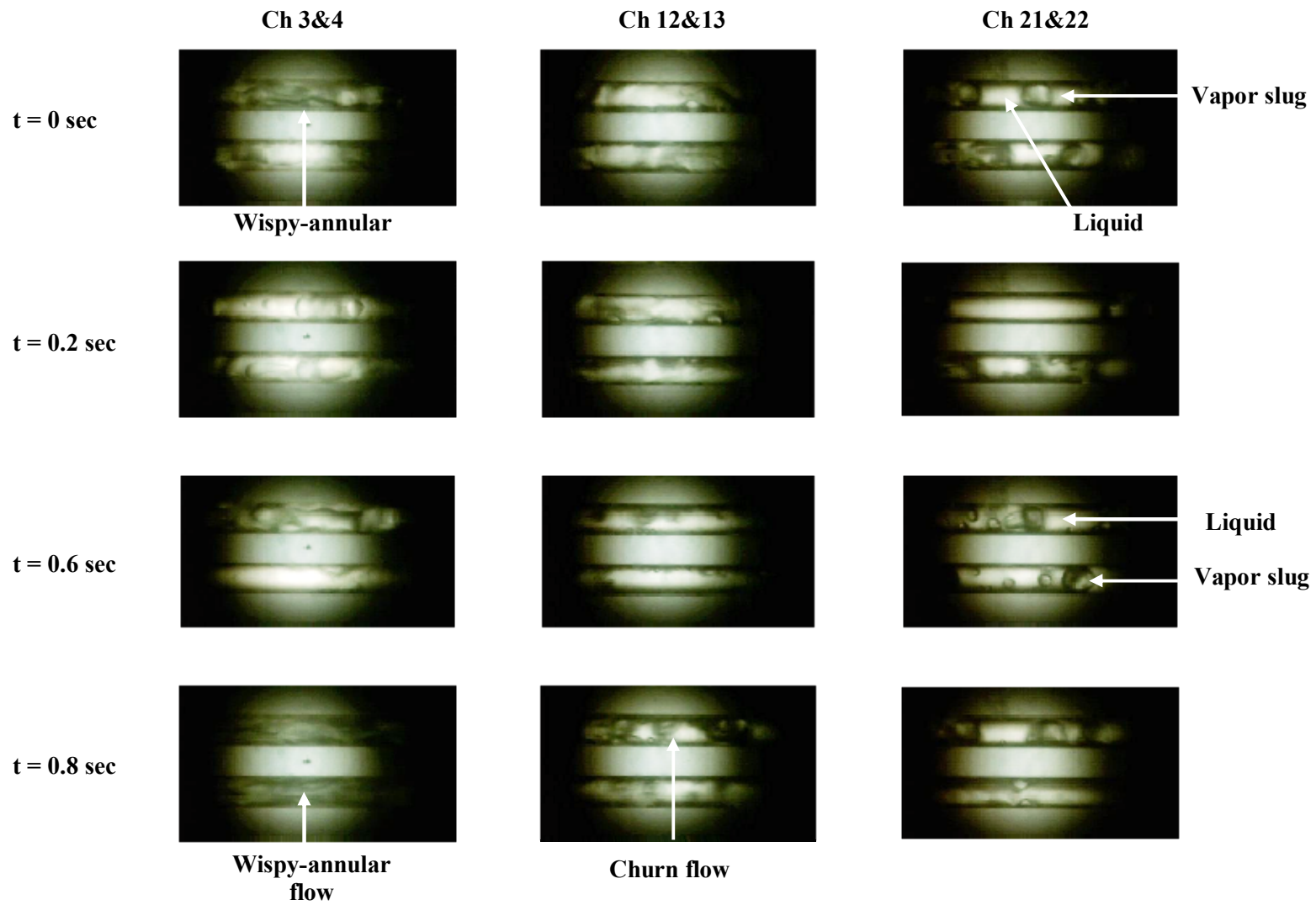


Figure 4-1: Flow pattern observations in different microchannels at different time intervals for $G = 341 \text{ kg/m}^2 \cdot \text{s}$ and $q = 130.6 \text{ kW/m}^2$, flow from right to left, $t = 0$ reference time

Flow
←



(a) bubbly flow at $x_e = 0.062$;



(b) bubbly flow at $x_e = 0.12$;



(c) slug flow at $x_e = 0.148$;



(d) slug flow at $x_e = 0.167$;



(e) slug flow at $x_e = 0.168$;



(f) slug flow at $x_e = 0.184$;



(g) slug flow at $x_e = 0.1978$;



(h) slug flow at $x_e = 0.2$;



(i) annular flow at $x_e = 0.252$.

Figure 4-2: Nucleation and flow pattern observations in the mid-channel, $G = 341$
 $\text{kg/m}^2 \cdot \text{s}$, flow from right to left.

However, a further increase in exit quality corresponds to a moderate increase of two-phase frictional pressure gradient.

Figure 4-5 illustrates the variation of Martinelli parameter, defined as the ratio of the frictional liquid pressure gradient to the frictional vapor pressure gradient, with exit quality for different heat fluxes. It is found that the Martinelli parameter decreases when the exit quality increases. Meanwhile, it shows the independence of Martinelli parameter on heat fluxes for different vapor qualities. These results show that this ratio is not function of heat flux and the frictional vapor pressure drop is higher as the exit quality increases. This trend is consistent with that reported by Lee and Mudawar (2005b) for flow boiling of water in a copper microchannels heat sink.

4.3 Assessment of Correlations

Although many correlations exist for two-phase flow in mini- and microchannels, their applicability to microchannels with a smaller diameter needs to be clarified. In Fig. 4-6, two-phase pressure drop experimental data are compared with those calculated from the literature correlations presented in Table 2-1. The mean absolute error (MAE) was defined as:

$$\text{MAE} = \frac{1}{N} \sum \left| \frac{\text{experimental data} - \text{predicted data}}{\text{experimental data}} \right| \times 100, \quad (4-1)$$

where N is the total number of data points.

As shown in Fig. 4-6, the Mishimi and Hibiki (1996) correlation gives a good prediction based on the experimental data, although it was developed for conventional and mini tubes of $D = 1$ to 4 mm. This can be explained by the effect of tube size included in the correlation. The Lee and Lee (2001a) correlation expressed the two-phase

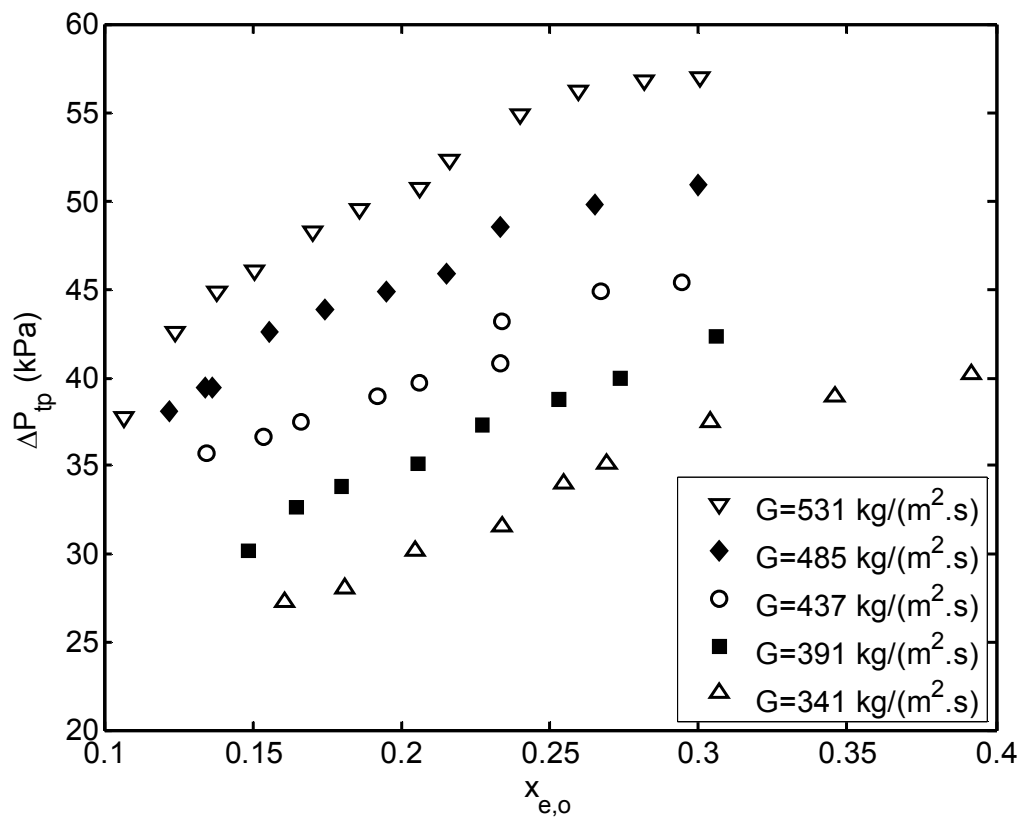


Figure 4-3: Two-phase pressure drop as a function of exit quality for different mass fluxes.

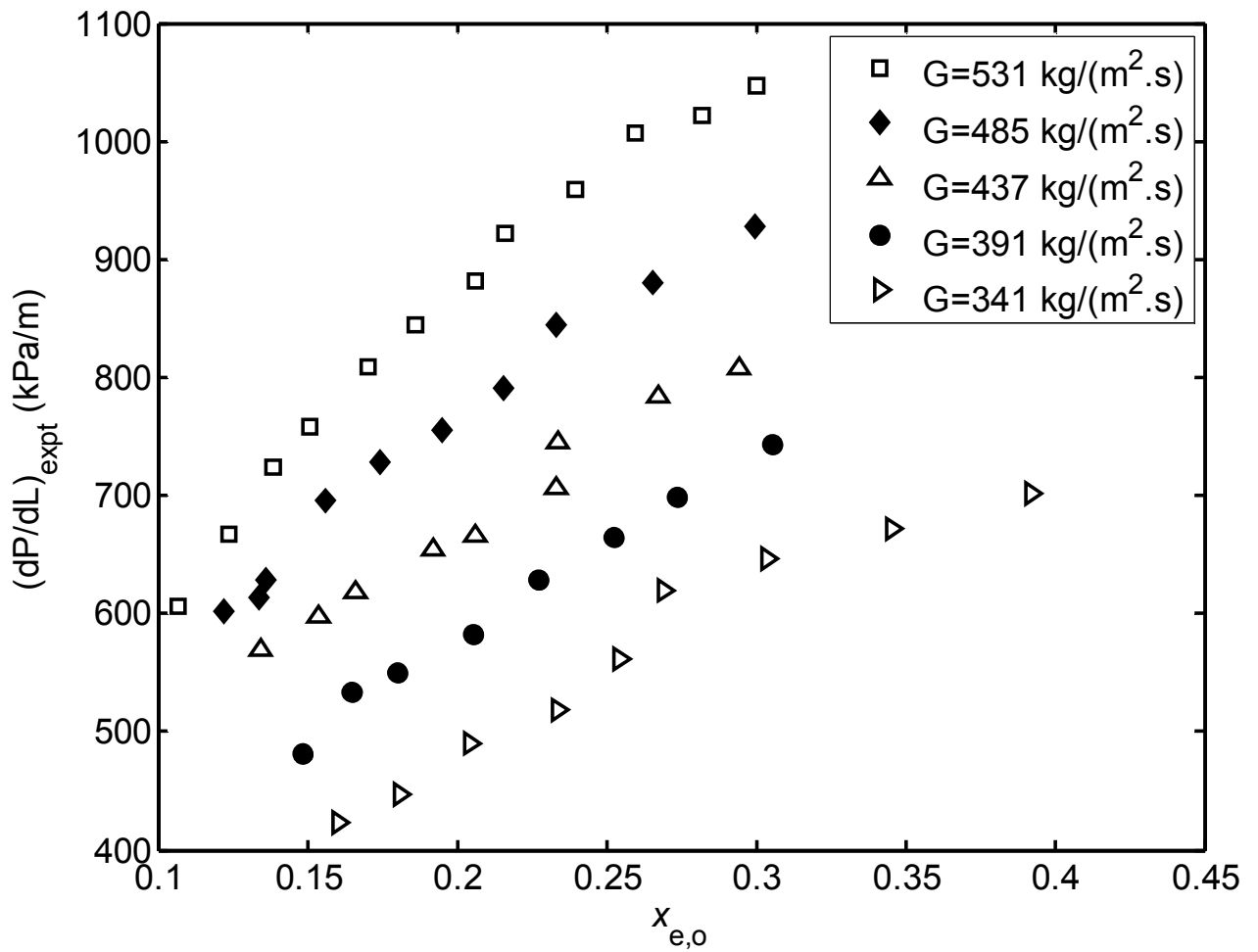


Figure 4-4: Frictional pressure gradient as a function of exit quality for different mass fluxes.

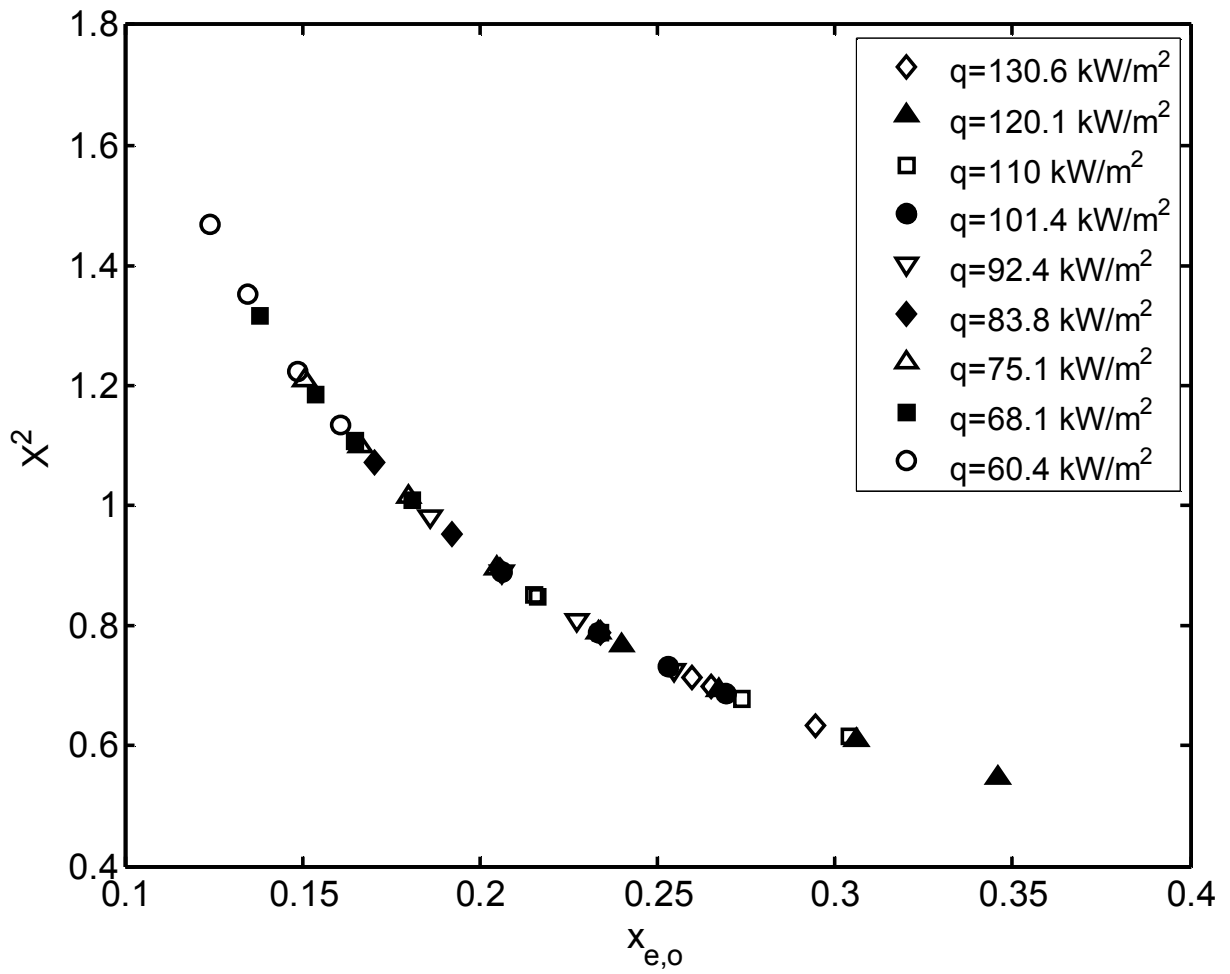


Figure 4-5: Martinelli parameter as a function of exit quality for different heat fluxes.

multiplication factor through dimensionless groups as a function of surface tension, viscosity, and inertial forces. Their correlation covers a wide range of conventional and mini size channels (780 to 6670 μm). It predicts the experimental data with a MAE of 14.7%. The Qu and Mudawar (2003a) correlation gives the best prediction among the correlations tested with a MAE of 10.4%, as can be seen in Fig. 4-6(c). This can be attributed to the combined effect of both channel size and coolant mass flux incorporated in their correlations. Their correlations were developed based on microchannel pressure data with a hydraulic diameter of 349 μm .

The correlation by Lee and Mudawar (2005a) allows the calculation of the two-phase pressure drop in terms of a two-phase multiplication factor as a function of an empirical combination of the liquid Reynolds and Weber numbers. This correlation has been developed by fitting the two-phase multiplication factor to 165 water and 87 R134a data points, collected by various authors, carried out in microchannels of $D_h = 349 \mu\text{m}$. They assumed that the pressure drop in slug and annular regimes is dominated by surface tension. It predicts the experimental data with high deviation as shown in Fig. 4-6(d). This can be explained by the difference in the working fluid properties. The surface tension of water is seven times higher than that of FC-72, which is used in the present study. However, the surface tension of R134a is almost the same as that of FC-72.

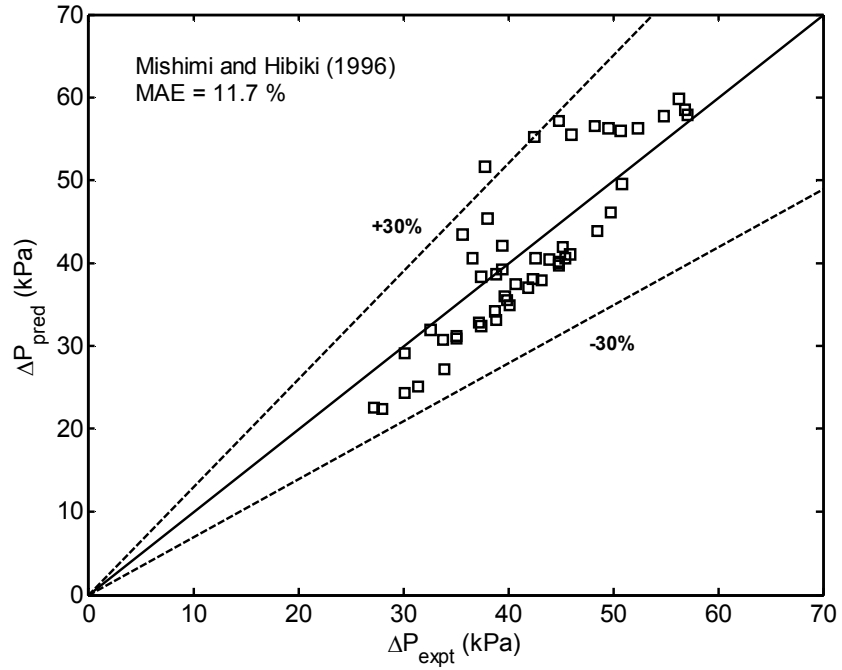
In a recent work Lee and Garimella (2008) proposed a new correlation to predict the two-phase pressure drop in microchannels for $D_h = 160$ to 538 μm . However, their experimental data were presented for a very narrow band of exit quality (0.058 to 0.2). The two-phase pressure drop is expressed in terms of a two-phase multiplication factor, which is assumed to be a function of the hydraulic diameter and mass flux. The Sun and

Mishima (2009) correlation was developed from 2092 pressure drop measurements obtained over a wide range of laminar and turbulent flow conditions. Nonetheless, it underpredicts the frictional pressure drop because this correlation has considered a wide range of diameters (506 to 12000 μm).

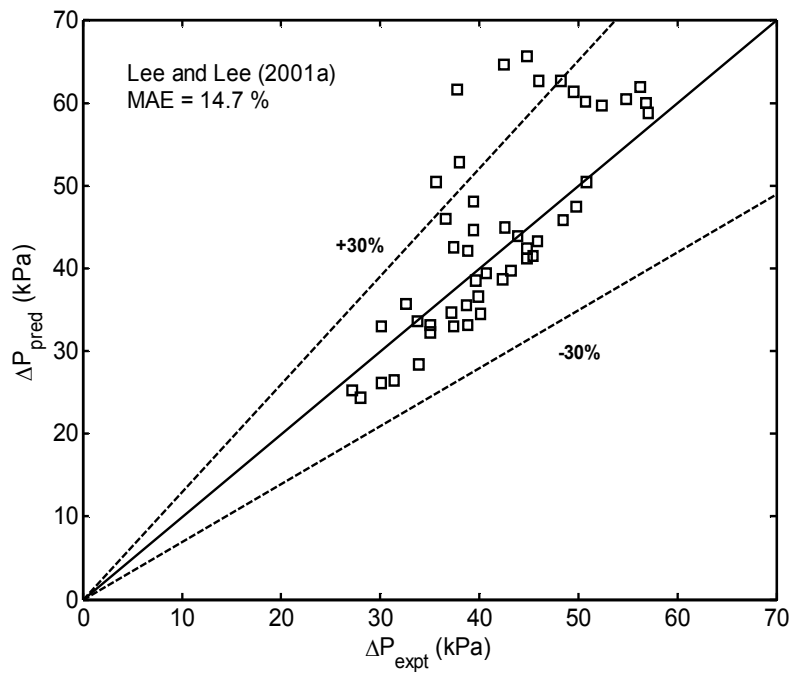
In summary, in the ranges covered by the experiment ($x_{e,o} = 0.1$ to 0.4 and $q = 55.5$ to 154.2 kW/m^2), all correlations agree with experimental results within 30% of the mean absolute error (MAE), except Lee and Mudawar's correlation. All data correlations predicted by Qu and Mudawar (2003a) and Lee and Garimella (2008) are well within the error band and represent a mean absolute error of 10.4 and 12.3%, respectively.

4.4 Development of a New Correlation

The frictional pressure drop has a significant contribution to the two-phase pressure drop in very small channels. Consequently, the frictional pressure drop in microchannels is expected to increase as the diameter decreases. Meanwhile, the acceleration pressure drop is expected to decrease as the diameter decreases. There have been a large number of exhaustive studies dealing with two-phase flow in microchannels with hydraulic diameters greater than 349 μm , and several correlations have been derived. Attempts are being made to develop prediction methods which are based on the separated model. The two-phase multiplier is correlated empirically using the measured results, to mass flux, hydraulic diameter, and Reynolds and Weber numbers as was shown in Table 2-1. All above-mentioned correlations still have reasonable deviation with the presented

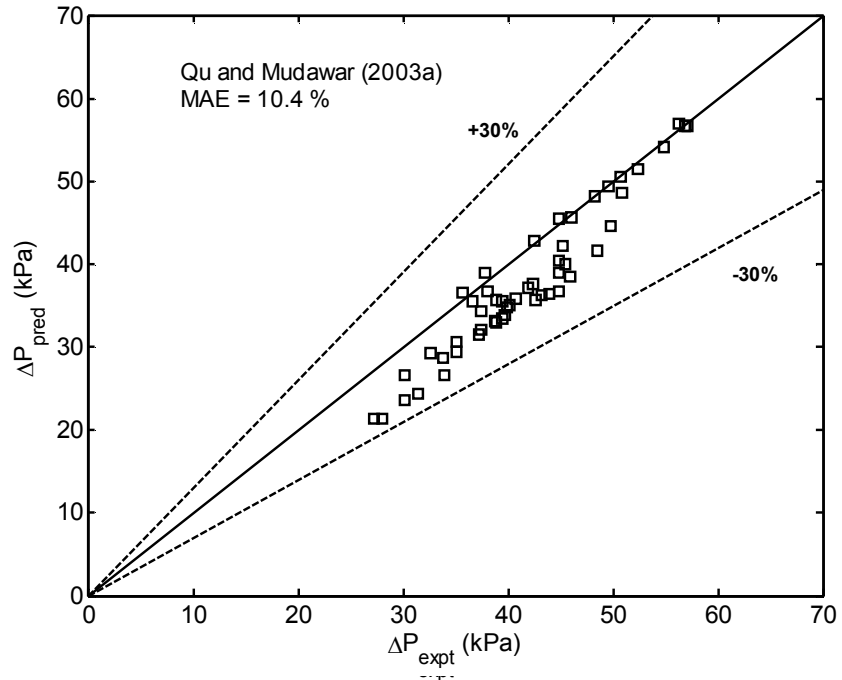


(a)

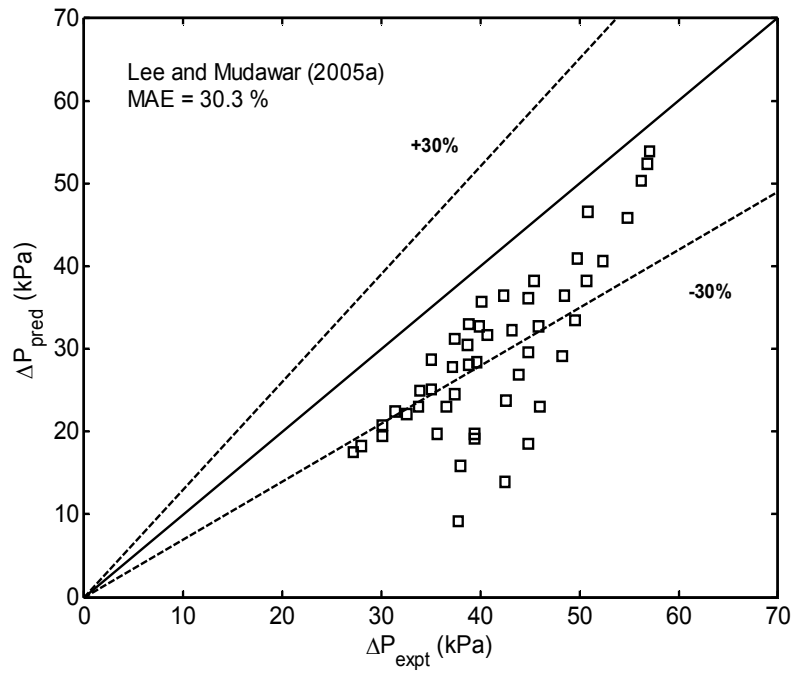


(b)

Figure 4-6: Comparison of measured pressure drop data with predicted data from macro and microchannel correlations.



(c)



(d)

Figure 4-6: (continued)

(e)

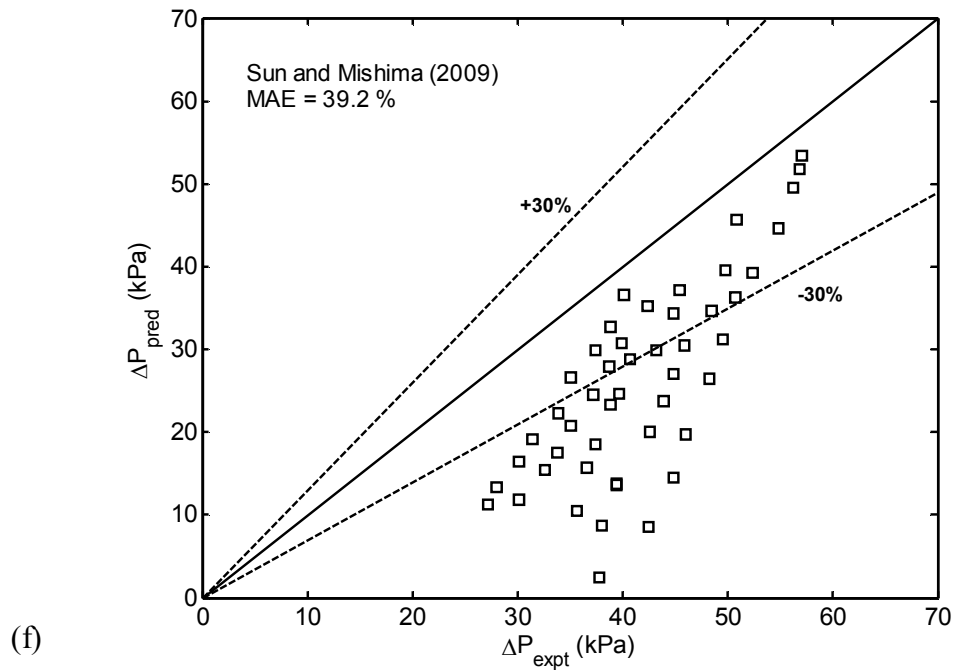


Figure 4-6: (continued)

experimental data. The disagreement between measured pressure and predicted pressure drops using these methods can easily be 10% or more. The objective of the proposed

correlation is to enhance the predictions of two-phase flow pressure drop correlations to cover laminar-liquid laminar-vapor and laminar-liquid turbulent-vapor flow in microchannels with smaller hydraulic diameters for different refrigerants.

In the present study, the two-phase multiplier parameter could be expressed by:

$$C = f(Re_{f_0}, Co, X^2) = c_1 Re_{f_0}^{c_2} Co^{c_3} (X^2)^{c_4} , \quad (4-2)$$

where Re_{f_0} is Reynolds number assuming the entire flow to be liquid, Co is the confinement number, and X^2 is the Martinelli parameter. The effect of the confinement number is found to have a significant influence on the correlation's predictions. The first dimensionless group in Eqn. (4-2), the Reynolds number, accounts for the influence of the forced convection term which becomes dominant at high values of vapor quality during the annular flow regime. The second dimensionless group is related to the confinement by the channel walls under the confined flow pattern observed at low vapor quality. The correlation evaluation was limited to three data sets since only two researchers provided enough information to calculate the frictional two-phase flow pressure gradient. Field (2007) presented data on the pressure drop during horizontal two-phase flow of R134a, propane, R410a, and ammonia in a microchannel heat sink with $D_h = 148 \mu\text{m}$. The mass flux ranges from 290 to 440 $\text{kg/m}^2\cdot\text{s}$, and the exit quality from 0.01 to 0.96. Tu (2004) reported experiments on two-phase flow with R134a in microchannel heat sinks of 70, 104, 141, 150, and 304 μm hydraulic diameters, for mass flux values ranging from 102 to 785 $\text{kg/m}^2\cdot\text{s}$ and exit qualities from 0.01 to 0.95. A total of 324 data points were analyzed in the present study. Table 4-1 lists the experimental data collected from the literature. The data included two-phase pressure drop data for five different refrigerants with hydraulic diameter in the range of 70 to 304 μm . The two-phase

multiplication factor in Eqn. (4-2) is given as a function of the viscous, surface tension, inertia, as well as buoyancy forces. This method will be applicable to very small cross-section microchannel and to a wide range of density, surface tension, and viscosity values. All refrigerant properties were obtained from The National Institute of Standards and Technology (NIST). Based on the experimental data and using data regression techniques, the correlation for predicting the two-phase multiplier parameter for laminar-liquid laminar-vapor flow could be obtained as:

$$C = \frac{0.0053Re_{fo}^{0.934}}{Co^{0.73}(X^2)^{0.175}} \quad (4-3)$$

similarly, for laminar-liquid turbulent-vapor flow as:

$$C = \frac{0.0002Re_{fo}^{1.7}}{Co^{0.7}(X^2)^{1.24}} \quad (4-4)$$

The predicted data, for the laminar-liquid laminar-vapor case, have very good agreement with the experimental data. Figure 4-7 shows a comparison of the experimental data with predictions by the new correlation for laminar-liquid laminar-vapor. It is found that the pressure drop could be predicted by the correlation with a MAE of 10.4%. Figure 4-8 presents validation results of the new correlation versus the experimental data over a range of laminar-liquid turbulent-vapor flow. The new correlation predicts the experimental two-phase pressure drop data with a MAE of 14.5%.

4.5 Conclusions

Two-phase flow pressure drop measurements were investigated in a silicon microchannel heat sink. The pressure drop across the heat sink was related to the exit

quality for different mass fluxes. The two-phase pressure drop depends strongly on the mass flux, and increases almost linearly with increasing exit quality at a constant mass flux. Flow visualization indicated that two-phase flow can be divided into three main flow regimes: bubbly, slug, and annular. The experimental pressure drop data were compared with the predicted values of previously reported correlations in the literature to prove their validity. A new correlation for the prediction of the two-phase flow in microchannels is obtained from the present work employing different values of hydraulic diameter ranging from 70 to 304 μm and its applicability extends to five different refrigerants. The new correlation shows a good agreement with the experimental data and predicts the evaporative pressure drop data in microchannels for laminar-liquid laminar vapor and laminar-liquid turbulent-vapor flow with mean absolute errors of 10.4 and 14.5%, respectively.

Table 4-1: Pressure drop data used in the present study.

Case	Reference	Fluid(s)	D_h (μm)	G ($\text{kg}/\text{m}^2.\text{s}$)	$x_{e,o}$	Re_L	Re_g	X^2	No. of Data points
	Present Study	FC-72	248	334-531	0.1-0.39	114-264	269-483	0.37-0.87	48
Laminar liquid – Laminar vapor	Field (2007)	R134a, Propane, R410a, Ammonia	148	290-440	0.01-0.49	529-111	19-897	1.43-57.5	17
	Tu (2004)	R134a	70, 104, 141, 150, 304	102-785	0.01-0.75	30-545	27-992	1.8-95	112
Laminar liquid - Turbulent vapor	Field (2007)	R134a, Propane, R410a, Ammonia	148	290-440	0.33-0.96	20-325	1036-3189	0.68-4.3	22
	Tu (2004)	R134a	70, 104, 141, 150, 304	102-785	0.21-0.95	17-452	1012-4443	1.8-5.4	125
	Summary	5 different refrigerants	70-304	102-785	0.01-0.96	17-545	19-4443	0.37-95	324

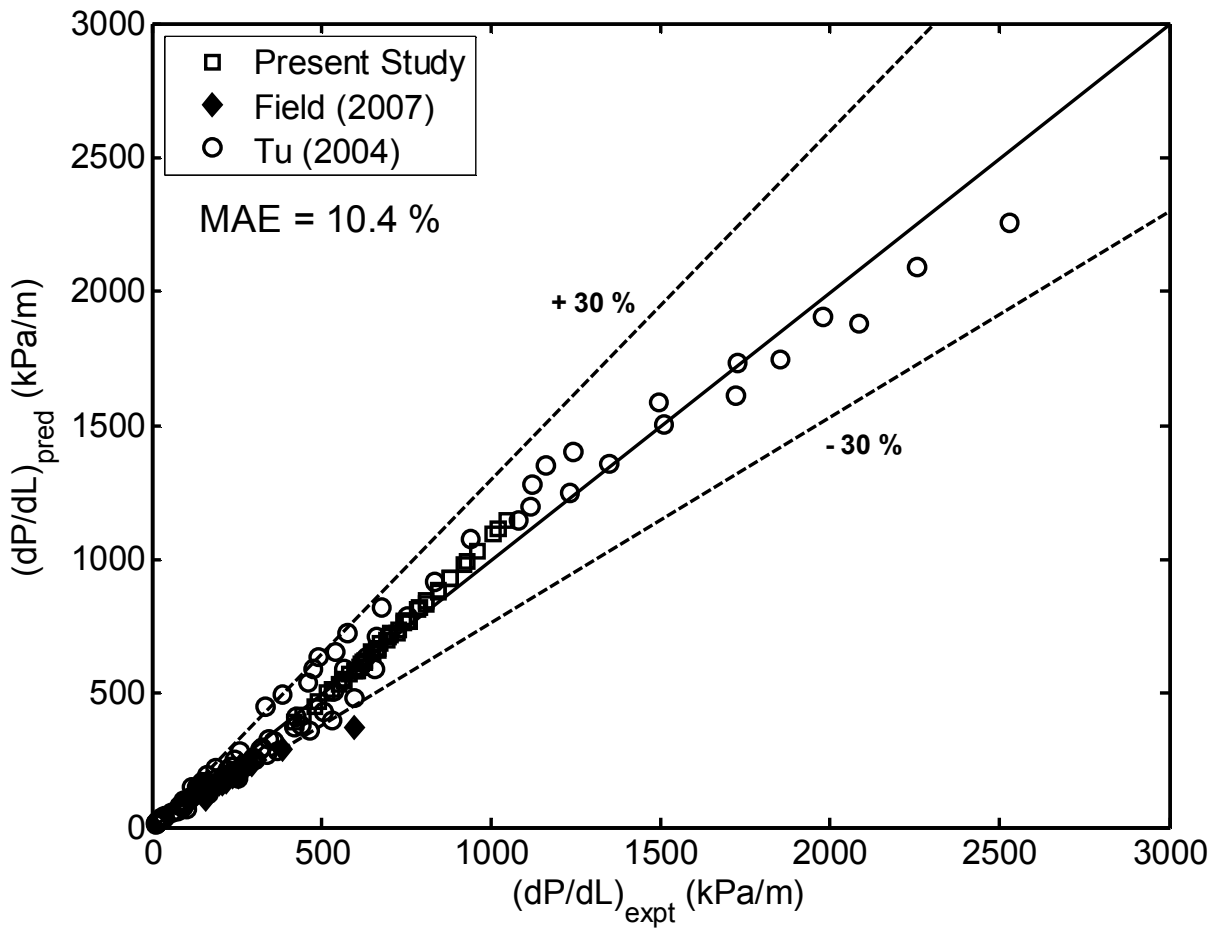


Figure 4-7: Comparison of measured pressure drop data with predicted data for laminar-liquid laminar-vapor flow.

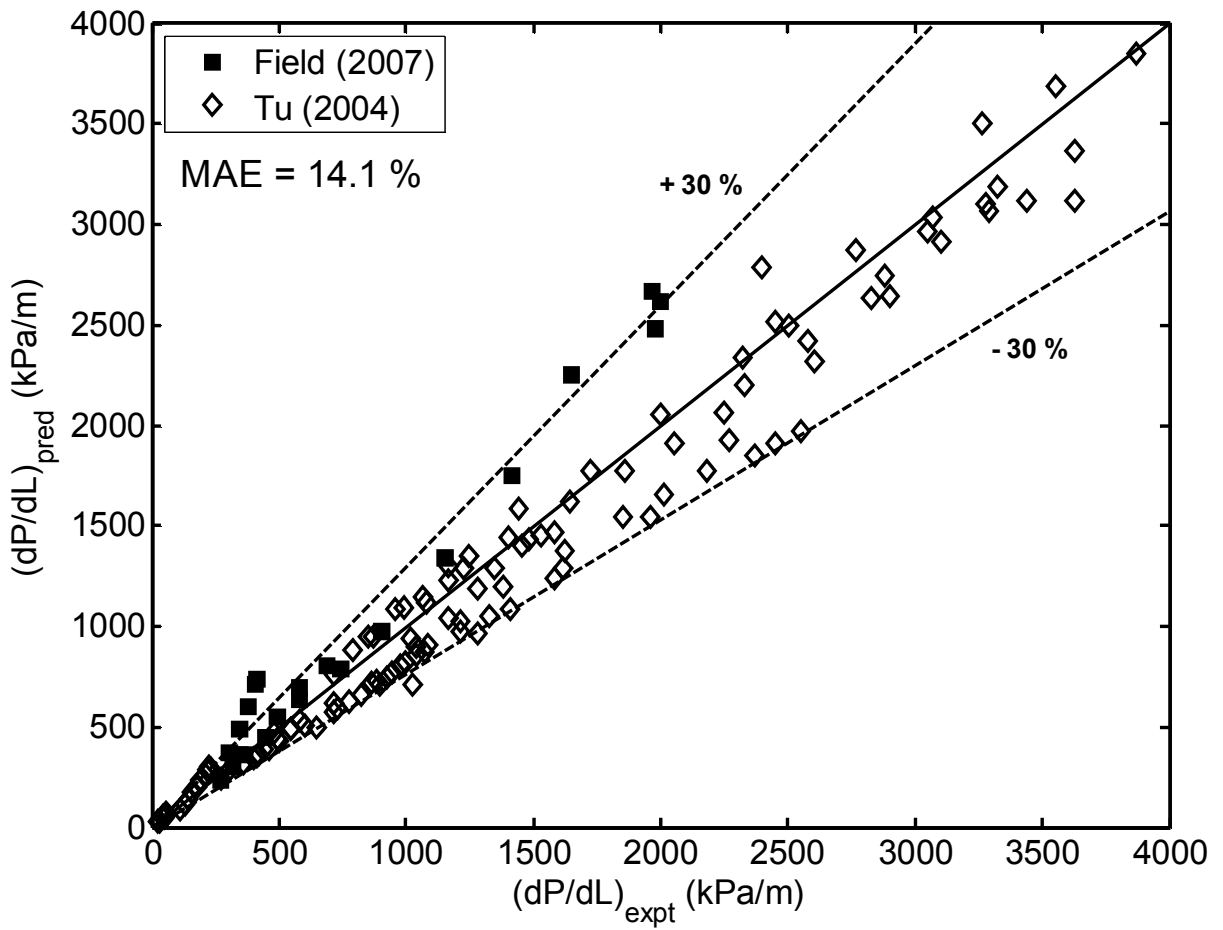


Figure 4-8: Predicted values of two-phase pressure gradient with the new correlation against the experimental data for laminar liquid-turbulent vapor.

CHAPTER 5

FLOW BOILING HEAT TRANSFER

CHARACTERISTICS IN STRAIGHT MICROCHANNEL

HEAT SINKS

This chapter experimentally investigates the onset of boiling (ONB) and the heat transfer characteristics for flow boiling in the straight microchannel heat sink. The boiling incipience and temperature thermal maps for the heat sink surface are provided from the localized measured data using Un-encapsulated Thermochromic liquid Crystals (TLC). This measuring technique is also used to determine the local heat transfer coefficient for saturated flow boiling. The experimental investigation will be assisted with two-phase flow visualization in microchannels, which would allow a better understanding of the experimental results. Experiments are carried out for a mass flux varying from 341 to 531 kg/m²s and a heat flux ranging from 55.5 to 154.2 kW/m². An assessment of the most commonly used flow boiling heat transfer models and correlations is provided. Finally, a new asymptotic model is proposed to predict the two-phase heat transfer coefficient based on the combined effect of nucleate and convective boiling.

5.1 Onset of Boiling

Un-encapsulated TLCs, by virtue of their vibrancy and property of changing color with temperature, provide continuous and high-resolution heat-transfer coefficient and surface temperature maps. Their ability to give continuous, quantitative, high-resolution

heat-transfer information at any desired location on the test surface, demonstrates the advantage of this measurement method over conventional thermal-measurement methods.

Figure 5-1 shows an example of a raw RGB image taken for the present investigation at $G = 340 \text{ kg/m}^2\cdot\text{s}$ and $q = 60.4 \text{ kW/m}^2$. The green color corresponds to the highest temperature, while yellow and reddish-brown represent decreasing temperature. This typical image is converted using an interactive in-house program in MATLAB software to a temperature map as shown in Fig. 5-2. It should be noted that the color legend bar in Fig. 5-2 shows the correspondence between colors and the converted temperature maps and not the original TLC colors. The major objective of this experiment was to map the quantitative temperature on the heat sink surface. By applying TLC to the uniformly heated heat sink surface and using a heat balance along with the measured electrical input power, the surface temperature was mapped in terms of the mass flux at different levels of input heat fluxes. A typical example of the results is shown in Fig. 5-2. Figure 5-2 shows a thermal map of the surface temperature distribution at mass flux of $340 \text{ kg/m}^2\cdot\text{s}$ and a heat flux of 60.4 kW/m^2 . A narrow temperature band indicates a small lateral temperature gradient on the heat sink surface.

Figure 5-3 is a demonstration of the variation of wall temperature along the dimensionless distance (x/D_h) during incipience of boiling (ONB) of FC-72 at a mass flux of $340 \text{ kg/m}^2\cdot\text{s}$ and heat flux of 60.4 kW/m^2 . This is the first study to present the ONB in heat sink microchannels using locally measured data. It divides the channel into a single phase and a two-phase zone, each characterized by a different mode of heat transfer. During single-phase liquid flow, the wall temperature is found to increase continuously until it exceeds the local saturation temperature. In this region, no bubbles are formed and

the heat transfer is governed by single phase forced convection laws. At a given (x/D_h) downstream position, further increase in heat flux results in a superheated temperature at the wall. As a result, the temperature difference between wall temperature and bulk temperature suddenly decreases due to the removal of the latent heat of vaporization, inherent in the phase change, indicating the ONB. This occurs because the liquid temperature is fractionally increased above its saturation temperature and is evaporated to form a bubble detached from the microchannels' wall. The ONB indicates the location where the vapor can first exist on the microchannel surface without condensing or collapsing. In the subcooled boiling region, the bulk liquid is still subcooled and the heat transfer is determined by the combined effects of single-phase forced convection and nucleate boiling. Compared to the single-liquid phase, the surface temperature rises at a fast rate, where a fraction of the heated surface is covered by bubbles and the remaining part is subjected to convective heat transfer. The surface temperature then remains constant in this region.

Flow visualization is used to present nucleate vapor-bubble growth at the heated wall and to complement ONB data presented in Fig. 5-3. Figure 5-4 depicts vapor bubbles nucleating at the heated wall and located between single-phase liquid and subcooled boiling flows. As shown in the figure, the flow enters the channel as a single-phase liquid, at nominally 4 °C subcooled, and is heated by the channel walls. When the wall superheat reaches a threshold value ($\Delta T_{\text{sat(ONB)}}$) at a certain distance into the channel, vapor bubble grows at the first nucleation site indicating ONB. Vapor bubbles grow to about $0.3D_h$ in width ($\approx 74 \mu\text{m}$) at the nucleation site for $q = 60.4 \text{ kW/m}^2$ and $G = 340 \text{ kg/m}^2\text{s}$. When the wall superheat is high enough, bubble generation frequency increases

and two or more successive bubbles from a given site or adjacent sites to be generated resulting in subcooled boiling. Then, vapor bubbles are forced to sweep the walls of the channel as they are conveyed down the channel by the forced flow evolving into bubbly flow regime. The individual bubbles which nucleated at the heated wall are nearly of the same size. As shown in Fig. 5-4, the bubble thickness is about $0.3D_h$ corresponding to the temperature drop observed after the onset of boiling as presented in Fig. 5-3.

Figure 5-5 shows the variation for wall temperature profiles along the dimensionless length of the channel for $G = 531 \text{ kg/m}^2\cdot\text{s}$ and $q = 69.4 \text{ kW/m}^2$. The typical behavior, as observed in Fig. 5-3, remains the same for higher values of mass and heat fluxes. However, the values of location of onset of boiling and the wall superheat necessary to cause nucleation are different. The typical variation of wall temperature indicates the presence of two different regimes of heat transfer in the channel namely, single-phase and two-phase. During single-phase liquid flow, the surface temperature increases linearly with distance along the channel length until the saturation condition is attained at the channel wall. When saturation conditions are attained, bubbles start nucleating at the channel surface resulting in the formation of a vapor phase in the channel. As discussed earlier, the wall temperature profile shows that there exists a point at which the bubbles start appearing at the surface, though the liquid is still below its saturation value. This is the onset of boiling where the bubbles are generated at the surface. Its effect is exhibited by a sudden drop in the wall temperature curve. The onset of boiling is linked to the superheat condition that is necessary to activate the nucleation sites on contacting surfaces. At $G = 531 \text{ kg/m}^2\cdot\text{s}$ and $q = 69.4 \text{ kW/m}^2$ (Fig. 5-5), the temperature curve moves to a lower value of $\Delta T_{\text{sat(ONB)}} = 0.2 \text{ }^\circ\text{C}$ corresponding to the higher mass flux

where the minimum wall superheat required is lower compared to $G = 341 \text{ kg/m}^2\cdot\text{s}$ ($\Delta T_{\text{sat(ONB)}} = 0.7 \text{ }^\circ\text{C}$). The superheat required for the onset of boiling may be expressed as (Collier and Thome, 1994)

$$\Delta T_{\text{sat(ONB)}}^2 \propto \frac{q}{G} . \quad (5-1)$$

Therefore, a higher incipient boiling superheat is achieved at a lower mass flux and a higher heat flux. As shown in Fig. 5-5, as the liquid moves through the channel, its temperature rises with additional bubbles generated at the wall. An asymptotic rise in the wall temperature is observed as the dimensionless distance (x/D_h) increases under uniform heat flux, followed by a constant wall superheat in its value. This increase in wall temperature, with a shallower slope compared to $G = 340 \text{ kg/m}^2\cdot\text{s}$, corresponds to subcooled boiling where the bulk liquid temperature did not yet attain its saturation value. This clearly indicates that there is a separation between the position where the first bubbles appear and the position where the flowing liquid reaches the saturation temperature. Then, the two-phase flow moves through the channel with an increasing quantity of vapor and, hence, changing flow patterns. This corresponds to the saturated boiling regime, as exhibited by the constant wall temperature profile.

The incipience of boiling during forced convection flow in microchannels was studied by Poh-Seng et al. (2005). They predicted incipience of boiling based on the assumption that the bubble nucleus does not change the surrounding single-phase temperature profile. In addition, their model assumed that the two phases, liquid and vapor, are at saturation conditions. The ONB results are compared with the Poh-Seng et al. model. Experimental data of ONB wall superheat was found to deviate less than 10% of that predicted from the model. However, Poh-Seng et al. expressed their model for

predicting ONB wall superheat in terms of the contact angle of the fluid and heater surface (Θ). It was found that there is a relatively strong influence of contact angle on model predictions. For contact angle $20^\circ < \Theta < 180^\circ$, the Poh-Seng et al. model overestimates the data of ONB superheat with minimum and maximum deviations of 6 and 9%, respectively. Figure 5-6 shows the effect of contact angle on model predictions for the present experimental data.

5.2 Heat Transfer Characteristics

The averaged heat transfer coefficient is plotted in Fig. 5-7 with respect to the vapor exit quality. To obtain the average heat transfer coefficient, the local heat transfer coefficient values are averaged over the shaded area in Fig. 5-1, which is the position furthest downstream corresponding to exit quality. The heat transfer coefficient demonstrates the same trend for all mass fluxes. At low exit quality ($x_{e,o} < 0.2$), the heat transfer is transmitted only by nucleate boiling and high values of heat transfer coefficients are seen in this region. For an exit quality higher than 0.2, the heat transfer coefficient decreases sharply, for which the heat transfer is determined by the combined effects of forced convection and nucleate boiling. As the exit quality increases, the heat transfer coefficient becomes nearly independent of mass flux. In this region, the heat transfer is governed by forced convection boiling. These results prove that nucleate boiling is dominant since the heat transfer coefficient is dependent on heat flux, not mass flux. This trend of heat transfer coefficient may be explained by the difference in flow patterns which were observed in this study. If the wall temperature in the microchannels rises above the saturation temperature while the bulk of the liquid is subcooled, nucleate boiling will take place. In this regime, bubbles are formed in microcavities adjacent to the

wall, and grow up to a critical size. At this point, bubbles separate from the wall and enter the fluid stream with a bubble diameter smaller than that of the microchannel, as shown in Fig. 5-8. Bubbles are characterized by a roughly spherical vapor region surrounded by continuous liquid, and are distributed in the flow. When surface tension forces are dominant, the departing bubbles are spherical. When inertial forces are dominant, the bubble has a hemispherical shape, whereas when both forces are significant, the bubble has an elongated oblate shape.

Figure 5-8 shows the observed flow patterns in the mid-channel of the heat sink for a constant mass flux of $340 \text{ kg/m}^2\text{s}$ and various vapor exit quality. An increase in heat flux increases the vapor bubble size, and thereby increasing the void fraction. However, the geometry of the microchannel causes the vapor bubbles to be elongated after attaining their maximum diameter which is the same as that of the microchannel. The reduction in heat transfer coefficient is a result of an increased dry region around the bubble, while the liquid is confined to the corners of the channels. Increasing heat flux leads to further elongation of the bubbles and a simultaneous decrease in the thickness of the liquid slug separating the elongated bubbles, and increases the thermal resistance. Further increase in heat flux results in bubble coalescence to form annular flow as presented in Fig. 5-8. In the annular flow, the gas occupies the central or core region of the microchannel, while the liquid remains in a thin layer adjacent to the microchannel wall. It can be noticed in Fig. 5-7 that the heat transfer coefficient after reaching a minimum value starts increasing slightly with increasing vapor quality. This tendency could be explained by the fact that with higher vapor quality, the flow becomes annular as shown in Fig. 5-8.

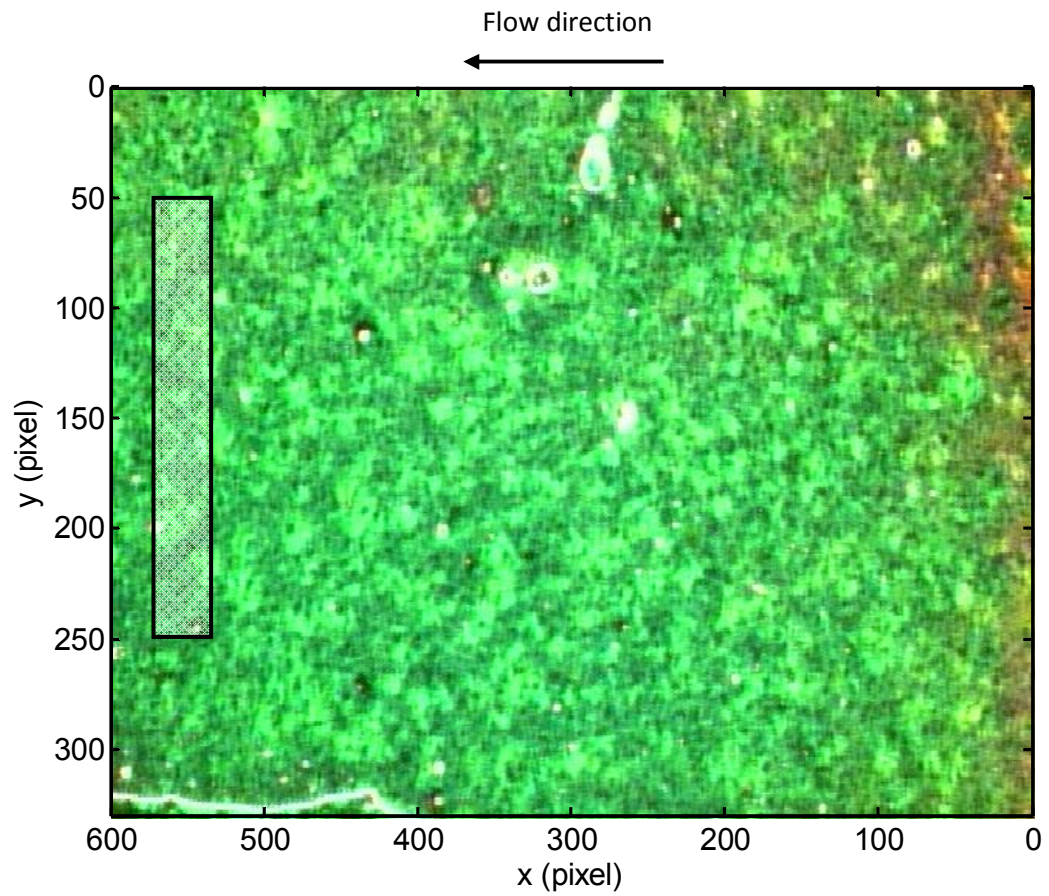


Figure 5-1: Example of a raw RGB image for the present investigation of the heat sink at

$$q = 60.4 \text{ kW/m}^2 \text{ and } G = 340 \text{ kg/m}^2 \text{ s.}$$

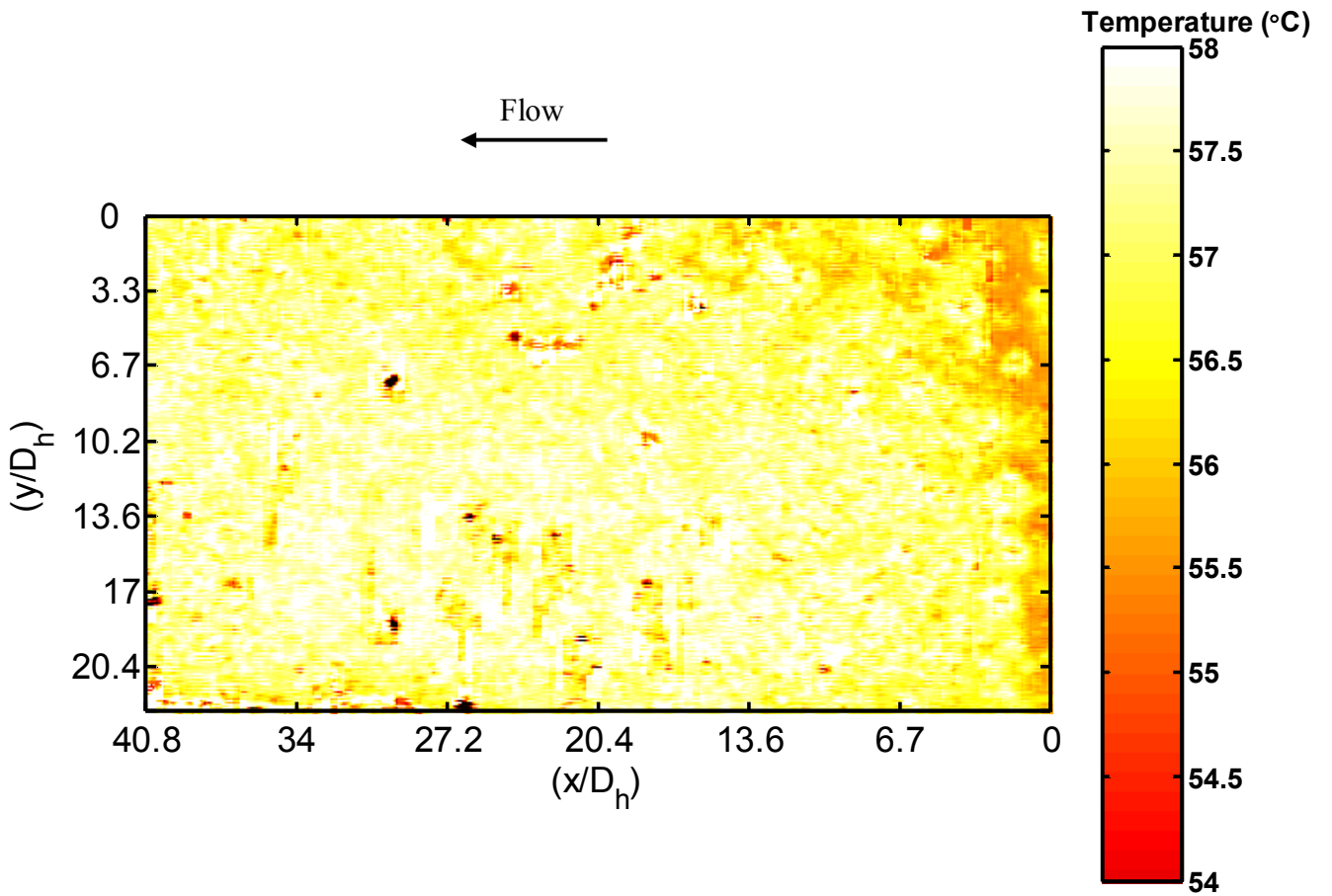


Figure 5-2: Local surface temperature distribution for the present investigation of the heat sink at $q = 60.4 \text{ kW/m}^2$ and $G = 340 \text{ kg/m}^2 \text{ s}$.

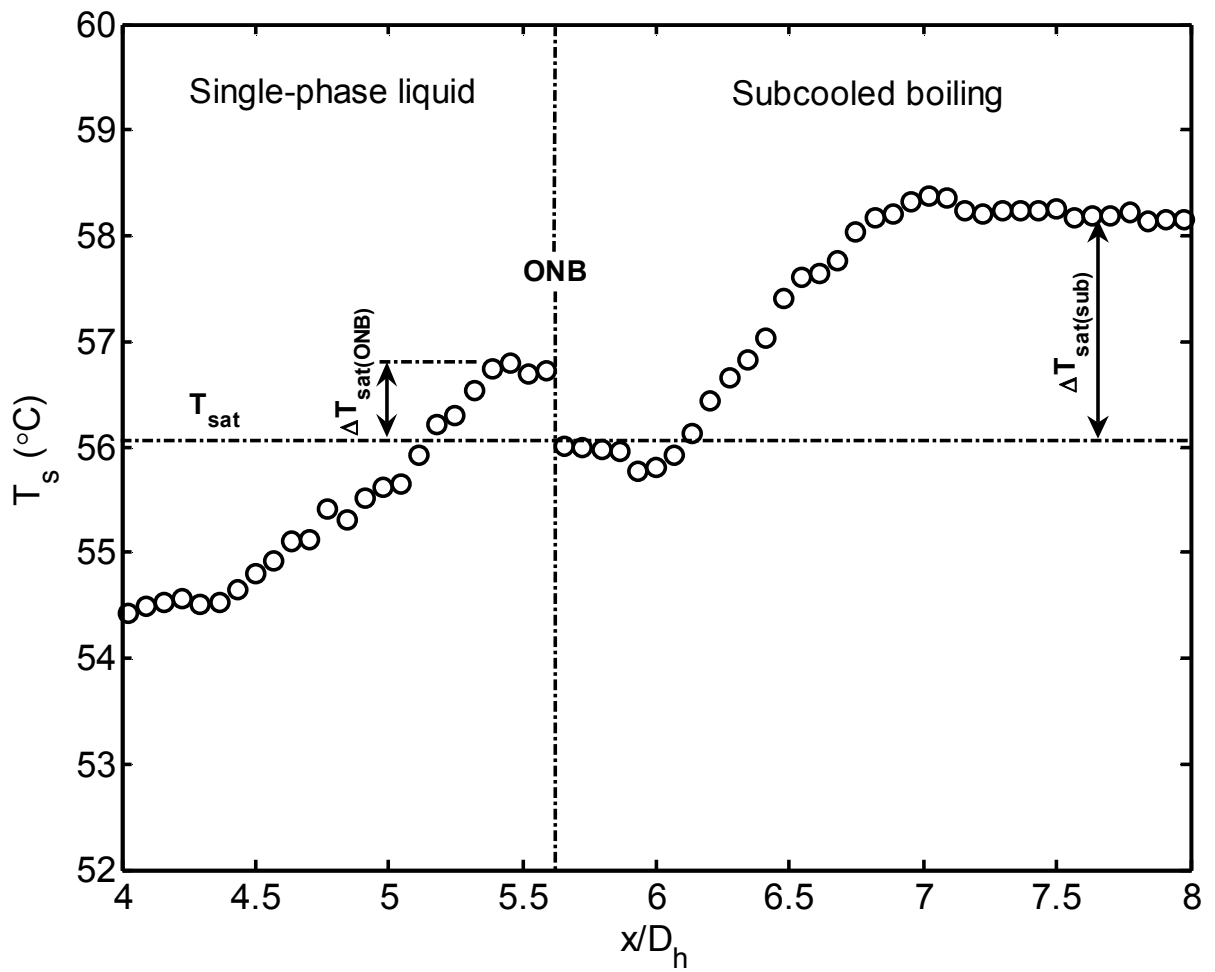


Figure 5-3: Stream-wise surface temperature showing ONB for $G = 340 \text{ kg/m}^2 \cdot \text{s}$ and $q = 60.4 \text{ kW/m}^2$.

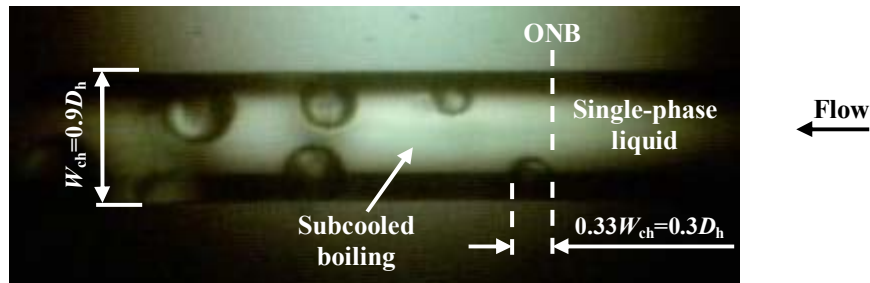


Figure 5-4: Bubble nucleation and onset of nucleate boiling for $G = 340 \text{ kg/m}^2 \cdot \text{s}$ and $q = 60.4 \text{ kW/m}^2$

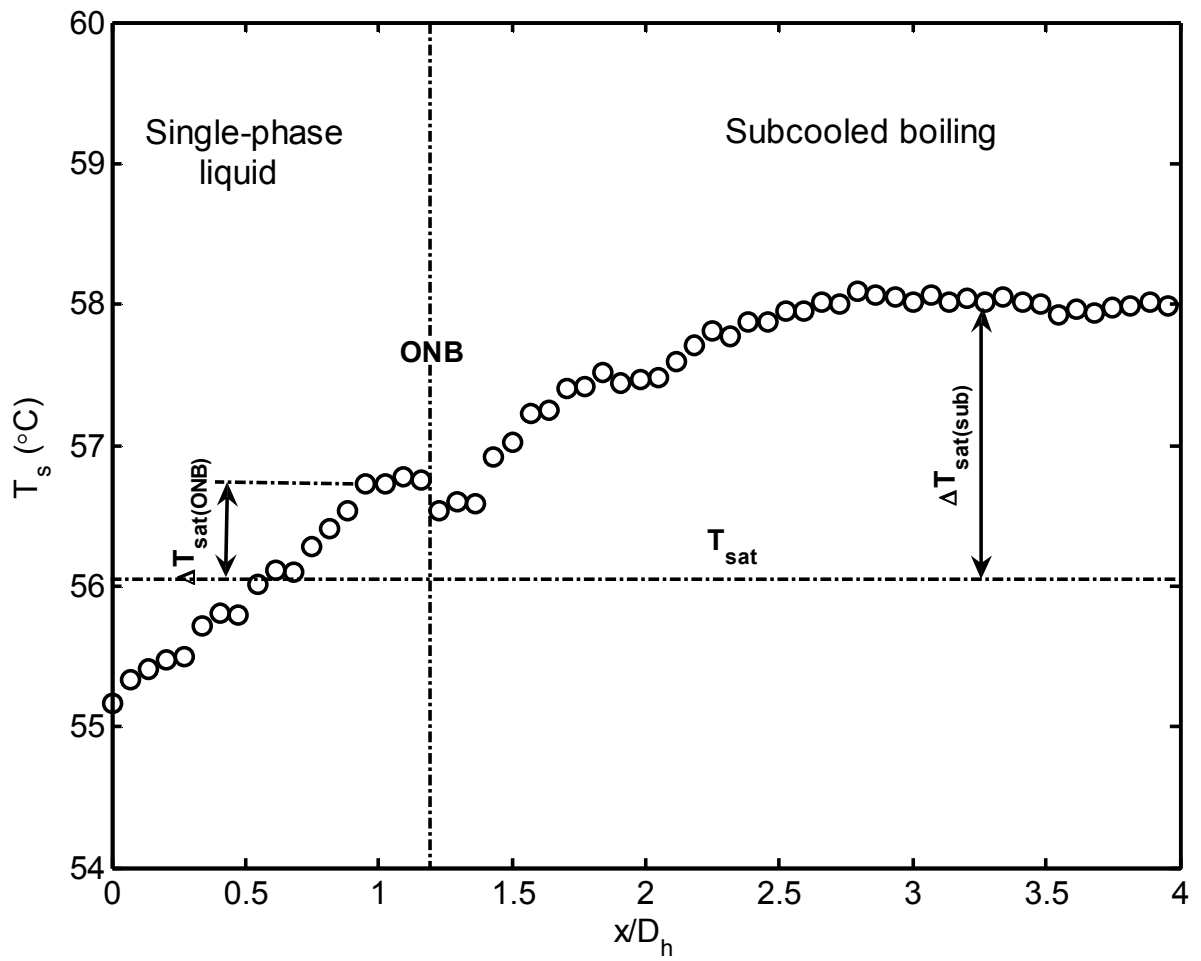


Figure 5-5: Stream-wise surface temperature showing ONB for $G = 531 \text{ kg/m}^2 \cdot \text{s}$ and $q = 69.4 \text{ kW/m}^2$.

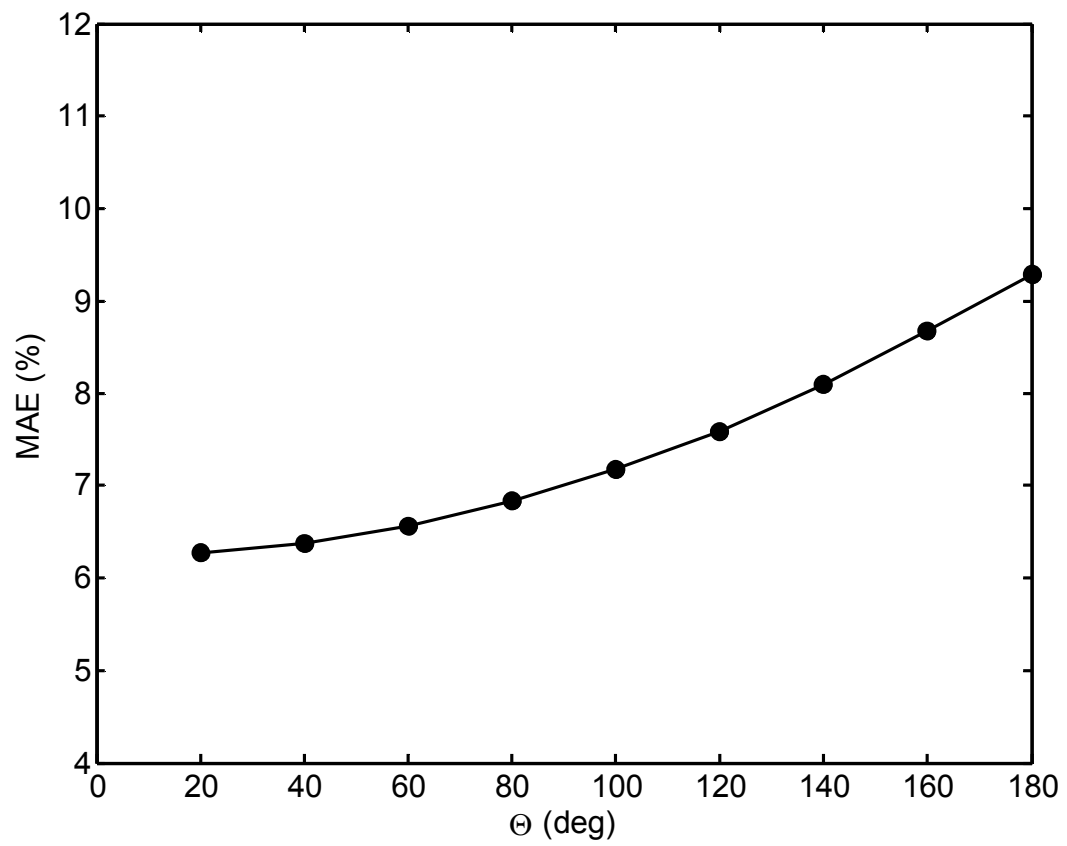


Figure 5-6: Effect of contact angle on Poh-Seng et al. model predictions.

As a result, the film layer adjacent to the wall enhances the heat transfer and the influence on the heat transfer coefficient becomes favorable.

Figure 5-9 presents a typical boiling curve, which is the variation of heat flux with wall superheat ($T_s - T_{sat}$) at different mass fluxes. A reduction in the mass flux shifted the boiling curve to higher wall superheat levels. However, the increase in the mass flux associated with higher pressure drop results in lower heat fluxes for a given wall temperature. Two boiling zones may be identified with two different slopes, represented by $q/(T_s - T_{sat})$. In the first zone, the partially developed boiling (PDB) regime, the wall temperature reaches a superheat high enough to initiate nucleation and a fraction of the heated surface is covered by bubbles while the other part remains subjected to convective heat transfer. In this region, both single-phase forced convection and nucleate boiling contribute to the two-phase heat transfer coefficient. The curvature in the same figure corresponds to the partial boiling regime where the straight lines begin to curve. Here, the wall is partially covered by bubbles and the heat transfer will be entirely governed by nucleate boiling. The wall superheat temperature has an overshoot or excursion at heat fluxes higher than 100 kW/m^2 . In this zone, more nucleation sites are activated and the heat flux steeply increases with the wall temperature difference, representing the fully developed nucleate boiling region (FDB). This typical increase in the slope and lines converging into a single line indicate the fully developed boiling.

5.3 Comparison of Heat Transfer Models and Correlations

The validity of available asymptotic models and correlations, presented in Table 2-3, for the boiling heat transfer in mini- and microchannels is assessed based on the measured data.

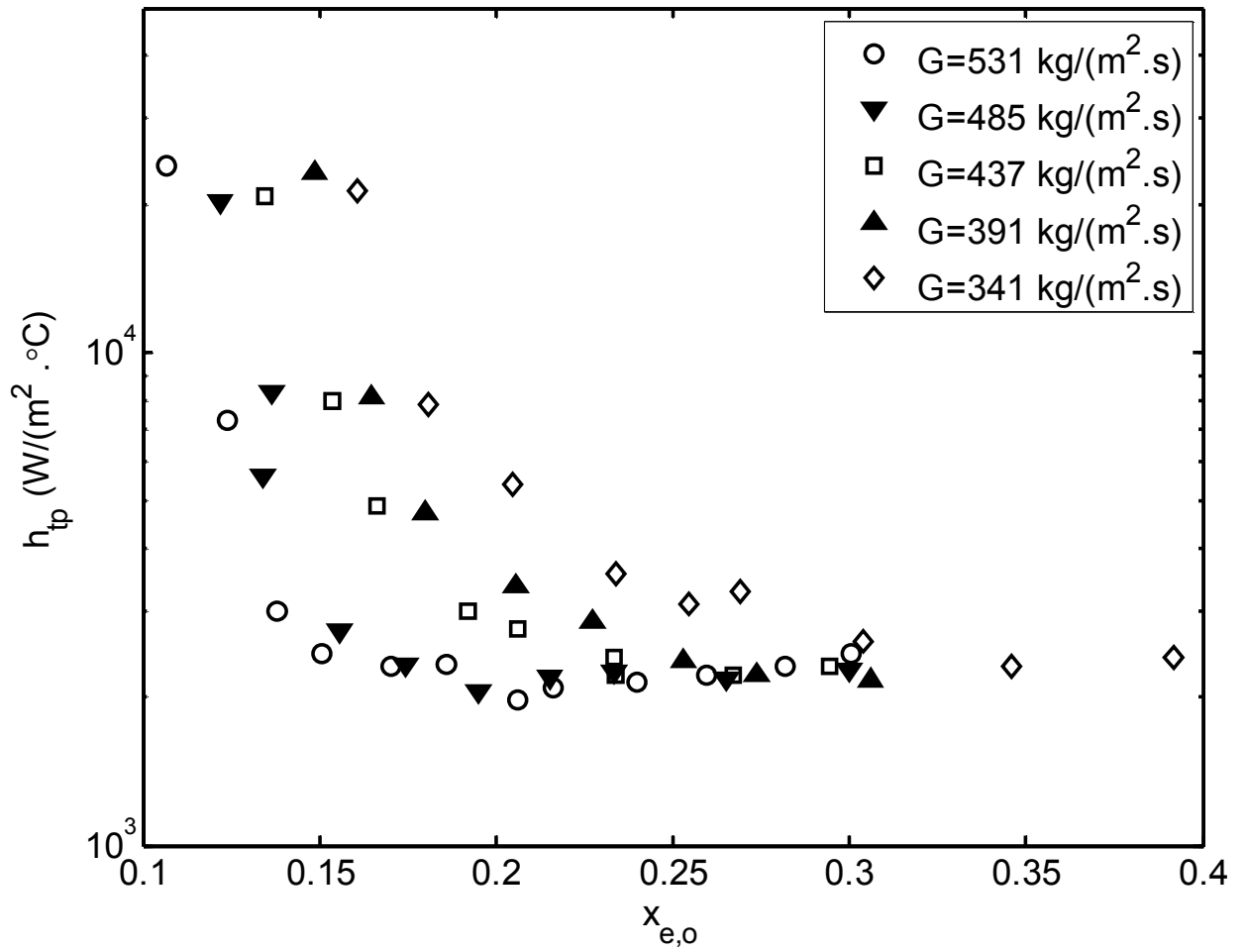


Figure 5-7: Mean heat transfer coefficient as a function of exit quality for different mass fluxes.

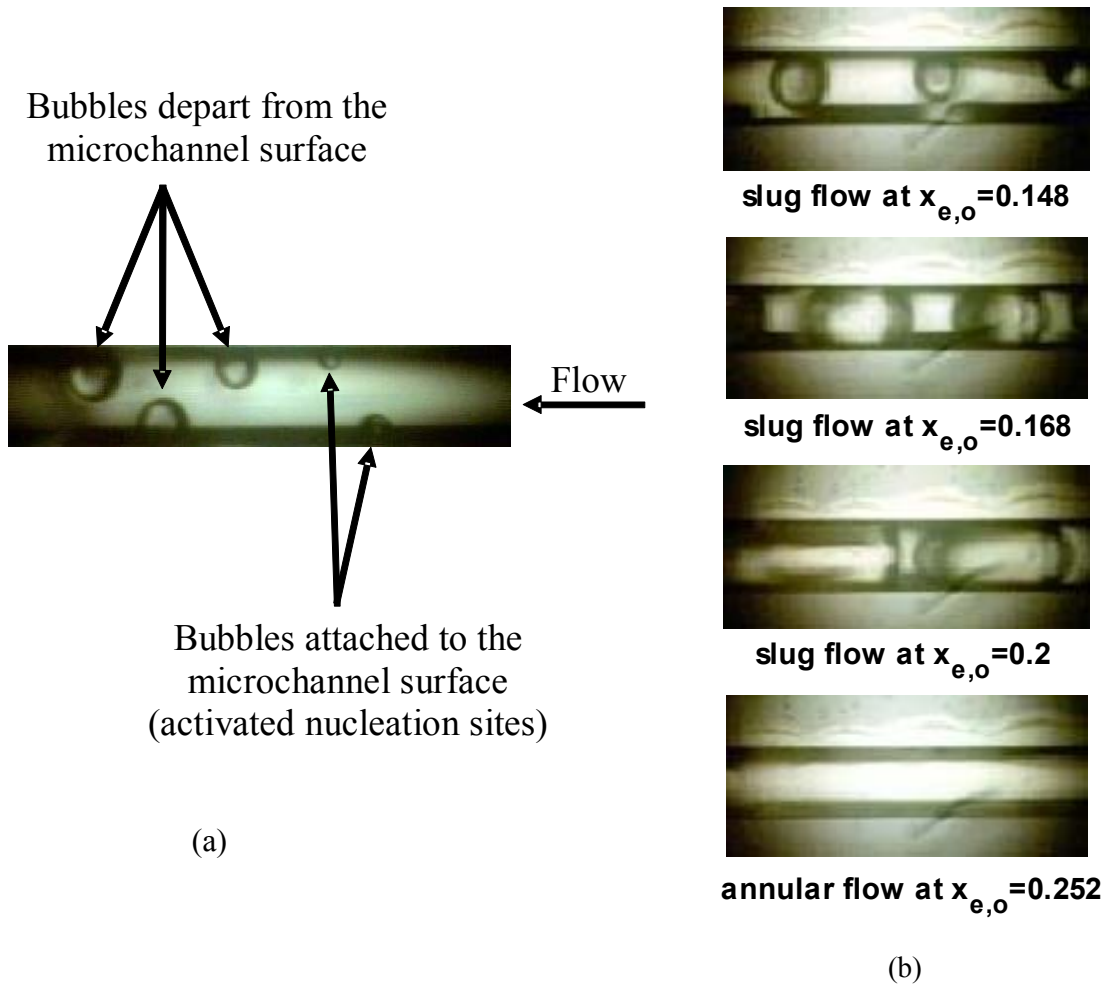


Figure 5-8: (a) Nucleation and (b) flow patterns observations for FC-72 in the mid-channel for $G = 340 \text{ kg/m}^2 \text{ s}$ (flow is from right to left).

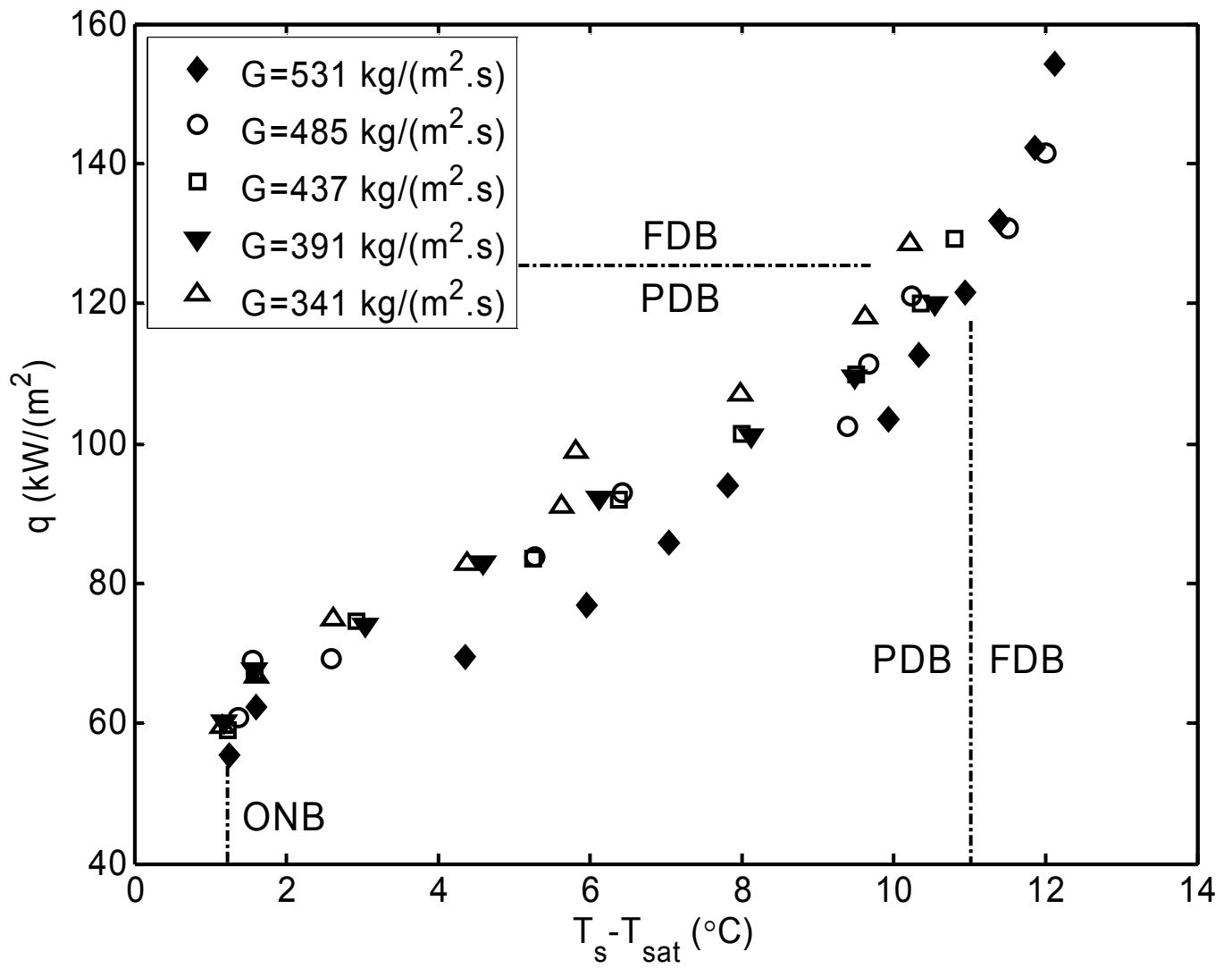


Figure 5-9: Boiling curves at different mass fluxes.

Figure 5-10 compares the experimental heat transfer coefficient to that predicted by the models and correlations available in literature. They are within an error band of 30%.

The mean absolute error (MAE) was defined as:

$$\text{MAE} = \frac{1}{N} \sum \left| \frac{\text{experimental data} - \text{predicted data}}{\text{experimental data}} \right| \times 100 . \quad (5-3)$$

The comparison shows that the correlation of Lee and Mudawar (2005b) underpredicts the experimental heat transfer coefficient data at low exit quality while experimental values are highly overpredicted by approximately 40 to 50% at high vapor quality with a MAE of 93.7%. The aforementioned correlation considers the two-phase convective effect and neglects the nucleate boiling contribution, which significantly enhances the heat transfer coefficient particularly at low exit quality. The asymptotic model of Zhang et al. (2005) included water, R113, R11, and R12 as working fluids. It underpredicts the present data with a MAE of 48.4%. The experimental heat transfer coefficient is underpredicted by the model of Zhang et al. in the low quality region and is fairly predicted in the high quality region. This is attributed to the combination of the two heat transfer mechanisms by a simple addition method ($n = 1$ in Eqn. 2-20) which is not appropriate and to the fact that the suppression factor was assumed equal to unity in their model. Furthermore, this model was developed for a wide range of mini and microchannels ($D_h = 780$ to $6000 \mu\text{m}$). The heat transfer coefficients, in the asymptotic models of Liu and Garimella (2007) and Lee and Garimella (2008), have been evaluated using a pressure correction factor as a function of water reduced pressure. Therefore, the applicability of these two models to other fluids may be questionable. A new factor is needed when these models are tested on FC-72. Liu and Garimella presented a modified version of Bennett's et al. (1980) model with the inclusion of an empirical constant,

which appeared only to estimate bubble departure radius. The Liu and Garimellia model provides reasonable agreement with the experimental data, specifically in the forced convective regime, with a mean absolute error of 56.4%. However, comparison of the present results with Lee and Garimellia's model shows that an appreciable difference occurred in the nucleate and forced convective boiling regions. The composite correlation of Bertsch et al. (2009a) assumed the suppression factor (S_p) in Eqn. 2-20 to be a linear function of exit quality only. The suppression factor cannot always be correlated with the exit quality in a linear relation, i.e., the linear approximation of the suppression factor by Bertsch et al. may not necessarily be satisfied. Their model did not consider the temperature difference between the temperature at which bubbles grow up and the surface temperature, which is not negligible. Furthermore, their model relies on data regression to the enhancement factor rather than analytical modeling. The mean absolute error between the experimental data and predicted values by the Bertsch et al. correlation is 82.6%.

Bertsch et al. (2009b) carried out an experimental study to investigate the flow boiling heat transfer coefficient in two arrays of microchannels of $D_h = 540$ and $1090 \mu\text{m}$. They showed that the correlations which have been developed specially for mini and microchannels, e.g. Lee and Mudawar (2005b), and Zhang et al. (2005), disagree considerably with the experimental data though these correlations agree well with their own experimental database. On the other hand, Bertsch et al. (2008a) have tested twenty five published flow boiling heat transfer correlations against a large number of experimental data collected from the open literature covering channels of hydraulic diameters ranging from 160 to $2000 \mu\text{m}$. Their assessment of reported correlations for

small channels showed that none of the tested correlations appear to provide good predictions over the conventional size tube correlations. This is mainly due to the fact that those correlations rely heavily on the regression analysis of the tested data rather than on analytical modeling. In addition, the database of each correlation does not cover a wide range of fluid properties and channel sizes.

A review of literature of heat transfer asymptotic models on flow boiling in microchannels indicates that the enhancement factor is found to be overestimated due to the adjusting parameters (ζ) used by these asymptotic models. Zhang et al. (2004) and (2005) used the value of $\zeta = 0.6$, and Lee and Garimellia (2008) used the values of $\zeta = 2$, while Bertsch et al. (2009a) assumed that ζ is a function of the confinement number and exit quality and was estimated using data regression.

In the nucleate boiling region, a large discrepancy in the heat transfer coefficients predicted by these correlations and models was found. This discrepancy can be attributed to the neglecting of the effect of effective wall superheat, which has a great influence on the suppression factor. The actual superheat is not constant across the boundary layer, but falls as shown in Fig. 5-11. Thus, the mean superheat of the fluid in which the bubble grows is lower than the wall superheat (ΔT_{sat}). The difference between this lower superheat (ΔT_e) and the wall superheat is significant and cannot be neglected since the boundary layer is thin and the temperature gradient is steep (Whally, 1987). Chen (1966) defined the suppression factor as the ratio of the mean superheat to the wall superheat as:

$$S_p = \left(\frac{\Delta T_e}{\Delta T_{\text{sat}}} \right). \quad (5-4)$$

In summary, the experimental results demonstrated reasonable agreement with some asymptotic models in the convective boiling regime, where $x_{e,o} > 0.2$, as shown in Fig. 5-10. However, the experiments conducted under $x_{e,o} < 0.2$ showed that the heat transfer coefficients surpassed the values obtained from the available correlations. The asymptotic models of Zhang et al. (2005) and Lee and Garimella (2008) are found to give the most appropriate predictions of the heat transfer coefficient in the forced convective boiling regime. All of the tested models and correlations, however, underestimate the heat transfer coefficient data in the nucleate boiling regime. It should be noted that the heat transfer coefficient found in the present study follows the same trend reported in the literature by many researchers for flow boiling heat transfer in microchannels (Steinke and Kandlikar, 2004; Lee and Mudawar; 2005b, Ravigururajan, 1998; Yen et al., 2006). It is concluded that the presented values of heat transfer coefficient of nucleate boiling regime do not match with the tested models and correlations. Further, these models and correlations could not capture the trend of the heat transfer coefficient as it decreases with an increase in exit quality, as presented in Fig. 5-10. This implies that the suppression factor could be better described by an analytical model differing from those available in the literature.

5.4 Suppression Factor Development

The proposed model assumes that both nucleation and convective mechanisms occur to some degree over the entire boiling curve and the contribution of each one is made by the exponent $n = 3$. Hence, the two-phase flow heat transfer coefficient is defined as:

$$h_{tp} = ((Fh_{sp})^3 + (S_p h_{nb})^3)^{\frac{1}{3}} . \quad (5-5)$$

Steiner and Taborek (1992) applied Eqn. (5-5) with $n = 3$. It should be noted that high values of n would indicate an abrupt transition, while low values would extend the transition range. This form of the equation suggests that Fh_{sp} is the dominant term in the convective boiling region and $S_p h_{nb}$ is the preponderant term in the nucleate boiling region. If the temperature gradient in Region A is assumed linear, as shown in Fig. 5-11, then

$$T_e - T_s = \frac{-qy}{k_L} \quad (5-6)$$

However, the temperature variation with distance from the heated wall during flow may be expressed as (Whalley, 1987):

$$T - T_{sat} = \left(\frac{2\sigma T_{sat}}{y h_{fg} \rho_g} \right) \quad (5-7)$$

Equations 5-6 and 5-7 are plotted against the distance from the heated wall as is illustrated in Fig. 5-12. At point (e), the temperatures are equal. Therefore,

$$T_s - T_{sat} = \frac{1}{y} \left(\frac{2\sigma T_{sat}}{h_{fg} \rho_g} + \frac{qy^2}{k_L} \right) \quad (5-8)$$

At the same point, the temperature gradient is equal. Then

$$\left. \frac{dT}{dy} \right|_{y=e} = \frac{-q}{k_L} = \frac{-2\sigma T_{sat}}{h_{fg} \rho_g y^2} \quad (5-9)$$

rearranging,

$$y^2 = \frac{2\sigma T_{sat} k_L}{h_{fg} \rho_g q} \quad (5-10)$$

substituting Eqn. (5-10) into Eqn. (5-7) yields

$$T_e - T_{\text{sat}} = \Delta T_e = \sqrt{\frac{2\sigma T_{\text{sat}} q}{h_{\text{fg}} \rho_g k_L}} . \quad (5-11)$$

Finally, the function for S_p in Eqn. (5-4) is expressed as

$$S_p = \frac{\Delta T_e}{\Delta T_{\text{sat}}} = \frac{1}{\Delta T_{\text{sat}}} \sqrt{\frac{2\sigma T_{\text{sat}} q}{h_{\text{fg}} \rho_g k_L}} . \quad (5-12)$$

Therefore, Eqn. (5-12) characterizes the contribution of nucleate boiling during forced convection boiling. In the convective boiling regime, Zhang et al. (2004) correlated the enhancement factor (F), for laminar-liquid turbulent-vapor two-phase flow in minichannels, as a function of the ratio of two-phase Reynolds number (Re_{tp}) to liquid-phase Reynolds number (Re_L) as

$$F = (Re_{\text{tp}} / Re_L)^{0.8} . \quad (5-13)$$

The form for F has been selected based on Zhang et al.'s relationship. The nucleate boiling heat transfer coefficient h_{nb} in Eqn. (5-5) is determined from Kutateladze's (1961) nucleate boiling correlation:

$$\frac{h_{\text{nb}} l^*}{k_L} = 0.44 \left(\frac{10^{-4} q P}{g h_{\text{fg}} \rho_g \mu_L} \frac{\rho_L}{\rho_L - \rho_g} \right)^{0.7} Pr^{0.35} , \quad (5-14)$$

where P is the pressure corresponding to the saturation temperature and l^* is defined as:

$$l^* = \left(\frac{\sigma}{g(\rho_L - \rho_g)} \right)^{0.5} . \quad (5-15)$$

5.5 Asymptotic Model Validation

Efforts were made to collect data for as many fluids and as wide a range of parameters as possible for flow boiling heat transfer in microchannels. While there are a large number of such studies, most of them do not provide analyzable data. For the data

to be analyzable, mass flux, heat flux, wall temperature, heat transfer coefficient, and quality at the heat sink outlet should be known. Most of the studies provide only the heat or mass flux and heat transfer coefficient. The proposed asymptotic model has been tested for validation on three datasets from three different sources containing 298 points as presented in Table 5-1. The proposed model describes most of the data within 30% error margin with a mean absolute error of 19.5% as shown in Fig. 5-13.

The predicted results outside of the 30% error margins, which correspond to low exit quality ($x_{e,o} < 0.2$), are associated with high uncertainties. These results show considerable disagreement with the experimental values, showing an under-prediction. In general, uncertainty in the estimation of low exit quality data points is considered high, even when accurate instrumentation is used. Special difficulties arise from heat loss estimation, mass flux fluctuations, and coolant outlet conditions. Hence, the uncertainty becomes so high that the estimated value has low validity. The present experimental heat transfer coefficients and their corresponding predicted values for different vapor quality values and constant mass flux are shown in Fig. 5-14. The predicted and experimental data agree well.

Figures 5-15(a) and 5-16(a) present the experimental data of Qu and Mudawar (2003b) and predicted two-phase heat transfer coefficients as a function of mass flux and exit quality. According to the experimental data of Qu and Mudawar (2003b), the heat transfer coefficient starts to decrease sharply with vapor quality for low mass flux $G = 135 \text{ kg/m}^2\cdot\text{s}$ as seen in Fig. 5-15(a). For higher mass flux $G = 323 \text{ kg/m}^2\cdot\text{s}$, the heat transfer coefficient values increase slightly at low vapor quality before decreasing at

high vapor quality as presented in Fig. 5-16(a). The new asymptotic model describes the experimental trends quite well and it is able to accurately predict the experimental values.

Figure 5-15(b) demonstrates the predicted factors F and S_p for a constant mass flux ($G = 135 \text{ kg/m}^2\cdot\text{s}$) as a function of exit quality. The S_p factor decreases sharply and then diminishes with increasing exit quality, whereas the F factor increases as vapor quality increases. Nucleate boiling is the significantly active component of flow boiling heat transfer because of the insignificant effect of convective boiling, especially at low exit quality. This is mainly because the nucleate boiling heat transfer reduces with decreasing saturation pressure, which is an important parameter in determining the intensity of nucleate boiling in Kutateladze's correlation (Eqn. 5-14). It also indicates that the effect of nucleate boiling is higher than forced convective boiling for heat transfer coefficients at low quality, thus the heat transfer coefficient is underestimated by forced convection correlations.

Figure 5-16(b) presents the effect of the convective and nucleate terms at higher mass flux and different exit qualities. The S_p decreases with an increase in exit quality at a constant mass flux as shown in the figure. The weak effect of the nucleate boiling may be explained by the increase in mass flux since F is a function of the ratio of Re_{tp} and Re_L . Hence, F would have a positive slope because of the decrease in the flow velocity of the liquid-phase component, and consequently the effect of convective boiling becomes significant. This is clear at low exit quality ($x_{e,o} < 0.2$) when the dominant flow pattern is the slug and plug regimes. However, when the flow has become annular, the effect of the convective component increases and becomes dominant, thus the effect of nucleate boiling is suppressed. Figure 5-16(b) also indicates early transition from nucleate to

forced convective boiling compared to Fig. 5-15(b), where transition took place at higher values of vapor quality. This is attributed to the effect of mass flux; the higher the mass flux the earlier the transition.

5.1 Conclusions

The present experimental work investigated the heat transfer characteristics of flow boiling in a silicon microchannel heat sink. TLCs were used to produce full-field global surface temperature distributions for two phase flow measurements in microchannel heat sinks, and to demonstrate incipience of boiling based on local measured data. The two-phase heat transfer coefficient decreases with increased exit quality, in contrary to trends in macro and minichannels. Nucleate boiling is dominant at low exit quality where the heat transfer coefficient is strongly dependent on heat flux. The effect of nucleate boiling decreases as exit quality increases, and the heat transfer coefficient becomes weakly dependent on exit quality as the flow transitioned progresses from slug to annular flow regimes. The existence of partially and fully developed boiling regions has been demonstrated through boiling curves. The convective boiling heat transfer coefficient is predicted with reasonable accuracy by two asymptotic models. However, existing flow boiling models and correlations under-predict the nucleate boiling heat transfer coefficient, especially at low exit quality. A single model, combining the effect of nucleate and convective boiling heat transfer, has been developed to predict the two-phase heat transfer coefficient in both regimes as well as in the transition regime with 19.5% mean absolute error. It is essential to have an analytical model to predict the flow boiling heat transfer in microchannel heat sinks based on fundamental conservation

principles. It is essential to have an analytical model to predict the flow boiling heat transfer in microchannel heat sinks based on fundamental conservation principles.

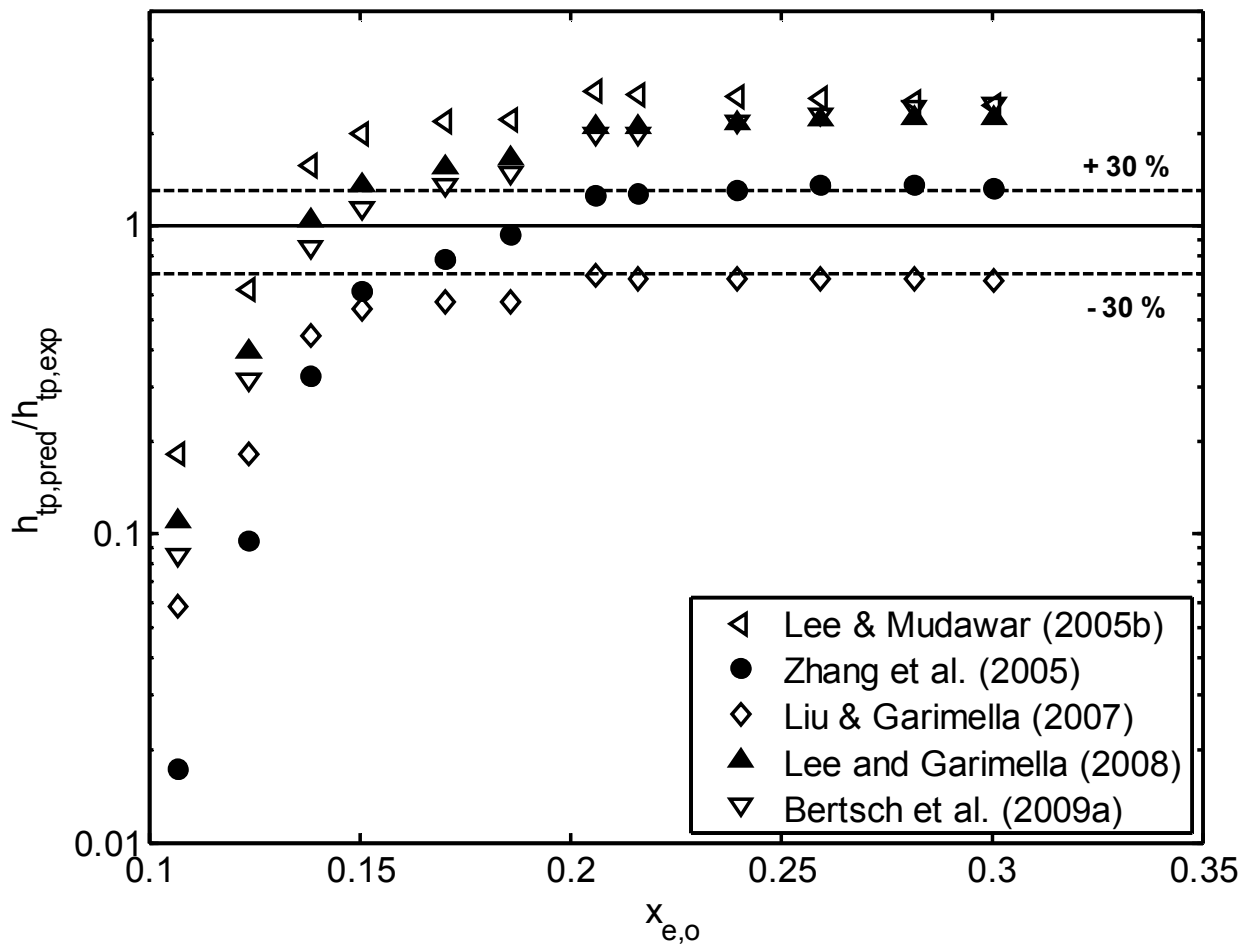


Figure 5-10: Comparison of measured heat transfer coefficient data with predicted data from mini and microchannel correlations for $G = 531 \text{ kg/m}^2 \text{ s}$.

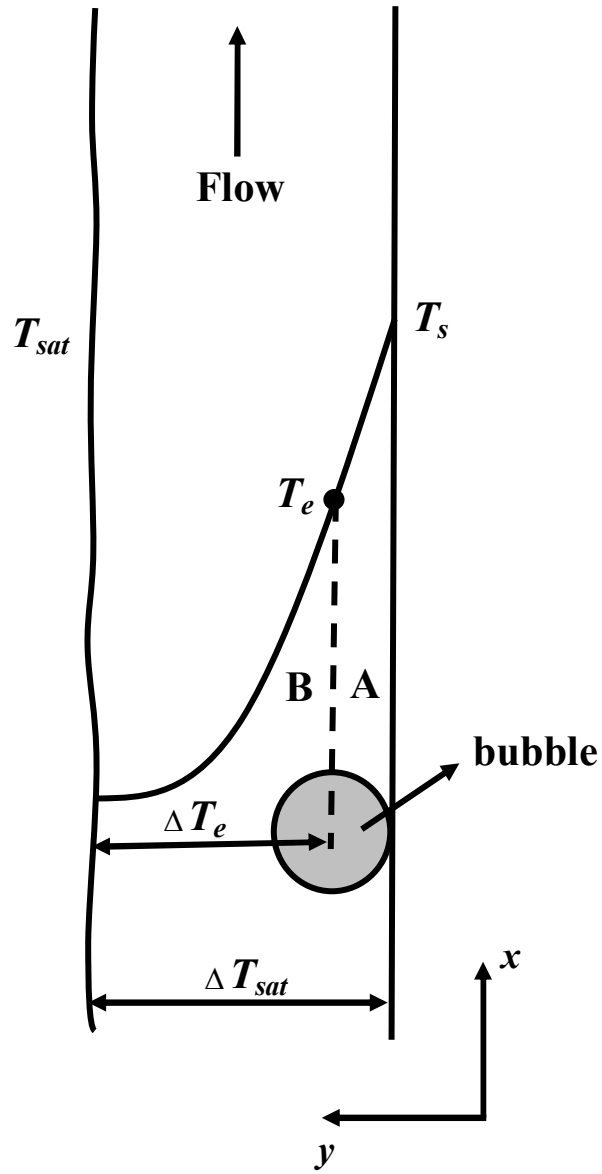


Figure 5-11: Temperature profile during convective flow boiling.

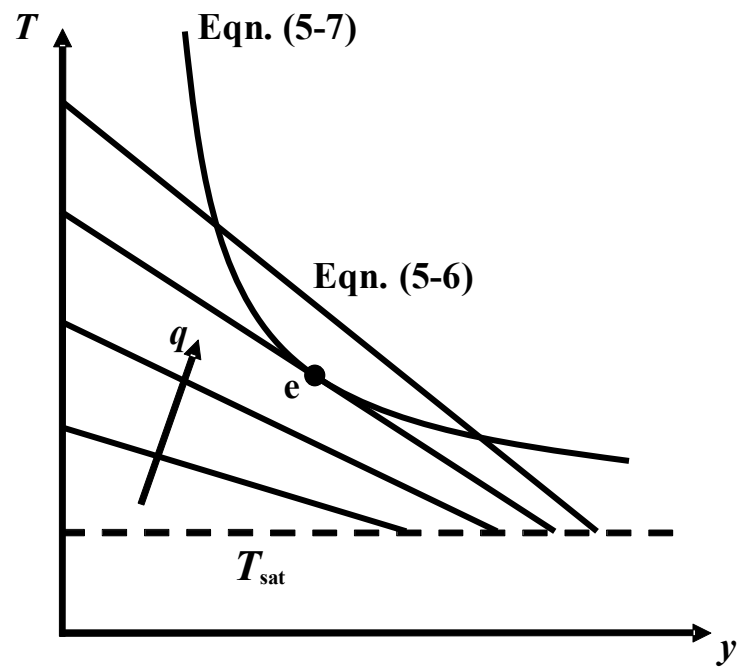


Figure 5-12: Temperature plots against distance from the wall.

Table 5-1: Investigated ranges and accuracy of the model.

Reference	Fluid	D_h (μm)	$x_{c,o}$	G $\text{kg/m}^2.\text{s}$	No. of Data Points	MAE (%)
Present data	FC-72	248	0.1-0.39	334-531	48	26
Dong et al. (2008)	R141b	92	0.04-0.74	500-900	68	16
Qu and Mudawar (2003b)	Water	350	0.006-0.17	135-402	182	19
Summary	3 different refrigerants	92-350	0.006-0.74	135-900	298	19.5

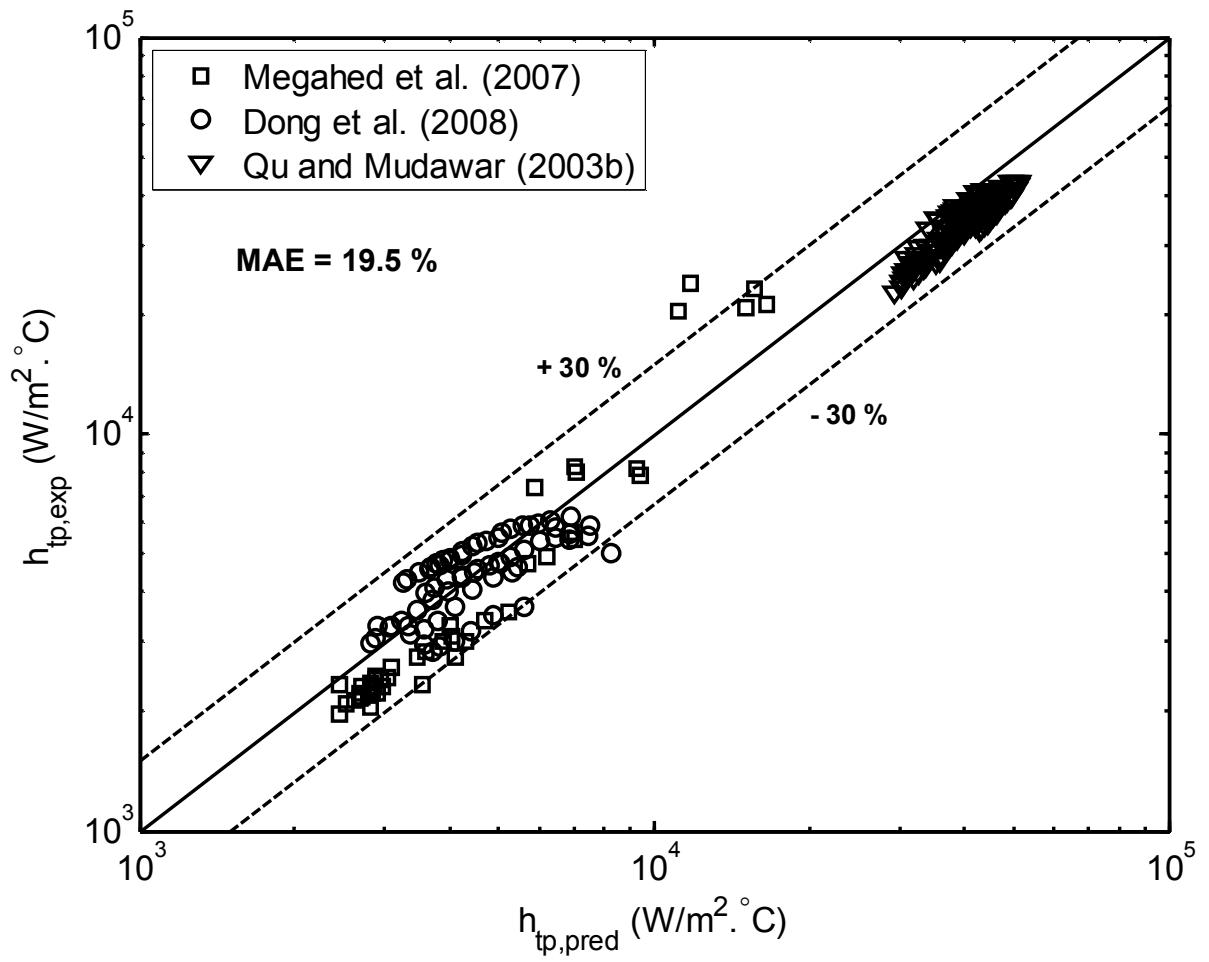


Figure 5-13: Comparison of model predictions with flow boiling heat transfer coefficient data

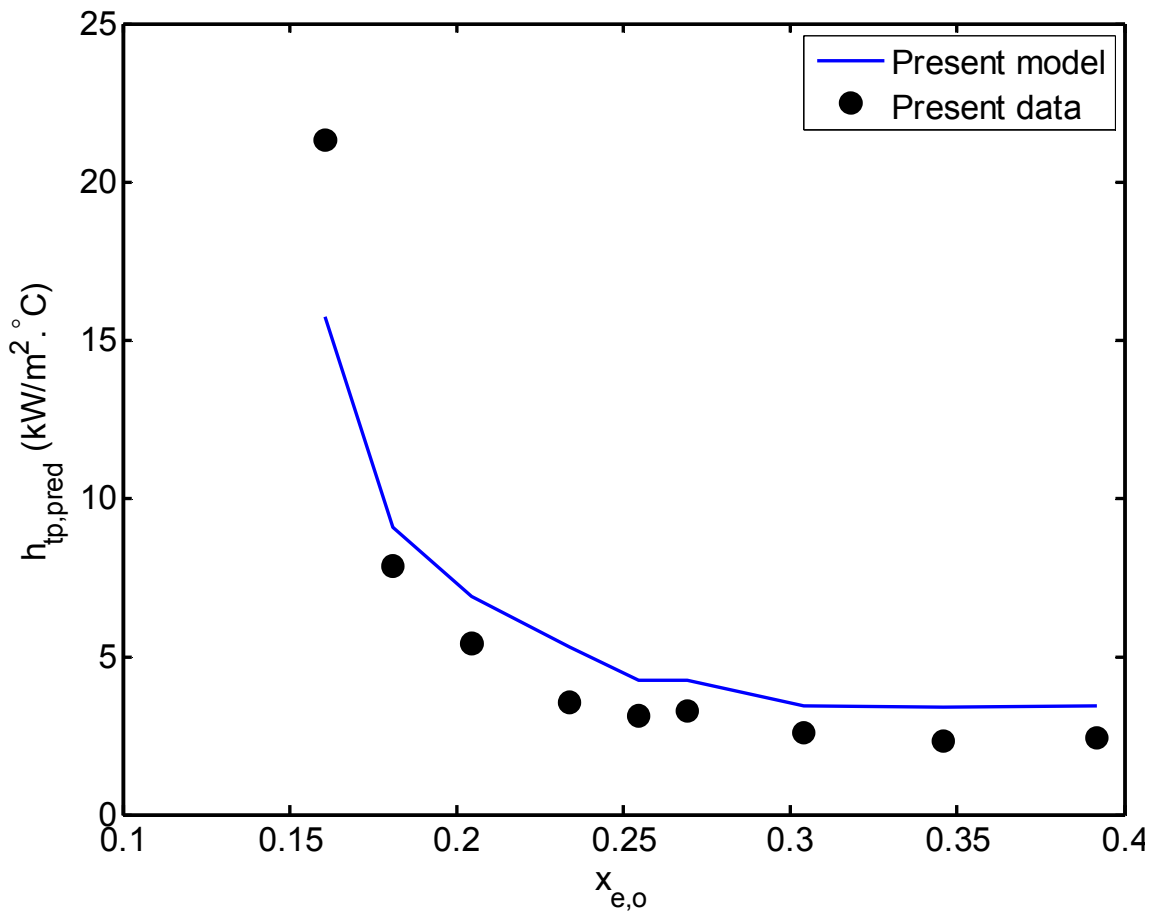


Figure 5-14: Comparison between the measured and predicted boiling heat transfer coefficients at $G = 341 \text{ kg/m}^2 \cdot \text{s}$

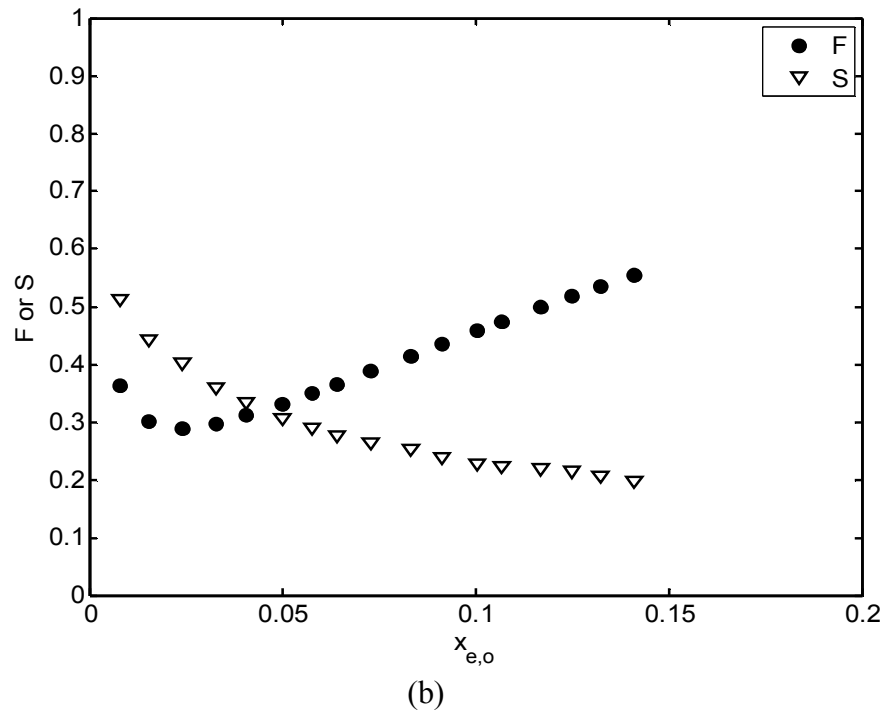
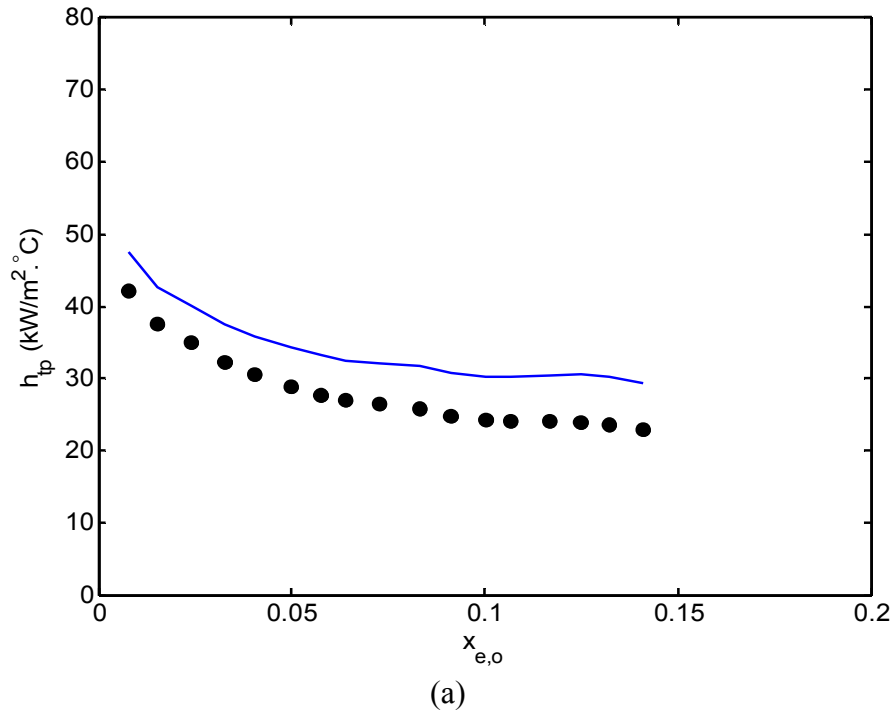
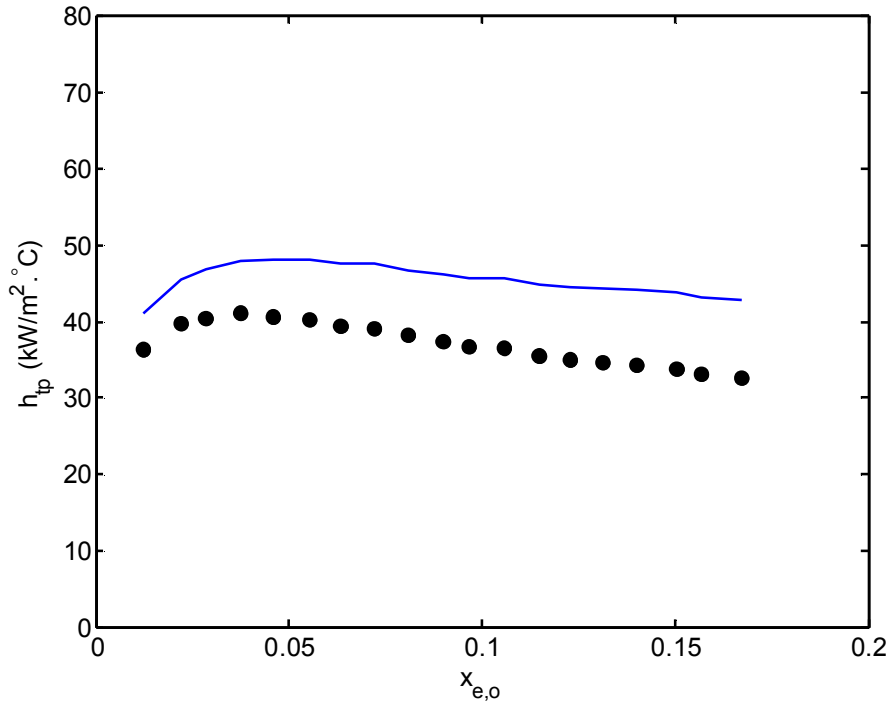
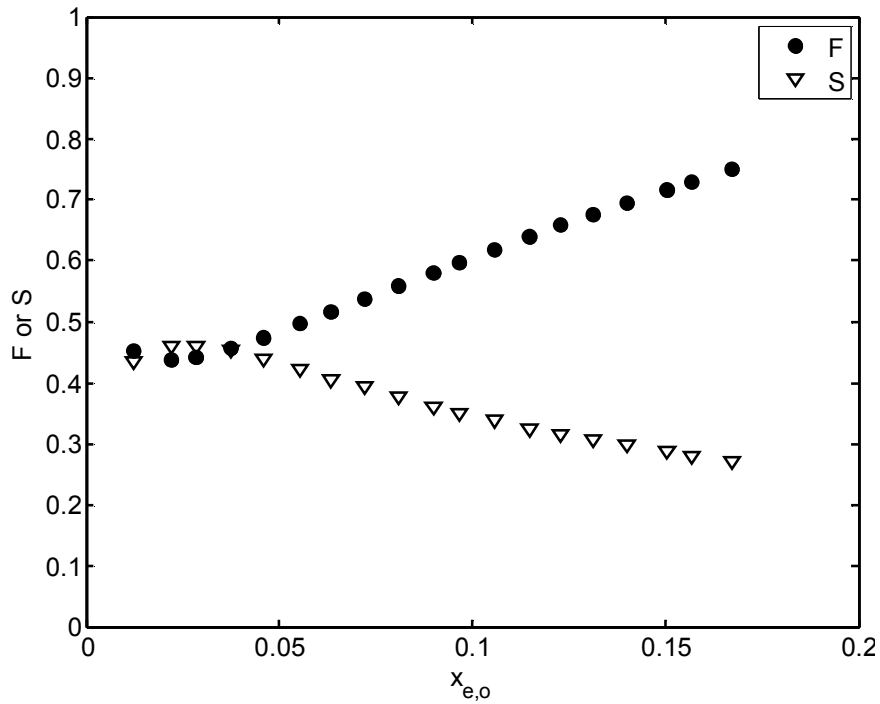


Figure 5-15: (a) Experimental and predicted flow boiling heat transfer coefficients for Qu and Mudawar (2003b) data at $G = 135 \text{ kg/m}^2 \cdot \text{s}$ (b) Nucleate boiling suppression factor and forced convective heat transfer enhancement factor at $G = 135 \text{ kg/m}^2 \cdot \text{s}$



(a)



(b)

Figure 5-16: (a) Experimental and predicted flow boiling heat transfer coefficients for Qu and Mudawar (2003b) data at $G = 323 \text{ kg/m}^2 \cdot \text{s}$ (b) Nucleate and convective boiling factor predictions based on developed model at $G = 323 \text{ kg/m}^2$.

CHAPTER 6

ANALYTICAL MODELING OF ANNULAR FLOW BOILING HEAT TRANSFER IN MINI- AND MICROCHANNEL HEAT SINKS

The objective of the present chapter is to develop an analytical model for determining the heat transfer coefficient for annular flow boiling inside rectangular mini- and microchannels. The solution for the heat transfer coefficient is dependent on the Reynolds' analogy. In relating the wall shear stress to the heat transfer coefficient, the heat transfer coefficient has been expressed in terms of liquid-phase friction and acceleration induced pressure drops. The model considers the characteristics of mini- and microchannels during laminar/transition liquid annular flow. The predicted heat transfer coefficients are evaluated and compared to the experimental results using seven data sets over wide ranges of exit quality, channel aspect ratios, and heat and mass fluxes.

6.1 Analytical Model

6.1.1 Assumptions

A physical model of the problem is shown schematically in Figs. 6-1 and 6-2. The following assumptions are made in the analysis:

(1) Annular flow configuration is assumed for the analysis. Annular flow implies that the vapor occupies the central or core region of the channel, while the liquid remains in a thin layer adjacent to the microchannel wall.

- (2) The thickness of the liquid film is assumed to be non-uniform all around the circumference of the channel, with a continuous central vapor core (Fig. 6-2).
- (3) Rectangular mini- or microchannels are considered with a depth H_{ch} and width W_{ch} .
- (4) The temperature and velocity gradients are linear across the liquid film.
- (5) The liquid vapor interface is assumed to be smooth. Hence, the liquid entrainment in the vapor core region can be neglected.
- (6) One dimensional, steady, and laminar flow are assumed in the liquid film. The flow in the vapor core may proceed from laminar to turbulent.
- (7) The liquid and vapor properties are assumed to be constant, at the saturation temperature.
- (8) The two phases flow separately in the channel.

6.1.2 Two-phase Heat Transfer Coefficient

The governing differential equations for momentum and heat transfer across the liquid film during laminar flow may be expressed as follows:

$$\tau_w = \mu_L \frac{\partial u}{\partial x} , \quad (6-1)$$

and

$$q_w = -k_L \frac{\partial T}{\partial x} . \quad (6-2)$$

The above Eqns. (6-1) and (6-2) are the basic definitions of the wall shear stress and the wall heat flux, respectively, during laminar flow in the liquid film. Following Reynolds' analysis and assuming that the shear stress and heat flux profiles are similar:

$$\frac{\tau(x)}{\tau_w} = \frac{q(x)}{q_w} = \text{fun}(x) . \quad (6-3)$$

Substituting Eqn. (6-1) and Eqn. (6-2) into Eqn. (6-3) results in:

$$\frac{q_w}{\tau_w} = -\frac{k_L \partial T}{\mu_L \partial u} = \frac{c_p \partial T}{Pr \partial u} , \quad (6-4)$$

where Pr is the Prandlt number. The temperature distribution in the liquid film can be obtained by separating the differentials of the variables T and u in Eqn. (6-4) above, and integrating the velocity from 0 to u_L , and the temperature from T_s to T_{sat} :

$$\int_0^{u_L} \frac{q_w}{k_L} \partial u = - \int_{T_s}^{T_{sat}} \frac{\tau_w}{\mu_L} \partial T . \quad (6-5)$$

Hence the temperature drop across the liquid film may be obtained from Eqn. (6-5) by performing the integration. After integrating, the result is

$$\frac{q_w u_L}{k_L} = \frac{\tau_w}{\mu_L} (T_s - T_{sat}) . \quad (6-6)$$

Using the definition of h_{tp} :

$$q_w = h_{tp} (T_s - T_{sat}) , \quad (6-7)$$

the two-phase heat transfer coefficient can be expressed in an alternative form as follows:

$$h_{tp} = \frac{q_w}{(T_s - T_{sat})} = \frac{\tau_w k_L}{u_L \mu_L} = \frac{\tau_w c_p}{u_L Pr} . \quad (6-8)$$

Equation (6-8) expresses the two-phase heat transfer coefficient in terms of the wall shear stress, liquid velocity, viscosity, and thermal conductivity.

6.1.3 Mass Conservation

The equation expressing the mass conservation in the vapor core is:

$$A_{ch} G_g = A_{ch} G x_e = \rho_g u_g A_g = \rho_g u_g \alpha A_{ch} , \quad (6-9)$$

where A_g is the vapor core area, defined as:

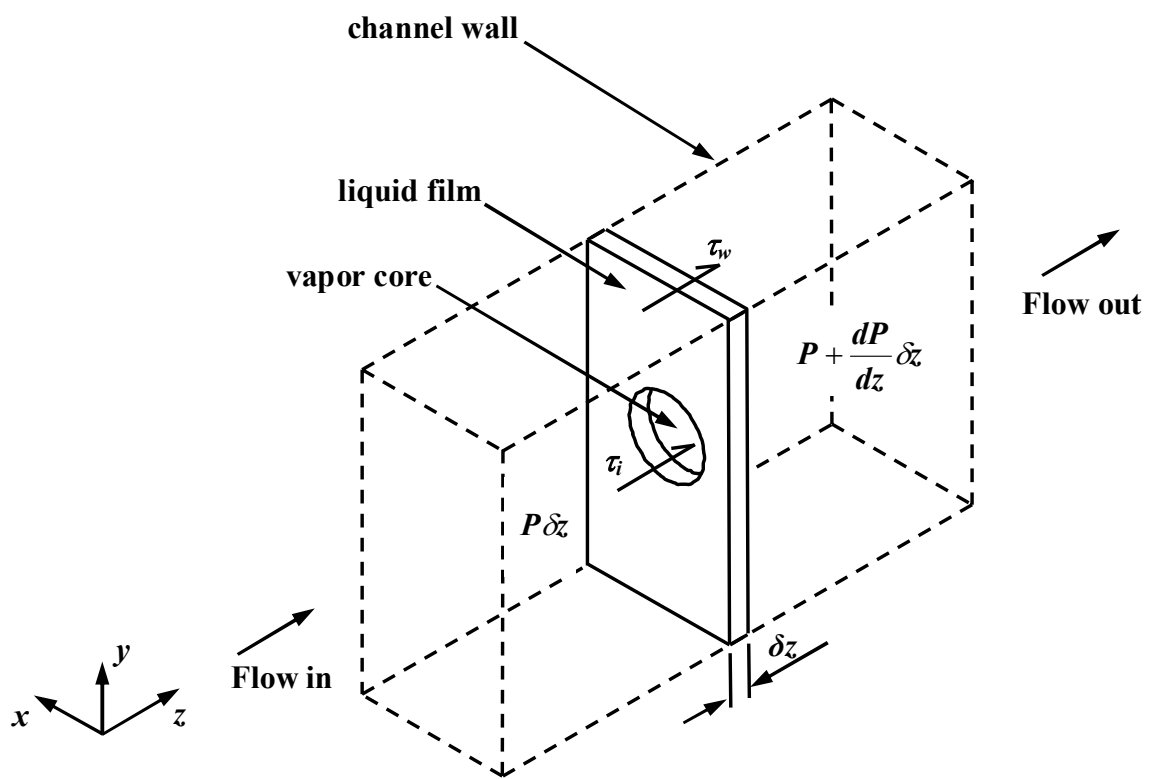


Figure 6-1: Parameters in annular flow for force balance on liquid film.

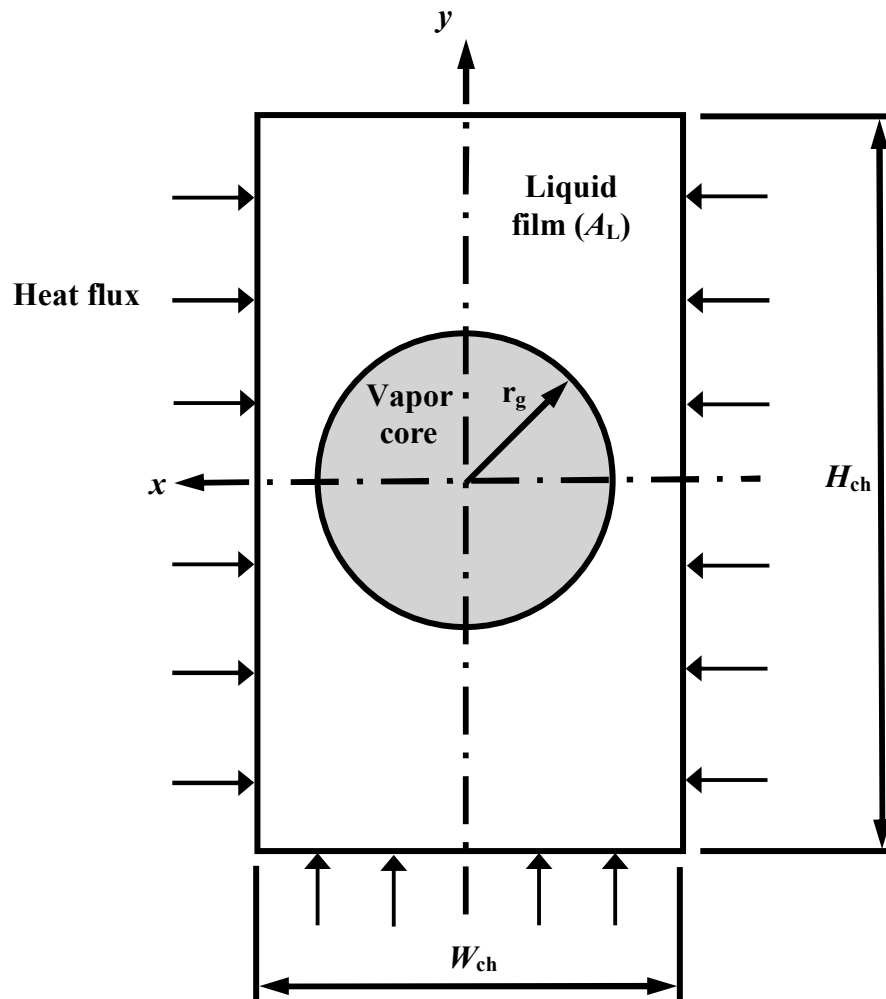


Figure 6-2: Schematic of annular flow in a rectangular channel.

$$A_g = \pi r_g^2, \quad (6-10)$$

and α is the void fraction, defined as:

$$\alpha = \frac{A_g}{A_{ch}} = \frac{\pi r_g^2}{W_{ch} H_{ch}}. \quad (6-11)$$

The conservation equation for the liquid film is given by

$$A_{ch} G_L = A_{ch} G(1 - x_e) = \rho_L u_L A_L = \rho_L u_L (1 - \alpha) A_{ch}, \quad (6-12)$$

and A_L is the liquid film area, defined as:

$$A_L = A_{ch} - A_g. \quad (6-13)$$

6.1.4 Momentum Conservation

6.1.4.1 Wall Shear Stress

Applying the principle of conservation of momentum to the differential liquid element, δz , as illustrated schematically in Fig. 6-1, gives:

$$\int_{S_{ch}} \tau_w \cdot \delta \mathbf{z} \cdot dS = \int_{S_i} \tau_i \cdot \delta \mathbf{z} \cdot dS_i + \int_{A_L} \left[P - \left(P + \frac{dP}{dz} \delta z \right) \right] \cdot dA_L, \quad (6-14)$$

where S_{ch} and S_i are the channel and vapor core peripheries, respectively. The term on the left-hand side represents the wall shear stress. The terms on the right-hand side of the equation correspond to, in order, the interfacial shear stress and the pressure gradient in the liquid film. Rearrangement of Eqn. (6-14) yields:

$$\tau_w = \left(\frac{S_i}{S_{ch}} \right) \tau_i - \left(\frac{A_L}{S_{ch}} \right) \left(\frac{dP}{dz} \Big|_L \right)_{tp}. \quad (6-15)$$

By neglecting the gravitational pressure drop component, the pressure gradient in the liquid film can be expressed in terms of the friction and acceleration related terms as follows:

$$\left(-\frac{dP}{dz}\right)_{\text{L}}\bigg|_{\text{tp}} = \left(-\frac{dP}{dz}F\right)_{\text{L}}\bigg|_{\text{tp}} + \left(-\frac{dP}{dz}a\right)_{\text{L}}\bigg|_{\text{tp}} . \quad (6-16)$$

Substituting Eqn. (6-16) into Eqn. (6-15) yields:

$$\tau_w = \left(\frac{S_i}{S_{\text{ch}}}\right)\tau_i - \left(\frac{A_{\text{L}}}{S_{\text{ch}}}\right)\left(\frac{dP}{dz}F\right)_{\text{L}}\bigg|_{\text{tp}} - \left(\frac{A_{\text{L}}}{S_{\text{ch}}}\right)\left(\frac{dP}{dz}a\right)_{\text{L}}\bigg|_{\text{tp}} . \quad (6-17)$$

Equation (6-17) involves the shear stress at the interface, as well as the friction and acceleration induced liquid phase pressure gradients.

6.1.4.2 Interfacial shear Stress

The interfacial shear stress can be obtained by making a force balance on a disc of radius r_g and length δz in the vapor core, as shown in Fig. 6-3. This differential element is bounded by the interface and not by the channel wall. Balancing forces gives:

$$2\pi r_g \delta z \tau_i = \pi r_g^2 \left[P - \left(P + \frac{dP}{dz}\bigg|_g \delta z \right) \right] . \quad (6-18)$$

The term on the left-hand side represents the interfacial shear stress, while the term on the right-hand side is the pressure gradient in the vapor core. Ignoring the gravitational and acceleration components, the pressure gradient in the vapor core is represented by the frictional term only. The acceleration term is ignored in the vapor core since the interfacial shear stress often has a value approximately equal to its value in adiabatic flow under the same flow conditions (Hewitt and Hall-Taylor, 1970). Equation (6-18) can be reduced to the following form:

$$\tau_i = -\left(\frac{r_g}{2}\right)\left(\frac{dP}{dz}F\right)\Big|_g\Big|_{tp} . \quad (6-19)$$

Substituting Eqn. (6-19) into Eqn. (6-17) gives:

$$\tau_w = \left(\frac{-S_i r_g}{2S_{ch}}\right)\left(\frac{dP}{dz}F\right)\Big|_g\Big|_{tp} - \left(\frac{A_L}{S_{ch}}\right)\left(\frac{dP}{dz}F\right)\Big|_L\Big|_{tp} - \left(\frac{A_L}{S}\right)\left(\frac{dP}{dz}a\right)\Big|_L\Big|_{tp} . \quad (6-20)$$

Based on the assumption of separated flow, the liquid and gas phase pressure drops are considered equal. When the acceleration and gravitational terms are negligible compared to the frictional term, the frictional pressure drop in the liquid phase must equal the frictional drop in the vapor phase:

$$\left(\frac{dP}{dz}F\right)\Big|_L\Big|_{tp} = \left(\frac{dP}{dz}F\right)\Big|_g\Big|_{tp} . \quad (6-21)$$

Combining Eqn. (6-21) and Eqn. (6-20) gives the following result relating the shear stress to the frictional and acceleration pressure gradients in the liquid film:

$$\tau_w = -\left(\frac{S_i r_g + 2A_L}{2S_{ch}}\right)\left(\frac{dP}{dz}F\right)\Big|_L\Big|_{tp} - \left(\frac{A_L}{S_{ch}}\right)\left(\frac{dP}{dz}a\right)\Big|_L\Big|_{tp} . \quad (6-22)$$

6.1.5 Frictional Pressure Gradient

The frictional pressure gradient, for the liquid phase, can be expressed in terms of the liquid-phase pressure gradient, which is considered to flow alone in the channel as follows:

$$\left(-\frac{dP}{dz}F\right)\Big|_L\Big|_{tp} = -\left(\frac{dP}{dz}F\right)_L \phi_f^2 , \quad (6-23)$$

where the two-phase frictional multiplier (ϕ_f^2) is then defined as:

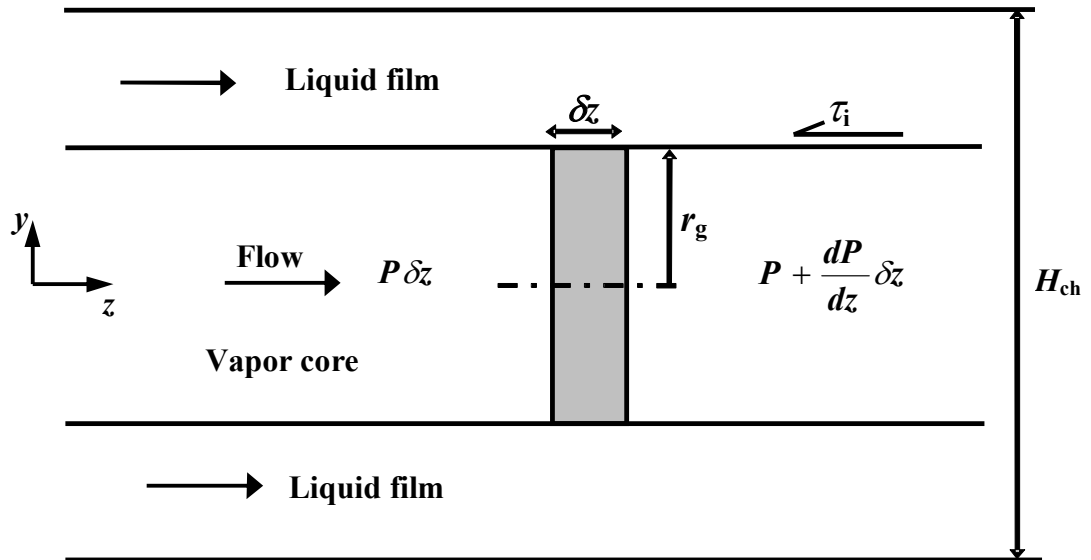


Figure 6-3: Control volume analysis of vapor differential element in annular flow.

$$\phi_f^2 = 1 + \frac{C}{X} + \frac{1}{X^2}, \quad (6-24)$$

where C is the two-phase multiplier parameter and X^2 is the Martinelli parameter. The liquid-phase friction pressure gradient is calculated from the standard equation:

$$-\left(\frac{dP}{dz} F\right)_L = \frac{2f_L G^2 (1-x_e)^2}{D_h \rho_L}, \quad (6-25)$$

where f_L is the friction factor defined as follows:

$$f_L = \frac{fRe}{Re_L}. \quad (6-26)$$

The fRe is defined as:

$$fRe = 24(1 - 1.355\gamma + 1.947\gamma^2 - 1.701\gamma^3 + 0.956\gamma^4 - 0.254\gamma^5), \quad (6-27)$$

and the superficial Reynolds number of the liquid-phase in the two-phase flow, Re_L , is defined as:

$$Re_L = \frac{Gx_e D_h}{\mu_L}. \quad (6-28)$$

6.1.6 Acceleration Pressure Gradient

The two-phase acceleration pressure drop of the separated model is given by Lockhart and Martinelli (1949)

$$\Delta P_{p,a} = G^2 v_L \left[\frac{x_{e,o}^2}{\alpha} \frac{v_L}{v_L} + \frac{(1-x_{e,o})^2}{1-\alpha} - 1 \right], \quad (6-29)$$

where α is the void fraction for conventional size tubes defined as Zivi (1964)

$$\alpha = \frac{1}{1 + \left(\frac{1-x_{e,o}}{x_{e,o}} \right) \left(\frac{v_L}{v_g} \right)^{2/3}}. \quad (6-30)$$

All mini- and microchannel void fraction correlations were developed based on the homogeneous two-phase flow void fraction (volumetric quality, β). The homogeneous two-phase flow void fraction assumes that the liquid and vapor densities travel at the same velocity. However, the present model has been developed based on the separated flow model. The separated flow model considers the two phases separately, with an inherent assumption that the two phases reach constant but not necessarily equal velocities. This assumption of different velocities is important when the densities of each phase are sufficiently different in the presence of large pressure gradients. Therefore, all mini- and microchannel void fraction correlations cannot be used to predict the acceleration pressure drop, since they have been developed based on the homogenous model and not the separated model. Based on these considerations, the void fraction model presented by Eqn. (6-30) has been selected to predict only the acceleration pressure drop based on the separated model due to the following reasons: (1) Eqn. (6-30) is a void fraction model developed specifically for annular flow, which matches with the present model. (2) This annular flow void fraction model, presented in Eqn. (6-30), was also developed assuming no liquid entrainment in the vapor core. It should be noted that no liquid entrainment is one of the basic assumptions in the present model. Therefore, Eqn. (6-30) has been used to estimate the acceleration pressure drop. The acceleration pressure gradient can be derived by applying the chain rule as follows:

$$\left(\frac{dP}{dz} a \Big|_L \right)_{\text{tp}} = \frac{dP}{dx_e} \frac{dx_e}{dz} . \quad (6-31)$$

dP/dx_e may be obtained by differentiating Eqn. (6-29) with respect to x_e , which leads to the following equation:

$$\frac{dP}{dx_e} = G^2 v_L \left[2 \cdot x_{e,o} \left(\frac{v_g}{v_L} - \left(\frac{v_g}{v_L} \right)^{\frac{2}{3}} - \left(\frac{v_g}{v_L} \right)^{\frac{1}{3}} + 1 \right) + \left(\left(\frac{v_g}{v_L} \right)^{\frac{2}{3}} + \left(\frac{v_g}{v_L} \right)^{\frac{1}{3}} - 2 \right) \right] \quad (6-32)$$

Alternatively, by applying a heat balance on the channel, it may be shown that:

$$q_w A_{\text{tot}} = \dot{m} x_e h_{\text{fg}} \quad (6-33)$$

In mini- and microchannel heat sinks, the heat flux is supplied through three walls only, since the adiabatic fourth wall is used to conduct flow visualization. Hence, the heat transfer area is introduced as:

$$A_{\text{tot}} = (2H_{\text{ch}} + W_{\text{ch}})L_{\text{ch}} \quad (6-34)$$

Hence, for a linear change of x_e over a length L , dx_e/dz could be given by

$$\frac{dx_e}{dz} = \frac{q_w (2H_{\text{ch}} + W_{\text{ch}})}{\dot{m} h_{\text{fg}}} \quad (6-35)$$

and remembering that

$$\dot{m} = GW_{\text{ch}}H_{\text{ch}} \quad (6-36)$$

dx_e/dz for three-sided heating is expressed as

$$\frac{dx_e}{dz} = \frac{q_w (2H_{\text{ch}} + W_{\text{ch}})}{H_{\text{ch}} W_{\text{ch}} G h_{\text{fg}}} \quad (6-37)$$

Similarly, for four-sided heating, dx_e/dz can be defined as

$$\frac{dx_e}{dz} = \frac{2q_w (H_{\text{ch}} + W_{\text{ch}})}{G h_{\text{fg}} H_{\text{ch}} W_{\text{ch}}} \quad (6-38)$$

Substituting Eqns. (6-32) and (6-37) into Eqn. (6-31) and rearranging, gives

$$\left(\frac{dP}{dz} a \right)_{\text{tp}} = \frac{q_w (2H_{\text{ch}} + W_{\text{ch}}) G v_L}{H_{\text{ch}} W_{\text{ch}} h_{\text{fg}}} \left[2 \cdot x_{e,o} \left(\frac{v_g}{v_L} - \left(\frac{v_g}{v_L} \right)^{\frac{2}{3}} - \left(\frac{v_g}{v_L} \right)^{\frac{1}{3}} + 1 \right) + \left(\left(\frac{v_g}{v_L} \right)^{\frac{2}{3}} + \left(\frac{v_g}{v_L} \right)^{\frac{1}{3}} - 2 \right) \right] \quad (6-39)$$

Substituting Eqn. (6-23) and Eqn. (6-39) into Eqn. (6-22) and rearranging, the resultant equation will give an equation for calculating τ_w , expressed as follows:

$$\tau_w = -\left(\frac{A_{ch}}{S_{ch}}\right)\left(\frac{dP}{dz}F\right)_L \phi_f^2 - (1-\alpha)\left(\frac{A_{ch}}{S_{ch}}\right)\left(\frac{dP}{dz}a\right)_L \Big|_{tp} . \quad (6-40)$$

Combining Eqn. (6-40) into Eqn. (6-8), the analytical solution of the two-phase heat transfer coefficient, for three side heating, can be expressed as follows:

$$h_{tp} = \frac{k_L(1-\alpha)A_{ch}}{\mu_L(1-x_{e,o})S_{ch}} \left[\frac{2\phi_f^2 f_L G(1-x_{e,o})^2}{D_h} - \frac{(1-\alpha)q_w \left(\frac{2}{\gamma} + 1\right)}{H_{ch} h_{fg}} \left(-2x_{e,o} \left(-\frac{v_g}{v_L} + 1 + \varepsilon \right) + \varepsilon \right) \right] . \quad (6-41)$$

A similar equation may be derived for four side heating; the results is

$$h_{tp} = \frac{k_L(1-\alpha)}{\mu_L(1-x_{e,o})} \left[\frac{2A_{ch}\phi_f^2 f_L G(1-x_{e,o})^2}{S_{ch}D_h} - \frac{(1-\alpha)q_w}{h_{fg}} \left(-2x_{e,o} \left(-\frac{v_g}{v_L} + 1 + \varepsilon \right) + \varepsilon \right) \right] , \quad (6-42)$$

where ε is defined as

$$\varepsilon = \left(\frac{v_g}{v_L}\right)^{\frac{2}{3}} + \left(\frac{v_g}{v_L}\right)^{\frac{1}{3}} - 2 . \quad (6-43)$$

6.2 Data Analysis

Although numerous studies in the literature have been devoted to the understanding of flow boiling heat transfer characteristics in mini- and microchannel heat sinks, the usage of some of the available experimental data sets is limited because not enough details about experimental conditions are provided. The presented model has been validated using experimental data sets published in the literature for seven different

refrigerants from different researchers with a total of 292 data points suitable for the scope of this study. Table 6-1 describes the range of the experimental conditions for all the data sets used to validate the proposed model. Experiments for the selected data are carried out in rectangular mini- and microchannels with heat fluxes ranging from 5 to 461 kW/m², mass fluxes ranging from 208 to 988 kg/m².s, vapor quality ranging from 0.1 to 0.85, and hydraulic diameters in the range of 92 to 1440 μm. It should be noted that the experimental data exhibiting the characteristics of partial dry out are omitted from the comparisons as they are unrepresentative of annular flow. The refrigerant's thermophysical properties were taken from the NIST refrigerant database.

A flow regime map should be consulted to ensure that annular flow has been achieved for a given set of operating parameters. While many researchers have reported microchannel flow regime maps, most are adiabatically based. One notable exception is the work by Revellin and Thome (2007). Their map was developed by measuring flow pattern data and bubble frequency of diabatic R134a and R245fa flows in 509 and 790 μm diameter glass channels using two laser beams. They found that several of flow regimes transitions could be described by the Reynolds and Weber numbers. The flow pattern map indicated that flow regimes, observed at low mass flux, are primarily annular and include slug and bubbly-slug regimes. The Revellin and Thome map is shown in Fig. 6-4. The solid line indicates the transition line of the experimental data from slug to annular flow. The dotted lines indicate model prediction's uncertainty ($\pm 20\%$).

Table 6-1: Description of data obtained for annular flow boiling heat transfer in mini- and microchannels

Reference	Fluid	D_h (μm)	G ($\text{kg}/\text{m}^2 \cdot \text{s}$)	$x_{e,o}$	Re_L	Re_g	q (kW/m^2)	h_{tp} ($\text{W}/\text{m}^2 \cdot ^\circ\text{C}$)	No. of Data points
Megahed et al. (2008)	FC-72	248	334-531	0.23-0.39	114-228	334-483	22-32	2139-2585	14
Yun et al. (2006)	R410A	1360-1440	300-400	0.29-0.69	858-2640	1063-20413	15-20	10513-18715	15
Dong et al. (2008)	R141b	92	500-900	0.15-0.77	28-186.5	988-5807.4	75-100	3003-6067	55
Yen et al. (2006)	R123	214	400-800	0.16-0.68	67-353	2039-9618	25-84	2602-6557	16
Lee and Lee (2001b)	R113	783	208	0.21-0.68	277-688	2622-8435	5-10	2773	25
Bertsch et al. (2008b)	R134a	540	250	0.39-0.85	99-529	5824-10837	150-196	4779-11606	9
Agostini et al. (2008a)	R236fa	336	413-988	0.1-0.57	273-1035	3230-15235	114-461	10960-25637	159
Total	7 different refrigerants	92-1440	208-988	0.1-0.85	28-2640	334-20413	5-461	2139-18715	292

As mass flux is increased, the bubble/annular transition boundary shifts to the left and starts to diminish with increasing mass flux. All the data within the annular regime in addition to the data within +20% transition regimes were selected to test the analytical model. The experimental data of Lee and Lee (2001b) have been tested on the flow map of Revellin and Thome. The flow map demonstrates that most of these data are identified to be in the bubbly coalescing regime, as presented in Fig. 6-4. This is because the aspect ratios of the Lee and Lee test sections were low enough, with $\gamma = 0.02$, to suppress the annular flow. However, Lee and Lee reported that the predominant flow pattern observed in all their tests was annular for a quality range of 0.15 to 0.75, thus, their experimental data set may be appropriate for this study. Ali et al. (1993) reported the same type of flow regime for their specific test conducted through a narrow passage.

Figure 6-5(a) and (b) show the superficial liquid and vapor Reynolds range of available data as a function of exit quality, respectively. The Liquid-phase Reynolds number varies from 28 to 2640 and decreases as the exit quality increases. A limited number of two-phase heat transfer coefficient measurements have been obtained during annular flow boiling under laminar-liquid conditions in channels with rectangular geometries. The superficial vapor core Reynolds number spans the laminar, transition and turbulent ranges, and increases with increasing exit quality. Most of the Reynolds number data for the vapor core are turbulent over the tested exit quality range, as shown in Fig. 6-5(b). The transition criteria where the liquid phase is characterized as being in the laminar or turbulent flow regime have to be indicated in the present study. Lockhart and Martinelli (1949) proposed that the transition from laminar to turbulent flow occurs at a superficial Reynolds number of about 1000 to 2000.

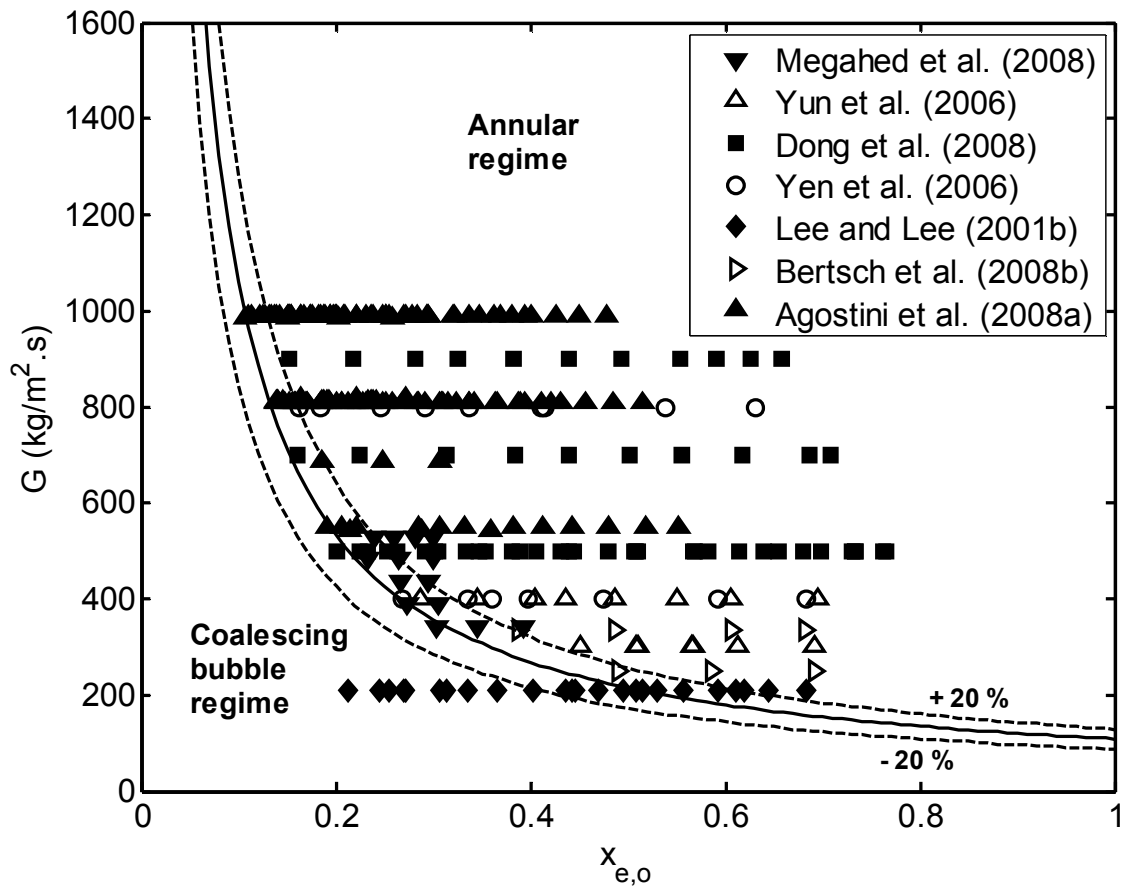
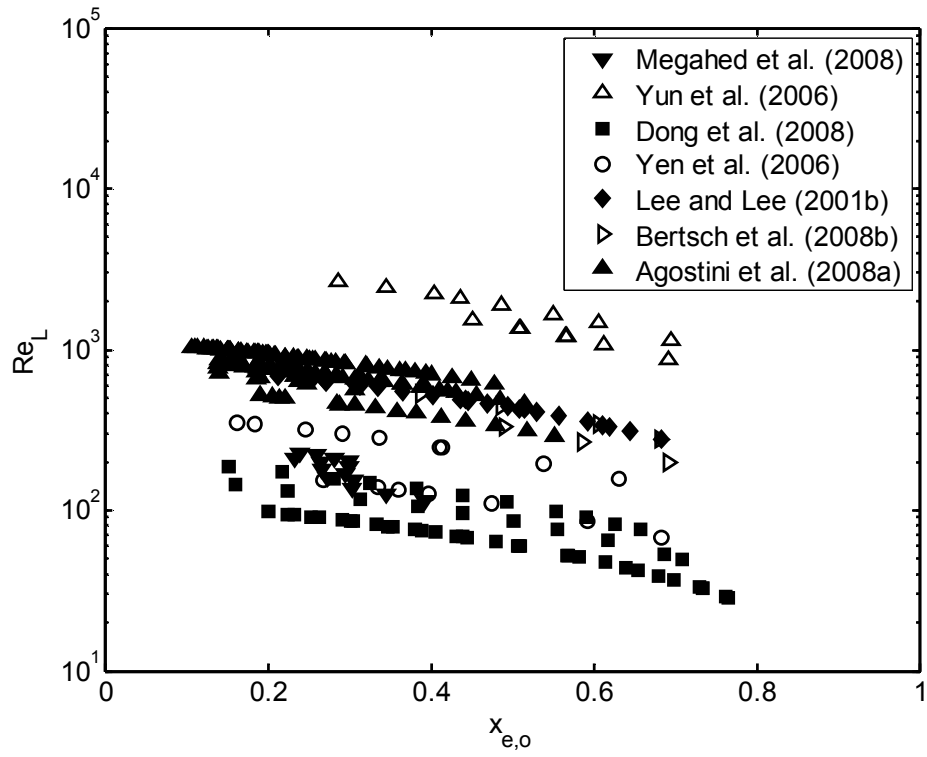


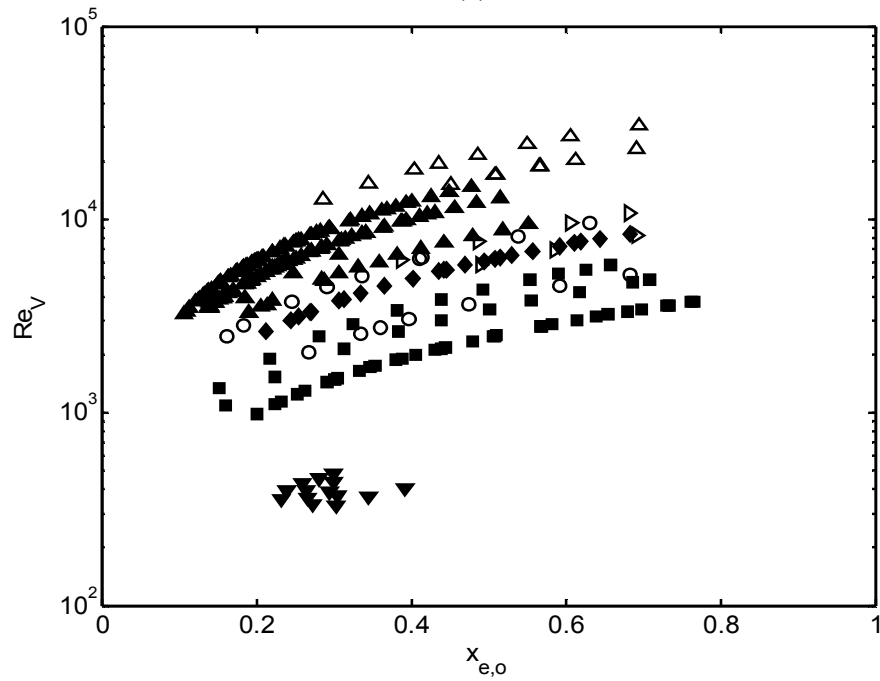
Figure 6-4: The Revellin and Thome (2007) flow regime map for diabatic two-phase flow in microchannels.

However, Kandlikar and Campbell (2004) stated that the transition from laminar to turbulent flow begins at a Reynolds numbers of approximately 1900 for the total flow considered as liquid. In their work, the laminar-to-turbulent flow transition was reported to occur over a range of Reynolds numbers between 1900 and 3500. Analyses of the present data, over a range of $122 < Re_{fo} < 3700$, are presented using the laminar and transition characterizations for the liquid phase Reynolds number based on the criteria defined by Kandlikar and Campbell.

Void fraction and two-phase frictional multiplier correlations are needed for the current model. Three different void fraction correlations are presented in Table 6-2. These are the only correlations that have been found in the literature that could be used in mini- and microchannels. The correlation of Xiong and Chung (2007) was developed from nitrogen and water data inside rectangular channels in addition to the data of Kawahara et al. (2005) from ethanol-water/nitrogen gas mixtures inside a microtube. The aforementioned void fraction correlations for small channels are based on the channel diameter and flow volumetric quality only. At the same time, these correlations have eliminated the influence of refrigerant physical properties. In the absence of refrigerant physical properties, the void fraction correlations may significantly over-predict the data for some refrigerants, and hence data comparisons may be altered in a significant manner. Caution should therefore be exercised before applying them to a different fluid. Table 6-2 lists these correlations along with their applicability to the tested refrigerants. Table 6-3 shows two of the existing correlations for the two-phase frictional multiplier (ϕ_f^2) in mini- and microchannels reported in the literature. The two-phase frictional multiplier is influenced by the choice of the two-phase multiplication factor (C).



(a)



(b)

Figure 6-5: (a) Liquid-phase Reynolds number as a function of exit quality (b) vapor-phase Reynolds number as a function of exit quality

The values of multiplication factors, depending on whether each phase is in turbulent-flow or laminar-flow conditions, for the various flow combinations are shown in Table 6-3.

Uncertainties in the two-phase heat transfer coefficient predictions from the present model may have the following three sources: (1) the transition between the coalescing bubble and the annular flow regimes, (2) estimation of refrigerant physical and thermodynamic properties at the outlet of the test section, and (3) actual dimensions of the channel. The mean absolute error (MAE) and average error (AE) were set as the criterions to determine the effectiveness of the heat transfer model. AE was defined as:

$$AE = \frac{1}{N} \sum_1^N \frac{(\text{experimental data} - \text{predicted data})}{\text{experimental data}} \times 100, \quad (6-45)$$

where N is the total number of data points.

6.3 Model Validation

The validity of the analytical model was assessed by comparing the predicted data of heat transfer coefficients versus experimental results obtained from the literature, as shown in Fig. 6-6. Very good agreement between the experimental results and the predicted values were observed, as only 1% of the data fall out of the error range of $\pm 30\%$. It is found that the experimental two-phase heat transfer coefficients could be predicted by the model with a MAE of 10%. The model successfully predicts the experimental data set of Lee and Lee (2001b) and Dong et al. (2008) and with a MAE of 5.7% and 7%, respectively. The heat transfer coefficient in the latter dataset has a maximum uncertainty of 3.2%. The data of Agostini et al. (2008a) are also well predicted by this model, as shown in Fig. 6-6 with a MAE of 10%.

Table 6-2: Void fraction correlations for mini- and microchannels.

Authors	Channel Size (μm)	Void fraction correlation	Refrigerants
Ali et al. (1993)	Minichannels $D_h = 1000$	$\alpha = 0.8\beta$	R113, R410A
Xiong and Chung (2007)	Microchannels $D_h = 209, 412, \text{ and } 622$	$\alpha = \frac{c\beta^{0.5}}{1 - (1 - C)\beta^{0.5}}$ $c = \frac{0.266}{1 + 13.8 \cdot e^{-6.88D_h}}$ <p>where the unit of D_h is mm.</p>	FC-72, R123, R141b
Kawahara et al. (2005)	Microchannels $D = 100$	$\alpha = \frac{C_1\beta^{0.5}}{1 - C_2\beta^{0.5}}$ $C_1 = 0.03 \text{ and } C_2 = 0.97$	R123, R141b, R134, R236fa

Table 6-3: Two-phase frictional multiplier for mini- and microchannels.

Reference	Fluid	D_h (μm)	G ($\text{kg}/\text{m}^2 \cdot \text{s}$)	$x_{e,0}$	Two-phase multiplication factor
laminar liquid – laminar/turbulent vapor:					
Lee and Garimella (2008)	Water	160-538	209-896	0-0.2	$\phi_f^2 = 1 + \frac{C_{vv}}{X_{vv}} + \frac{1}{X_{vv}^2}$ $X_{vv} = \left(\frac{\mu_L}{\mu_g} \right)^{0.5} \left(\frac{1-x_e}{x_e} \right)^{0.5} \left(\frac{v_L}{v_g} \right)^{0.5}$ $C_{vv} = 2566G^{0.5466} D_h^{0.8819} (1-e^{-319D_h})$
laminar liquid - turbulent vapor:					
Lee and Mudawar (2005a)	R134a and water	349	127-654	0.49-1	$\phi_f^2 = 1 + \frac{C_{vt}}{X_{vt}} + \frac{1}{X_{vt}^2}$ $X_{vt} = \left(\frac{f_L Re_g^{0.25}}{0.079} \right)^{0.5} \left(\frac{1-x_e}{x_e} \right)^{0.5} \left(\frac{v_L}{v_g} \right)^{0.5}$ $C_{vt} = 1.45 Re_{fo}^{0.25} We_{fo}^{0.23}$

The model over-predicts the FC-72 data sets from Megahed et al. (2008) by 14%. The experimental data points of Bertsch et al. (2008b) have the maximum deviation and are under-predicted by the model by 26%. This experiment was conducted using R134a. The detailed results of this comparison are summarized in Table 6-4.

The conditions of the test by Megahed et al. (2008) obtained at $q = 25 \text{ kW/m}^2$ and $G = 391 \text{ kg/m}^2\cdot\text{s}$ using FC-72 are very similar to those of the test by Yen et al. (2006), carried out at $q = 25.3 \text{ kW/m}^2$ and $G = 400 \text{ kg/m}^2\cdot\text{s}$ using R123. In both experiments, the saturation pressures for FC-72 and R123 were almost equal, at atmospheric conditions, while the corresponding saturation temperatures were $56 \text{ }^\circ\text{C}$ and $28 \text{ }^\circ\text{C}$, respectively. However, the experimental heat transfer coefficients obtained by Yen et al. are two times larger at low exit quality ($x_{e,o} < 0.2$). For higher values of exit quality ($x_{e,o} > 0.2$), the experimental values of the two-phase heat transfer coefficient are almost equal. The experimental data uncertainty of Megahed et al. is much larger than that of Yen et al., being 15% and 10%, respectively. The agreement in heat transfer coefficients, for $x_{e,o} > 0.2$, can be attributed to the difference in vapor density and latent heat of vaporization. Comparing the thermophysical properties of FC-72 and R123 at atmospheric conditions, it is observed that the two refrigerants have almost the same parameter values for liquid density, viscosity, thermal conductivity, and vapor viscosity. However, FC-72 has a vapor density and liquid thermal conductivity about two times higher than R123 at the same saturation pressure. The two-phase heat transfer coefficient is inversely proportional to the vapor density and the latent heat of vaporization, as shown in Eqn. (6-41). The higher vapor density of FC-72 may contribute to a higher acceleration pressure drop.

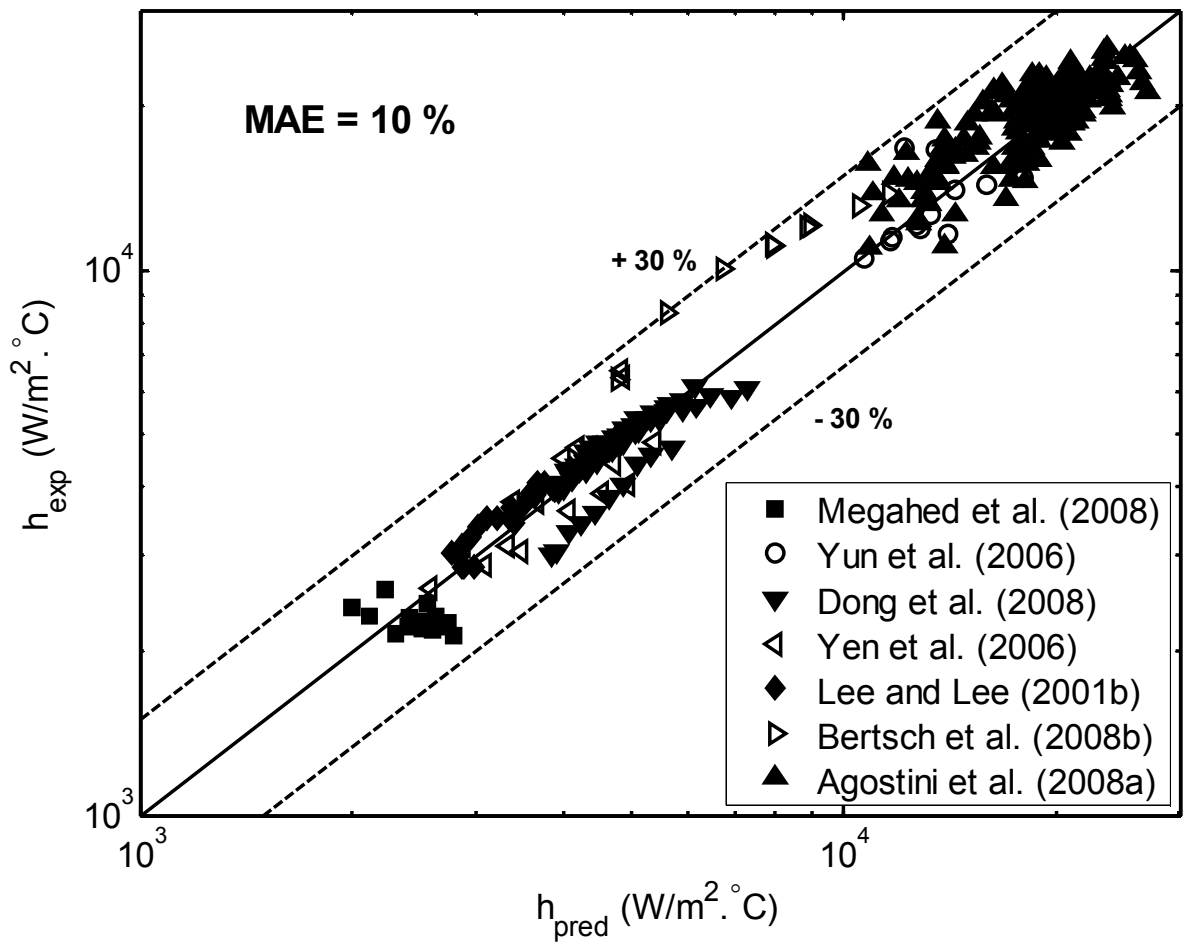


Figure 6-6: Predicted and experimentally determined two-phase heat transfer coefficient.

Table 6-4: MAE and AE between the experimental data and the predicted results
for the present model.

Reference	Data points	MAE (%)	AE (%)
Megahed et al. (2008)	14	14	8.5
Yun et al. (2006)	15	11	3.5
Dong et al. (2008)	55	7.0	3.6
Yen et al. (2006)	16	11.9	0.45
Lee and Lee (2001b)	25	5.7	-5.1
Bertsch et al. (2008b)	9	26.2	-26.2
Agostini et al. (2008a)	159	10	-2
Total	292	10	-1

It is also noted that R123 has a latent heat of vaporization about two orders of magnitudes higher than FC-72 at atmospheric conditions. These physical properties can explain the qualitative agreement in the experimental results.

The effectiveness of the presented analytical model to correctly predict the two-phase heat transfer coefficient trend in rectangular mini and microchannels is assessed through comparison with experimental results. Results obtained using the proposed model are compared to the experimental results obtained by Lee and Lee (2001b) and Yun et al. (2006) as shown in Fig. 6-7. The tests conducted by Lee and Lee and Yun et al. were carried out in minichannels at a higher hydraulic diameter and relatively low heat and mass fluxes, as was presented in Table 6-1. The predicted results are well correlated with experimental values, and show that as the exit quality increases, the heat transfer coefficient increases. On the other hand, a completely different behavior for the heat transfer coefficient is observed in the data of Dong et al. (2008) and Yen et al. (2006), as shown in Fig. 6-8. These data present a smooth and constantly decreasing heat transfer coefficient with increasing vapor quality. Nevertheless, the present model predicts the appropriate trend of the heat transfer coefficient with exit quality increase. Recently, Agostini et al. (2008a) presented an experimental study of R236fa flow boiling in microchannels. The researchers reported that the two-phase heat transfer coefficients remain almost constant for the boiling region up to an exit quality of about 0.3. At constant heat and mass fluxes, the measurements reported by Agostini et al. showed very small variations for the heat transfer coefficient through the vapor quality range. Figure 6-9 presents the two-phase heat transfer coefficient experimental data obtained by Agostini et al. and those predicted by the proposed model. It is clear that the current

model also follows the correct trend of the experimental data for the two-phase heat transfer coefficient.

In comparison with published experimental datasets, the model is shown to well predict the experimental data of Yun et al. (2006) and Yen et al. (2006) using refrigerants R410A and R123 in mini- and microchannels with hydraulic diameters of 1440 and 214 μm , respectively. Figures 6-7(b) and 6-8(b) show the heat transfer coefficient as a function of exit quality for the same mass flux and comparable heat flux. In the R410A data of Yun et al., the heat transfer coefficient is shown to increase with increasing exit quality. On the other hand, experimental results of Yen et al. show a contrary trend of heat transfer coefficient. It was found to decrease with increasing exit quality as presented in Fig. 6-8(b). Therefore, the two data sets presented in Figs. 6-7(b) and 6-8(b), of constant mass flux held at $G = 400 \text{ kg/m}^2\cdot\text{s}$ and heat flux maintained at $q = 20$ and 25.32 kW/m^2 , have been selected to explain the different trends of flow boiling heat transfer coefficient in mini- and microchannels. The solution for the two-phase heat transfer coefficient, Eqn. (6-41), is dependent on fluid properties, channel geometry, heat flux, void fraction, two-phase frictional multiplier, and mass flux. Equation (6-41) can be simplified to provide a form that is suitable to carefully examine the contribution of each term to the estimated heat transfer coefficient. The two-phase heat transfer coefficient, Eqn. (6-41), can be expressed by a function of three terms as

$$h_{\text{tp}} = f_1(f_2 - f_3) , \quad (6-46)$$

where

$$f_1 = \frac{k_L(1-\alpha)A_{\text{ch}}}{\mu_L(1-x_{\text{e,o}})S_{\text{ch}}} = \text{Constant} \frac{(1-\alpha)}{(1-x_{\text{e,o}})} , \quad (6-47)$$

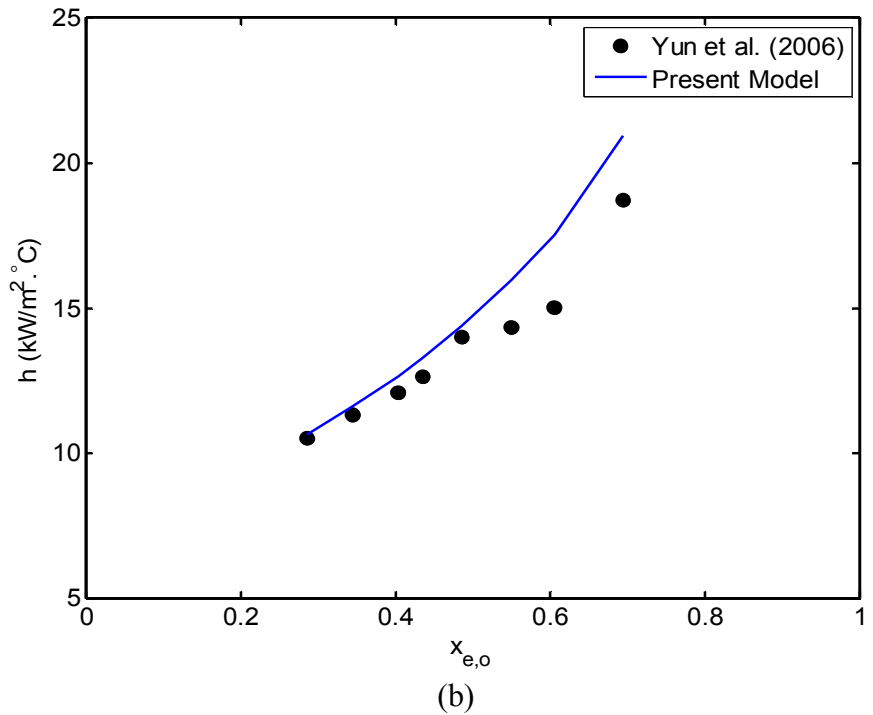
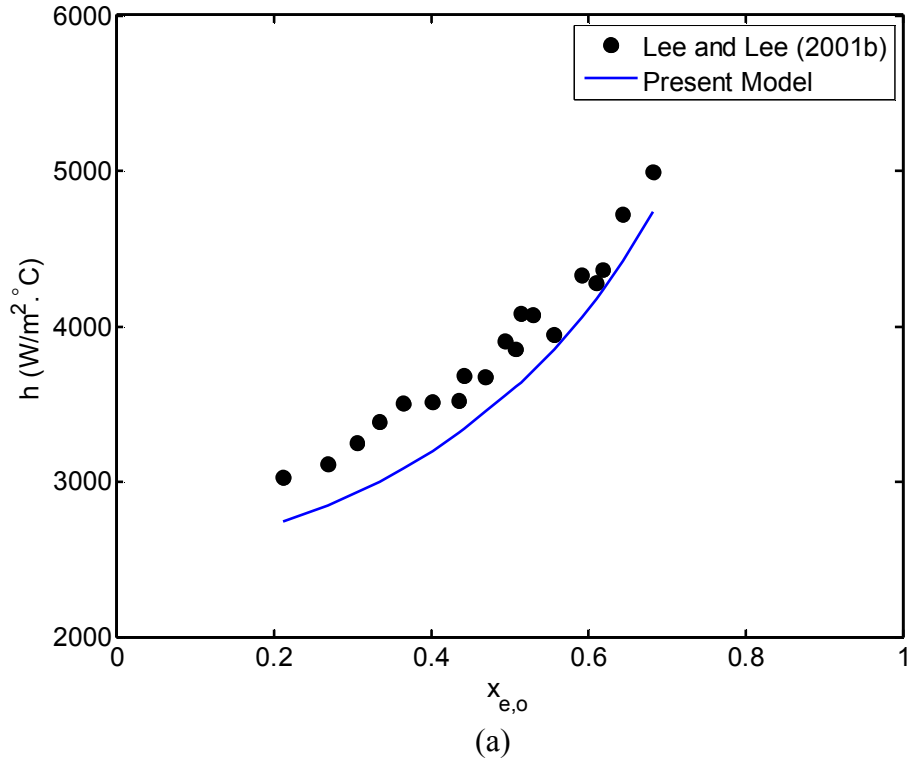


Figure 6-7: Comparison of heat transfer coefficient at constant mass flux: (a) Lee and Lee (2001b), R113, $G = 208$ kg/m².s, $q = 5$ kW/m². (b) Yun et al. (2006), R410A, $G = 400$ kg/m².s, $q = 20$ kW/m².

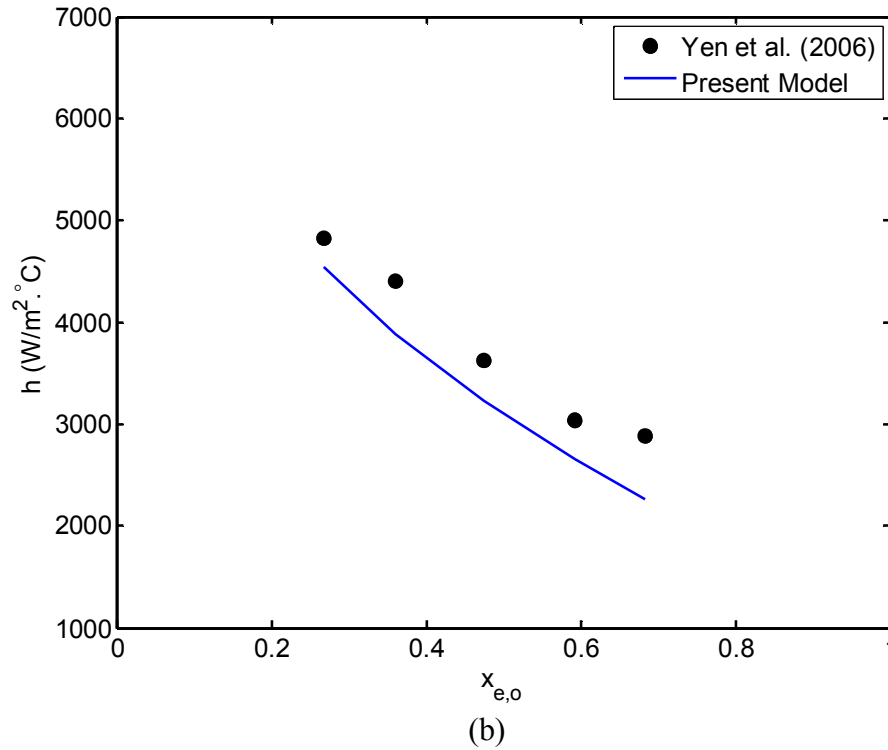
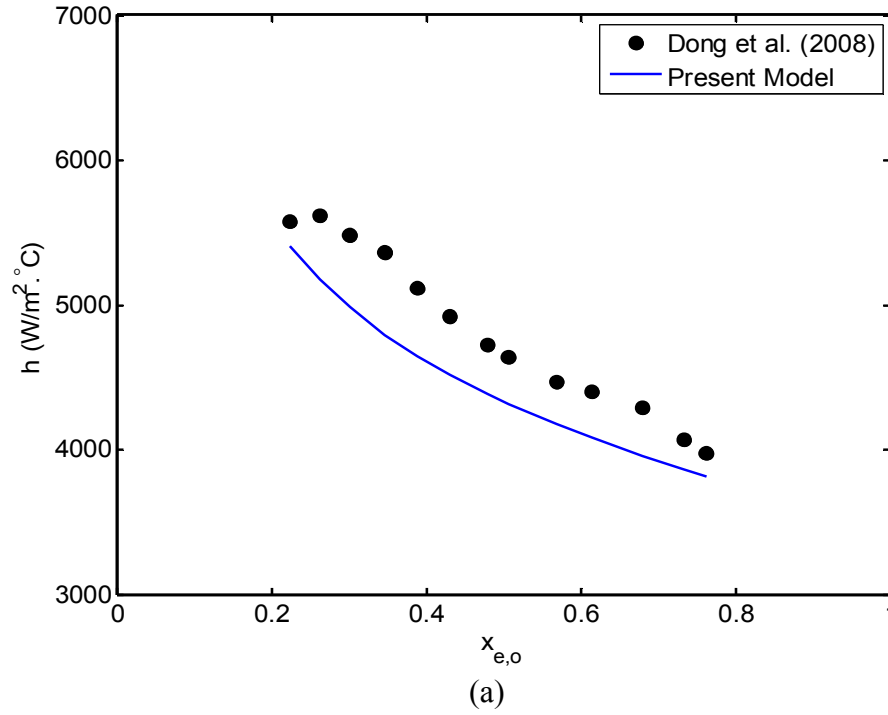


Figure 6-8: Heat transfer coefficient predictions by the analytical model compared with:
 (a) Dong et al. (2008), R141b, $G = 500 \text{ kg/m}^2 \cdot \text{s}$, $q = 100 \text{ kW/m}^2$ and (b) Yen et al. (2006),
 R123, $G = 400 \text{ kg/m}^2 \cdot \text{s}$, $q = 25.32 \text{ kW/m}^2$

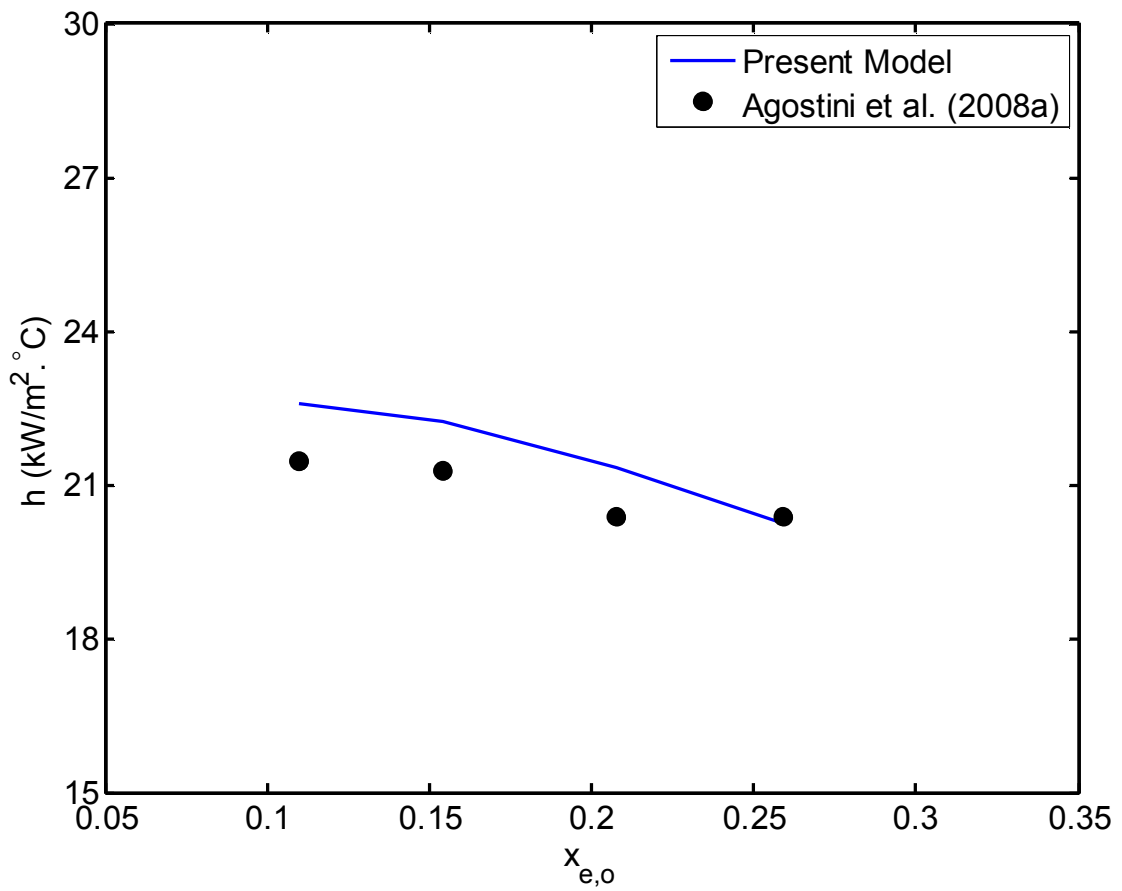


Figure 6-9: Two-phase heat transfer coefficient as a function of exit quality predicted by the analytical model compared with Agostini et al. (2008a) data, R236fa, $G = 984$ kg/m².s.

$$f_2 = \frac{2\phi_f^2 f_L G(1-x_{e,o})^2}{D_h}, \quad (6-48)$$

and

$$f_3 = \frac{(1-\alpha)q_w \left(\frac{2}{\gamma} + 1 \right)}{h_{fg}} \left(-2x_{e,o} \left(-\frac{v_g}{v_L} + 1 + \varepsilon \right) + \varepsilon \right), \quad (6-49)$$

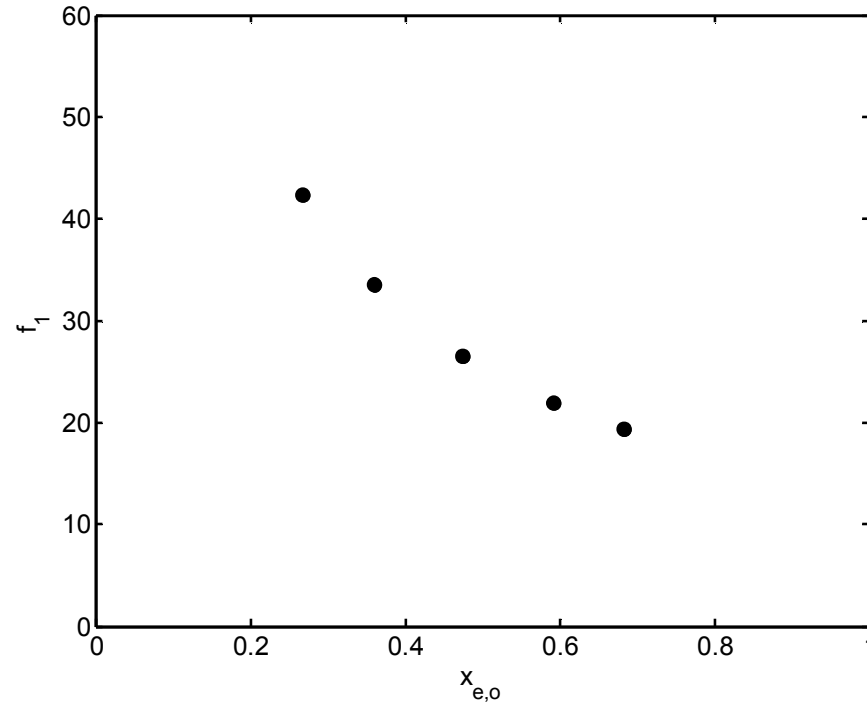
The first term, f_1 , represents the effect of the void fraction. The second and third terms, f_2 and f_3 , account for the effect of the frictional and acceleration pressure gradients, respectively. In this case, the annular two-phase flow heat transfer coefficient is expressed in terms of void fraction, frictional, and acceleration pressure gradients. In order to illustrate the contributions of each of the three terms in comparison to the model, the results are plotted in Figs. 6-10 and 6-11 as a function of exit quality to provide a quantitative measure of the importance of each term, which explain the different trends in heat transfer coefficients observed during flow boiling in mini- and microchannel heat sinks. Table 6-5 shows a comparison of thermophysical properties and channel geometry used in the experiments by Yen et al. (2006) and Yun et al. (2006). For test results of Yen et al., the contribution of the f_2 term can be seen to increase asymptotically with exit quality. Meanwhile, the contribution of the f_3 term is shown to increase linearly with increasing exit quality. Based on the ratio of f_2/f_3 , the acceleration component, f_3 , cannot be neglected as compared to the frictional component f_2 (Fig. 6-10(b) and (c)). Another important aspect in explaining the experimental heat transfer coefficients in the data by Yen et al. is the change of void fraction with respect to exit quality (f_1 term). The ratio of $(1-\alpha)/(1-x_{e,o})$ decreases steeply with the increase in quality as illustrated in Fig. 6-10(a). Hence, the sum of the contributions of the above-mentioned terms explains the decreasing trend of the experimental heat transfer coefficient. The frictional pressure gradient, f_2 term, is relatively independent of the vapor quality in the experimental data of

Yun et al. as shown in Fig. 6-11(b). However, it dominates the pressure gradient where the effect of acceleration pressure gradient, f_3 term, could be ignored compared to f_2 (Fig. 6-11(c)). However, contrary to microchannel behavior, the ratio of $(1-\alpha)/(1-x_{e,o})$ is shown to increase with increasing exit quality as presented in Fig. 6-11(a). As a result, the contribution of the void fraction term, f_1 , attributes to increase the estimated heat transfer coefficient with increasing exit quality. It can be noticed that the acceleration term (f_3) of R410A is much lower than that of R123. This effect is probably due to the small difference in density of the two phases of R123 ($\rho_L/\rho_g = 6.4$) compared with R410A ($\rho_L/\rho_g = 35.9$). For a constant mass flux, a higher vapor density yields a lower flow velocity, and then further results in a lower acceleration pressure drop.

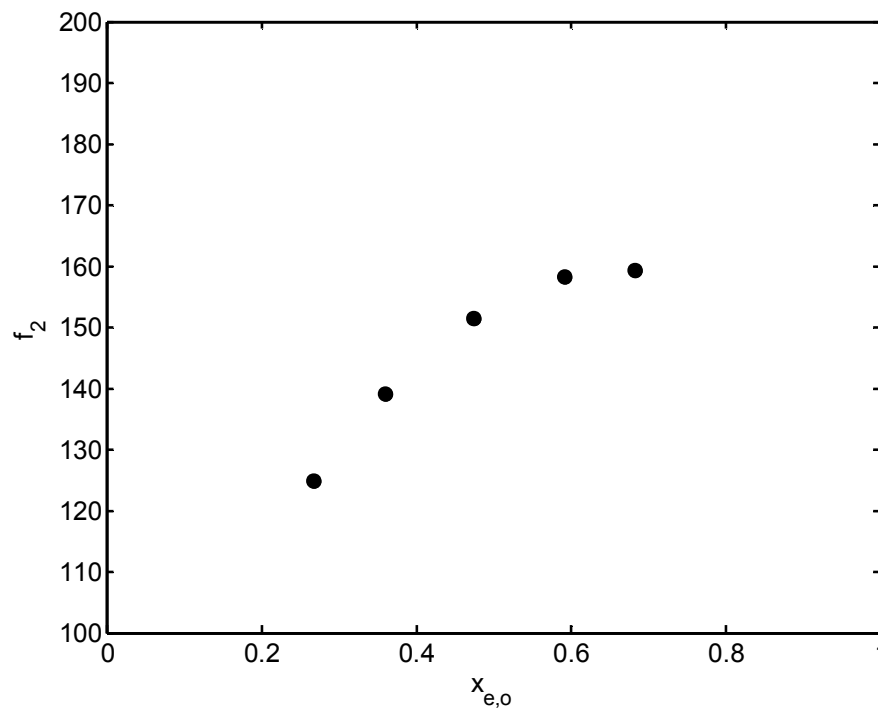
The effect of mass flux on the predicted results for the heat transfer coefficient is examined using the experimental results presented by Dong et al. (2008). Figure 6-12 presents the measured values along with the predicted values as a function of exit quality at a constant heat flux of 100 kW/m^2 and a mass flux which varies from 500 to 900 $\text{kg/m}^2\cdot\text{s}$. The model is in excellent agreement with the experimental results and is sensitive to change in mass flux. Another comparison with the model predictions for local heat transfer coefficient versus vapor quality for various mass fluxes is depicted in Fig. 6-13 for the data of Agostini et al. (2008a). This figure is also included to demonstrate the effect of mass flux on the prediction. The model prediction is highly sensitive to change in mass flux, as shown in the figure.

Table 6-5: A comparison of refrigerant's physical properties and channel geometry used in Yun et al. (2006) and Yen et al. (2006) experiments.

Parameter	Yun et al.	Yen et al.
Refrigerant	R410A	R123
ρ_L / ρ_g	32.2	227
k_L / μ_L (m ² /s ² °C)	646.6	189.2
h_{fg} (J/kg)	216318	170350
A_{ch} / S_{ch} (m)	3.6×10^{-4}	5.4×10^{-5}

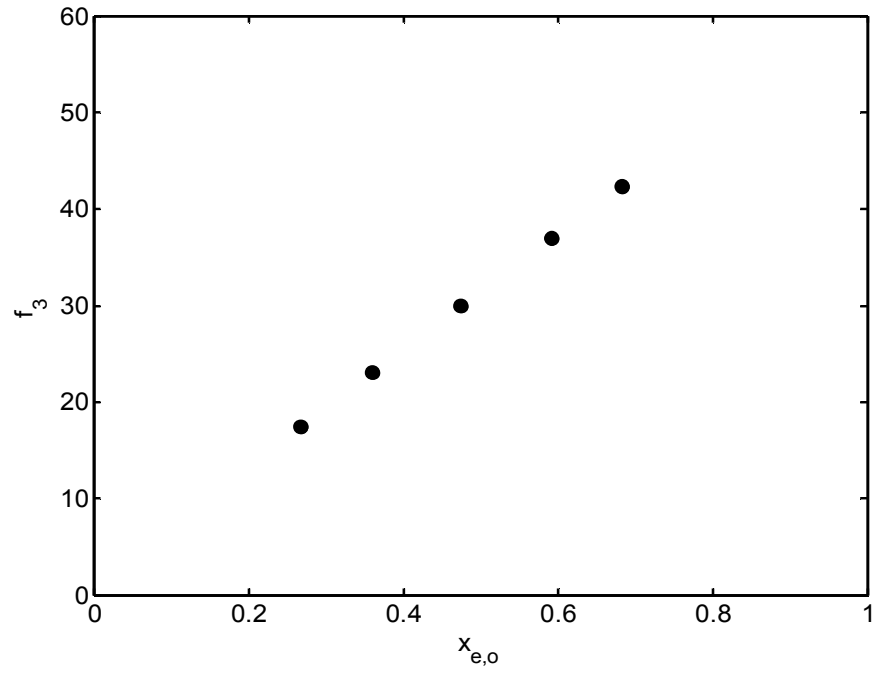


(a)



(b)

Figure 6-10: Contributions of f_1 , f_2 and f_3 terms to the estimated heat transfer coefficient, data of Yen et al. (2006), R123, $G = 400 \text{ kg/m}^2 \cdot \text{s}$, $q = 25.32 \text{ kW/m}^2$.



(c)
Figure 6-10: (*continued*)

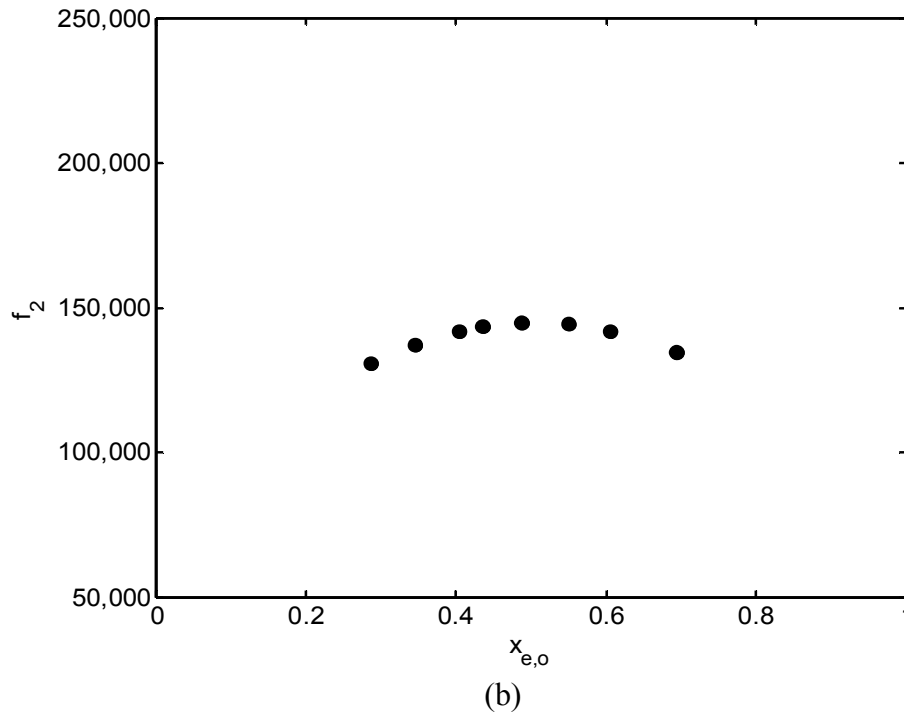
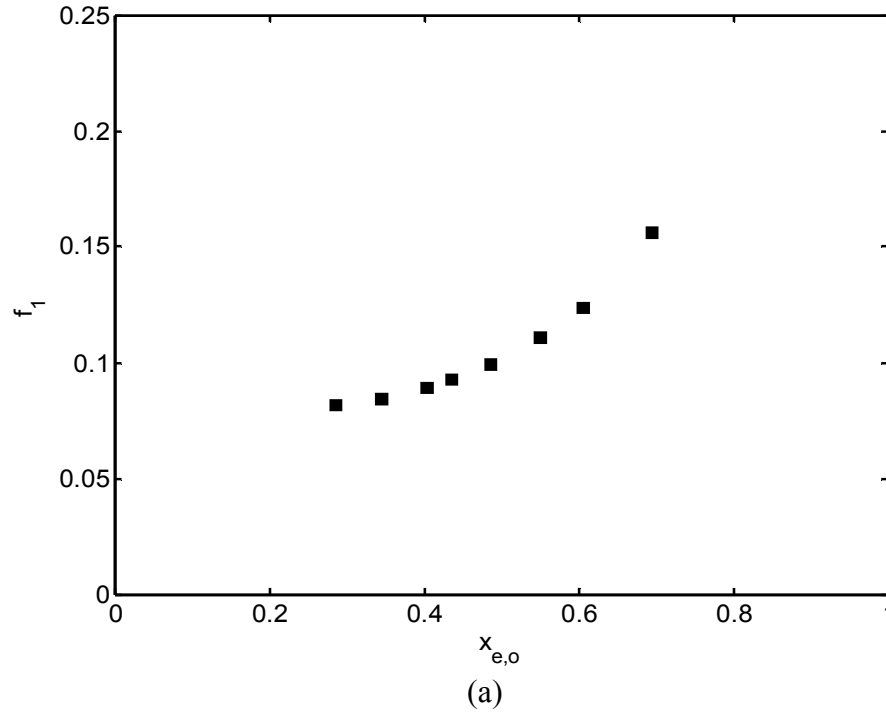
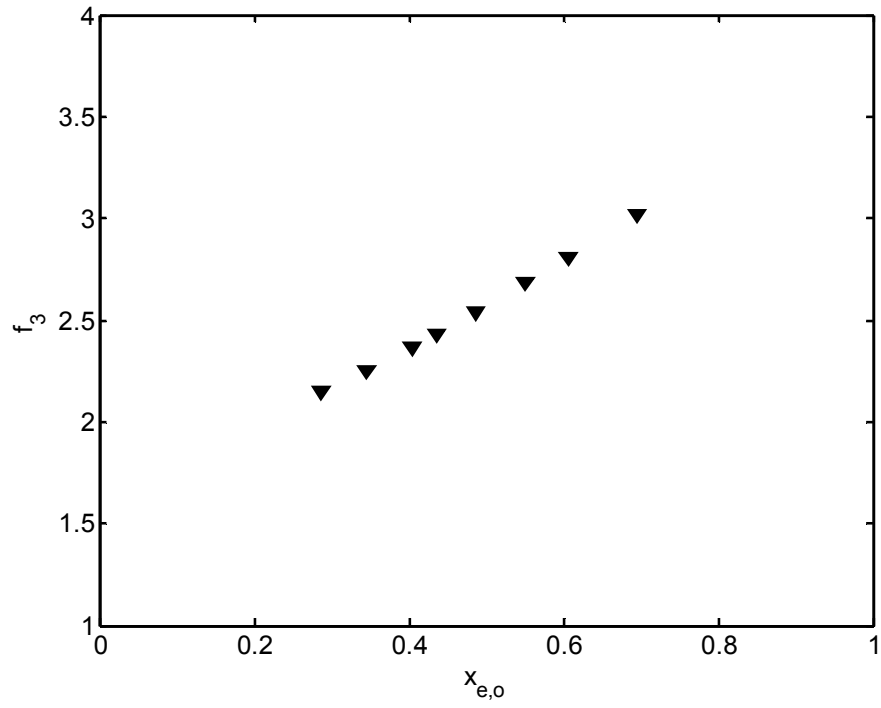


Figure 6-11: Contribution of different terms representing the predicted heat transfer coefficient, data of Yun et al. (2006), R410A, $G = 400 \text{ kg/m}^2 \cdot \text{s}$, $q = 20 \text{ kW/m}^2$.



(c)
Figure 6-11: (*continued*)

The predicted two-phase heat transfer coefficient as a function of exit quality are compared with those obtained from the experiment of Dong et al. (2008) at a constant mass flux of $900 \text{ kg/m}^2\cdot\text{s}$ and a heat flux which varies from 75 to 100 kW/m^2 , as shown in Fig. 6-14. While the data obtained by Dong et al. showed that the heat flux significantly influences the heat transfer coefficient over the range of exit quality investigated in their study, the predicted results do not correspond to the experimental results and are not well predicted by the model. The effect of the heat flux on the experimental heat transfer coefficient becomes smaller as the exit quality is increased. The data are over-predicted at low heat flux and under-predicted as the heat flux increases. As shown in the same figure, the prediction is better at higher heat flux values. On the other hand, the model predictions show very good agreement with the experimental data presented by Agostini et al. at a constant mass flux of $810 \text{ kg/m}^2\cdot\text{s}$ and different heat fluxes, varying from 201 to 456 kW/m^2 , as shown in Fig. 6-15. The heat transfer coefficient was seen to increase at first as the heat flux increased, and then decreased sharply as the exit quality increased for a constant heat and mass fluxes. The ability of the model to map the correct trends of the heat transfer coefficient with changing heat flux can be clearly seen.

In order to demonstrate the dependence of the model predictions on the saturation temperature, the predicted results from the model were combined with the experimental results of Agostini et al. (2008a), as presented in Fig. 6-16. It should be noted that varying the saturation temperature over the range 14 to $19 \text{ }^\circ\text{C}$ can result in changes of heat transfer coefficient of 40% as shown in the figure. Nonetheless, the model provides very good agreement for the experimental data over the examined range of saturation

temperatures, and the influence of saturation temperature changes on the predicted heat transfer coefficient was found to be consistent with experimental results.

6.4 Model Limitations

A comparison between predictions of the model and experimental data of Steinke and Kandlikar (2004), Bertsch et al. (2009b), and Agostini et al. (2008b) showed an under-prediction of the heat transfer coefficient. The under-prediction is due mainly to the fact that the void fraction correlations proposed by Xoing and Chung (2007) and Kawahara et al. (2005) significantly over-predict all the tested data for water and refrigerant R245. The over-predicted values of the void fraction mean that dry out took place in the channel, and annular flow does not exist. At low liquid superficial velocities, if the superficial velocity of the gas is high enough, the annular flow pattern will be formed. Consequently, a low liquid superficial velocity gives a higher volumetric quality that leads to a void fraction close to unity even at moderate values of exit quality. As a result, over-predicted values of void fraction highly under-predicted values of the heat transfer coefficient, as suggested by Eqn. (6-41), which affects the model applicability. These results suggest the need for further development of void fraction correlations in microchannels and to consider refrigerant physical properties in future correlations, which would result in extending the applicability of the present model to include many refrigerants. In addition, the present model has been limited to annular laminar/transition liquid phase flow in rectangular mini- and microchannels.

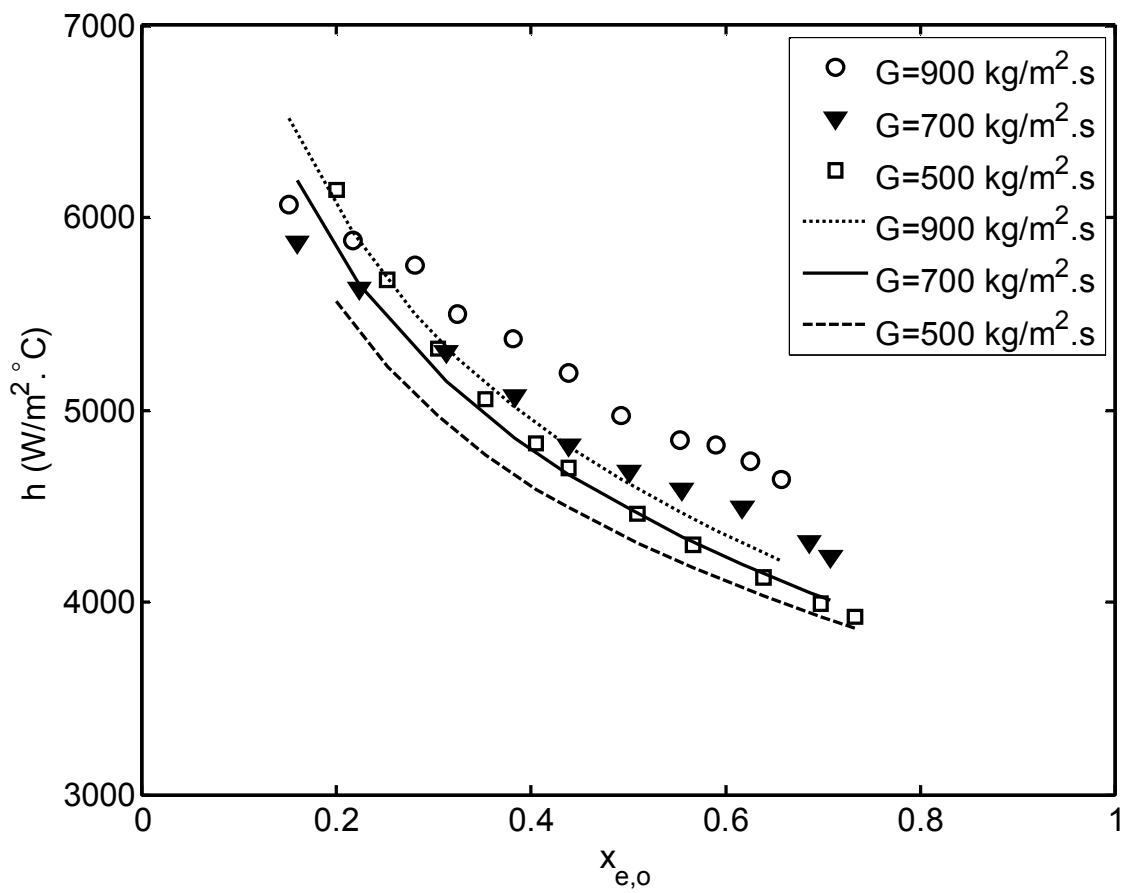


Figure 6-12: The effect of mass flux on the experimental and predicted heat transfer coefficient, experimental data of Dong et al. (2008), $q = 100 \text{ kW/m}^2$.

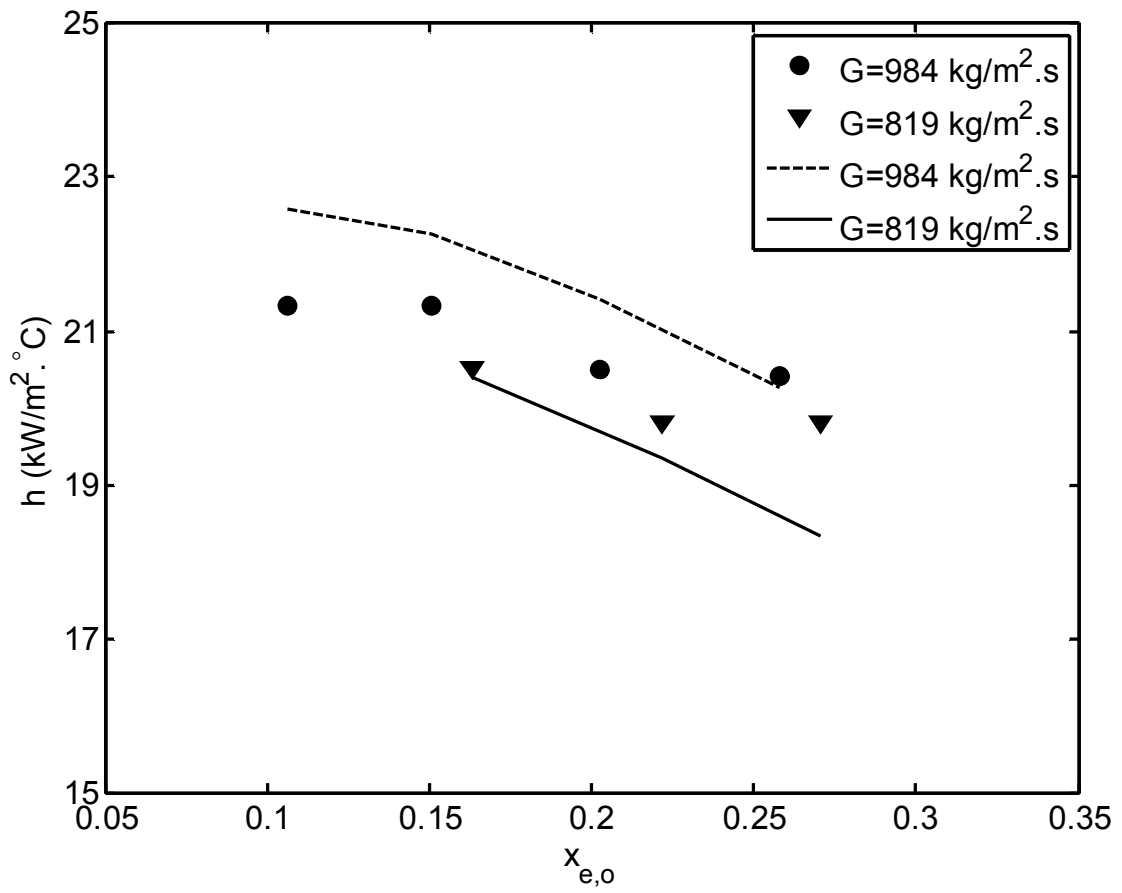


Figure 6-13: The dependence of the predicted two-phase heat transfer coefficient on the exit quality for different mass fluxes, data of Agostini et al. (2008a) $q = 236 \text{ kW/m}^2$.

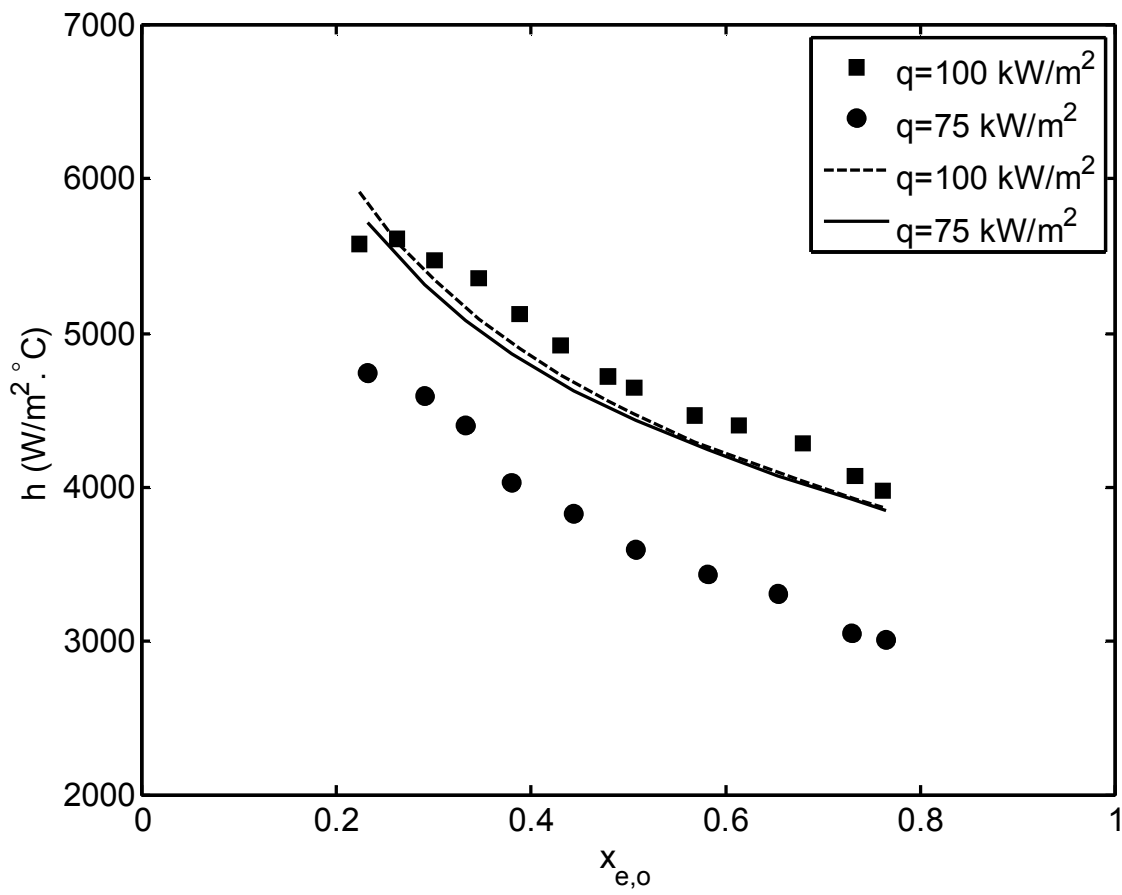


Figure 6-14: Comparison between the present model and the experimental results by Dong et al. (2008) for the variation of the heat flux for $G = 500$ kg/m 2 .s.

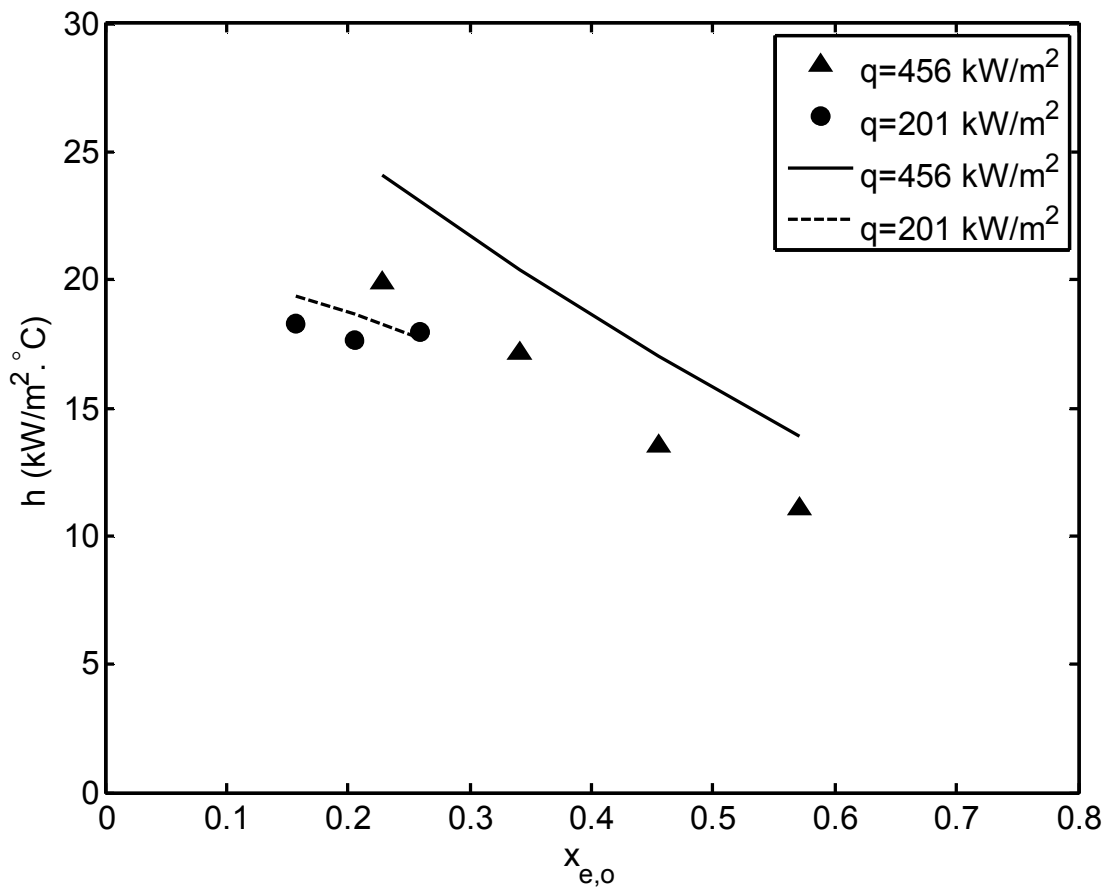


Figure 6-15: Predicted influence of heat flux on the two-phase heat transfer coefficient as a function of exit quality, comparing with experimental data of Agonstini et al. (2008a) $G = 810 \text{ kg/m}^2\cdot\text{s}$.

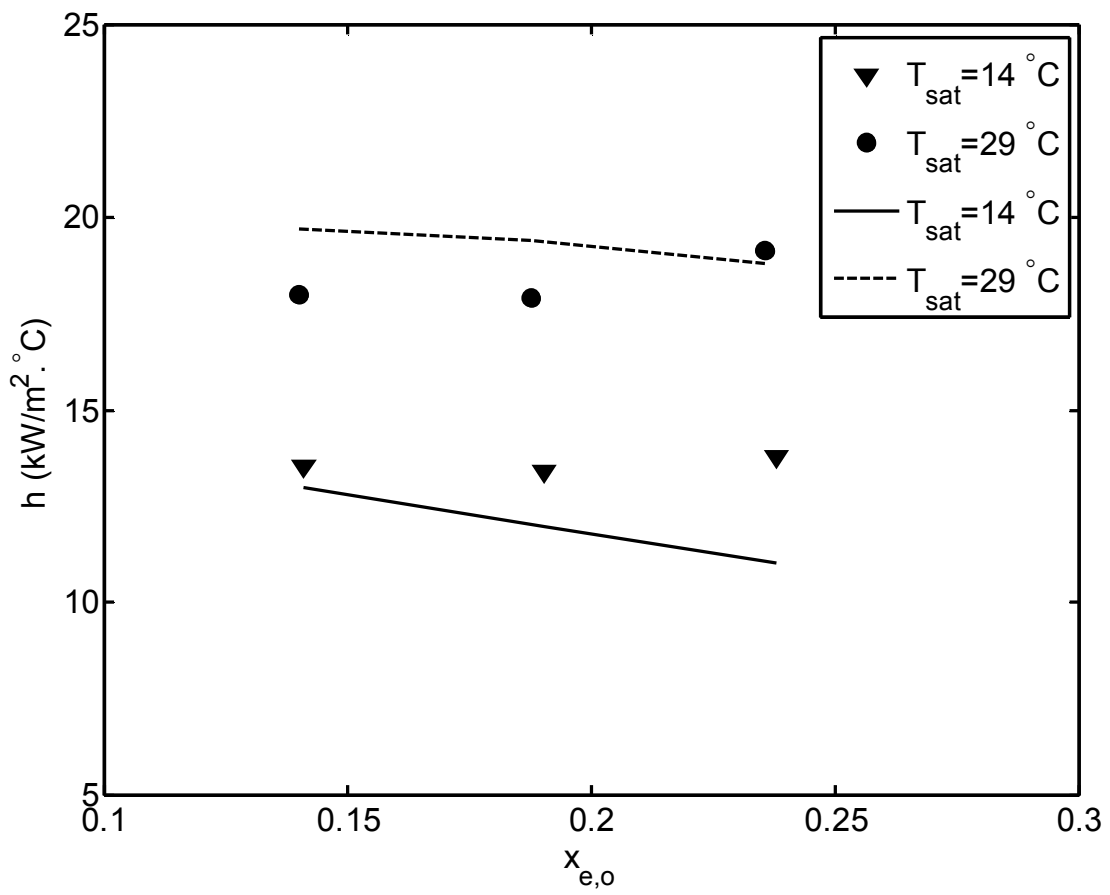


Figure 6-16: Effect of saturation temperature on the two-phase heat transfer coefficient, analytical predictions versus experimental data of Agostini et al. (2008a), $G = 810 \text{ kg/m}^2 \cdot \text{s}$ and $q = 18.6 \text{ kW/m}^2$.

6.5 Conclusions

An analytical model has been developed to predict the flow boiling heat transfer coefficient in the annular flow regime in rectangular mini- and microchannels. The Reynolds' analogy has been used to develop the analytical model. The model takes into account the frictional and acceleration pressure drops in the liquid phase as well as the wall and interfacial shear stress. The model provides a convenient and effective method for calculating the two-phase heat transfer coefficient based on the void fraction, frictional multiplier, two-phase flow thermophysical properties, and flow conditions. Predictions from the analytical model show excellent agreement with experimental data published in the open literature. For flow boiling in mini- and microchannels with uniform heat fluxes over the examined range of aspect ratios, heat and mass fluxes, the agreement between experimental and analytical results is within 10%. The model predicted the correct trends of the heat transfer coefficient variation with exit quality. This model proved to have a very good adaptability in predicting the flow boiling heat transfer coefficient during annular flow for different mass fluxes, heat fluxes, and saturation temperatures. It can also be used for predicting the heat transfer coefficient during annular flow boiling in narrow mini- and microchannels with very low aspect ratios.

CHAPTER 7

EXPERIMENTAL INVESTIGATION OF FLOW BOILING CHARACTERISTICS IN CROSS-LINKED MICROCHANNEL HEAT SINKS

This chapter experimentally investigates flow boiling characteristics in a cross-linked microchannel heat sink at low mass fluxes and high heat fluxes. Three cross-links, of width 500 μm , were introduced in the present microchannel heat sink to achieve better temperature uniformity and to avoid flow mal-distribution. Flow visualization, flow instability, two-phase pressure drop, and two-phase heat transfer measurements were conducted for the range of heat flux from 7.2 to 104.2 kW/m^2 , mass flux from 99 to 290 $\text{kg/m}^2\cdot\text{s}$, and exit quality from 0.01 to 0.71.

7.1 Test Matrix

A test matrix was devised to study the flow boiling characteristics of a cross-linked microchannel heat sink through a series of experiments. These characteristics are: effect of cross-links, flow instability, two-phase pressure drop, and two-phase heat transfer characteristics. The full test matrix for this study and details of the studied parameters are summarized in Table 7-1 and Fig. 7-1. The test matrix for the effect of cross-links was designed to visualize flow characteristics within the cross-link at a constant mass flux and heat flux, but at different locations. Six different locations (*I-1* to *I-23* and *II-1* to *II-23*) were introduced to analyze the flow characteristics in cross-links. The second flow visualization experiment was performed to investigate the effect of cross-links on flow

distribution in different sections of the heat sink in terms of mass flux, heat flux, and exit quality. The flow distribution was also examined at six selected different locations as presented in Table 7-1 and Fig. 7-1. The mass flux and exit quality range from 109 to 195 $\text{kg/m}^2\cdot\text{s}$ and 0.2 to 0.4, respectively. Two-phase flow instability measurements were studied for three different mass and heat fluxes. For the two-phase pressure drop and heat transfer experiments, a total of six different mass fluxes, ranging from 99 to 290 $\text{kg/m}^2\cdot\text{s}$, were investigated for which the exit quality varied from 0.01 to 0.71. Measurements were made at a series of mass fluxes with a constant inlet subcooling temperature of 4 °C.

7.2 Flow Visualization

The flow visualization results were used to obtain a better insight regarding the flow characteristics in the cross-link at $G = 109 \text{ kg/m}^2\cdot\text{s}$ and $x_{e,o} = 0.2$. As shown in Fig. 7-2(a), at position *I-23* (see Fig. 7-1), as the bubble is swept to the cross-link, the bubble is seen to rapidly expand in both directions of the cross-link before it experiences channel confinement again. Thereafter, the bubble goes through several cycles of expansion and contraction caused by the inlet and outlet of the channels as it is conveyed down the channel by the forced flow. In Fig. 7-2(b) at position *I-12*, the confined bubble is spread out swiftly in the lateral direction. At the same time, a part of the bubble moves away from the channel centerline in the direction of the channels of the lowest mass flux. In Fig. 7-2(c) at position *I-1*, the vapor bubble gradually expands where a thin layer of liquid is seen trapped between the bubbles. As soon as the confined bubbles expand, the liquid in the slugs between the bubbles begins to shrink because the expanded bubble occupies the cross-link channel. Similar flow pattern configurations have been observed at locations *II-1*, *II-12*, and *II-23*.

Table 7-1: Cross-linked microchannel heat sink test matrix

Case study	Locations/Parameter(s)	G (kg/m ² .s)	q (kW/m ²)	$x_{e,o}$
Flow Instability	P_{in} , T_{out} , and G	105 - 201	24 - 46	0.1 - 0.3
Effect of cross-links	$I-1$, $I-12$, $I-23$	105	24	0.2
	$II-1$, $II-12$, $II-23$			
Flow regimes and flow distribution	$A-1$, $A-12$, $A-23$	109 - 195	37 - 69.6	0.2 - 0.4
	$B-1$, $B-12$, $B-23$			
Two-phase pressure drop	ΔP_{tp}	111 - 290	20.1 - 104.2	0.02 - 0.65
Two-phase heat transfer	h_{tp}	99 - 275	7.2 - 88.8	0.01 - 0.71

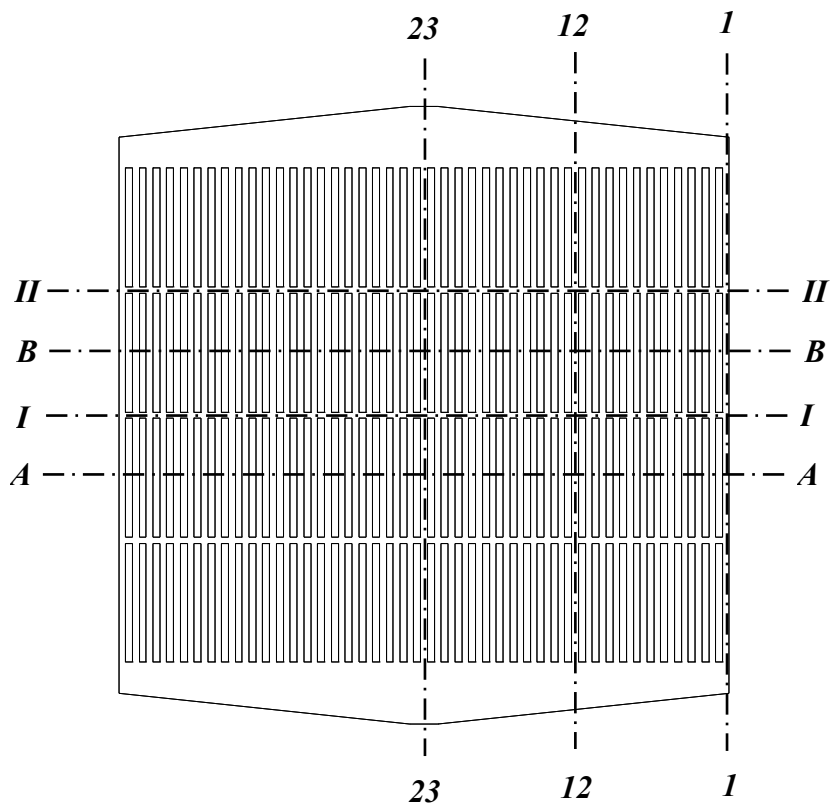


Figure 7-1: Schematic of flow visualization positions.

Flow visualization in the cross-link at position *I-23* indicates the presence of bubbles attached to the cross-link walls as shown in Fig. 7-3. The time is indicated on each frame. The first frame at t_1 , at region *A*, shows the start of the generation of bubbles. The bubbles grow with time due to evaporation, as liquid is converted to vapor at the cross-link wall at $(t_1+0.1 \text{ s})$. The bubbles start to expand and the contact area between the bubbles and the cross-link channel wall becomes the entire side wall of the cross-link. The bubbles expand further and reach their maximum size at $t_1+0.2 \text{ s}$, so the cross-link heated wall is always covered with bubbles. The bubbles are subjected to hydrodynamic instabilities generating intense motions; however, they are still attached to the heated walls due to the effect of surface tension along the interface. Thereafter, the bubbles finally detach from the heated wall under the effect of liquid flow and buoyancy at $t_1+0.5 \text{ s}$, and new bubbles start to grow. On the opposite side of the cross-link, at region *B*, bubbles are aligned with the flow and start to slide along the wall from their nucleation sites before the onset of their separation from the wall due to forced convection flow. The tiny area where the bubble meets the heated wall is of significant importance because the evaporation rate is high and induces a strong local cooling of the heated wall. These flow visualization results are consistent with the results of Dang et al. (2008) in their numerical simulations to explore the effects of cross-links in scaled microchannel heat sinks under adiabatic conditions. Using their numerical results, they were able to clearly demonstrate that circulations exist in the cross-links and in the channels after the flow goes through the cross-links. In region *B* (Fig. 7-3), flow reversal was observed by Dang et al., which tends to draw the bubble downward toward the inner wall. Therefore, the bubble detachment is

delayed, until the buoyancy force overcomes the surface tension force and then the bubble departs.

Qualitative photographs of typical flow patterns observed in the channel segments through the clear Pyrex cover are shown in Figs. 7-4 and 7-5 to investigate the effect of cross-links on flow distribution within the test section. Flow visualization was obtained for heat flux ranges from 37 to 69.6 kW/m², mass flux ranges from 109 to 195 kg/m².s, and vapor quality ranges from 0.2 to 0.4. As shown in Fig. 7-4(a), at a low mass flux ($G = 109 \text{ kg/m}^2\cdot\text{s}$), individual slug bubbles occupying the width of the channel can be seen in the mid-channel at location *A-23* for all examined values of exit quality. At locations *A-1* and *A-12*, the flow pattern is revealed to be slug flow with elongated bubbles and the thickness of the liquid film decreases as the exit quality increases. Figure 7-4(b) shows the flow distribution as a function of positions *B-1*, *B-12*, and *B-23* for a constant mass flux and three different heat fluxes and exit qualities. As the heat flux is increased, the thickness of the trapped liquid layer is observed to decrease and the bubbles start to elongate further (*B-12* and *B-23*). The pattern is seen to exhibit almost the same behavior in the examined channels with increasing exit quality while the mass flux is held constant. In the same figure, the presented images also indicate the absence of an annular flow regime within the section.

Figure 7-5(a) shows bubble shapes observed in experiments at a higher mass flux ($G = 195 \text{ kg/m}^2\cdot\text{s}$). At position *A-23*, two short slug bubbles of almost the same size are seen at $x_{e,o} = 0.3$ and 0.4. The shapes seen in both cases are very similar though not necessarily at the exact same time.

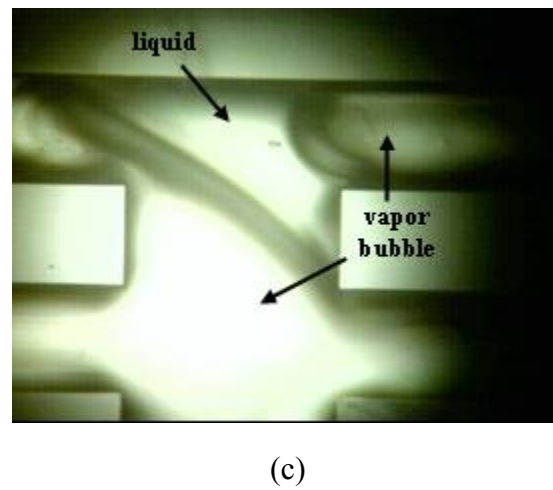
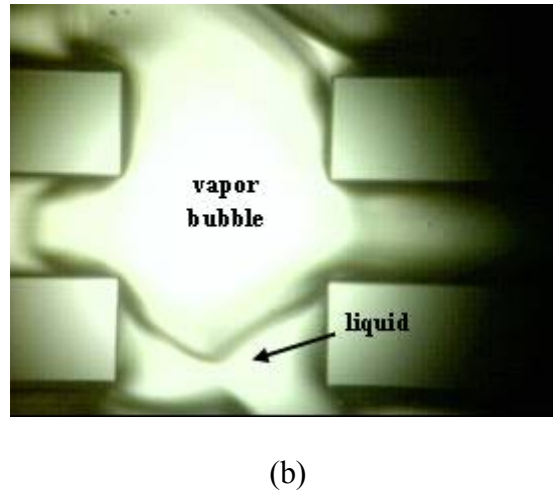
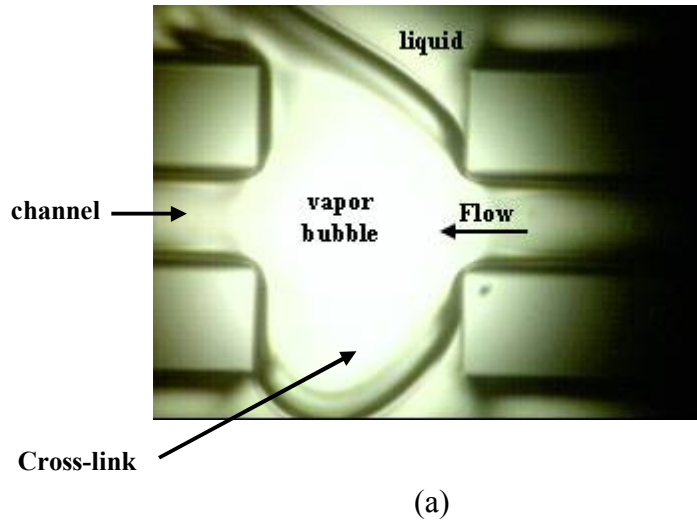


Figure 7-2: Observed flow characteristics within the cross-link, $G = 109 \text{ kg/m}^2 \cdot \text{s}$, $x_{e,0} = 0.2$, at positions: (a) *I-23*, (b) *I-12*, (c) *I-1*

The trapped liquid layer between the bubbles is observed to diminish as exit quality increases. On the other hand, elongated bubbly flow appears in *A-1* and *A-12* as shown in the same figure. Figure 7-5(b) shows the flow visualization in section *B* at $G = 195 \text{ kg/m}^2\cdot\text{s}$. The flow patterns look very similar to those presented in Fig. 7-4(b) within section *A* under the same flow conditions. The constant continuous increase of heat flux results in elongated bubbles, cylindrical in shape, in a continuous slug flow trapping a layer of liquid between them. A notable feature of the slug flow is the bullet-shaped bubbles which can be seen at location *B-23* at different values of exit quality as well as *B-12* at $x_{e,o} = 0.4$.

Flow visualization shows that only one major flow pattern exists in channels namely slug flow for all experiments conducted. Bubbly and annular flow regimes were not detected in the examined range of exit quality, heat and mass fluxes. Flow regime transition from slug to annular flow did not take place in the heat sink sections. This behavior could be attributed to the relatively short sections in the cross-linked design compared to the channel length in the straight channel design and due to the effect of transverse flow within the cross-links.

7.3 Two-phase Pressure Drop

Figure 7-6 presents the two-phase pressure drop (frictional and acceleration) as a function of the exit vapor quality. As shown in the figure, the two-phase pressure drop increases almost linearly with the increase of exit quality at a constant mass flux. It is also clear that the two-phase pressure drop strongly increases with the increase of mass flux at the same exit quality.

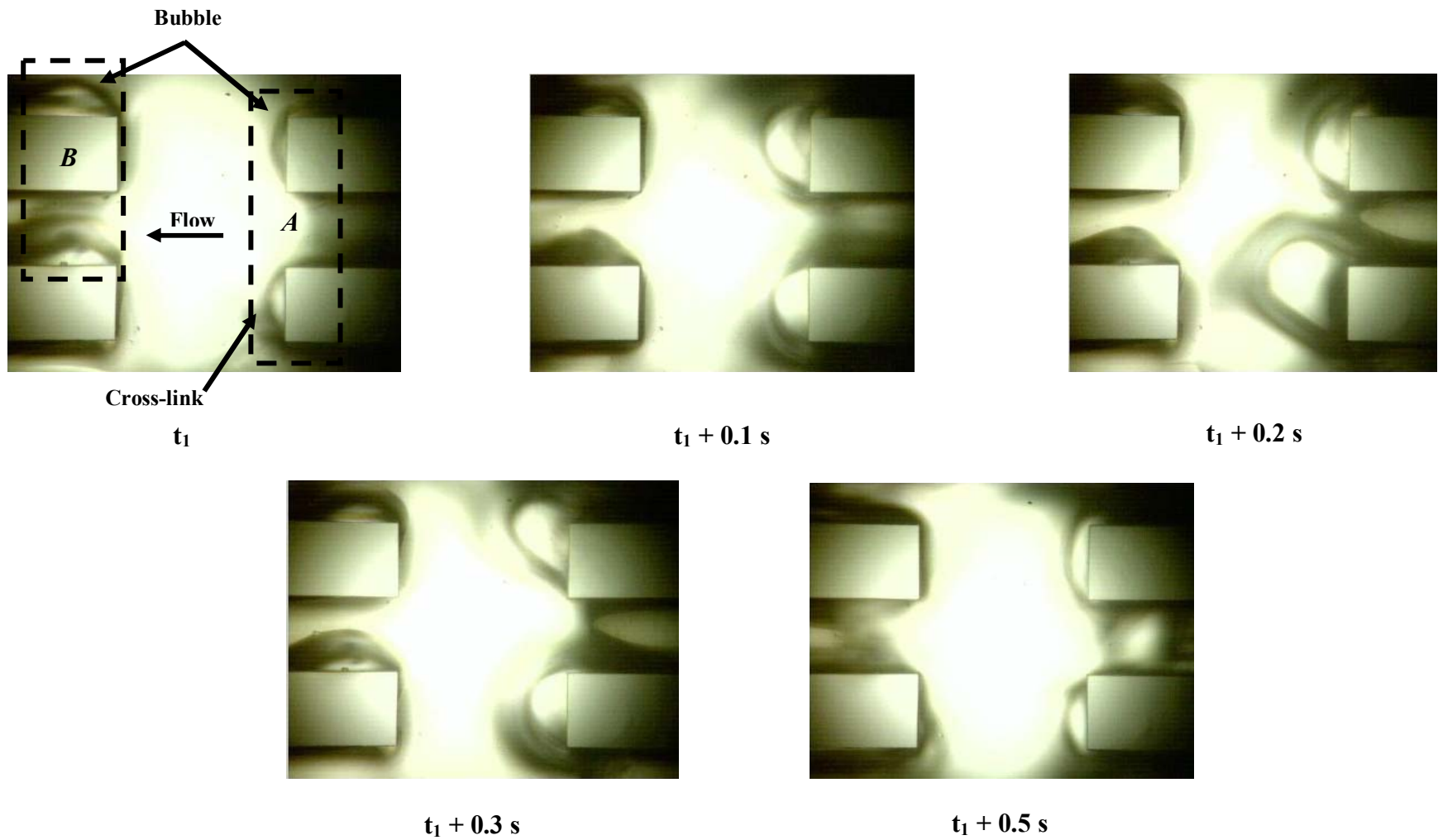
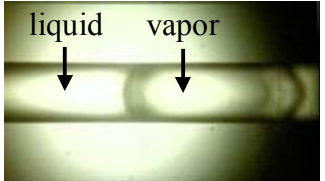
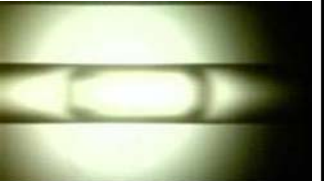
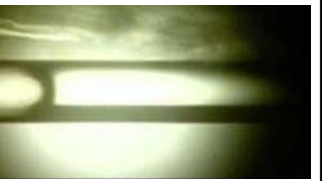
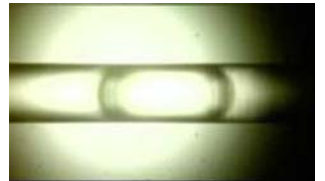
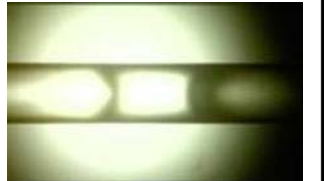

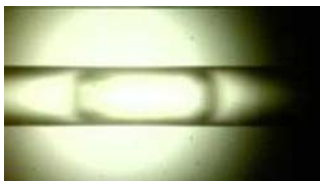


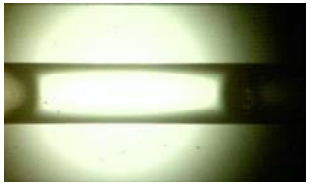
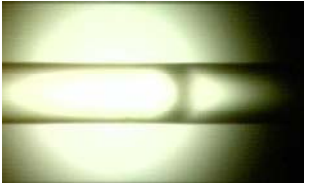

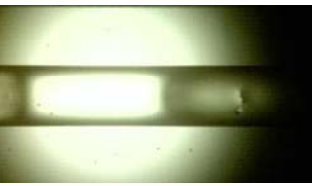
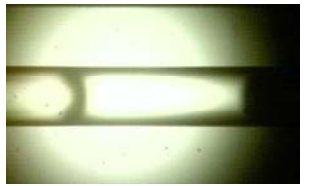
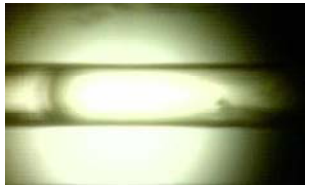
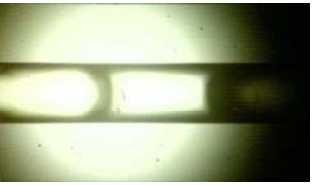
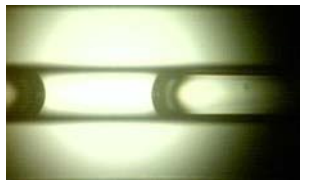



Figure 7-3: Sequential images of bubbles growing at $I=23$, $G = 147 \text{ kg/m}^2 \cdot \text{s}$, $q = 27.6 \text{ kW/m}^2$

		$G = 109 \pm 10 \% \text{ (kg/m}^2\cdot\text{s)}$				
$q \text{ (kW/m}^2\text{)}$	37				$0.2 \pm 10 \%$	x_{exit}
	38.5				$0.3 \pm 7 \%$	
	41.1				$0.4 \pm 5 \%$	
		<i>A-23</i>	<i>A-12</i>	<i>A-1</i>		
		Location				

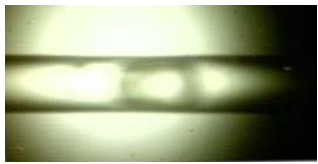


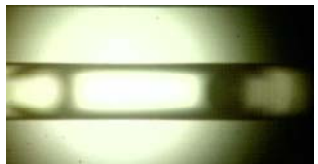
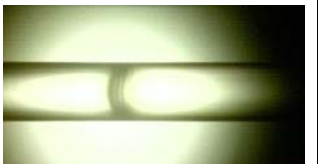

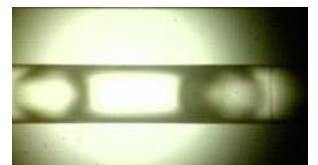
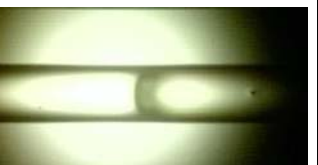

(a)

Figure 7-4: Flow patterns at different exit quality, heat flux, and locations of the test section, $G = 109 \text{ kg/m}^2\cdot\text{s}$, flow from right to left.

$G = 109 \pm 10 \% \text{ (kg/m}^2\cdot\text{s)}$						
$Q \text{ (kW/m}^2\text{)}$	37				$0.2 \pm 10 \%$	X_{ep}
	38.5				$0.3 \pm 7 \%$	
	41.1				$0.4 \pm 5 \%$	
		<i>B-23</i>	<i>B-12</i>	<i>B-1</i>		
Location						

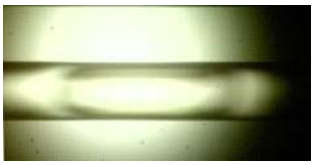
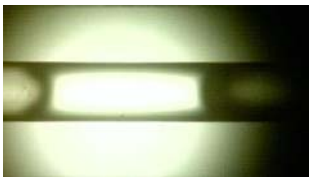

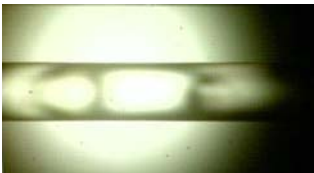


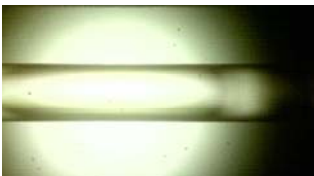


(b)

Figure 7-4: (continued)

		$G = 195 \pm 10 \% \text{ (kg/m}^2\cdot\text{s)}$				
\bar{Q} (kW/m ²)	64.3				$0.2 \pm 10 \%$	x_{50}
	66.4				$0.3 \pm 7 \%$	
	69.6				$0.4 \pm 5 \%$	
		<i>A-23</i>	<i>A-12</i>	<i>A-1</i>		
		Location				

(a)

Figure 7-5 : Two-phase flow patterns observed at a high mass flux, $G = 195 \text{ kg/m}^2\cdot\text{s}$.

		$G = 195 \pm 10 \% (\text{kg/m}^2 \cdot \text{s})$				
$Q (\text{kW/m}^2)$	64.3				$0.2 \pm 10 \%$	ϵ_{xy}
	66.4				$0.3 \pm 7 \%$	
	69.6				$0.4 \pm 5 \%$	
		<i>B-23</i>	<i>B-12</i>	<i>B-1</i>		
		Location				

(b)

Figure 7-5: (continued)

At low mass fluxes, there is a slight increase in the slope of pressure drop lines with the increase of exit quality. At higher mass fluxes, a sharp increase in pressure drop is clearly seen where the pressure drop lines start diverging. This is attributed to the effect of the cross-links, which add additional pressure losses and are represented in the abrupt expansion and contraction in the channels' cross-sectional area in addition to the cross flow. Experimental results also indicate significant flow instability and pressure drop fluctuations associated with measurements even after installing a throttling valve prior to the test section. In this regard, Cubaud and Ho (2004) and Dukler et al. (1988) commented that for slug flow, the data displays much more scatter than in bubbly and annular regimes. Furthermore, Yadigaroglu (1981) and Bergles et al. (1967) observed that slug flow, particularly as a transition regime from bubbly to annular flow, amplifies flow disturbance. Lee and Pan (1999) also reported that an increase in the channel number and channel-to-channel interaction causes an increase in flow instability, which may explain flow instability in the present heat sink design due to the presence of cross-links.

Many researchers have conducted experiments to study pressure drop during two-phase flow in straight microchannel heat sinks (Qu and Mudawar, 2003a; Lee and Mudawar, 2005a; Lee and Garimella, 2008). They have demonstrated that the channel size and mass flux are critical parameters in predicting two-phase flow pressure drop in microchannels. Lee and Garimella (2008) proposed a correlation for the two-phase multiplier as a function of hydraulic diameter and mass flux. The experimental two-phase frictional pressure drop of the cross-linked design is compared with the above mentioned correlation in order to compare the two-phase pressure drop in the present design with the

straight design as shown in Fig. 7-7. The two-phase pressure drop through the microchannel heat sink with the cross-links is higher than that of the straight microchannel heat sink at the same mass flux due to the cross-links effect. As seen from Fig. 7-7, it is clear that the Lee and Garimella correlation underpredicts the experimental data within -30% at low mass flux ($G = 111 \text{ kg/m}^2\cdot\text{s}$) in the low vapor quality region ($x_{e,o} < 0.3$). However, the magnitude of the two-phase pressure drop at the same mass flux does not have a comparable difference between the cross-link and straight microchannel heat sinks in the region of higher vapor qualities ($x_{e,o} > 0.3$). It is observed from Fig. 7-7 that this correlation tends to underestimate the present experimental data for a higher mass flux at $x_{e,o} < 0.3$. The two-phase pressure drop in the cross-linked design is nearly 1.5 times that in the straight design for all mass fluxes tested, except for the minimum value of mass flux. At higher vapor quality, ($x_{e,o} > 0.3$), it is seen that the correlation predicts the present data of two-phase pressure drop within -30%. This could be explained by the fact that in transitional flow, where slug and plug flow patterns exist in the channel, a larger frictional pressure gradient is experienced compared to the higher quality conditions in the straight design where annular flow is established. Huh et al. (2007) suggested that very long and fast elongated slugs behave like a semi annular flow. Therefore, as the liquid film thins near the wall, an increase in quality will lead to an increase in two-phase frictional pressure drop.

7.4 Two-phase Flow Instability

Figures 7-8 and 7-9 show amplitude oscillations of typical instability data of inlet pressure and outlet temperature acquired at a sampling rate of 2 Hz for 500 seconds, respectively.

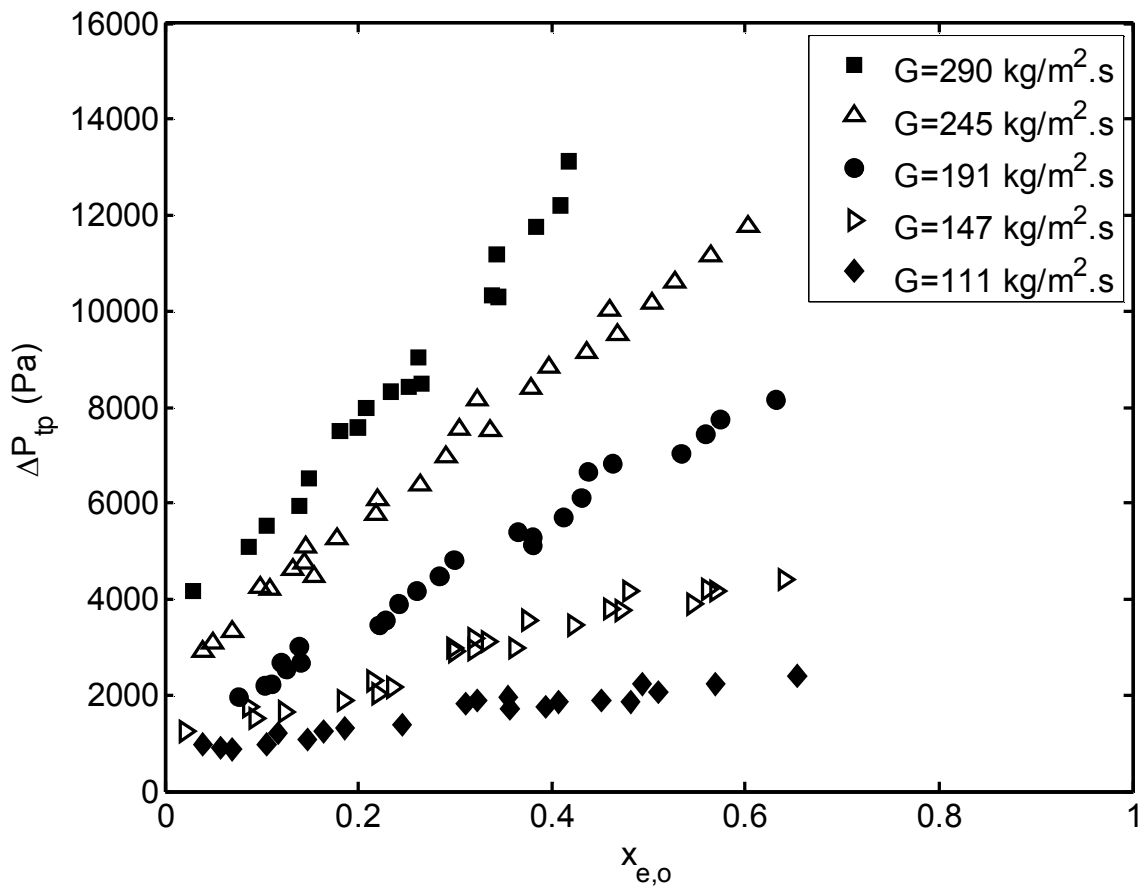


Figure 7-6: Two-phase pressure drop as function of vapor exit quality for different mass fluxes

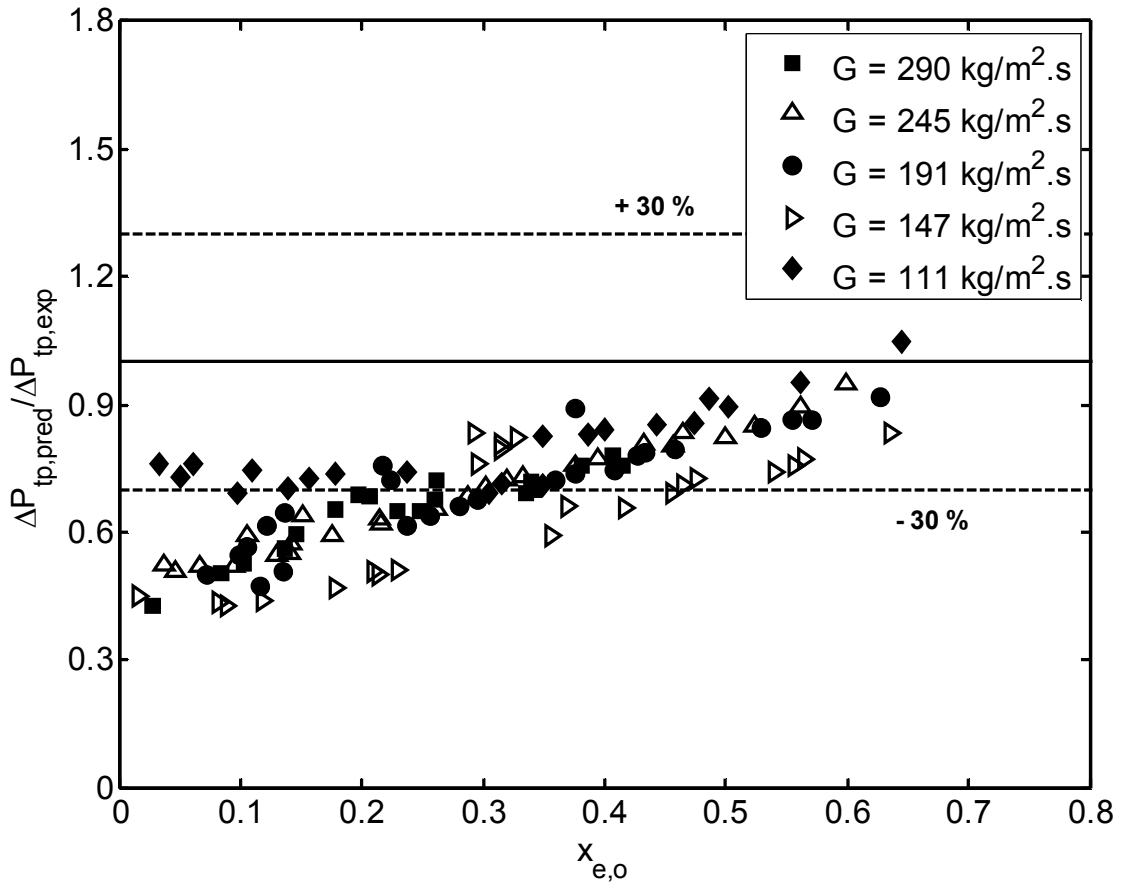


Figure 7-7 : Comparison of the present measurements and the correlation by Lee and Garimella (2008)

The oscillating inlet pressure amplitude dissipates with increasing mass flux, as shown in Fig. 7-8. The results also show that the amplitude value at low mass flux is about three times the amplitude value at higher values of mass flux. At the same time, the oscillation period of the inlet pressure increases at low mass flux and presents a long oscillation period of about 14 seconds. This phenomenon is consistent with the results of Huh et al. (2007) and Wang and Cheng (2008), in which the amplitude of pressure drop oscillations rises significantly at a lower mass flux.

The influence of the mass flux on the instability outlet saturation temperature is shown in Fig. 7-9. The amplitude and frequency of saturation temperature oscillations rise at low mass flux as shown in the figure. It is found that the oscillation amplitude decreases when the mass flux is higher, which means that the flow becomes more stable. The amplitude of waves at low heat and mass fluxes (corresponding to $x_{e,o} = 0.1$) is about seven times higher than the amplitude of waves at a higher heat and mass fluxes (corresponding to $x_{e,o} = 0.3$) with an oscillation period of nearly 11 seconds.

The inlet pressure amplitudes are almost half of those presented by Muwanga et al. (2007) for flow boiling in cross-linked microchannel heat sinks using water, while the present oscillation periods are longer. On the other hand, the data recorded by Muwanga et al. showed that the outlet temperature oscillates with higher amplitudes compared to the present study. Nonetheless, the outlet temperature periods of oscillation exhibited in Fig. 7-9 are found to be longer than the oscillation periods previously presented by Muwanga et al. Pan and Chang (2007) provided experimental data on flow boiling instability of de-ionized water microchannel heat sinks. Their results showed that significant pressure drop oscillations appear at unstable conditions.

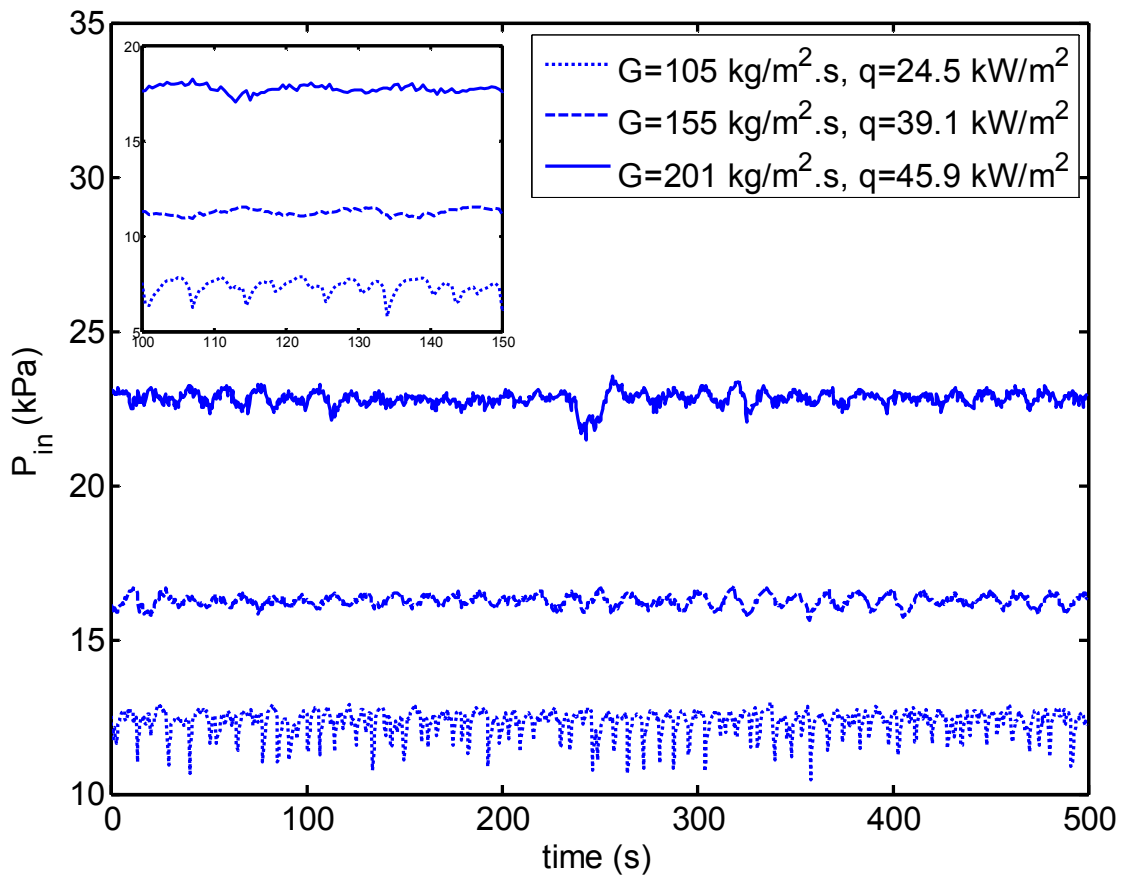


Figure 7-8 : Oscillations of inlet pressure measurements.

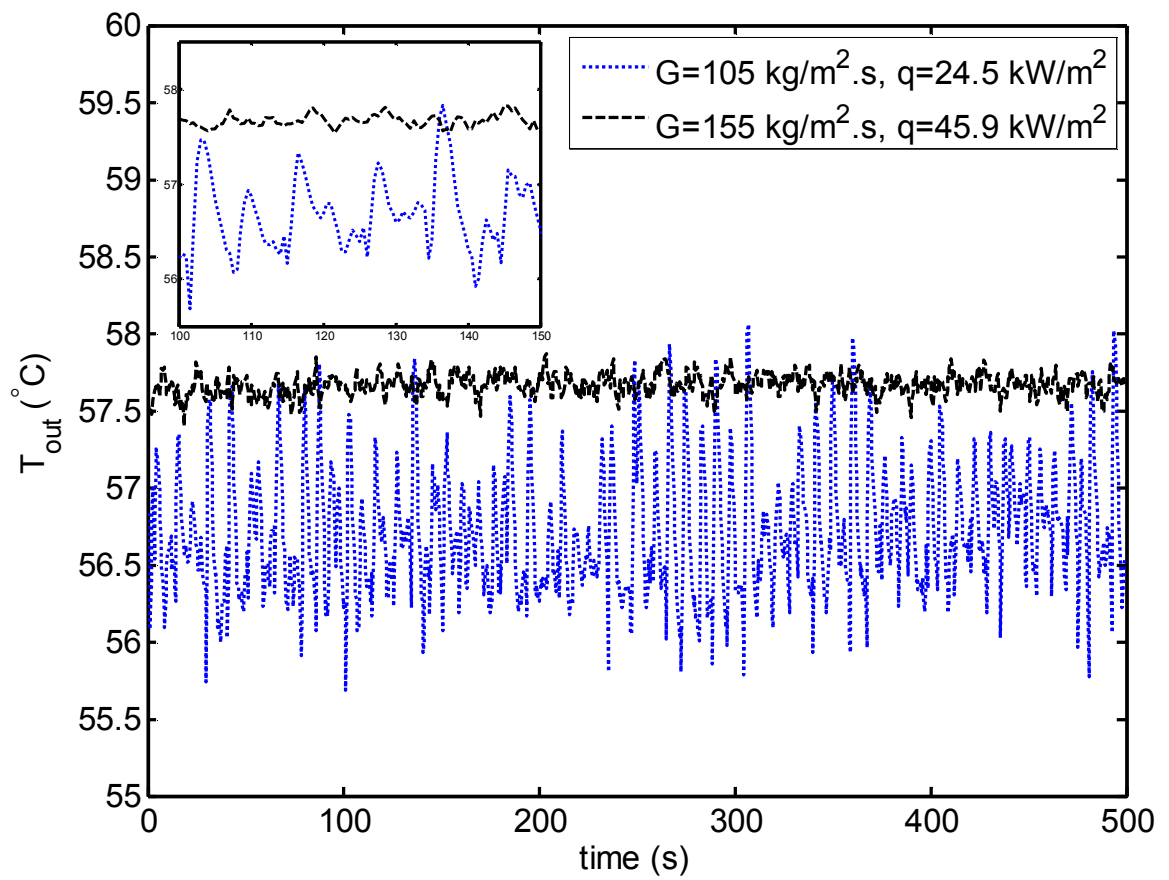


Figure 7-9 : Oscillations of outlet temperature measurements.

With the aid of flow visualization, they found that large pressure drop oscillations could be attributed to the length of bubble slugs growing and shrinking within the channel.

7.5 Flow Boiling Heat Transfer

The color change of Thermochromic Liquid Crystals (TLC) with temperature has been effectively utilized in the present study to provide high-spatial resolution temperature maps for the heat sink surface temperature. Figures 7-10 and 7-11 illustrate selected images of the painted TLC and the derived spatially resolved temperature map acquired at $G = 99 \text{ kg/m}^2\cdot\text{s}$, and different values of heat flux. Initially clear when below its activation temperature, the TLC changes color from red to green to blue as the surface temperature increases. Figures 7-10(a) and 7-11(a) show the original images of TLC that were recorded during the experiment at a constant mass flux but different heat flux. From the TLC image shown in Fig. 7-10(a), it can be clearly seen that a lower temperature is noted at the heat sink inlet manifold indicating subcooling liquid flow at $x_{e,o} = 0.15$ and $q = 12.6 \text{ kW/m}^2$. Red reveals a lower temperature demonstrating a distinct difference in the boiling length between channels and the influence of cooling mass flow rate is evident, suggesting that the flow is distributed non-uniformly over the channels because of the inlet manifold design. The heat sink surface is at approximately $61 \text{ }^\circ\text{C}$ in the saturated boiling region, while the temperature of the subcooled region is above $56 \text{ }^\circ\text{C}$ (Fig. 7-10(b)). Figure 7-11(a) and (b) show a TLC color image and the corresponding surface temperature variation map obtained at the same mass flux but at $x_{e,o} = 0.3$ and $q = 17.3 \text{ kW/m}^2$. The surface temperature map shows that the temperature distribution on the test surface is almost uniform with a temperature gradient less than $2 \text{ }^\circ\text{C}$.

Figure 7-12 presents the two-phase heat transfer coefficient as a function of the exit quality for four different values of mass flux. The two-phase heat transfer coefficient increases with exit quality for a constant mass flux. The two-phase heat transfer coefficient is strongly sensitive to quality as shown in Fig. 7-12. Different mass fluxes have similar curves, indicating that the heat transfer coefficient is weakly dependent on mass flux but strongly dependent on heat flux, which suggests that the nucleate boiling heat transfer mechanism dominates the flow boiling heat transfer coefficient. The flow boiling heat transfer coefficient, for a given mass flux, exhibited a distinct trend compared to results previously presented in the literature for flow boiling heat transfer in straight microchannel heat sinks. The two-phase heat transfer coefficient has been found to significantly decrease with increasing exit quality at a constant mass flux for flow boiling in straight microchannel heat sinks (Steinke and Kandlikar, 2004; Yen et al. 2006; Ravigururajan, 1998). An interesting feature of flow boiling heat transfer in the cross-linked design is that the two-phase heat transfer coefficient increases with increasing exit quality because of the contribution caused by nucleate boiling in the cross-links. The aforementioned conclusion is supported by flow visualization images presented in Fig. 7-3. It shows that cross-linked microchannels provide plenty of nucleation sites for bubble formation. At these sites, bubbles grow to a critical size and then depart from the heating surfaces.

Numerous studies on nucleate boiling effects in microchannels have been conducted and correlations were developed to predict two-phase heat transfer coefficients. The applicability of previously proposed correlations for two-phase heat transfer coefficient in microchannels has also been investigated.

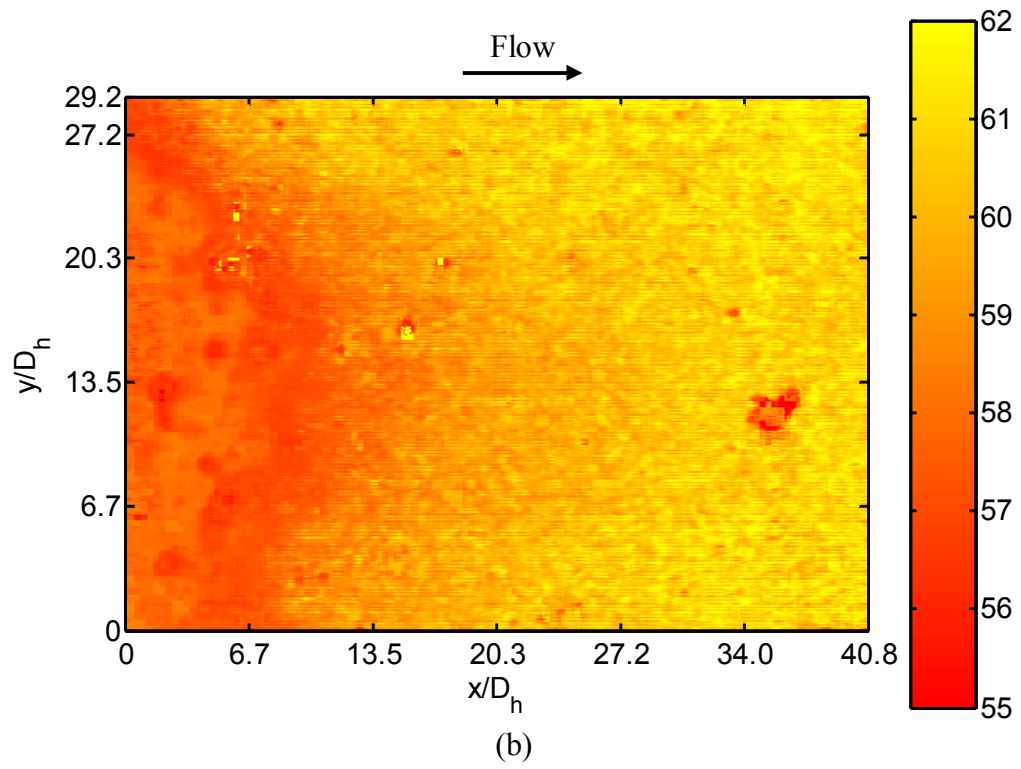
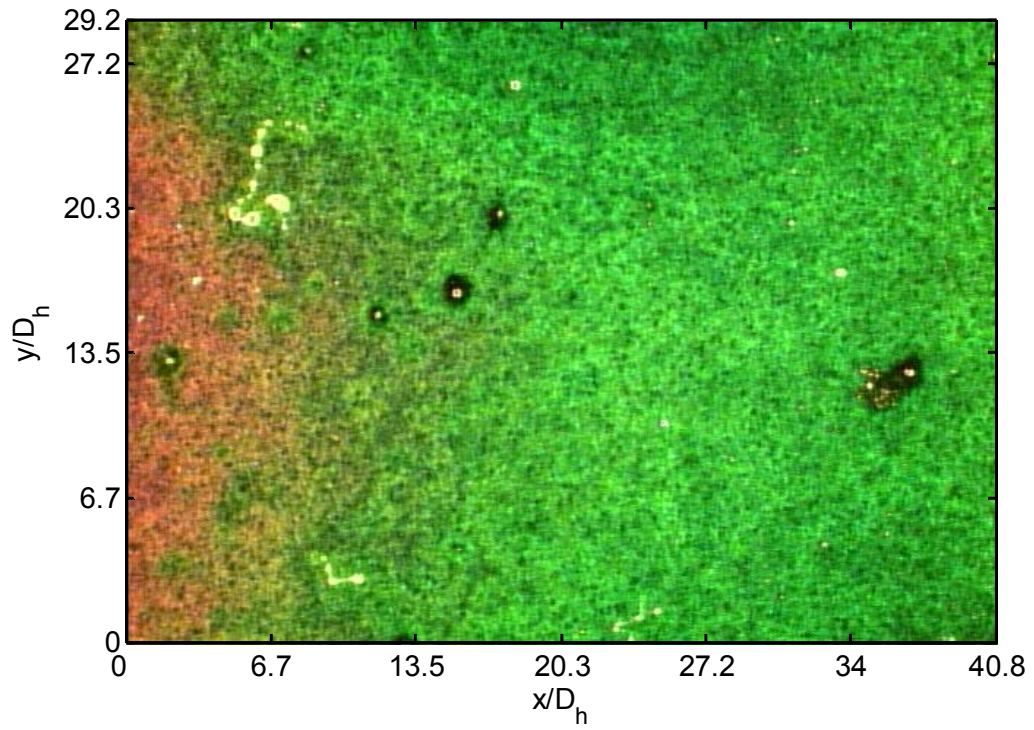
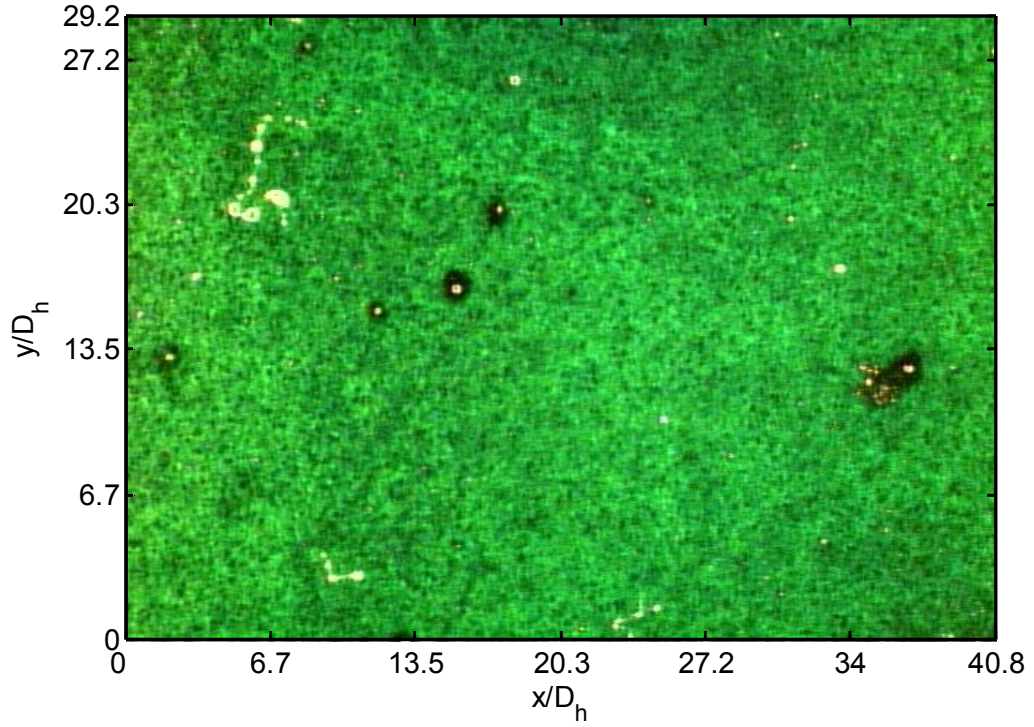
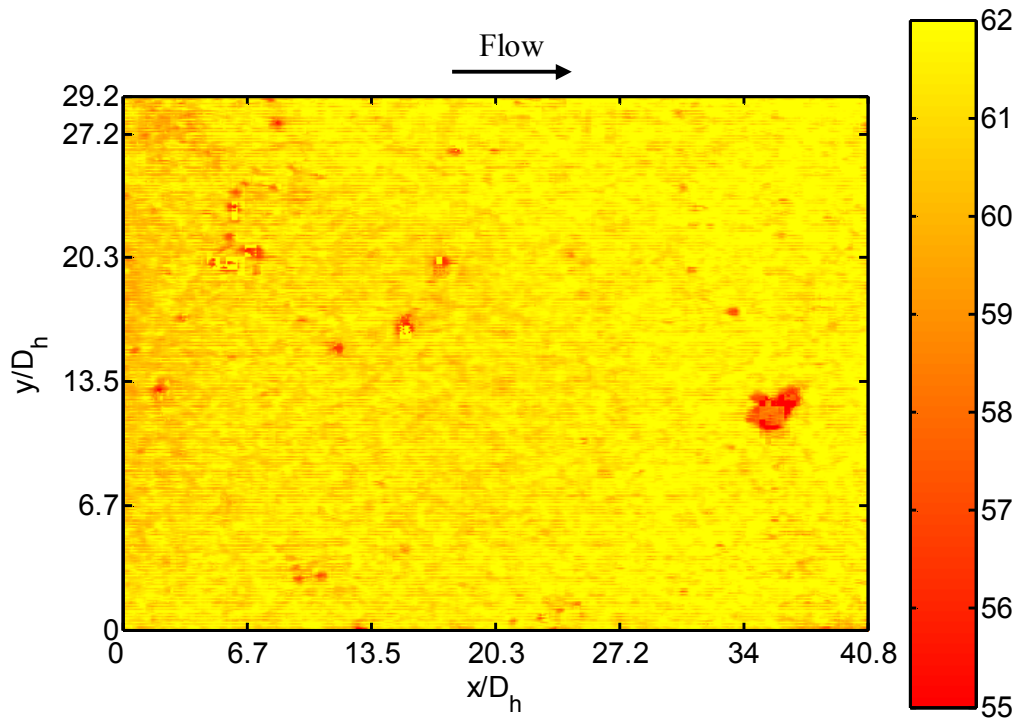


Figure 7-10: Sample of spatially resolved temperature map and TLC-painted surface at $G = 99 \text{ kg/m}^2 \cdot \text{s}$ and $x_{e,0} = 0.15$.



(a)



(b)

Figure 7-11: Sample of spatially resolved temperature map and TLC-painted surface at G

$= 99 \text{ kg/m}^2 \cdot \text{s}$ and $x_{e,o} = 0.3$.

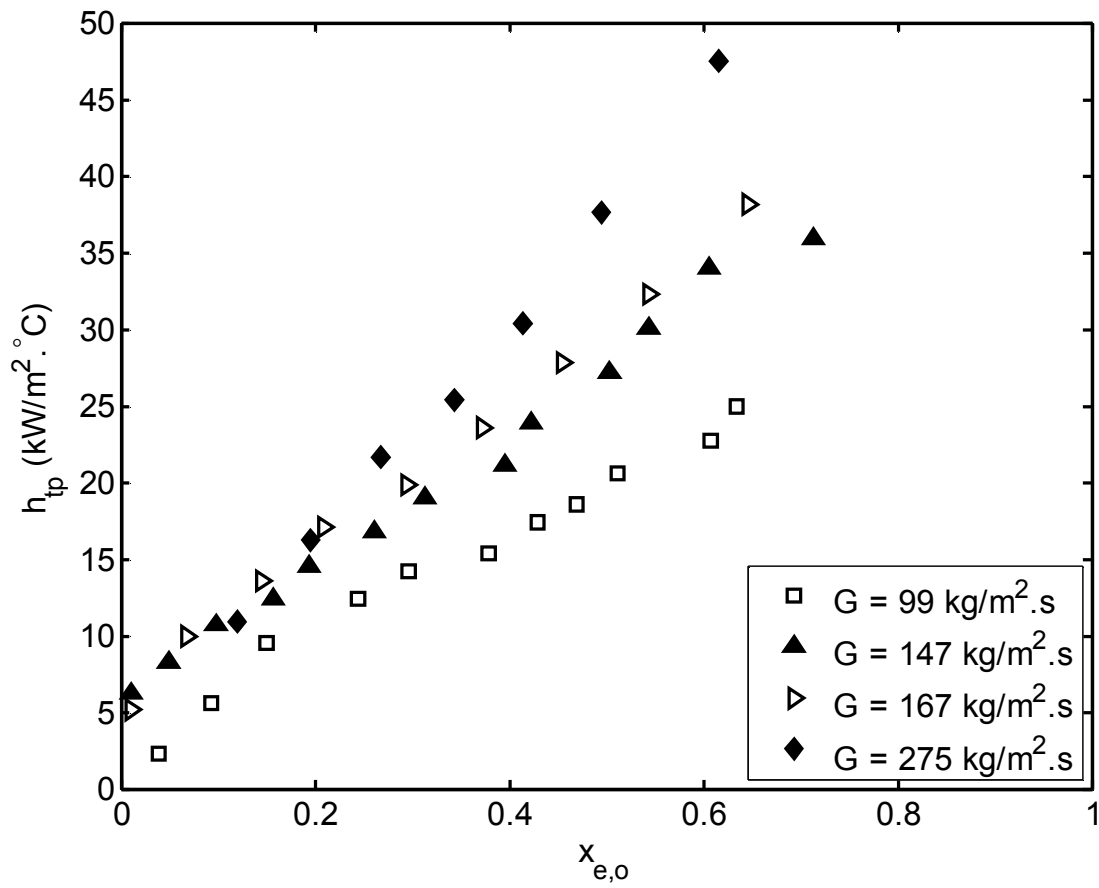


Figure 7-12: Variation of two-phase heat transfer coefficient with vapor exit quality at different mass fluxes.

Results show that most microchannel correlations under-predict the experimental two-phase heat transfer coefficient, since these correlations were developed based on forced convection boiling. The correlation of Yu et al. (2002) was found to give reasonably good agreement with the experimental data at $x_{e,o} > 0.2$, as seen in Fig. 7-13. However, it over-predicts the data at low exit quality ($x_{e,o} < 0.2$). Yu et al. have performed an experimental study for horizontal flow boiling pressure drop, heat transfer, and critical heat flux of water flow in a minitube with a heated length of 0.91 m and an inside diameter of 2.98 mm for a range of mass fluxes from 50 to 200 kg/m².s. Their experimental results were consistent with those previously carried out by Tran et al. (1996). Tran et al. indicated that the domination of nucleation boiling mechanism over the convective boiling mechanism, over a wide range of mass fluxes and exit qualities, is primarily due to the large-slug-flow regime. It should be noted that the current visual observations of flow patterns, shown in Figs. 7-4 and 7-5, also indicated that the slug flow exists in the present study over the examined range of mass flux and exit quality. Since the two-phase heat transfer coefficient was influenced more by the heat flux than by the mass flux in the nucleate boiling region, Yu et al. found that it can be correlated well with the Boiling number, the Weber number, and the density ratio of the two phases (ρ_l/ρ_g). The dependence on the boiling number in the Yu et al. correlation in addition to the dominant nucleation boiling heat transfer mechanism associated with the large-slug-flow regime in their experiment yielded a reasonable agreement between the experimental data and correlation's predictions.

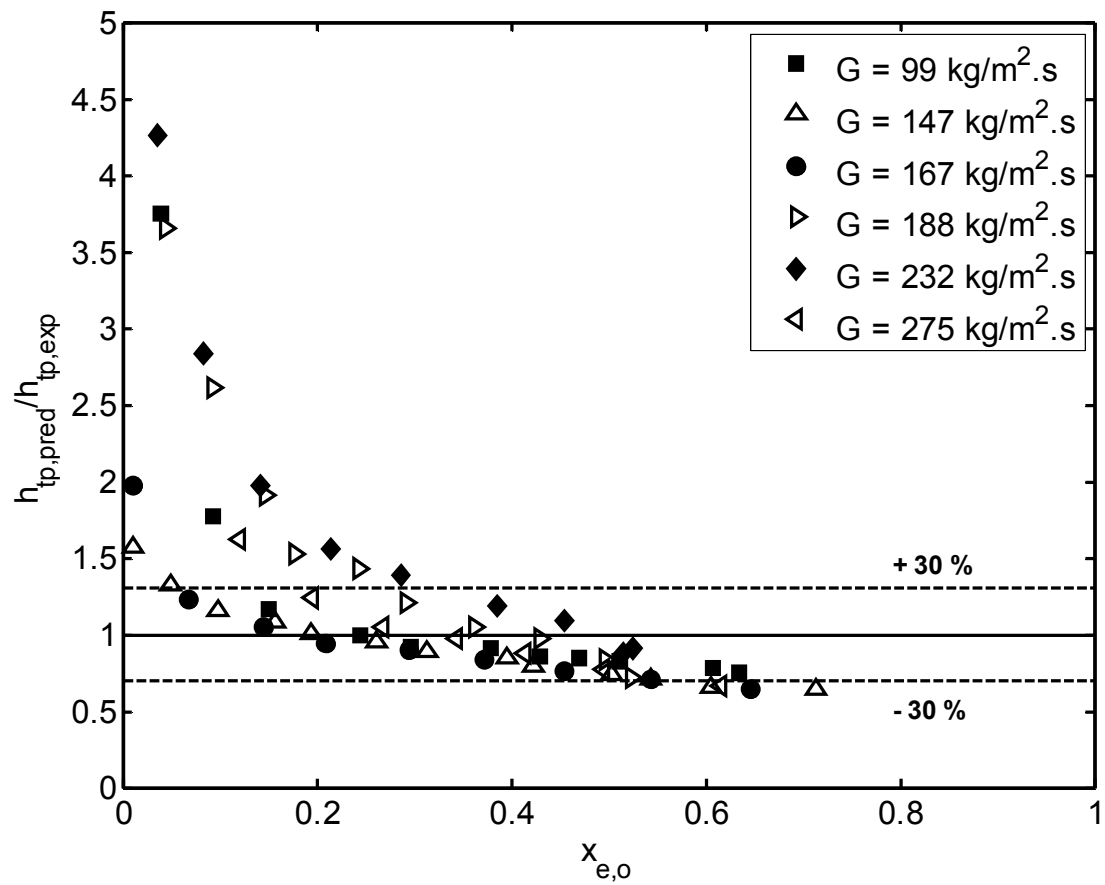


Figure 7-13 : Ratio of predicted to measured two-phase heat transfer coefficient at different mass fluxes as a function of exit quality using the Yu et al. correlation (2002).

Figure 7-14 presents the experimental boiling curve for FC-72 in the cross-linked microchannel heat sink for various mass fluxes. At a low value of wall superheat ($\Delta T_{\text{sat}} = 2.8 \text{ }^\circ\text{C}$), the wall heat flux is 24.9 kW/m^2 and the corresponding mass flux is only $167 \text{ kg/m}^2\cdot\text{s}$, compared to 40.6 kW/m^2 and the corresponding mass flux is $232 \text{ kg/m}^2\cdot\text{s}$ at the same wall superheat. High values of wall heat flux and low values of surface superheats reflect a high heat transfer coefficient associated with the nucleate boiling regime. The importance to electronic cooling applications is to maintain relatively low surface temperatures while dissipating high heat fluxes, which suggest that the present design is a very good candidate for future thermal management. The boiling curve exhibits a distinct trend for the mass flux dependence, as shown in Fig. 7-14. This trend may be attributed to the effect of higher mass fluxes, thus a lower contribution of nucleation boiling is expected. As the mass flux decreases the residence time of the bubbles on the cross-link surface increases, which together with the domination of nucleation boiling in the microchannels explain the observed two distinct trends in the boiling curve. The trends are separated by the boiling curve at $G = 167 \text{ kg/m}^2\cdot\text{s}$. For relatively intermediate heat fluxes ($\approx 49 \text{ kW/m}^2$), the surface superheat reaches approximately $8.6 \text{ }^\circ\text{C}$ for $G = 147 \text{ kg/m}^2\cdot\text{s}$. Increasing the mass flux to $232 \text{ kg/m}^2\cdot\text{s}$ produces an offset in the wall superheat of approximately $4 \text{ }^\circ\text{C}$. For the maximum mass flux ($G = 275 \text{ kg/m}^2\cdot\text{s}$), the maximum value of heat flux reaches approximately 88.8 kW/m^2 for a wall superheat of $7.2 \text{ }^\circ\text{C}$ only.

7.6 Conclusions

Flow boiling characteristics of FC-72 have been experimentally investigated in a cross-linked microchannel heat sink with a hydraulic diameter of $248 \text{ }\mu\text{m}$. Flow

visualization experiments demonstrate that the observed flow regime is predominantly slug over the range of experimental parameters investigated in the present study. The introduction of the cross-link channels resulted in providing more nucleation sites as well as uniform flow and surface temperature distributions. Furthermore, circulations generated in the cross-links assisted in rapid bubble formation and growth, and delayed bubble detachment from the nucleation sites. Results have showed that the instability increased when the mass flux is decreased. The inlet pressure and outlet saturation temperature oscillated with higher amplitudes as the mass flux decreased. The two-phase pressure drop through microchannel heat sinks, with cross-links, was much higher compared to the straight microchannel heat sinks due to the cross-link effect. The cross-linked microchannel heat sink presented a significant increase in two-phase heat transfer coefficient compared to the straight microchannel heat sink. The two-phase heat transfer coefficient was strongly increased with the exit quality because of the domination of the nucleation boiling mechanism in the cross-link region. It was found that the two-phase heat transfer coefficient is relatively well-correlated by the Yun et al. correlation (2002), although this correlation was derived from flow boiling data in mini tubes.

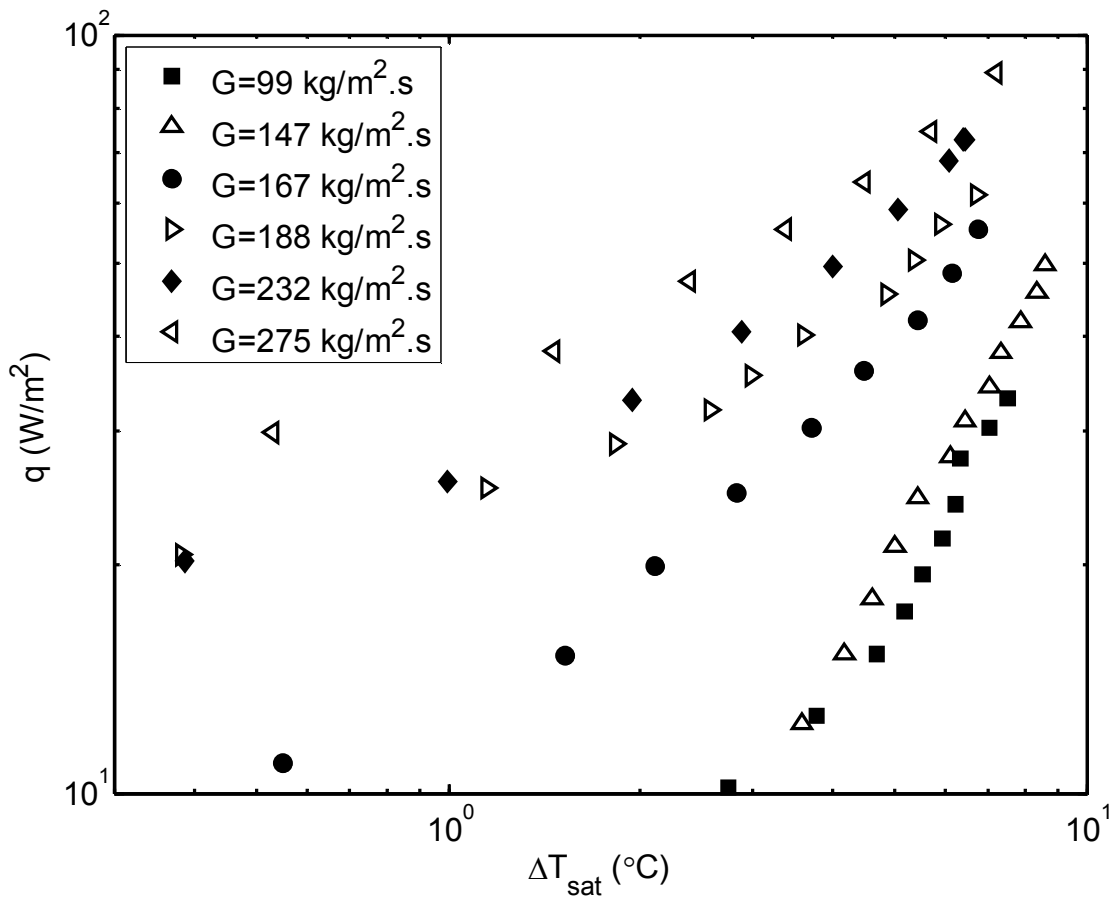


Figure 7-14 : Typical boiling curve for FC-72 in the cross-linked microchannel heat sink,

$$\Delta T_{\text{sub}} = 4^{\circ}\text{C}.$$

CHAPTER 8

CONCLUSIONS AND FUTURE WORK

Flow boiling experiments were carried out with refrigerant FC-72 in rectangular microchannels of 248 μm hydraulic diameter. Microchannels were covered with Pyrex to allow flow visualization during the experiments. Experimental investigation of flow boiling characteristics in straight and cross-linked microchannel heat sinks included pressure drop, heat transfer, incipience of boiling, two-phase flow instability, and flow patterns. In addition, an analytical model was developed to describe flow boiling heat transfer coefficient for the annular flow regime. Key accomplishments of the present thesis work are summarized below.

8.1 Conclusions

8.1.1 Straight Microchannel Heat Sink

- The increase in vapor quality and mass flux increased the two-phase pressure drop in the straight microchannel heat sink. The measured two-phase pressure drop data was in good agreement with the correlations proposed by Qu and Mudawar (2003a) and Lee and Garimella (2008). Nonetheless, two-phase pressure drop measurements were combined with two-phase pressure drops data of multiple refrigerants from the literature to develop a new two-phase pressure drop correlation based on the separated flow model. For microchannels of $D_h < 349 \mu\text{m}$, the two-phase frictional multiplier indicated a dependence on confinement and Reynolds numbers. Therefore, a new correlation was proposed which

incorporates the confinement and Reynolds numbers to improve pressure drop predictions for laminar-liquid laminar-vapor and laminar-liquid turbulent-vapor flow.

- The flow patterns observed in the straight microchannel heat sink were: bubbly, slug and annular.
- The use of thermochromatic liquid crystals allowed for non-intrusive temperature measurements and high spatial resolution. TLC provided many advantages over traditional bulk temperature measurement methods, such as thermocouples. The use of TLC allowed observing a unique flow boiling onset in microchannels, a benefit that is not available through use of thermocouples.
- Flow boiling heat transfer results showed that the nucleate boiling mechanism dominant region extends from $x_{e,o} = 0$ to 0.2. The heat transfer coefficient in the nucleate boiling region decreased as vapor quality increased. It was a strong function of heat flux, and only a weak function of mass flux. At a higher vapor quality, there was a convection dominant region where the transition point from the nucleate boiling region to the convection boiling region was observed by flow visualization.
- Heat transfer coefficient experimental data were presented and compared with other mini- and microscale asymptotic models and correlations provided by other researchers. On the basis of the channel size tested, the two-phase flow characteristics are very different from those obtained in minichannels, and minichannel correlations no longer apply. Flow boiling heat transfer coefficient did not yield any conclusive correlation in the present study. All microscale

correlations and asymptotic models underpredicted the experimental data at vapor quality below 0.2.

- An analytical model for predicting flow boiling heat transfer coefficient for annular flow boiling regime was developed. It was assumed that velocity and temperature profiles are identical, based on Reynolds' analogy, to determine the heat transfer coefficient within the channel. Very good agreement was achieved between the experimental data and model predictions with a mean absolute error of 10%. This model proved that it can accurately predict the heat transfer characteristics in mini- and microchannel heat sinks for the annular flow regime.

8.1.2 Cross-linked Microchannel Heat Sink

- For the cross-linked design, flow visualization identified only the slug flow regime under the flow conditions investigated. The nonexistence of annular flow in the cross-linked microchannel heat sink was attributed to the effect of cross-links. Flow visualization also indicated that bubbles nucleate, grow up, and slide in the channels downstream during the flow boiling in the cross-linked microchannel heat sink.
- The cross-linked microchannel heat sink presented a significant increase in two-phase heat transfer coefficient compared to the straight heat sink. The two-phase heat transfer coefficient strongly increased with the exit quality. The enhancement of flow boiling heat transfer in the cross-linked design was attributed to nucleation in the cross-links region. Nucleate boiling ameliorates the rate of heat removal and served as nucleation sites.

- High amplitude oscillations of outlet saturation temperature were observed at low mass flux, which was explained by the existence of slug flow. However, these oscillations were found to decrease as the mass flux increased.
- The applicability of previously proposed correlations for the two-phase heat transfer coefficient in microchannels was also investigated. All existing correlations for mini- and microchannel flow boiling heat transfer were found to underpredict the heat transfer coefficient in the cross-linked design. Among them, a comparison has been made of the experimental data with the correlation proposed by Yu et al. (2002) and yielded good agreement. This was attributed to the domination of slug flow in both experiments. However, the present experimental data did not agree well with the Yu et al. correlation at a mass flux higher than $G = 200 \text{ kg/m}^2 \cdot \text{s}$. This disagreement was due to the extrapolation of the correlation to a much higher mass flux.

8.2 Future Research

Future research to further understand the micro-scale pressure-driven flow can be performed both experimentally and analytically.

8.2.1 Experimental Study

- To completely study the cross-linked microchannel heat sinks, experimental studies need to be performed in order to study the influence of non-uniform heating conditions on flow boiling characteristics namely, flow distribution, flow instability, and the flow boiling heat transfer coefficient.

- Different studies for heat transfer enhancement techniques in microchannels indicated that microroughness, microporous, and laser drilled cavities are effective in decreasing boiling incipience superheat as well as enhancing nucleate boiling. Micropin fins were shown to have a superior performance compared to the plain microchannel heat sink by dissipating very high heat fluxes at low temperature rise. A new design is proposed aiming at developing innovative high-performance liquid-cooled microchannel heat sinks for electronic packages with high heat fluxes. High heat sink performance can be achieved by making heat sinks with pin fins and generating vortices. The cooling method selected will combine the cross-linked heat sink design along with 380 staggered elliptically shape microfins with major to minor axes ratio of 4:1, a technique that has not been used before. A schematic is presented in Fig. 8-1. The effect of staggered elliptical microfins is expected to increase the turbulence around the pins, due to their location, and thus increasing the cooling rate significantly. In addition, they include small gaps to create vortices and hence bubbles are expected to grow in these gaps, which would serve as nucleation sites as shown in Fig. 8-2. Restrictive inlets are proposed at the flow inlet to serve as throttling devices to reduce any flow instabilities.

8.2.2 Analytical Study

- Developing a theoretical micro-scale two-phase flow model to predict void fraction is recommended. It would include inertia, viscous, and surface tension forces.

- A new analytical model is needed to predict the flow boiling heat transfer characteristics during slug flow regime in microchannels.

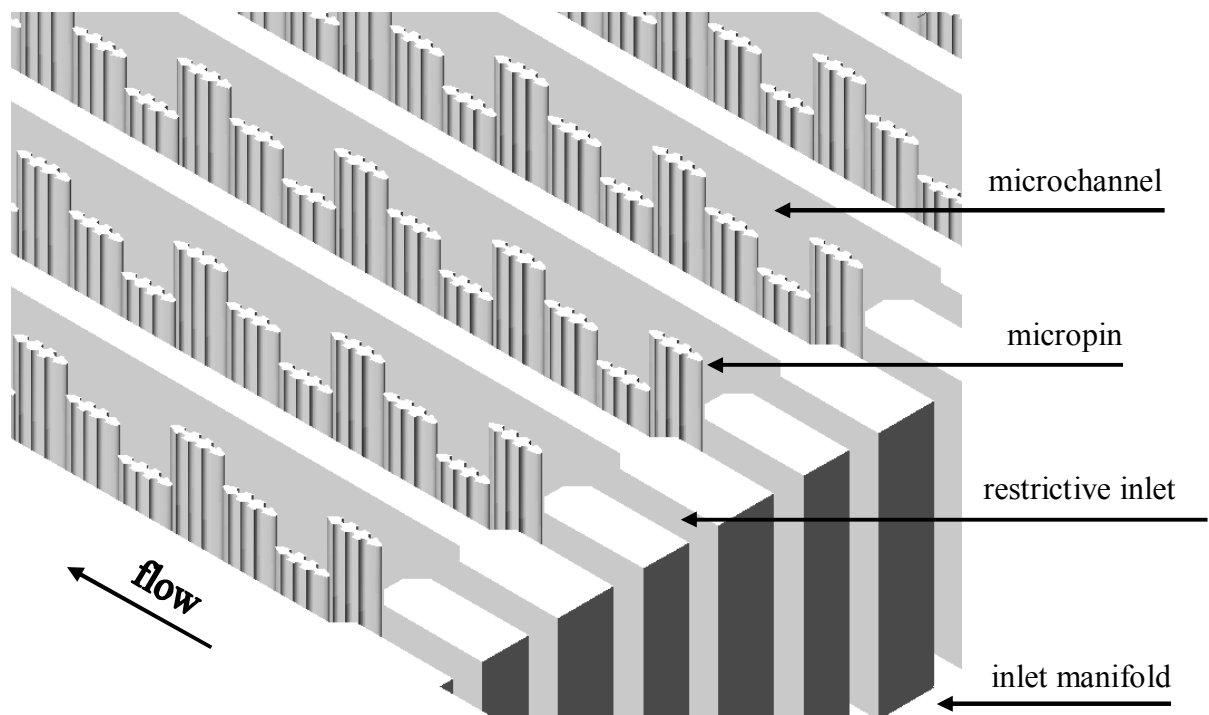


Figure 8-1: Proposed enhanced microchannel heat sink.

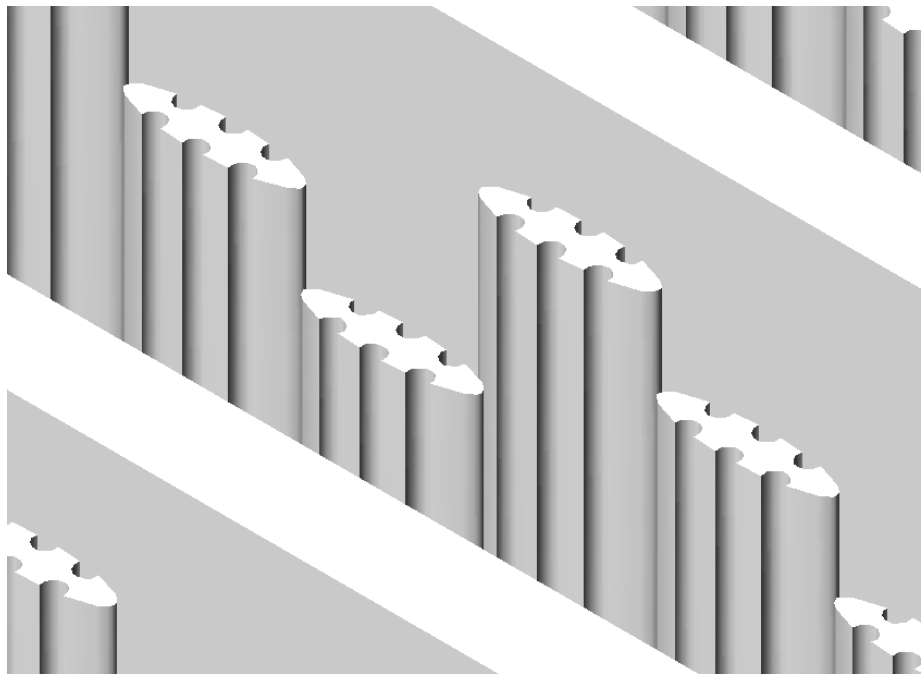


Figure 8-2: Micropins geometry developed to enhance boiling characteristics.

REFERENCES

- Agostini, B., Thome, J. R., Fabbri, M., Michel, B., Calmi, D., and Kloter, U., 2008a, "High heat flux flow boiling in silicon multi-microchannels- Part I: Heat transfer characteristics of refrigerant R236fa," *International Journal of Heat and Mass Transfer*, 51(21-22), pp. 5400-14.
- Agostini, B., Thome, J. R., Fabbri, M., Michel, B., Calmi, D., and Kloter, U., 2008b, "High heat flux flow boiling in silicon multi-microchannels- Part II: Heat transfer characteristics of refrigerant R245fa," *International Journal of Heat and Mass Transfer*, 51(21-22), pp. 5415-25.
- Ali, M.I., Sadatomi, M., and Kawaji, M., 1993, "Adiabatic two-phase flow in narrow channels between two flat plates," *Canadian Journal of Chemical Engineering*, 71(5), pp. 657-666.
- Balasubramanian, P., and Kandlikar, S., 2005, "Experimental study of flow patterns, pressure drop, and flow instabilities in parallel rectangular minichannel," *Heat Transfer Engineering*, 26(3), pp. 20-27.
- Bennett, L., and Chen, J. C., 1980, "Forced Convective Boiling in Vertical Tubes for Saturated Components and Binary Mixtures," *AIChE Journal*, 26, pp. 454-461.
- Bergles, A.E., Lopina R.F., and Fiori, M.P., 1967, "Critical-Heat Flux and Flow Pattern Observations for Low Pressure Water Flowing in Tubes," *Journal of Heat Transfer*, 89, pp. 69-74.

- Bertsch, S. S., Groll, E. A., and Garimella, S. V. , 2008a, "Review and comparative analysis of studies on saturated flow boiling in small channels," *Nanoscale and Microscale Thermophysical Engineering*, 12(3), pp. 187-227.
- Bertsch, S. S., Groll, E. A., and Garimella, S. V., 2008b, "Refrigerant flow boiling heat transfer in parallel microchannels as a function of local vapor quality," *International Journal of Heat and Mass Transfer*, 51(19-20), pp. 4775-87.
- Bertsch, S. S., Eckhard, A. G., and Garimella, S. V., 2009a, "A composite heat transfer correlation for saturated flow boiling in small channels," *International Journal of Heat and Mass Transfer*, 52 (7-8), pp. 2110-18.
- Bertsch, S.S., Groll, E.A., and Garimella, S.V., 2009b, "Effects of heat flux, mass flux, vapor quality, and saturation temperature on flow boiling heat transfer in microchannels," *International Journal of Multiphase Flow*, 35(2), pp. 142-54.
- Bowers, M.B., and Mudawar, I., 1994, "Two-phase electronic cooling using mini-channel and micro-channel heat sinks. 2. Flow rate and pressure drop constraints," *Transactions of the ASME Journal of Electronic Packaging*, 116(4), pp. 298-305.
- Brauner, N., and Moalem-Maron, D., 1992, "Identification of the range of small diameter conduits, regarding two-phase flow pattern transitions," *International Communications in Heat and Mass Transfer*, 19, pp. 29-39.
- Chen, J.C., 1966, "A Correlation for boiling heat transfer to Saturated fluids in convective flow," *Ind. Eng. Chem. Process Design Develop.*, 5(3), pp. 322-29.
- Cheng, P., Wang, G., and Quan, X., 2009, "Recent Work on Boiling and Condensation in Microchannels," *Journal of Heat Transfer*, 131(4), pp. 0432111-15.

- Cho, E.S., Koo, J., Jiang, L., Prasher, R.S., Kim, M.S., Santiago, J.G., Kenny, T.W., and Goodson, K.E., 2003, "Experimental study on two-phase heat transfer in microchannel heat sinks with hotspots," *Proceedings of 19th Annual IEEE Semiconductor Thermal Measurement and Management Symposium*, Mountain View, CA, USA, pp. 242-6.
- Cho, H., and Cho, K., 2004, "Mass flow rate distribution and phase separation of R-22 in multi-microchannel tubes under adiabatic condition", *Microscale Thermophysical Engineering*, 8, pp. 129-139.
- Collier, J.G., and Thome, J.R., 1994, *Convective Boiling and Condensation*, University Press, Oxford, Chap. 3.
- Consolini, L., and Thome, J.R., 2009, "Micro-channel flow boiling heat transfer of R-134a, R-236fa, and R-245fa," *Microfluidics and Nanofluidics*, 6(6), pp. 731-46.
- Cubaud, T., and Ho, C.-M., 2004, "Transport of bubbles in square microchannels," *Physics of Fluids*, 16(12), pp. 4575-85.
- Dang, M., Hassan, I., and Kim, S.I., 2008, "Numerically investigating the effects of cross-links in scaled microchannel heat sinks," *Journal of Fluids Engineering*, 130(12), pp. 1211031-13.
- Dang, M., Hassan, I., Muwanga, R., 2007, "Adiabatic two phase flow distribution and visualization in scaled microchannel heat sinks", *Experiments in Fluids*, 43(6), pp. 873-85.
- Dang, M., and Hassan, I., 2008, "Adiabatic two-phase flow in scaled microchannel heat sinks with cross links," *Journal of Thermophysics and Heat Transfer*, 22(4), pp. 587-97.

- Dong, T., Yang, Z., Bi, Q., and Zhang, Y., 2008, "Freon R141b flow boiling in silicon microchannel heat sinks: experimental investigation," *International Journal Heat and Mass Transfer*, 44 (3), pp. 315-24.
- Dukler, A.E., Fabre, J.A., Mcquillen, J.B. and Vernon, R., 1988, "Gas-liquid flow at microgravity conditions - flow patterns and their transitions," *International Journal of Multiphase Flow*, 14(4), pp. 389–400.
- Dupont, V., Thome, J.R., and Jacobi, A.M., 2004, "Heat transfer model for evaporation in microchannels. Part II: comparison with the database," *International Journal of Heat and Mass Transfer*, 47(14-16), pp. 3387-401.
- Field, B.S., Two-Phase Pressure Drop and Flow Regime of Refrigerants and Refrigerant-Oil Mixture in Small Channels, Ph.D. Thesis, University of Illinois, Urbana-Champaign, IL, 2007.
- Fitzsimmons, D. E., 1964, "Two-phase pressure drop in piping components," HW 80970 Rev. 1.
- Fossa, M., 1995, "A Simple model to evaluate direct contact heat transfer and flow characteristics in annular two-phase flow," *International Journal of Heat and Fluid Flow*, 16(4), pp. 272-279.
- Fu, F., and Klausner, J., 1997, "Separated flow model for predicting two-phase pressure drop and evaporative heat transfer for vertical annular flow," *International Journal of Heat and Fluid Flow*, 18(6), pp. 541-549.
- Fukano, T., and Kariyasaki, A., 1993, "Characteristics of gas-liquid two-phase flow in a capillary tube," *Nuclear Engineering and Design*, 141, pp. 59-68.

- Garimella, S.V., and Chen, T., 2006, "Measurements and high-speed visualizations of flow boiling of a dielectric fluid in a silicon microchannel heat sink," *International Journal of Multiphase Flow*, 32(8), pp. 957-71.
- Gurrum, S.P., Suman, S.K., Joshi, Y.K., and Fedorov, A.G., 2004, "Thermal issues in next-generation integrated circuits," *IEEE Transactions on Device and Materials Reliability*, 4(4), pp. 709-14.
- Harirchian, T., and Garimella, S.V., 2009, "Effects of channel dimension, heat flux, and mass flux on flow boiling regimes in microchannels," *International Journal of Multiphase Flow*, 35(4), pp. 349-62.
- Harirchian, T., and Garimella, S.V., 2008, "Microchannel size effects on local flow boiling heat transfer to a dielectric fluid," *International Journal of Heat and Mass Transfer*, 51(15-16), pp. 3724-35.
- Hay, H. L., and Hollingsworth, D. K., 1996, "A comparison of trichromic systems for use in the calibration of polymer-dispersed thermochromic liquid crystals," *Journal of Experimental Thermal and Fluid Science*, 12, pp. 1-12.
- Hetsroni, G., Klein, D., Mosyak, A., Segal, Z., and Pogrebnyak, E., 2004, "Convective boiling in parallel microchannels," *Journal of Microscale Thermophysical Engineering*, 8(4), 2004, pp. 403-21.
- Hewitt, G. F., and Hall-Taylor, N. S., 1970, *Annular Two-phase Flow*, Pergamon, New York.
- Hozejowska, S., Piasecka, M., and Poniewski, M.E., 2009, "Boiling heat transfer in vertical minichannels: Liquid crystal experiments and numerical investigations," *International Journal of Thermal Sciences*, 48(6), pp. 1049-59.

- Huh, C., Jeongbae, K., and Kim, M. H., 2007, "Flow pattern transition instability during flow boiling in a single microchannel," *International Journal of Heat and Mass Transfer*, 50(5-6), pp. 1049-60.
- Incropera, David P. DeWitt, 2002, *Fundamentals of Heat and Mass Transfer*, John Wiley and Sons, 5th edition, New York.
- Jacobi, A.M., and Thome, J.R., 2002, "Heat transfer model for evaporation of elongated bubble flows in microchannels," *Journal of Heat Transfer*, 124(6), pp. 1131-36.
- Jiang, L., Koo, J., Wang, E., Bari, A., Cho, E.S., Ong, W., Prasher, R.S., Maveety, J., Kim, M.S., Kenny, T.W., Santiago, J.G., and Goodson, K.E., 2002, "Cross-linked microchannels for VLSI hotspot cooling," *Proceedings of ASME International Mechanical Engineering Congress and Exposition, IMECE2002*, Louisiana, USA, pp. 13-17.
- Jiang, L., Wong, M., and Zohar, Y., 2001, "Forced convection boiling in a microchannel heat sink," *Journal of Microelectromechanical Systems*, 10(1), pp. 80-87.
- Kaew-On, J., and Wongwises, S., 2009, "Experimental investigation of evaporation heat transfer coefficient and pressure drop of R-410A in a multiport mini-channel," *International Journal of Refrigeration*, 32(1), pp. 124-37.
- Kandlikar, S. G., 2002, "Fundamental issues related to flow boiling in minichannels and microchannels," *Experimental Thermal and Fluid Science*, 26(2-4), pp. 398-407.
- Kandlikar, S.G., 2001, "Two-phase flow patterns, pressure drop and heat transfer during boiling in minichannel and microchannel flow passages of compact heat exchangers," *Compact Heat Exchangers and Enhancement Technology for the Process Industries*, Begell House, New York, pp. 319-34.

- Kandlikar, S. G., and Balasubramanian, P., 2004, "An Extension of the Flow Boiling Correlation to Transition, Laminar, and Deep Laminar Flows and Microchannels," *Heat Transfer Engineering*, 25(3), pp. 86-93.
- Kandlikar, S.G., and Campbell, L., 2004, "Effect of entrance condition on frictional losses and transition to turbulence," *Proceedings of the Second International Conference on Microchannels and Minichannels (ICMM2004)*, pp. 229-235.
- Kawahara, A., Sadatomi, M., Okayama, K., Kawaji, M., and Chung, P. M.-Y., 2005, "Effects of channel diameter and liquid properties on void fraction in adiabatic two-phase flow through microchannels," *Heat Transfer Engineering*, 26(3), pp. 13-19.
- Kays, W.M., and London, A.L., 1984, *Compact heat exchangers*, McGraw-Hill, New York.
- Kew, P.A., and Cornwell, K., 1997, "Correlations for the prediction of boiling heat transfer in small-diameter channels," *Applied Thermal Engineering*, 17(8-10), pp. 705-15.
- Kline, J., and McClintock, F.A., 1953, "Describing uncertainties in single-sample experiments," *Journal of Mechanical Engineering*, 75, pp. 3-8.
- Kutateladze, S.S., 1961, "Boiling heat transfer", *International Journal of Heat and Mass Transfer*, 4, pp. 31-45.
- Kuznetsov, V. V., Shamirzaev, A. S., 2007, "Boiling Heat Transfer for Freon R21 in Rectangular Minichannel," *Heat Transfer Engineering*, 28(8-9), pp. 738-745.

- Landram, C. S., 1994, "Microchannel flow boiling mechanisms leading to burnout," *ASME Heat Transfer Division, Heat Transfer in Electronic Systems*, 292, pp. 129-136, 1994,
- Lazarek, G.M., and Black, S.H., 1982, "Evaporative heat transfer, pressure drop and critical heat flux in a small diameter vertical tube with R-113," *International Journal of Heat and Mass Transfer*, 25(7), pp. 945–60.
- Lee, J.D., and Pan, C., 1999, "Dynamics of multiple parallel boiling channel systems with forced flows," *Nuclear Engineering and Design*, 192(1), pp. 31-44.
- Lee, H.J., and Lee, S.Y., 2001b, "Heat transfer correlation for boiling flows in small rectangular horizontal channels with low aspect ratios," *International Journal of Multiphase Flow*, 27(12), pp. 2043–62.
- Lee, H.J., and Lee, S.Y., 2001a, "Pressure drop correlations for two-phase flow within horizontal rectangular channels with small heights," *International Journal of Multiphase Flow*, 27(5), pp. 783–796.
- Lee, J., and Mudawar, I., 2005a, "Two-phase flow in high-heat-flux micro-channel heat sink for refrigeration cooling applications: Part I-pressure drop characteristics," *International Journal of Heat and Mass Transfer*, 48(5), pp. 928–940.
- Lee, J., and Mudawar, I., 2005b, "Two-phase flow in high-heat-flux micro-channel heat sink for refrigeration cooling applications: Part II-heat transfer characteristics," *International Journal of Heat and Mass Transfer*, 48(5), pp. 941–55.
- Lee, M., Wong, Y.Y., Wong, M., and Zohar, Y., 2003, "Size and shape effects on two-phase flow patterns in microchannel forced convection boiling," *Journal of Micromechanics and Microengineering*, 13(1), pp. 155–164.

- Lee, P.S., Garimella, S.V., 2008, "Saturated flow boiling heat transfer and pressure drop in silicon microchannel arrays," *International Journal of Heat and Mass Transfer*, 51 (3-4), pp. 789-806.
- Liu, Z., and Winterton, R.H.S., 1991, "A general correlation for saturated and subcooled flow boiling in tubes and annuli, based on a nucleate pool boiling equation," *International Journal of Heat and Mass Transfer*, 34, pp. 2759–66.
- Liu, D., and Garimella, S.V., 2007, "Flow Boiling Heat Transfer in Microchannels", *Journal of Heat Transfer*, 129(10), pp. 1321-32.
- Lockhart, R.W., and Martinelli, R.C., 1949, "Proposed correlation of data for isothermal two-phase," two-component flow in pipes, *Chemical Engineering Progress*, 45, pp. 39–48.
- Megahed, A., Hassan, I., and Ahmed, T., "Flow Boiling Heat Transfer in a Silicon Microchannel Heat Sink Using Liquid Crystal Thermography," *Proceedings of the Sixth International ASME Conference on Nanochannels, Microchannels and Minichannels (ICNMM2008)*, June 23-25, 2008, Darmstadt, Germany.
- Mishima, K., and Hibiki, T., 1996, "Some characteristics of air–water two-phase flow in small diameter vertical tubes," *International Journal of Multiphase Flow*, 22, pp. 703–712.
- Moore, G. E., 1965, "Cramming more components onto integrated circuits," *Electronics*, 38 (8), pp. 114-117.
- Moriyama, K., Inoue, A., and Ohira, H., 1992, "The thermohydraulic characteristics of two-phase flow in extremely narrow channels: the frictional pressure drop and heat

- transfer of boiling two-phase flow, analytical model,” *Heat Transfer - Japanese Research*, 21(8), pp. 838-56.
- Muller-Steinhagen, H., and Heck, K., 1986, “A simple friction pressure drop correlation for two-phase flow pipes,” *Chemical Engineering Progress*, 20, pp. 297–308.
- Muwanga, R., Hassan, I., and MacDonald, R., 2007, “Characteristics of Flow Boiling Oscillations in Silicon Microchannel Heat Sinks”, *Journal of Heat Transfer*, 129(10), pp. 1341-51.
- Muwanga, R., and Hassan, I., 2006, “Local heat transfer measurements in microchannels using liquid crystal thermography: Methodology development and validation,” *Journal of Heat Transfer*, 128, pp. 617–26.
- Muwanga, R., and Hassan, I., 2007, “Thermo- fluidic characteristics in a cross-linked silicon microchannel heat sink,” *Proceedings of the ASME/JSME Thermal Engineering Summer Heat Transfer Conference*, HT 2007, Vancouver, British Columbia, Canada, 2, pp. 969-78.
- Nino, V.G., Hrnjak, P.S., and Newell, T.A., 2003, “Two-phase flow visualization of R134A in a multiport microchannel tube,” *Heat Transfer Engineering*, 24(1), pp. 41-52.
- Pan, C., and Chang, K.H., 2007, “Two-phase flow instability for boiling in a microchannel heat sink,” *International Journal of Heat and Mass Transfer*, 50(11-12), pp. 2078-88.
- Peles, Y.P., and Haber, S.A, 2000, “A steady state, one dimensional, model for boiling two phase flow in triangular micro-channel,” *International Journal of Multiphase Flow*, 26(7), pp. 1095-115.

- Qu, W., and Mudawar, I., 2003a, "Measurement and prediction of pressure drop in two-phase micro-channel heat sinks," *International Journal of Heat and Mass Transfer*, 46, pp. 2737–53.
- Qu, W., and Mudawar, I., 2003b, "Flow boiling heat transfer in two-phase micro-channel heat sinks-I: Experimental investigation and assessment of correlation methods," *International Journal of Heat and Mass Transfer*, 46(15), pp. 2755-71.
- Qu, W., and Mudawar, I., 2003c, "Flow boiling heat transfer in two-phase micro-channel heat sinks-II. Annular two-phase flow model," *International Journal of Heat and Mass Transfer*, 46(15), pp. 2773-84.
- Ravigururajan, T. S., 1998, "Impact of Channel Geometry on Two-Phase Flow Heat Transfer Characteristics of Refrigerants in Microchannel Heat Exchangers," *Journal of Heat Transfer*, 120(2), pp. 485-504.
- Revellin, R., and Thome, J.R., 2007, "A new type of diabatic flow pattern map for boiling heat transfer in microchannels," *Journal of Micromechanics and Microengineering*, 17(4), pp. 788-796.
- Rohsenow, W. M., 1952, "A Method of Correlating Heat Transfer Data for Surface Boiling of Liquids," *Transactions of ASME*, 74, pp. 969–76.
- Shah, M.M., 1976, "New correlation for heat transfer during boiling flow through pipes", *ASHRAE Transactions*, 82(2), pp. 66-86.
- Shah, R.K., and London, A.L., 1978, Laminar flow forced convection in ducts, *Advances in Heat Transfer Supplement 1*, Academic Press.

- Shao, N., Gavriilidis, A., and Angeli, P., 2009, "Flow regimes for adiabatic gas-liquid flow in microchannels," *Chemical Engineering Science*, 64(11), pp. 2749-61.
- Singh, S.G., Kulkarni, A., Duttagupta, S.P., Puranik, B.P., and Agrawal, A., 2008, "Impact of aspect ratio on flow boiling of water in rectangular microchannels," *Experimental Thermal and Fluid Science*, 33(1), pp. 153-60.
- Steinke, M.E., and Kandlikar, S.G., 2004, "An experimental investigation of flow boiling characteristics of water in parallel microchannels," *Journal of Heat Transfer*, 126(4), pp. 518-26.
- Steiner, D., and Taborek, J., 1992, "Flow boiling heat transfer in vertical tubes correlated by an asymptotic model," *Heat Transfer Engineering*, 13(2), pp. 43-69.
- Steinke, M.E., and Kandlikar, S.G., 2006, "Single-phase liquid friction factors in microchannel," *International Journal of Thermal Sciences*, 45(11), pp. 1073-1083.
- Steinke, M.E., and Kandlikar, S.G., 2005, "Review of single-phase liquid heat transfer in microchannels," *Proceedings of the Third International Conference on Microchannels and Minichannels*, Toronto, ON, Canada, Paper No. ICMM2005-75114.
- Streeter, V.L., 1961, *Handbook of Fluid Dynamics*, McGraw-Hill, New York.
- Sun, L., and Mishima, K., 2009, "Evaluation analysis of prediction methods for two-phase flow pressure drop in mini-channels," *International Journal of Multiphase Flow*, 35(1), pp. 47-54.
- Taitel, Y., and Dukler, A.E., 1976, "A model for predicting flow regime transitions in horizontal and near horizontal gas-liquid flow," *AIChE Journal*, 22, pp. 47-55.

The National Institute of Standards and Technology (NIST), website:
<http://webbook.nist.gov/>

Thome, J.R., Dupont, V., and Jacobi, A.M., 2004, "Heat transfer model for evaporation in microchannels. Part I: presentation of the model," *International Journal of Heat and Mass Transfer*, 47(14-16), pp. 3375-85.

Tran, T.N., Wambsganss, M.W., and France, D.M., 1996, "Small circular- and rectangular-channel boiling with two refrigerants," *International Journal of Multiphase Flow*, 22, pp. 485-98.

Triplett, K.A., Ghiaasiaan, S.M., Abdel-Khalik, S.I., and Sadowski, D.L., 1999, "Gas-liquid two-phase flow in microchannels, Part I: Two-phase flow patterns," *International Journal of Multiphase Flow*, 25, pp. 377-94.

Tuckerman, D., 1984, "Heat transfer microstructures for integrated circuits," Ph.D Thesis, Stanford University, CA.

Tuckerman, D.B., and Pease, R.F.W., 1981, "High-performance heat sinking for VLSI," *IEEE Electron Device Letters*, EDL-2(5), pp. 126-129.

Tu, X., Flow and Heat Transfer in Microchannels 30 to 300 Microns in Hydraulic Diameter, Ph.D. Thesis, University of Illinois, Urbana-Champaign, IL, 2004.

Turner, R. G., Hubbard, M. G., and Dukler, A. E., 1969, "Analysis and prediction of minimum flow rate for the continuous removal of liquid from gas wells," *Journal of Petroleum Technology*, 21, pp. 1475.

- Warrier, G.R., Dhir, V.K., and Momoda, L.A., 2002, "Heat transfer and pressure drop in narrow rectangular channels," *Experimental Thermal and Fluid Science*, 26, pp. 53–64.
- Wang, G., and Cheng, P., 2008, "An experimental study of flow boiling instability in a single microchannel," *International Communications in Heat and Mass Transfer*, 35(10), pp. 1229-34.
- Whalley, P.B., 1987, *Boiling, Condensation and Gas-Liquid Flow*, Oxford Science Publications, Oxford University Press, New York.
- Xiong, R., and Chung, J.N., 2007, "An experimental study of the size effect on adiabatic gas-liquid two-phase flow patterns and void fraction in microchannels," *Physics of Fluids*, 19(3), pp. 33301-1-8.
- Xu, J.L., Gan, Y.H., Zhang, D.C., and Li, X.H., 2005, "Microscale heat transfer enhancement using thermal boundary layer redeveloping concept," *International Journal of Heat and Mass Transfer*, 48(9), pp. 1662-74.
- Xu, J.L., Zhang, W., Wang, Q.W., Su, Q.C., 2006, "Flow instability and transient flow patterns inside intercrossed silicon microchannel array in a micro-timescale," *International Journal of Multiphase Flow*, 32(5), pp 568-92.
- Yadigaroglu, G., 1981, "Two-phase flow instabilities and propagation phenomena. In: Delhaye, J.M., Giot, M. and Riethmuller, M.L., Editors, *Thermohydraulics of Two-Phase systems for Industrial Design and Nuclear Engineering*, Hemisphere, Washington DC, pp. 353–403.

- Yen, T.-H., Shoji, M., Takemura, F., Suzuki, Y., Kasagi, N., 2006, "Visualization of convective boiling heat transfer in single microchannels with different shaped cross-sections," *International Journal of Heat and Mass Transfer*, 49 (21-22), pp. 3884-94.
- Yu, W., France, D.M., Wambsganss, M.W., and Hull, J.R., 2002, "Two-phase pressure drop, boiling heat transfer, and critical heat flux to water in a small-diameter horizontal tube", *International Journal of Multiphase Flow*, 28(6), pp. 927-41.
- Yun, R., Heo, J. H., and Kim, Y., 2006, "Evaporative heat transfer and pressure drop of R410A in microchannels," *International Journal of Refrigeration*, 29(1), pp. 92-100.
- Zhang, W., Hibiki, T., and Mishima, K., 2005, "Correlation for flow boiling heat transfer at low liquid Reynolds number in small diameter channels," *Journal of Heat Transfer*, 127(11), pp. 1214-21.
- Zhang, W., Hibiki, T., Mishiba, K., 2004, "Correlation for flow boiling heat transfer in mini-channels," *International Journal of Heat and Mass Transfer*, 47 (26), pp. 5749-63.
- Zivi, S.M., 1964, "Estimation of steady-state stem void-fraction by means of the principle of minimum entropy production," *Journal of Heat Transfer*, 86, pp. 247-252.

PUBLICATIONS

Journal

- **A. Megahed**, and I. Hassan, “Analytical Modeling of Annular Flow Boiling Heat Transfer in Mini- and Microchannel Heat Sinks”, *ASME Journal of Heat Transfer*, 2010, Vol. 132, Issue 4, 041012 (11 pages).
- **A. Megahed**, and I. Hassan, “Two-phase Pressure Drop and Flow Visualization of FC-72 in a Silicon Microchannel Heat Sink”, *International Journal of Heat and Fluid Flow*, 2009, Vol. 30, No. 6, pp. 1171-1182.
- **A. Megahed**, and I. Hassan, “Experimental Investigation of Flow Boiling Characteristics in a Cross-linked Microchannel Heat Sink using Thermo-Chromic Liquid Crystals”, accepted for publication in *ASME Journal of Heat Transfer* (in press).
- **A. Megahed**, and I. Hassan, “Local Flow Boiling Heat Transfer in Silicon Microchannel Heat Sinks Using Liquid Crystal Thermography”, submitted to *ASME Journal of Heat Transfer*.

Conference

- **A. Megahed**, and I. Hassan, “Experimental Investigation of Flow Patterns, Pressure Drop, and Flow Instability during Flow Boiling in a Cross-linked Microchannel Heat Sink”, will be presented at the 8th *International Conference on*

Nanochannels, Microchannels and Minichannels (ICNMM2010), August 1-5, 2010, Montreal, Canada.

- **A. Megahed**, I. Hassan, and K. Cook, “Experimental Investigation of Flow Boiling Heat Transfer Characteristics of FC-72 in Cross-linked Microchannel Heat Sinks using Thermochromatic Liquid Crystals”, *ASME 2009 2nd Micro/Nanoscale Heat & Mass Transfer International Conference (MNHMT2009)*, December 18-21, 2009, Shanghai, China.
- **A. Megahed**, and I. Hassan, “An Analytical Model for Annular Flow Boiling Heat Transfer in Microchannel Heat Sinks”, *ECI International Conference on Boiling Heat Transfer*, May 3-7, 2009, Florianópolis, Brazil.
- **A. Megahed**, and I. Hassan, “A New Correlation for Local Boiling Heat Transfer Coefficients of FC-72 in Microchannels Heat Sinks”, *Proceedings of the 1st European Conference on Microfluidics (Microfluidics 2008)*, December 10-12, 2008, Bologna, Italy.
- **A. Megahed**, I. Hassan, and T. Ahmad, “Flow Boiling Heat Transfer in a Silicon Microchannel Heat Sink Using Liquid Crystal Thermography”, *Proceedings of the 6th International ASME Conference on Nanochannels, Microchannels and Minichannels (ICNMM2008)*, June 23-25, 2008, Darmstadt, Germany.

APPENDIX A: EXPERIMENTAL DATA

Table 8-1 : Two-phase flow pressure drop data in the straight microchannel

heat sink ($\Delta T_{\text{sub}} = 4 \text{ }^\circ\text{C}$)

No.	$x_{e,o}$	G (kg/m ² .s)	q (kW/m ²)	$\Delta P_{\text{tp,fr}}$ (Pa)	$\Delta P_{\text{tp,a}}$ (Pa)
1	0.30	516.4	154.2	24405.7	2788.4
2	0.28	520.9	142.3	25408.6	2578.4
3	0.26	533.5	131.8	25472.0	2393.0
4	0.24	531.6	121.7	26205.9	2119.6
5	0.22	538.9	112.5	25197.6	1874.9
6	0.21	531.3	103.5	25306.1	1703.3
7	0.19	537.0	93.9	25453.0	1507.0
8	0.17	539.1	85.8	25552.9	1346.5
9	0.15	539.4	76.8	25135.7	1142.3
10	0.14	539.7	69.4	25153.8	1019.6
11	0.12	531.3	62.3	24678.5	856.3
12	0.11	524.3	55.5	21796.2	690.0
13	0.30	470.7	141.5	23790.7	2308.5
14	0.27	476.3	130.7	24642.6	1971.1
15	0.23	488.1	121.1	24703.5	1714.9
16	0.22	479.9	111.3	24163.0	1480.4
17	0.19	483.6	102.5	24451.2	1304.3
18	0.17	493.6	92.9	24250.3	1164.3
19	0.16	498.7	83.7	24021.9	1022.2
20	0.13	483.5	69.2	23640.0	786.3
21	0.14	488.9	68.9	23211.1	821.2
22	0.12	494.7	60.7	22580.2	727.5
23	0.29	425.5	129.3	23490.2	1836.8
24	0.27	434.1	120.1	23834.1	1654.0
25	0.23	442.9	109.9	23456.8	1416.4
26	0.23	424.8	101.5	22692.1	1301.6
27	0.21	428.8	92.0	22870.6	1111.3
28	0.19	435.8	83.4	22503.8	1039.0
29	0.17	444.5	74.7	22137.8	884.6
30	0.15	448.0	67.5	21905.8	808.1
31	0.13	456.4	59.1	21682.7	703.2
32	0.31	392.1	120.0	23156.4	1651.5
33	0.27	392.6	109.5	22323.0	1403.7
34	0.25	391.3	101.2	22383.1	1240.0
35	0.23	392.8	92.2	22086.1	1070.1

Table 9-1: (continued)

36	0.21	387.2	83.0	21417.8	900.8
37	0.18	392.7	74.0	21055.8	771.1
38	0.16	398.6	67.7	20318.2	703.3
39	0.15	384.8	60.4	19392.1	570.9
40	0.39	333.8	60.4	22928.4	1752.4
41	0.35	342.0	128.4	22641.8	1514.3
42	0.30	352.4	117.9	22040.0	1322.1
43	0.27	360.6	107.0	20482.5	1153.6
44	0.25	341.8	98.8	21309.0	955.8
45	0.23	333.7	91.0	20186.9	805.1
46	0.20	340.0	82.9	19597.1	689.5
47	0.18	334.5	74.7	18608.3	562.7
48	0.16	337.6	66.8	18454.7	487.2

Table 8-2: Flow boiling heat transfer data in the straight microchannel
heat sink ($\Delta T_{\text{sub}} = 4 \text{ }^{\circ}\text{C}$)

No.	$x_{e,o}$	G (kg/m ² .s)	q (kW/m ²)	h_{tp} (W/m ² .°C)	T_w (°C)
1	0.30	516.4	154.2	2441.0	68.0
2	0.28	520.9	142.3	2311.2	67.7
3	0.26	533.5	131.8	2220.8	67.3
4	0.24	531.6	121.7	2138.9	66.5
5	0.22	538.9	112.5	2085.0	66.0
6	0.21	531.3	103.5	1966.2	65.3
7	0.19	537.0	93.9	2336.9	64.3
8	0.17	539.1	85.8	2311.8	62.8
9	0.15	539.4	76.8	2449.7	61.6
10	0.14	539.7	69.4	2986.4	59.3
11	0.12	531.3	62.3	7308.6	58.2
12	0.11	524.3	55.5	23957.5	57.0
13	0.30	470.7	141.5	2261.4	67.6
14	0.27	476.3	130.7	2184.1	67.1
15	0.23	488.1	121.1	2257.7	65.7
16	0.22	479.9	111.3	2199.0	64.8
17	0.19	483.6	102.5	2054.3	64.0
18	0.17	493.6	92.9	2326.7	61.6
19	0.16	498.7	83.7	2735.2	60.3
20	0.13	483.5	69.2	5632.0	58.1
21	0.14	488.9	68.9	8299.0	58.0
22	0.12	494.7	60.7	20306.1	57.1
23	0.29	425.5	129.3	2307.4	66.4
24	0.27	434.1	120.1	2207.9	65.7
25	0.23	442.9	109.9	2217.7	64.4
26	0.23	424.8	101.5	2398.3	63.7
27	0.21	428.8	92.0	2740.9	61.7
28	0.19	435.8	83.4	2987.5	60.5
29	0.17	444.5	74.7	4881.1	58.5
30	0.15	448.0	67.5	7979.8	58.0
31	0.13	456.4	59.1	20772.7	56.9
32	0.31	392.1	120.0	2158.7	66.0
33	0.27	392.6	109.5	2212.2	64.6
34	0.25	391.3	101.2	2367.7	63.8
35	0.23	392.8	92.2	2837.1	61.5
36	0.21	387.2	83.0	3368.6	59.7
37	0.18	392.7	74.0	4723.1	58.7

Table 9-2: (continued)

38	0.16	398.6	67.7	8142.9	57.5
39	0.15	384.8	60.4	23205.6	56.8
40	0.39	333.8	60.4	2400.0	65.9
41	0.35	342.0	128.4	2311.6	64.8
42	0.30	352.4	117.9	2584.6	63.6
43	0.27	360.6	107.0	3278.7	61.3
44	0.25	341.8	98.8	3090.7	60.8
45	0.23	333.7	91.0	3558.1	59.4
46	0.20	340.0	82.9	5409.0	58.2
47	0.18	334.5	74.7	7870.0	57.5
48	0.16	337.6	66.8	21326.0	56.8

Table 8-3 : Two-phase flow pressure drop data in the cross-linked microchannel
heat sink ($\Delta T_{\text{sub}} = 4 \text{ }^{\circ}\text{C}$)

No.	$x_{e,o}$	G (kg/m ² .s)	q (kW/m ²)	ΔP_{tp} (Pa)
1	0.03	307.0	59.0	4162.4
2	0.09	292.2	61.1	5092.5
3	0.11	292.5	63.3	5526.9
4	0.14	283.4	65.1	5945.2
5	0.15	292.2	67.2	6508.6
6	0.18	298.2	70.6	7509.4
7	0.20	290.5	72.9	7591.0
8	0.21	294.0	72.8	7978.4
9	0.23	289.9	76.9	8327.9
10	0.25	283.6	79.2	8415.6
11	0.26	290.0	82.2	9043.3
12	0.26	280.6	75.0	8498.3
13	0.34	283.5	90.8	10341.1
14	0.34	293.6	94.6	11181.3
15	0.34	280.8	89.1	10293.6
16	0.38	288.4	97.1	11773.0
17	0.41	286.6	99.4	12202.8
18	0.42	295.0	104.2	13111.2
19	0.10	256.8	59.1	4252.8
20	0.13	249.8	61.6	4624.6
21	0.14	248.4	64.4	4755.8
22	0.15	256.8	63.6	5074.0
23	0.18	247.1	65.3	5276.6
24	0.22	243.6	67.9	5764.0
25	0.22	249.8	70.3	6073.2
26	0.26	240.5	72.4	6370.7
27	0.29	243.9	75.6	6973.4
28	0.31	249.8	78.4	7538.7
29	0.32	254.7	81.1	8137.0
30	0.34	240.5	78.5	7509.8
31	0.38	243.8	83.2	8408.2
32	0.40	245.3	85.6	8823.6
33	0.44	241.1	87.9	9155.7
34	0.46	247.6	93.1	10039.3
35	0.47	239.0	90.2	9513.7
36	0.50	239.8	95.5	10152.6
37	0.53	240.6	97.9	10615.0

Table 9-3: (continued)

38	0.56	239.9	100.4	11154.1
39	0.60	239.9	102.7	11757.0
40	0.04	241.2	38.6	2895.9
41	0.05	243.3	40.6	3083.7
42	0.07	240.8	43.1	3321.1
43	0.11	251.4	47.8	4213.3
44	0.16	237.6	49.9	4490.3
45	0.12	187.9	55.2	2677.0
46	0.14	193.6	56.9	3000.5
47	0.24	190.9	61.0	3913.3
48	0.26	192.7	62.8	4174.2
49	0.28	194.3	64.7	4480.2
50	0.30	198.3	66.3	4803.3
51	0.36	196.2	71.1	5400.8
52	0.38	190.8	70.8	5277.5
53	0.41	192.3	73.7	5688.4
54	0.43	196.3	76.5	6118.1
55	0.44	204.0	79.9	6663.7
56	0.46	202.2	81.9	6835.8
57	0.53	193.8	84.4	7042.7
58	0.56	195.7	86.6	7448.0
59	0.57	197.5	89.0	7755.3
60	0.63	194.8	91.8	8146.5
61	0.08	174.0	30.9	1952.6
62	0.10	177.2	32.4	2209.2
63	0.11	175.9	31.8	2231.5
64	0.13	185.0	32.3	2553.0
65	0.14	185.1	32.8	2674.1
66	0.22	187.6	37.4	3458.4
67	0.23	189.1	38.3	3571.9
68	0.38	190.5	50.3	5107.6
69	0.02	149.4	34.6	1244.7
70	0.09	157.2	48.5	1756.2
71	0.09	142.7	43.8	1530.4
72	0.12	141.2	45.5	1659.7
73	0.18	138.0	48.6	1892.8
74	0.21	147.6	54.2	2310.3
75	0.22	136.8	50.1	2036.0
76	0.24	139.0	52.1	2175.3
77	0.36	142.6	61.9	2974.3
78	0.37	154.9	67.9	3553.6

Table 9-3: (continued)

79	0.42	146.0	67.0	3459.0
80	0.46	148.5	70.5	3800.4
81	0.47	146.2	70.2	3752.1
82	0.48	153.4	74.0	4173.8
83	0.55	140.4	72.0	3882.4
84	0.56	144.7	74.8	4199.2
85	0.57	143.2	74.8	4169.9
86	0.64	140.7	77.5	4416.2
87	0.30	157.2	36.8	2981.5
88	0.30	153.6	40.4	2906.5
89	0.32	151.6	41.4	2954.3
90	0.33	153.6	42.0	3109.8
91	0.32	157.8	42.6	3184.9
92	0.04	121.7	21.6	965.5
93	0.06	111.7	20.6	894.7
94	0.07	107.8	20.1	873.0
95	0.11	107.3	22.3	959.6
96	0.12	121.4	25.8	1218.2
97	0.15	106.5	24.2	1058.7
98	0.16	114.1	26.6	1240.9
99	0.19	114.0	27.7	1310.6
100	0.25	108.2	28.9	1364.9
101	0.36	109.3	32.0	1714.0
102	0.39	107.1	32.9	1764.9
103	0.41	109.0	34.3	1863.6
104	0.45	106.0	35.8	1903.0
105	0.48	101.5	35.8	1840.2
106	0.49	111.3	40.3	2239.5
107	0.51	105.4	38.9	2065.3
108	0.57	104.8	41.3	2219.1
109	0.65	102.8	44.8	2385.0
110	0.31	117.4	36.5	1832.0
111	0.32	118.3	37.5	1896.2
112	0.36	116.2	38.2	1950.9

Table 8-4 : Two-phase flow heat transfer data in the cross-linked microchannel
heat sink ($\Delta T_{\text{sub}} = 4 \text{ }^\circ\text{C}$)

No.	$x_{e,o}$	G (kg/m ² .s)	q (kW/m ²)	h_{tp} (W/m ² .°C)	T_w (°C)
1	0.04	98.2	7.9	2.3	57.8
2	0.09	99.9	10.2	5.6	59.6
3	0.15	103.9	12.6	9.5	60.9
4	0.24	99.4	15.3	12.3	61.5
5	0.30	100.2	17.3	14.2	61.8
6	0.38	95.9	19.4	15.4	61.7
7	0.43	96.3	21.7	17.3	62.0
8	0.47	96.0	24.0	18.6	61.8
9	0.51	100.6	27.6	20.6	61.8
10	0.61	96.6	30.4	22.8	61.9
11	0.63	103.7	33.2	25.0	62.0
12	0.01	147.7	9.9	6.2	59.6
13	0.05	149.9	12.4	8.3	60.1
14	0.10	147.4	15.3	10.7	60.6
15	0.16	142.1	18.0	12.4	60.7
16	0.19	148.2	21.1	14.5	60.9
17	0.26	148.8	24.5	16.7	61.0
18	0.31	149.7	27.7	19.0	61.2
19	0.40	142.8	30.9	21.1	61.2
20	0.42	149.0	34.4	23.9	61.4
21	0.50	143.5	38.0	27.2	61.6
22	0.54	150.7	41.9	30.0	61.7
23	0.61	150.7	45.8	33.9	61.9
24	0.71	142.7	49.6	35.9	61.8
25	-0.04	170.6	7.2	1.1	57.3
26	0.01	165.9	10.9	5.2	57.8
27	0.07	168.7	15.2	10.0	58.3
28	0.14	163.8	19.9	13.6	58.7
29	0.21	167.4	24.9	17.0	58.8
30	0.30	167.3	30.3	19.8	59.1
31	0.37	167.0	36.1	23.5	59.3
32	0.45	169.7	42.1	27.8	59.5
33	0.54	166.4	48.4	32.3	59.8
34	0.65	165.1	55.5	38.1	60.1
35	0.04	186.5	20.6	3.9	57.4
36	0.09	192.5	25.3	6.2	57.9
37	0.15	186.3	28.8	9.1	58.6

Table 9-3: (continued)

38	0.18	191.2	32.0	12.0	58.9
39	0.24	182.2	35.5	13.6	59.1
40	0.29	188.2	40.2	17.2	59.3
41	0.36	189.1	45.5	21.1	59.4
42	0.43	186.5	50.5	24.0	59.7
43	0.50	185.5	56.2	29.8	59.6
44	0.52	197.1	61.5	36.1	59.2
45	0.04	233.3	20.2	3.4	59.8
46	0.08	229.9	25.8	5.8	60.2
47	0.14	233.0	33.0	9.4	60.3
48	0.21	229.0	40.6	13.3	60.5
49	0.29	234.2	49.5	16.7	60.8
50	0.39	228.9	58.9	21.5	61.1
51	0.45	238.5	68.2	25.4	56.7
52	0.53	229.5	72.7	31.4	58.2
53	0.52	233.1	72.8	32.6	59.4
54	0.12	275.0	29.9	10.9	59.8
55	0.20	270.3	38.2	16.2	60.0
56	0.27	272.8	47.3	21.7	60.0
57	0.34	275.3	55.3	25.4	60.1
58	0.41	275.9	64.0	30.4	60.3
59	0.49	278.7	74.4	37.6	60.4
60	0.62	275.6	88.8	47.5	60.6